Predictive Modelling and Experimental Measurement of Composite Forming Behaviour

by

Jinhuo Wang

BEng.(Hons.)

Thesis submitted to The University of Nottingham for the degree of Doctor of Philosophy

August 2008

ABSTRACT …. 5

ACKNOWLEDGEMENTS 6

NOMENCLATURE 7

CHAPTER 1 INTRODUCTION 12

1.1 INTRODUCTION TO COMPOSITE MATERIALS 12
1.1.1 Types of reinforcements 12
1.1.2 Types of fibre 13
1.1.3 Types of matrix 14
1.1.4 Classification of polymers 14
1.1.5 Pre-impregnated composites (prepregs) 15
1.2 MANUFACTURING TECHNIQUES 17
1.2.1 Prepreg manufacture 17
1.2.2 Matched-die moulding 18
1.2.3 Autoclave forming 19
1.2.4 Diaphragm forming 20
1.3 DEFORMATION MECHANISMS OF TEXTILE COMPOSITES 21
1.3.1 Introduction to fabric types 21
1.3.2 Deformation mechanisms of textile fabrics 23
1.4 PROJECT FRAMEWORK 27
1.5 SUMMARY OF OBJECTIVES AND OVERVIEW OF THESIS 28

CHAPTER 2 EXPERIMENTAL TECHNIQUES 31

2.1 INTRODUCTION 31
2.2 MATERIALS USED 32
2.2.1 Thermosetting resins 32
2.2.2 Unidirectional thermoset composites 32
2.2.3 Woven thermoset composites 33
2.3 MATERIAL CHARACTERISATION TESTS 33
2.3.1 Rheological characterisation of resin 33
2.3.2 Shear behaviour in picture frame tests 37
2.3.3 Shear behaviour in bias extension tests 41
2.3.4 Bending behaviour in 3-point bending tests 44
2.3.5 Bending behaviour in buckling tests 46
2.4 FORMABILITY CHARACTERISATION EXPERIMENTS 48
2.4.1 Overview of methodology 48
2.4.2 Hemisphere forming 49
2.5 OPTICAL MICROSCOPY 51

CHAPTER 3 PREDICTIVE MODELLING OF COMPOSITE VISCOSITIES 53

3.1 INTRODUCTION 53
3.2 REVIEW OF PREVIOUS WORK 55
3.2.1 Theoretical modelling 55
3.2.2 Experimental measurements 63
3.2.3 Discussion 77
3.2.4 Summary 86
3.3 MODELLING OF TRANSVERSE VISCOSITY 90
3.4 MODELLING OF LONGITUDINAL VISCOSITY 97
3.5 RESULTS, VALIDATION AND DISCUSSION 99
3.6 CONCLUSIONS 104

CHAPTER 4 BENDING BEHAVIOUR OF VISCOUS COMPOSITES 105

4.1 INTRODUCTION 105
4.2 REVIEW OF RELATED WORK 107
4.2.1 Experimental characterisation 107

4.2.2 Theoretical modelling ... *110*
4.2.3 Implementation in forming simulations ... *111*
4.3 EXPERIMENTAL CHARACTERISATION ... 113
4.3.1 Introduction ... *113*
4.3.2 Advantages/disadvantages of characterisation method ... *114*
4.3.3 Interpretation of buckling curves ... *115*
4.3.4 Investigation of bending shape ... *117*
4.3.5 Rate dependence ... *118*
4.3.6 Temperature dependence ... *120*
4.3.7 Effects of lay-up (fibre orientation) ... *123*
4.3.8 Investigation of viscoelastic behaviour ... *125*
4.3.9 Investigation of sample thickness using optical micrograph ... *128*
4.3.10 Effects of micro-buckling ... *130*
4.3.11 Summary ... *135*
4.4 THEORETICAL MODELLING ... 137
4.4.1 Introduction ... *137*
4.4.2 Prediction of bending shape ... *138*
4.4.3 Assumptions in the bending model ... *139*
4.4.4 Modelling of 'elastic' buckling ... *140*
4.4.5 Modelling of 'plastic' buckling ... *147*
4.5 MODEL PREDICTIONS FOR A BUCKLING TEST ... 152
4.6 EFFECTS OF LONGITUDINAL VISCOSITY MODELS ... 153
4.7 EVALUATION OF BENDING MODEL FOR RATE DEPENDENCE ... 155
4.8 EVALUATION OF BENDING MODEL ON EFFECT OF FIBRE ORIENTATIONS ... 156
4.9 VALIDATION OF BENDING MODEL USING A STANDARD 3-POINT TEST ... 158
4.9.1 Experimental results ... *158*
4.9.2 Model predictions ... *159*
4.10 CONCLUSIONS ... 162

CHAPTER 5 SHEAR BEHAVIOUR OF VISCOUS COMPOSITES ... 165

5.1 INTRODUCTION ... 165
5.2 REVIEW OF PREVIOUS WORK ... 166
5.2.1 Experimental characterisation ... *166*
5.2.2 Theoretical modelling ... *169*
5.3 EXPERIMENTAL CHARACTERISATION ... 170
5.3.1 Introduction ... *170*
5.3.2 Effect of boundary conditions ... *171*
5.3.3 Influence of direction of shear deformation ... *173*
5.3.4 Influence of tow-meander ... *174*
5.3.5 Experimental reproducibility ... *176*
5.3.6 Investigation of aging effects ... *178*
5.3.7 Investigation of viscoelastic behaviour ... *179*
5.4 THEORETICAL MODELLING ... 182
5.4.1 Introduction ... *182*
5.4.2 Review of Multi-Scale Energy Model ... *183*
5.4.3 Experimental measurements of tow kinematics ... *189*
5.4.4 Predictive modelling of tow kinematics ... *191*
5.4.5 Validation of tow-kinematics model ... *194*
5.5 EVALUATION OF SHEAR MODEL FOR RATE DEPENDENCE ... 197
5.6 EVALUATION OF SHEAR MODEL FOR WEAVE ARCHITECTURE ... 199
5.7 EVALUATION OF SHEAR MODEL ON UNIDIRECTIONAL PREPREG ... 201
5.8 EVALUATION OF SHEAR MODEL USING BIAS-EXTENSION TESTS ... 203
5.9 CONCLUSIONS ... 205

CHAPTER 6 DISCUSSION AND CONCLUSIONS ... 208

6.1 INTRODUCTION ... 208
6.2 DISCUSSION ... 208
6.2.1 Micro-mechanical modelling ... *208*
6.2.2 Bending behaviour study ... *210*
6.2.3 Shear behaviour study ... *212*

6.3 MAJOR CONCLUSIONS 214
6.4 RECOMMENDATIONS FOR FUTURE WORK 216

REFERENCES…… 220

REFERENCES…… 220

APPENDIX 1.A PUBLICATIONS ARISING FROM THESIS..... 230

APPENDIX 3.A REVIEW OF UNIAXIAL CONTINUUM THEORY..... 231

APPENDIX 4.A: DETERMINATION OF OPTIMUM BENDING SPECIMEN DIMENSIONS..... 237

APPENDIX 4.B: EXPERIMENTAL REPRODUCIBILITY OF BUCKLING TESTS 241

APPENDIX 4.C: DERIVATION OF THE EQUATION OF OFFSET CURVES FOR BENDING SHAPE..... 243

Abstract

Optimised design of textile composite structures based on computer simulation techniques requires an understanding of the deformation behaviour during forming of 3-dimensional double-curvature components. Purely predictive material models are highly desirable to facilitate an optimised design scheme and to significantly reduce time and cost at the design stage, such as experimental characterisation. In-plane shear and out-of-plane bending are usually thought to be the key forming mechanisms. Therefore, this thesis is concerned with studies of the shear and bending behaviour by experimental characterisation and theoretical modelling.

Micromechanical interaction between fibre and matrix offers fundamental understanding of deformation mechanisms at the micro-scale level, leading to development of composite viscosity models, as input to shear and bending models. The composite viscosity models were developed based on rheological behaviour during movement of fibres, and validation was performed using experimental results collected from the literature. A novel characterisation method for measuring the bending behaviour, by means of a large-displacement buckling test, was attempted due to some significant advantages over other methods. Development of a bending model was also undertaken for unidirectional composites but experimental validation suggests further study may be required for woven composites. The shear behaviour was characterised using a picture frame test for viscous polymer composites. To obtain reliable experimental data, some efforts of improving the characterisation method were made. The experimental results were then used to validate a shear model, suggesting that further improvement is required, in terms of weave patterns, rate and temperature dependence.

Acknowledgements

The author wishes to thank his academic supervisors, Professor Andrew Long and Dr. Mike Clifford for their outstanding support during the course of this work, as well as Dr. Phil Harrison and Dr. Hua Lin for assistant supervision on 1st and 2nd year respectively. Great appreciation for the patient help, encouragement and excellent inspiration from my supervisor is also expressed. Without my kind supervisors, Without my PhD, Without my future achievements. Professor Tom Hyde, head of the School of Mechanical, Materials and Manufacturing Engineering, is also thanked for the use of the University facilities. The financial support of the Engineering and Physical Sciences Research Council (EPSRC), the School of Mechanical, Materials and Manufacturing Engineering (School of M3) and Ministry of Defence (MOD), and the collaborative support of Cambridge University, Hexcel Composites Ltd, MSC Software Ltd, QinetiQ Ltd, Ford Motor Company, Polynorm Plastics B.V., ESI Software, Granta Design Ltd and Saint-Gobain Vetrotex International are gratefully acknowledged. In particular the patient help and invaluable discussion from Dr. Michael P. F. Sutcliffe from Cambridge University, during my 2-year DOTComp involvement and the TexComp 8 conference, are also acknowledged.

Appreciation for the technical support of Roger Smith, Geoff Tomlinson and Paul Johns is also expressed. The help, guidance and opportunities for valuable discussion provided by Wout Ruijter, Dr. Kok Hoong Wong, Dr. Jon Crookston, Dr. Tong Wan, Dr. Dhiren Modi, Dr. Lee Harper, Dr. Tom Turner, Dr. Martin Sherburn, Dr. Kevin Brown, Dr. Peter Schubel, Dr. Sophie Cozien-Cazuc, Dr. Xuesen Zeng, Dr. Guozhan Jiang, Dr. Jing Yang, Dr. Liguo Zhao are sincerely acknowledged. Thanks are also expressed for the assistance given and contributions to the working environment made by the Composites Research Group. My lovely housemates, Dr. Minjie Xing, Dr. Jinghui Wang and Dr. Qiang Liu, who brought me unforgettable time, are also gratefully thanked.

Most importantly, the unconditional love, support and care of my family and my beloved wife have been unsurpassed at all times; for this I am eternally indebted.

Nomenclature

SYMBOLS	DESCRIPTION	IS UNIT
$\mathbf{A}$	Dyadic product of $\boldsymbol{a}$	-
A	Area	m^2
a	Fitting parameter	-
$\boldsymbol{a}$	Unit vector of fibre direction	-
a_T	Shift factor for Arrhenius model	-
$\mathbf{B}$	Dyadic product of $\boldsymbol{b}$	-
$\boldsymbol{b}$	Unit vector of fibre direction	-
b	Fitting parameter	-
$\mathbf{C}$	Dyadic product of $\boldsymbol{a}$ and $\boldsymbol{b}$	-
C	Constant parameter in integration	-
c	Fitting parameter	-
c_p	The phase-lag	rad
$\mathbf{D}$	The rate of deformation tensor	s^{-1}
d	Displacement	m
d_f	Fibre diameter	m
E	Elastic modulus	N/m^2
F	Force	N
G'	In-phase storage modulus	N/m^2
G''	Quadrature loss modulus	N/m^2
g	Gap	m
H	Height of resin film between two neighbour fibres	m

ΔH	The flow activation energy	Kmole/KJ
h	Thickness of the composite	m
$\mathbf{I}$	Unit tensor	-
I	Second moment of area	m^3
K	A constant factor in Coffin's model	-
k	Spring stiffness	-
L	Length	m
l	Length of the composite	m
M	Mass	Kg
P	Power (the rate of dissipation of energy)	Watt
p	Pressure	N/m^2
$(Q_{ij})_k$	Reduced stiffness matrix of the k^{th} layer of a laminate	N/m^2
R	Radius	
T	Temperature	K
T_a	Arbitrary tension in the fibre direction $\boldsymbol{a}$	N
T_b	Arbitrary tension in the fibre direction $\boldsymbol{b}$	N
t	Time	s
Δt	Time step	
U_e	Strain energy due to elastic deformation	J
u	Displacement	m
ν_{LT}	Longitudinal Poisson ratio	-
$\boldsymbol{v}$	Velocity in vector form	m/s
v	Velocity	m/s

υ	Amplitude ratio	-
W	Energy	J
w	Width of the composite	m
ω	Angular velocity	rad/s
ω_o	Natural frequency	Hz
$\mathbf{X}$	Position vector in the Lagrangian description	-
X_R	Material coordinates in the Lagrangian description	-
$\boldsymbol{x}$	Position vector in the Eulerian description	-
x_i	Spatial coordinates in the Eulerian description	-
α	The angular coordinate in a polar coordinate system	rad
Λ	Applied velocity	m/s
δ_{ij}	Kronecker delta	-
ρ	Density	Kg/m^3
ϑ	Phase angle	rad
γ	Shear strain	-
$\dot{\gamma}$	Shear strain rate	s^{-1}
η	Viscosity	Pa.s
η^*	Complex viscosity	Pa.s
η'	Dynamic viscosity	Pa.s
Φ	The frame angle of a picture frame	rad
θ	The material shear angle	rad
λ	Aspect ratio of a bias extension test	-
Δ	Minimum fibre gap	m

Δ_e	Difference in displacement of element	m
$\boldsymbol{\tau}$	Extra stress tensor	N/m^2
$\zeta_{ij}, \xi_{ij}, \varsigma_{ij}$	Stiffness constants	N/m^2
$\boldsymbol{\sigma}$	Stress tensor	N/m^2
σ	Stress	N/m^2
ε	Strain	-

SUBSCRIPT	DESCRIPTION
0	Initial
1,2,3	Principal directions
BE	Bias Extension test
c	Compressive
CY	Carreau-Yasuda model
e	element
eff	Effective
eq	Equivalent
f	Fibre
i, j, R	Indices of Cartesian coordinates
k	the k^{th} layer
L	Longitudinal
m	Matrix resin
n	Normal
p	Platen
PF	Picture frame

ref	Reference
rel	Relative
s	Shear
T	Transverse
t	Tangential
u	Unit volume
x, y, z	Global Cartesian coordinates

Chapter 1 Introduction

1.1 Introduction to composite materials

There are many examples of composite materials in our everyday lives, such as paper, wood, teeth and so on. A good example is concrete used in buildings. Concrete is made of cement (binder) and gravel (reinforcement), and is then transformed into a three-phase composite by adding another reinforcement, steel. In most cases composite materials can be defined as comprised of matrix and reinforcement. The objective of the matrix is to hold the reinforcement together in a required pattern. The reinforcement is usually much stiffer and stronger than the matrix, and gives the composite good properties. The reinforcement carries most of the external load that the composite is subjected to, while the matrix can effectively transfer the external loads to the reinforcement and protect it from adverse environmental effects.

1.1.1 Types of reinforcements

Basically, the reinforcement has three forms, particulate, discontinuous (short) fibre and continuous (endless) fibre. The particles of a particulate reinforcement generally have roughly equal dimensions in all directions [1]. For example, gravel is the particulate reinforcement in concrete. Fibres are reinforcements with one dimension significantly longer than others. Discontinuous fibres, such as chopped and milled fibres, have a variety of lengths, ranging from a few millimetres to a few centimetres. Usually the diameter of most fibres is a few microns, thus it does not need much length for

a particle to become a fibre. The reinforcement may be randomly oriented or ordered (aligned).

1.1.2 Types of fibre

In composite applications the most common types of fibrous reinforcement are glass, carbon and aramid. Glass fibres are amorphous and thus isotropic. Glass fibres have some advantages, such as high temperature-tolerance, good corrosion-resistance, radar transparency, and low cost. However, some disadvantages, such as abrasiveness, and low stiffness, limit their applications. Several different glass compositions are available, such as E-glass (E for electrical), C-glass (C for corrosion) and S-glass (S for strength). E-glass has excellent electrical and weathering properties, durability, and relatively low price, which makes it the most commonly used. C-glass has lower strength than E-glass but better corrosion-resistance, while S-glass offers higher strength, Young's modulus and temperature-tolerance than E-glass but is more expensive. Carbon fibres, typically 5 – 10 μm in diameter, are comprised of microscopic crystals of 'turbostratic' graphite, one of the allotropic forms of carbon. The carbon atoms are held together by strong covalent bonds in small crystallites, arranged in a regular hexagonal pattern, most of which are aligned along the long fibre axis. The good crystal alignment gives the fibre very high axial modulus and strength. These basic crystal units are highly anisotropic. Carbon fibres are mainly produced from polyacrylonitrile fibres, mesophase pitch and pyrolytic deposition. Carbon fibres have extremely high strength, stiffness, low weight and low thermal expansion, leading to popularity in

industrial applications, such as aerospace, automotive and motorsports. Carbon fibres are lighter and have higher axial modulus than glass fibres, but are more expensive. Aramid fibre is a generic form for a class of synthetic organic fibres named as aromatic polyamide fibres [2]. Aramid fibres have lower strength and stiffness than carbon fibres but are cheaper. They have better mechanical performance than glass fibres and exhibit good impact resistance. There are many other types of fibre available, such as natural fibres, boron fibres, polyethylene fibres, ceramic fibres, nonoxide fibres, and so on.

1.1.3 Types of matrix

According to the types of matrices used, composite materials can be classified as polymer matrix composites (PMCs), metal matrix composites (MMCs) and ceramic matrix composites (CMCs). Polymer is clearly the dominant matrix in most composite applications, and MMCs and CMCs are only used to a limited degree in specialised applications. For PMCs the reinforcement dominates the modulus and strength of the composite as polymers usually have lower modulus and strength than the reinforcing phase.

1.1.4 Classification of polymers

Figure 1.1 shows a simple classification of polymers used in PMCs. There are three important categories, thermosets, thermoplastics and rubbers. Within any class there are numerous different types of polymers available, e.g. thermosets include epoxy, polyester, polyimide, etc. Even for a given polymer, many forms may exist. For example, a different degree of cure (chemical

crosslinking) gives a different type of epoxy. Crosslinking, which links between polymer chains using covalent bonds, occurs during the curing reaction. Thermosetting polymers are resins in which the molecules are crosslinked in the form of a network and do not soften on heating. Thermoplastics soften and melt on heating, which allows them to be used in thermoforming. They become solid and maintain their shape in the mould when cooled. Scraps of thermoplastics can be recycled as they can be repeatedly heated, fabricated and cooled, although the properties will degrade due to a reduction in molecular weight.

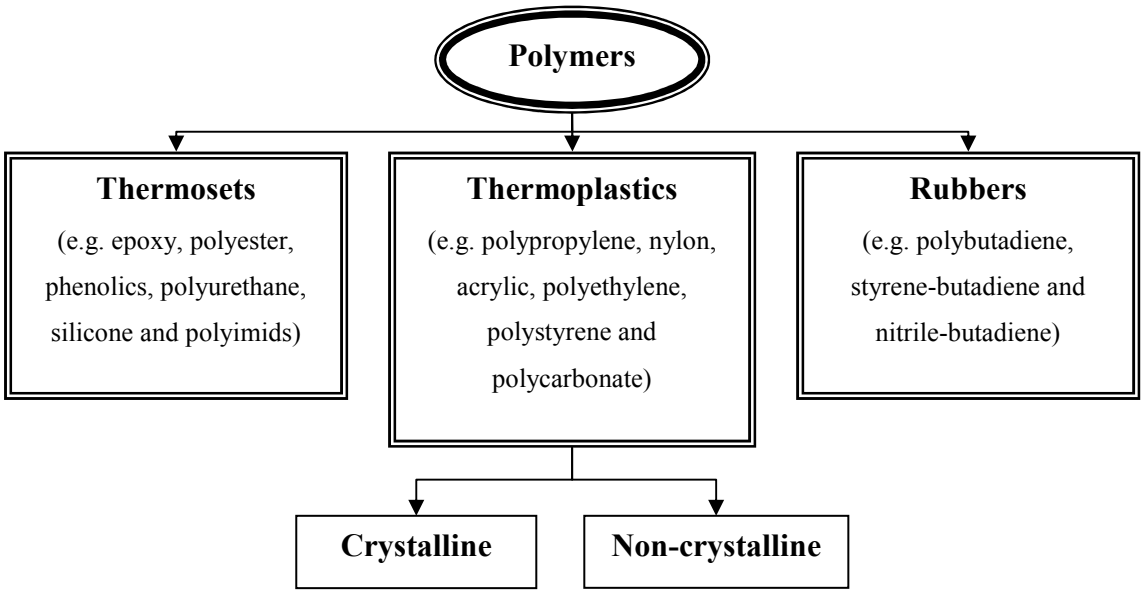

Figure 1.1. Flow chart of a classification of polymers. Reproduced from [3].

1.1.5 Pre-impregnated composites (prepregs)

Prepreg consists of a fibrous reinforcement (tow, fabric or mat) impregnated with thermoset or thermoplastic organic resin matrices under heat and pressure or with solvent, and capable of storage for later use. The useful life of

thermoset prepregs can be several weeks or sometimes several months when stored in a freezer (the shelf life can be 6-12 months if stored at below -18^{o}C). However, for thermosets curing process progresses all the time whatever the stored temperature. As resins are usually nearly solid at ambient temperatures, the thermoset prepreg is slightly sticky like adhesive tape. Thermoplastic prepregs are processed by heating above the melting point of the matrix and consolidating with pressure, and usually have no limit to shelf life due to chemical stability of resins when stored in their original packaging, away from humidity and at room temperature.

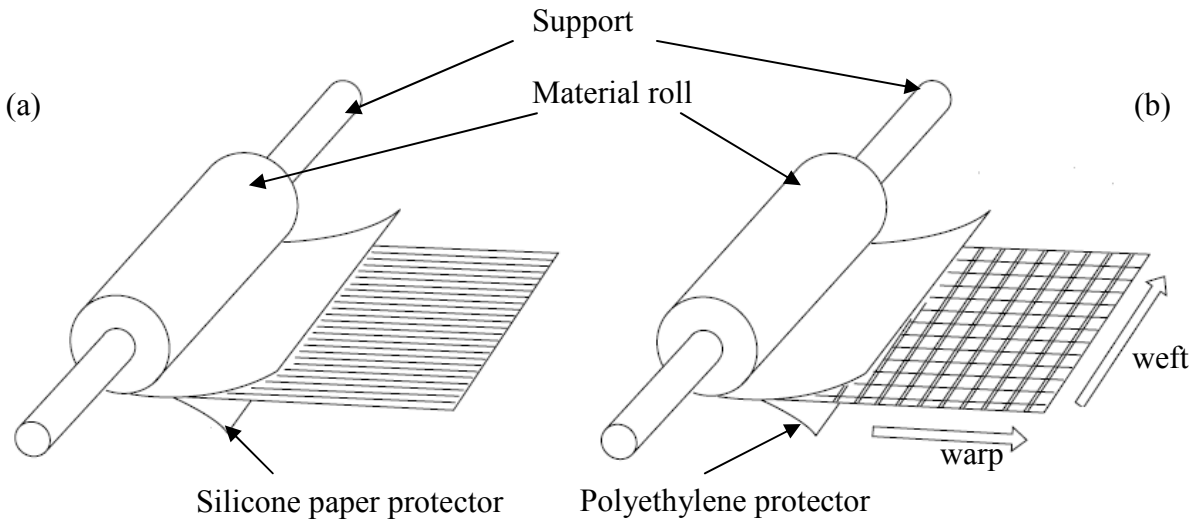

Figure 1.2. Schematic of two general forms of prepregs, (a) unidirectional reinforcement (b) fabric reinforcement. Reproduced from [4].

The most commonly used resins are thermosets, where epoxy dominates (other types of resins are available, such as polyester, phenolic and high temperature resins like polyimides, cyanate esters and bismaleimides). For thermosetting matrices, resins are usually partially cured or at a controlled viscosity, called B-stage (A-stage and C-stage mean that resins are not cured at all and fully cured

respectively). Any type of fibres and fabrics can be used to make prepregs. Prepregs are generally made in two forms, unidirectional (UD) and fabric forms, shown in Figure 1.2. UD prepreg has maximum translation of fibre mechanical properties, such as tensile and compression strength. It can be supplied in a variety of weights and thicknesses. Fabric prepreg is popular due to ease of handling and can be supplied in several weave styles.

Prepregs are popular due to a number of advantages, such as very precisely controlled fibre/resin ratios, ease of controlling fibre placement and angle, low fabrication cost, good mechanical performance (e.g. fatigue, tensile, stiffness, etc.), and so on. Prepregs can be applied to many processes ranging from hand lay-up to highly automated placement processes such as automated fibre, tow or tape placement. Prepregs can be used in applications ranging from sport and leisure to aerospace.

1.2 Manufacturing techniques

1.2.1 Prepreg manufacture

Figure 1.3 shows the process for manufacturing thermoset prepreg. The dry reinforcement is passed through a solution where the polymer is dissolved to significantly lower its viscosity to ease wetting and impregnation. Rollers or bars in the matrix bath are used to guide the reinforcement and to ensure impregnation. After the impregnated reinforcement emerges from the bath, it passes through nip rollers of a metering device which can carefully control the reinforcement-to-solution ratio. Following that, the impregnated reinforcement

enters a drying oven where the solvent is driven off and recovered. Before being rolled up in the final step, the prepregs are sandwiched between separation films (or backing papers) to prevent layers from adhering to each other.

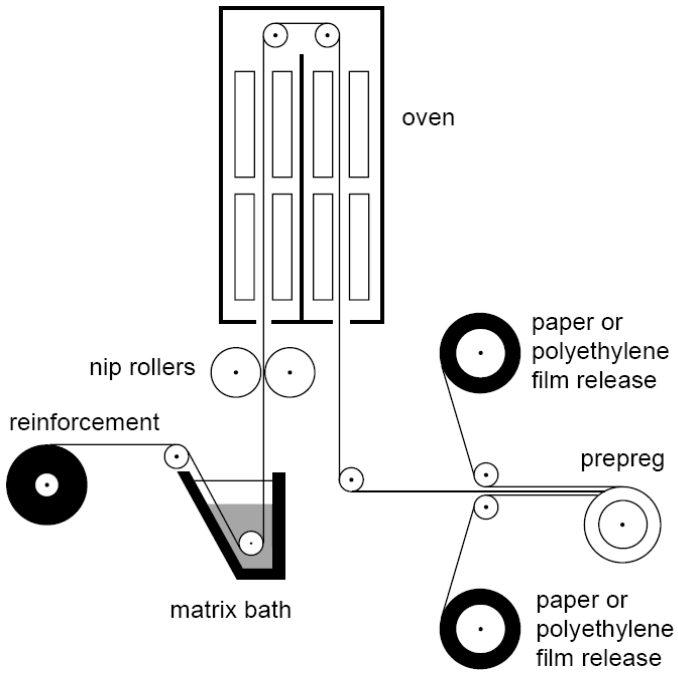

Figure 1.3. Schematic of making prepregs. Reproduced from [5].

1.2.2 Matched-die moulding

Matched-die moulding is also known as stamping as its process is similar to sheet metal stamping. A pair of matched metal dies (an example is shown in Figure 1.4) is mounted in a press which would supply pressure during forming of a composite material. The composite sheet is heated to the required temperature to soften the matrix. Following that, dies are closed at a pre-determined rate to force the blank to conform to the mould shape, and then sufficient pressure and temperature are maintained by the press and oven

during component curing and/or cooling to ensure that the shape is restrained. Once the component can maintain its new shape, it is demoulded from dies. Formability characterisation experiments in Section 2.4 employ this manufacturing technique.

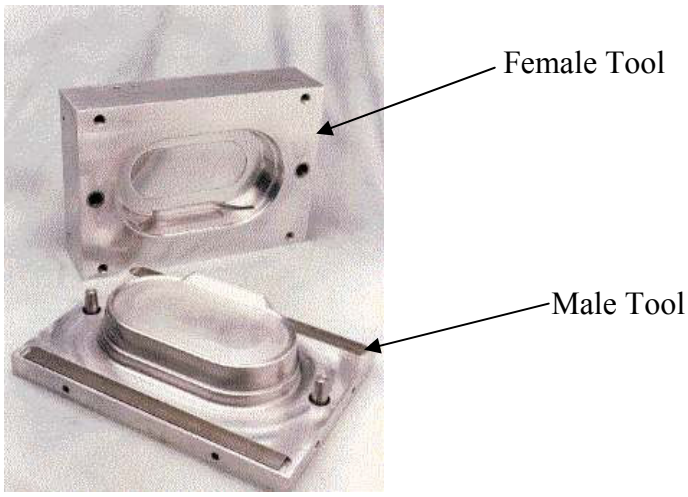

Figure 1.4. An example of male/female dies used in matched-die compression moulding. Reproduced from [6].

1.2.3 Autoclave forming

Autoclaves, closed and heated pressure vessels, can be applied to moulding processes where high pressure and temperatures are required (usually thermoset prepreg). Void content and thickness tolerances can be controlled accurately, but the efficiency is reduced in terms of the number of parts made per day. Autoclave forming can be applied to the manufacturing of superior quality structural component with high fibre volume fraction, but requires high cost due to expensive equipment and long cure cycle time. During autoclave forming of composites, the autoclave temperature is raised to the required value with a prescribed heat up rate, and then the pressure is increased to effect

forming, and finally the component is cooled under consolidation pressure. High processing pressures allow the moulding of thicker sections of complex shapes. Long cure cycles are usually required as the autoclave mass is large and takes a long time to heat up and cool down. An even temperature distribution on the tooling and composite components can be achieved using slow heat up rates.

1.2.4 Diaphragm forming

Diaphragm forming involves a composite laminate held between two thin plastically deformable sheets known as diaphragms, heated and formed against a mould by a combination of air pressure above the diaphragm and a vacuum drawn beneath the diaphragm [7]. Diaphragm forming is generally performed either in a pressure chamber or an autoclave. During forming, only the diaphragms are clamped around the mould edge and the composite can slide within the diaphragms, where subsequently surface friction imparts tension on the composite as the diaphragms are stretched, consequently suppressing wrinkling and splitting. The diaphragms are usually polymeric and are able to undergo high processing temperatures and substantial deformation without rupture. Advantages of this technique are primarily the degree of complexity achievable and the component quality. There are also some disadvantages, such as relatively long cycle time and limited deformation of diaphragm materials.

1.3 Deformation mechanisms of textile composites

1.3.1 Introduction to fabric types

In composite materials, a textile fabric is a manufactured assembly of long fibres, which is a flat sheet of one or more layers of fibres. These layers can be held together using manufacturing technologies originally developed for textile processes, such as weaving, braiding and knitting. Fabric types can be classified according to the orientation of fibres used and the method used to hold the fibres together. Some commonly used fabrics in textile composites are unidirectional (UD), woven, braided, knitted, multiaxial and random.

This thesis focuses on unidirectional and woven textile composites. UD fabrics have the majority or all of fibres running in one direction only. UD fabrics are used in prepreg composites (see Section 1.1.5). Woven fabrics are produced on looms by interlacing warp (0^o) and weft (90^o) fibres in a regular arrangement or weave pattern, with a large variety of weave patterns, weights and widths. The integrity of woven fabrics is maintained by the mechanical interlocking of fibres. The weave pattern dominates the characteristics of a fabric, such as surface smoothness, stability and drape, which is the ability to conform to a complex shape. Three examples of the weave pattern are shown in Figure 1.5.

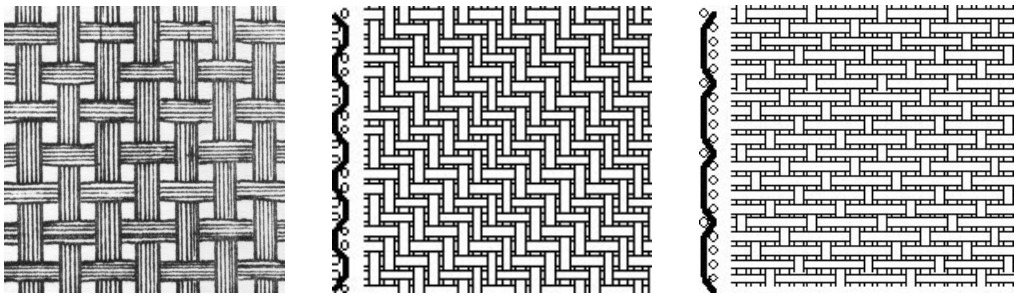

Plain weave 2x2 twill weave 5-harness satin weave

Figure 1.5. Three examples of different weave styles used in textile composites. Reproduced from [8].

Braided fabrics are produced by interlacing fibres in a spiral pattern to form tubular fabrics. Applications are those that require torsional strength, such as masts, propeller blades and drive shafts. Multiaxial warp knitted fabrics are processed by laying layers of long fibres atop one another in any arrangement and then stitching together, as shown in Figure 1.6. Due to reduced crimp, these fabrics make better use of the inherent strength of fibres and are more pliable than woven fabrics.

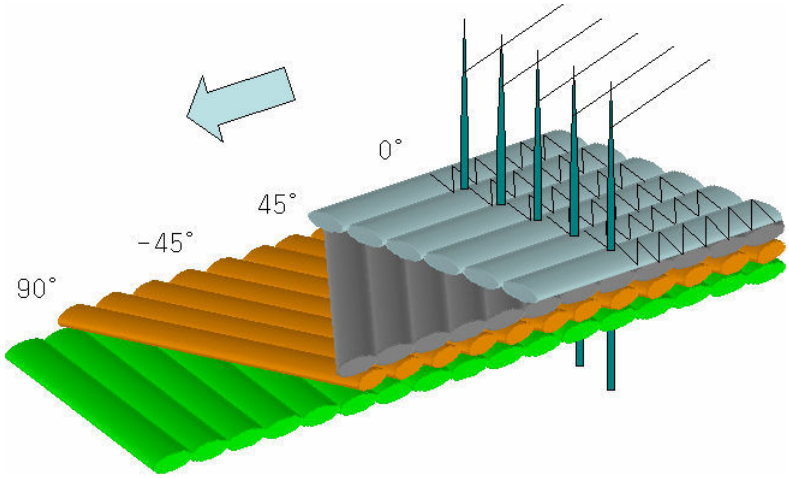

Figure 1.6. Schematic of a multiaxial warp knitted fabric. Reproduced from [9].

1.3.2 Deformation mechanisms of textile fabrics

When textile composite sheet is formed into complex shapes, a large number of deformation mechanisms may occur, such as trellising (shearing), bending, straightening, buckling, stretching, inter-fibre/inter-layer slipping, inter-layer rotation, and so on. They may be classified on three levels, macro-scale, meso-scale and micro-scale.

At the macro-scale, relative motions, such as translation and rotation, between adjacent layers can occur during forming of a multi-layer composite sheet, i.e. inter-ply slip and rotation. When forming a composite sheet with a single layer, intra-ply shear is the dominant mechanism [10, 11]. However, a small degree of intra-ply extension may occur due to the straightening of crimped tows (defined as fibre bundles or yarns) of woven textile composites. Intra-ply shear and extension are shown schematically in Figure 1.7.

At the meso-scale, deformation mechanisms may be classified into three regions, crossover (the intersection of two orthogonal tows), intra-tow and inter-tow (the region between two adjacent tows in the plane of the composite sheet). At crossover regions, the upper and lower tows may have both translational and rotational relative motion, as shown in Figure 1.8, which for viscous polymer composites would result in shearing of the thin polymer film between the superposed tows (dry frictional shearing for textiles). A viscous polymer composite is the composite with its polymer matrix at a viscous fluid state (such as a thermoset prepreg). Translational and rotational relative motion are denoted crossover slip and crossover shear respectively. At inter-tow

regions, inter-tow shear (Figure 1.8) arises from the translational relative motion between two adjacent tows in the plane. At tow regions, shown in Figure 1.9, during forming a tow may be subjected to a torque, bending moments, shear force and compression force, which will yield various deformation mechanisms, tow-twisting, tow-bending, tow-shear and tow-squeezing respectively.

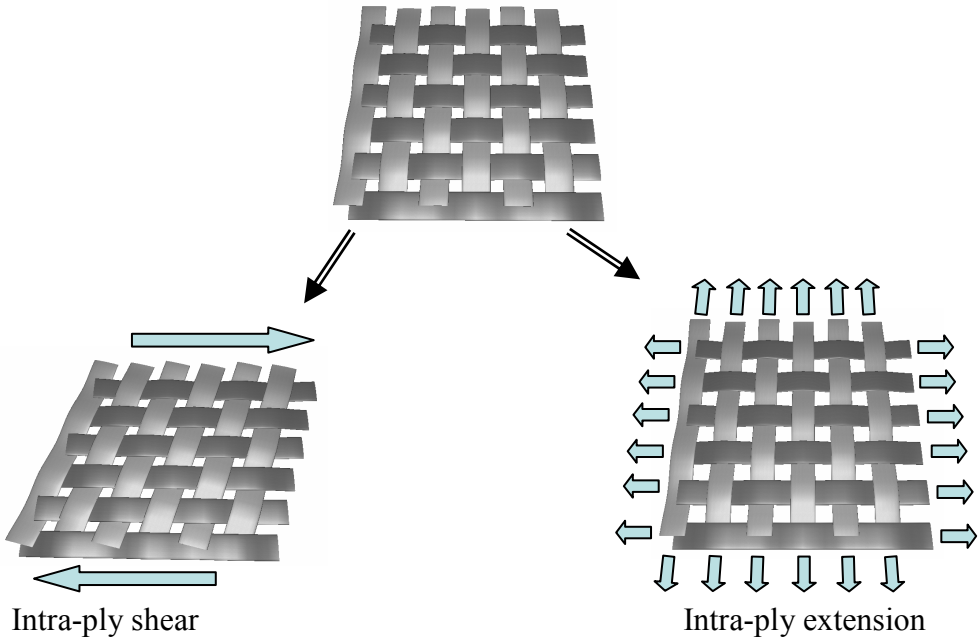

Figure 1.7. Schematic of different deformation mechanisms in macro-scale during forming of a textile composite sheet with a single layer. Reproduced from [11].

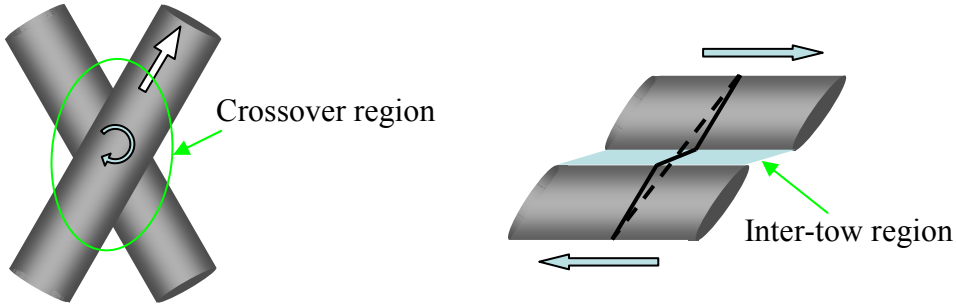

Figure 1.8. Schematic of different deformation mechanisms in meso-scale during forming of a textile composite sheet. Reproduced from [11].

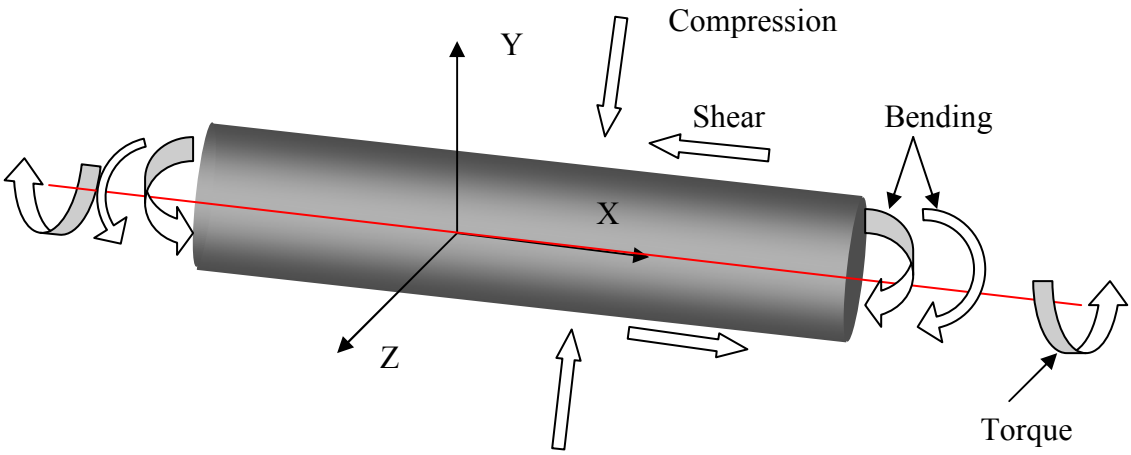

Figure 1.9. Free body diagram of a tow during forming of a composite sheet. The tow may be subjected to a torque about X axis and two bending moments about Y and Z axes, a compression force in the Y-Z plane and a shear force along X axis. Reproduced from [11].

At the micro-scale, deformation mechanisms may be classified as intra-fibre and inter-fibre. Analysis of intra-fibre deformation is analogous to that in Figure 1.9, while fibre interactions within a tow can be classified according to the shearing direction. Intra-tow axial shear (Figure 1.10(a)) and intra-tow transverse shear (Figure 1.10(b)) are caused by the shearing of the composite

sheet parallel and transverse to the fibre direction respectively. For a viscous polymer composite, the resistance of the fibres to shear along and perpendicular to the fibre direction is represented by longitudinal viscosity (η_L) and transverse viscosity (η_T) respectively. Predictive modelling of these two individual tow deformation mechanisms is attempted in Chapter 3, using basic material parameters available from manufacturers, such as fibre volume fraction and matrix rheology.

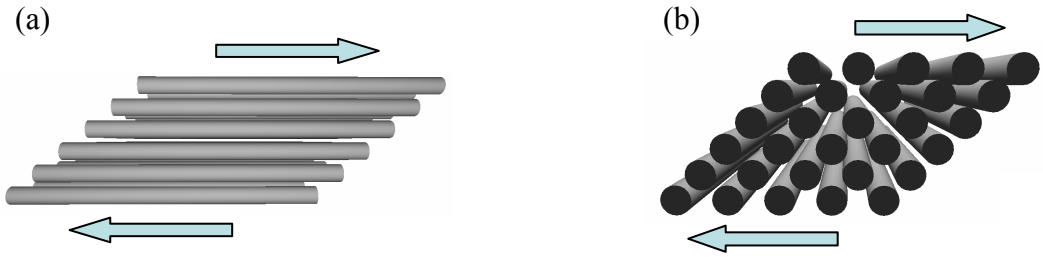

Figure 1.10. (a) Shearing the composite parallel to the fibre direction gives a measure of the longitudinal viscosity, η_L. (b) Shearing the composite across or transverse to the fibre direction gives a measure of the transverse viscosity, η_T. Reproduced from [11].

1.4 Project framework

This PhD research was carried out in the School of Mechanical, Materials and Manufacturing Engineering at the University of Nottingham, within the framework of a project entitled 'Design Optimisation of Textile Composite Structures (DOTComp)' which was funded by the UK Engineering and Physical Sciences Research Council (EPSRC) and Ministry of Defence (MOD). The project was supported by academic and industrial partners, Cambridge University, Hexcel Composites Ltd, MSC Software Ltd, QinetiQ Ltd, Ford Motor Company, Polynorm Plastics B.V., ESI Software, Granta Design Ltd and Saint-Gobain Vetrotex International. The aim of DOTComp was to develop advanced material models for forming and consolidation of composite structures, and new optimisation techniques by using these models in design and manufacturing, accounting for both material and process variables. Essentially, these material models are to predict the deformation behaviour of composite materials during forming into complex three-dimensional shapes at various temperatures, speeds and boundary conditions. Particular attention was paid to design and internal standardisation of appropriate characterisation methods for measuring the forming behaviour, and also to develop a theoretical schema for optimisation based on computer simulation technology and design methodologies. Some technical papers have been published as a result of work conducted within this project, as listed in Appendix 1.A.

1.5 Summary of objectives and overview of thesis

The aim of this thesis is to study composite forming behaviour using experimental characterisation and theoretical modelling, concentrating mainly on viscous polymer composite materials, in order to facilitate optimisation techniques in design of material structures. Chapter 2 describes the materials used and the experimental techniques essential for material characterisation within the framework of the DOTComp project. The rheological behaviour of polymers used as matrix phase are characterised in Section 2.3.1. Material forming behaviour, such as out-of-plane bending and in-plane shear, were characterised by various test methods which were used to validate theoretical models developed in chapters 4 and 5.

To develop an approach which can simulate and subsequently optimise composite formability at the design stage, various predictive techniques were required. As such, micro-mechanical models at the micro-scale (fibre/matrix), a bending model and a complementary shear model are developed in Chapter 3, 4 and 5 respectively. These theoretical models were studied along with experimental characterisation under various conditions, such as different rates and temperatures, which would be used in conjunction with a computer-based finite element forming simulation. Prior to understanding materials of more complex structure, fibre-matrix-fibre micro-mechanical interaction behaviour of a unidirectional composite was studied through modelling the shear behaviour along and transverse to the fibre direction, which provides a fundamental understanding of composite deformation at the micro-scale. These micro-mechanical models predict longitudinal and transverse viscosities, which

are reported in Chapter 3, and serve as two primary input material parameters for the bending model in Chapter 4 and the shear model in Chapter 5.

Out-of-plane bending and in-plane shear are usually thought to be the key deformation mechanisms during forming of composite sheets into double-curvature components. Bending stiffness of viscous textile composites was characterised by means of a large-displacement buckling test at a variety of displacement rates and temperatures. This method has some advantages, such as simplicity of set-up, usage of thin samples and ease of applying different rates and temperatures, compared to standard bending tests. Some aspects, such as rate/temperature dependence, were investigated. Although the test method has not yet been standardised, experimental measurements were used to compare with the theoretical model. The bending model is an energy summation approach, accounting for energy contributions from deformations of two constituents of viscous composites. The elastic contribution is mainly due to fibre bending, while the viscous behaviour is primarily due to matrix shearing. As the bending model must be independent of the characterisation method, a standard 3-point test was performed to assess its validity and to explore its limitations. These are presented in Chapter 4.

Chapter 5 is concerned with the in-plane shear behaviour of viscous composites, with efforts on standardisation of the test method and development of a fully predictive model. A predictive model referred to as the multi-scale energy model (MSEM) predicts the shear behaviour of viscous textile composites using matrix rheology, fibre volume fraction and textile

architecture. This was developed further to improve the predictive capability and to provide further validation. One of the experimentally determined inputs, tow kinematics from a heterogeneous shear strain profile which reflects the relationship between shear within the individual tows and the whole material, was predicted using an energy minimisation method based on contributions from various regions within the material structure. The method was validated by both comparing predicted tow kinematics with experimental measurements on formed components and comparing shear force predictions with experimental results.

Finally, the key outcomes are discussed and major conclusions within the main body of this thesis are summarised, and several recommendations for future work are made.

Chapter 2 Experimental techniques

2.1 Introduction

This chapter describes the equipment, methodologies and experimental procedures used to characterise viscous composites forming, in addition to materials used in this thesis. The techniques associated with characterisation experiments are presented along with typical results.

The first part of this chapter is on fundamental material behaviour. As predictions of the bending and shear behaviour are based on the properties of the matrix resin, rheological characterisation, obtaining the viscosity data of epoxy resin at different temperatures and shear rates, is presented. Following this, characterisation techniques for the forming mechanisms, using a picture frame or bias extension test for shear and a 3-point bending or buckling test for bending, are described. Measurements based on these tests are used to validate the models presented in Chapters 4 and 5.

The second part is about material formability. Good formability of a composite material means that the material can be formed to produce components in the desired shape with few defects. Formability depends not only on material constituents but also on the processing conditions. To obtain a fundamental understanding of effects of processing conditions on formability, it is essential to perform formability characterisation experiments. Besides this, formability results could be used to assess the bending and shear models. Therefore,

hemisphere forming experiments were conducted to characterise formability of viscous polymer composites.

Finally, optical microscopy, related to studies of the shear and bending behaviours, is also presented.

2.2 Materials used

2.2.1 Thermosetting resins

In this thesis three partially-cured epoxy thermosetting resins were characterised, as used in unidirectional and woven prepregs, which were provided by the manufacturer, Hexcel Composites, UK. The first one, HexPly® M47 (1947), was characterised using a Bohlin Rheometer, presented in Section 2.3.1. The second and third resins, HexPly® M21 and HexPly® 8552, were characterised by the manufacturer. Data sheets of the three resins can be found in [12-14].

2.2.2 Unidirectional thermoset composites

Two unidirectional (UD) thermosetting carbon/epoxy prepregs were used. Material codes are respectively: M21/35%/268/T800S and 8552/34%/194/AS4. M21 and 8552 are the resin types (see Section 2.2.1). 35% and 34% represents the resin weight percentage. 268 and 194 are the fibre areal weights (in g/m^2). T800S and AS4 are fibre types, where details can be found in [15, 16].

The measured thickness for these two uncured UD prepregs is approximately 0.3 mm. Fibre volume fraction (v_f) can be calculated as

$$v_f = \frac{M_f}{\rho_f V_{comp}} \tag{2.1}$$

where M_f, ρ_f and V_{comp} are fibre areal weight, fibre density and composites volume per unit area respectively. The fibre density of these two UD prepregs can be found in technical data sheets. From this, the fibre volume fractions prior to consolidation for M21 and 8552 UD prepregs are 50% and 36% respectively.

2.2.3 Woven thermoset composites

The woven thermoset carbon/epoxy prepreg (automotive prepreg) is M47N/42%/280T4X4/CHS-3K. The interpretation of the material codes and the determination of fibre volume fraction are similar to the previous section. The fibre volume fraction is 43%. Measurements of thickness, tow width and spacing are 0.36, 1.31 and 0.11 mm.

2.3 Material characterisation tests

2.3.1 Rheological characterisation of resin

The main aim here is to obtain viscosity of the matrix resin at different shear strain rates and temperatures for use in subsequent models for composite forming behaviour. The resins used were described in Section 2.2.1. The rheology was characterised using a Bohlin Rheometer with rotational

viscometry, shown in Figure 2.1. An oven was used for tests at elevated temperatures. Specimens were located between two parallel aluminium plates with a diameter of 25 mm. The resin specimens were circular discs with 25 mm diameter and about 1.2 mm thickness. The disc was loaded at room temperature via the circular plates and squeezed to a gap of 1 mm.

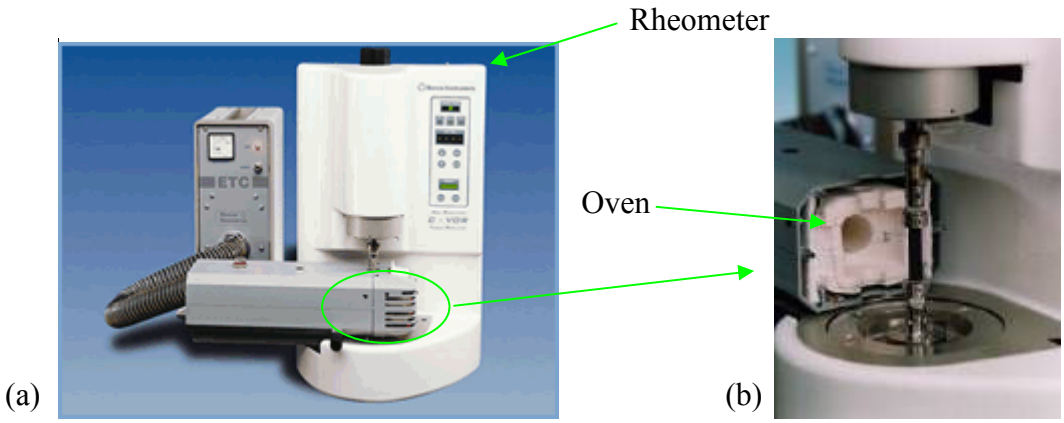

Figure 2.1. (a) Photograph of a Bohlin Rheometer (b) Photograph showing the oven.

Experiments were performed at room temperature (23^{o}C), 40, 50, 60, 70, 80, 90, and 100^{o}C. Due to the high viscosity of partially-cured epoxy at room temperature, oscillatory tests were initially performed. The dynamic viscosity was measured instead of the steady state viscosity. According to [17], the Cox-Merz rule can be applied to translate the measured dynamic viscosities to steady state viscosities. However, in [18], doubts regarding the validity of this method for cross-linked epoxy were expressed. Therefore, rotational viscometry was used, but with maximum shear rate restricted to 1 s^{-1}. Higher rates at room temperature were impossible to achieve using the Rheometer. Therefore, viscosity data at higher rates at room temperature had to be obtained via extrapolation.

To produce a master curve for all temperatures, shift factors [19] for each temperature at a chosen reference temperature can be determined by:

$$a_T = \frac{\eta_0(T)}{\eta_0(T_{ref})} \tag{2.2}$$

where $\eta_0(T)$ and $\eta_0(T_{ref})$ are the plateau values of the steady state viscosity at zero shear rate at temperature T (in K) and reference temperature T_{ref} (in K) respectively. These data were then fitted with the Arrhenius equation [19]:

$$\log(a_T) = \frac{\Delta H}{2.303R_g}(T^{-1} - T_{ref}^{-1}) \tag{2.3}$$

where ΔH is the flow activation energy and R_g is the Boltzman gas constant. Finally, a combination of the Arrhenius and Carreau-Yasuda models [19] can be used to fit experimental data:

$$\eta = \eta_o a_T \{1 + (a_T c_{CY} \dot{\gamma})^{a_{CY}}\}^{(b_{CY}-1)/a_{CY}} \tag{2.4}$$

where η is the viscosity measured, η_0 is the viscosity at zero shear strain rate, c_{CY}, a_{CY} and b_{CY} are fitting parameters of the Carreau-Yasuda model.

Experimental results for HexPly® M47 and HexPly® M21 shown in Figure 2.2 are the viscosities against shear strain rate at different temperatures. Due to high viscosity, the maximum shear strain rate that the Rheometer can reach at room temperature is 1 s^{-1}. The Arrhenius and Carreau-Yasuda models (Equations (2.2)-(2.4)) were then used to fit these data using a least squares method. The fitted parameters are shown in Table 2.1.

Table 2.1. The fitted parameters of Carreau-Yasuda model.

Model Parameters	η_0 (Pas)	a_{CY}	b_{CY}	c_{CY}	ΔH (Kmole/KJ)	T_{ref} (K)
HexPly® M47	137.8	2	0.92	5.56	108.5	333
HexPly® M21	1507.0	2	0.93	8.39	127.6	333

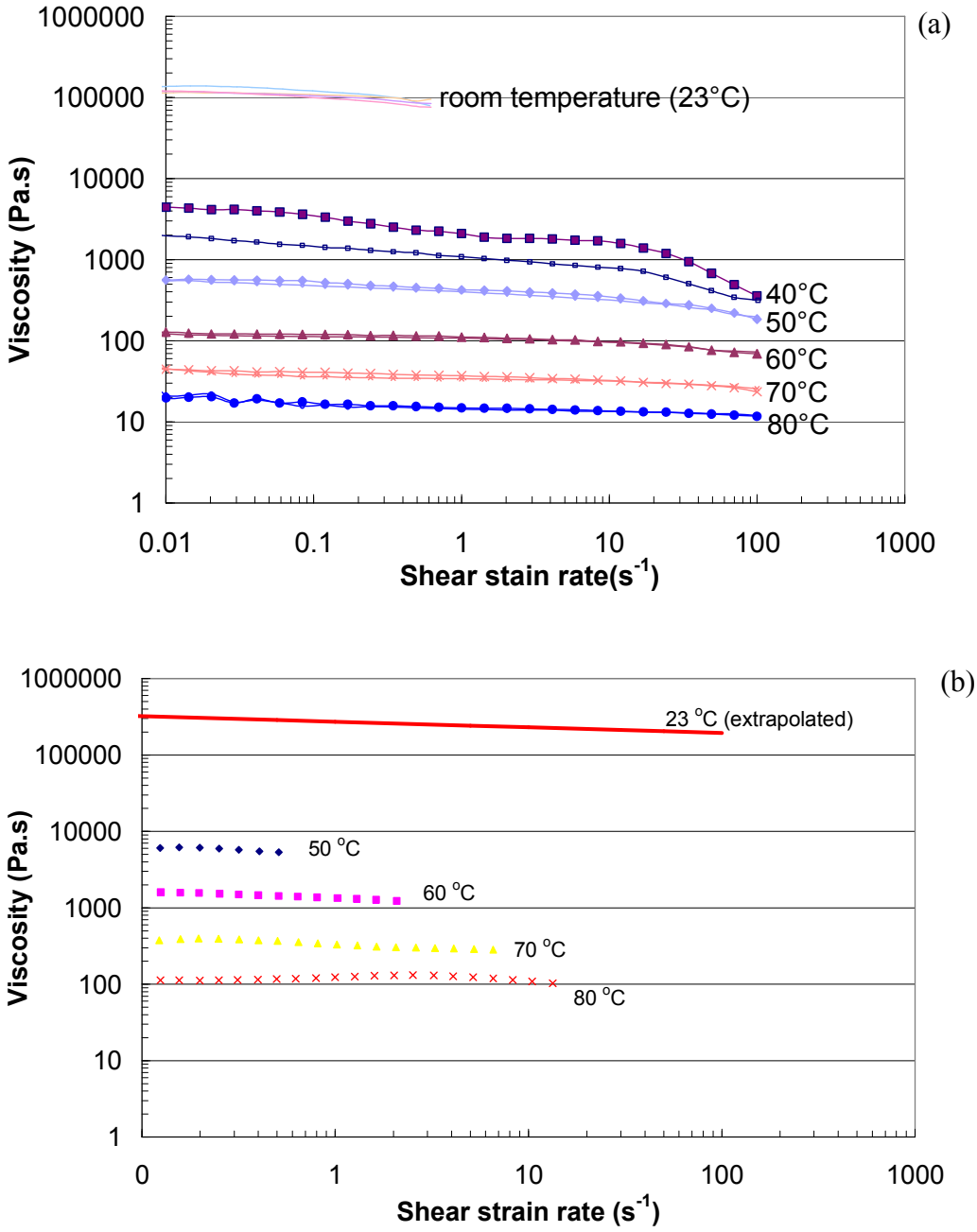

Figure 2.2. Viscosities of partially-cured epoxy at different temperatures (a) HexPly® M47 (b) HexPly® M21 (data from the manufacturer).

2.3.2 Shear behaviour in picture frame tests

Picture frame tests have been used widely to characterise the in-plane shear behaviour of thermoset and thermoplastic continuous fibre-reinforced composites in addition to textile materials [19-25]. The test method used has been standardised internally at the University of Nottingham. Material sheets were cut into a cruciform shape shown in Figure 2.3(a) using a template shown in Figure 2.3(b). The tows were parallel or perpendicular to the outer edges of the sample.

(a) (b)

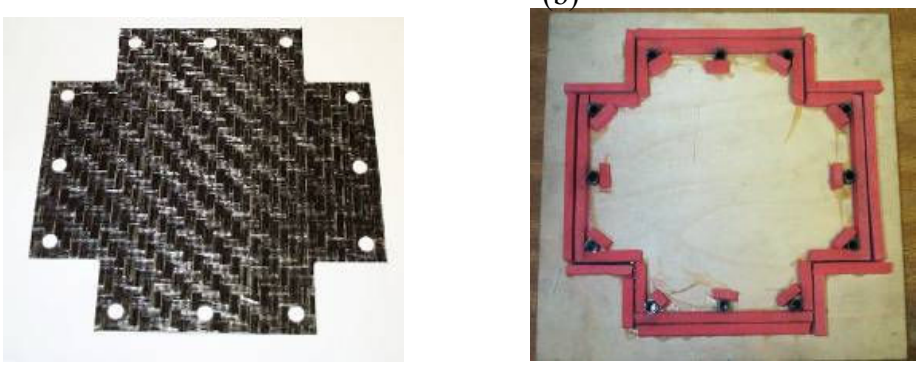

Figure 2.3. (a) sample shape (b) the template

The cut specimens were then held in picture frame test apparatus (Figure 2.4) comprising of a four-bar linkage loaded by a Universal Testing machine through a load cell connected to the crosshead. Great care must be taken to eliminate any misalignment which could cause large scatter in measured data due to fibre tensile stresses being induced. Four bars were hinged at each corner such that the initially square frame became a rhombus when loaded. The axial force versus displacement at various rates was recorded by a PC which controls the machine at a prescribed displacement rate. For UD prepregs,

usually two layers are used, oriented parallel to the sides of the picture frame shown in Figure 2.4 (i.e. $0/90^{o}$) in order to balance the picture frame rig during shearing. According to the investigation of the boundary condition used in the PF test method for prepregs in Chapter 5, a clamped condition was used to avoid wrinkling in the samples. The specimen is thus fastened into the frame using clamps with a grooved surface to prevent slip. For all experiments three repeats were performed for each condition to assess the variability of the shear response.

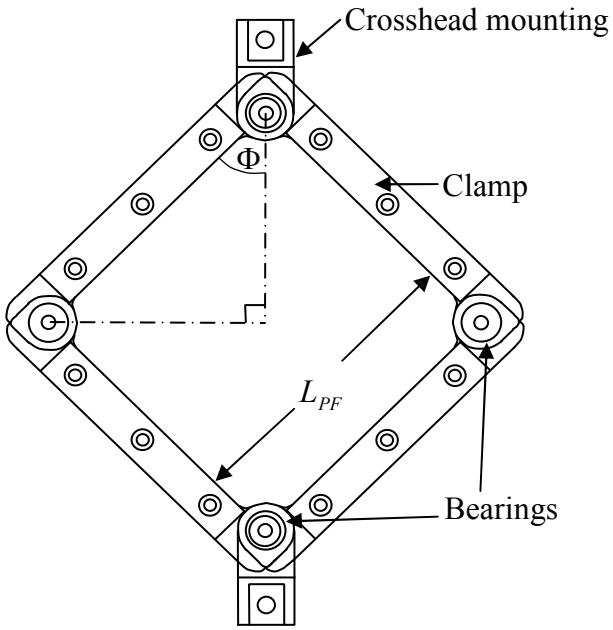

Figure 2.4. Picture frame shearing test apparatus prior to shear, where L_{PF} =145mm.

If investigation of temperature dependence is required, an environmental chamber is used to heat samples. To minimise heat-up times the picture frame rig and clamps were heated to the required temperature in the chamber prior to mounting the sample. Once prepreg samples were clamped within the frame,

heat-up times of samples were consistently 10 minutes to obtain uniform temperature distribution.

During the test, a constant displacement rate was applied to the crosshead and the axial picture frame force (F_{PF}) and the displacement (d_{PF}) of the crosshead are measured. F_{PF} and d_{PF} can be normalised by the side length of the picture frame L_{PF} [20]. If data of shear force (F_s) versus shear angle (θ) are required, then F_{PF} and d_{PF} need to be converted through Equations (2.5) and (2.6).

$$F_s = \frac{F_{PF}}{2\cos\Phi} \tag{2.5}$$

where Φ is the frame angle, which can be related to the shear angle (θ) through $\theta = \pi/2 - 2\Phi$.

$$\theta = \frac{\pi}{2} - 2\cos^{-1}\left[\frac{1}{\sqrt{2}} + \frac{d_{PF}}{2L_{PF}}\right] \tag{2.6}$$

where the shear deformation of the entire specimen is assumed to be uniform and under pure shear, i.e. the actual shear angle measured from the fabrics at any point is equal to that calculated from the crosshead displacement. This has been proved reasonable by several research groups using various techniques [26-28].

The viscoelastic behaviour and the elastic contribution of viscous composites during shearing can be investigated by performing stress relaxation tests following a picture frame (PF) test. A stress relaxation test involves stopping the test at a fixed displacement and then measuring the decay in force with

time. For the purpose of illustration, the results of a schematic stress relaxation test are shown in Figure 2.5. During the relaxation tests, the force decay is measured after stopping the crosshead displacement at 15, 30, 45 and 60 mm. A typical result is shown in Figure 2.6. To ensure fully relaxed forces at the relaxation time of 1200 sec, the force which was relaxed at longer relaxation time of 2400 sec is compared. If the variation between these two relaxation times is negligible, then 1200 sec is approximately the relaxation time to obtain fully relaxed forces. At each displacement, the axial force relaxes to an elastic force, which can be used to determine the elastic contribution of the composite material in a PF test with increasing displacement.

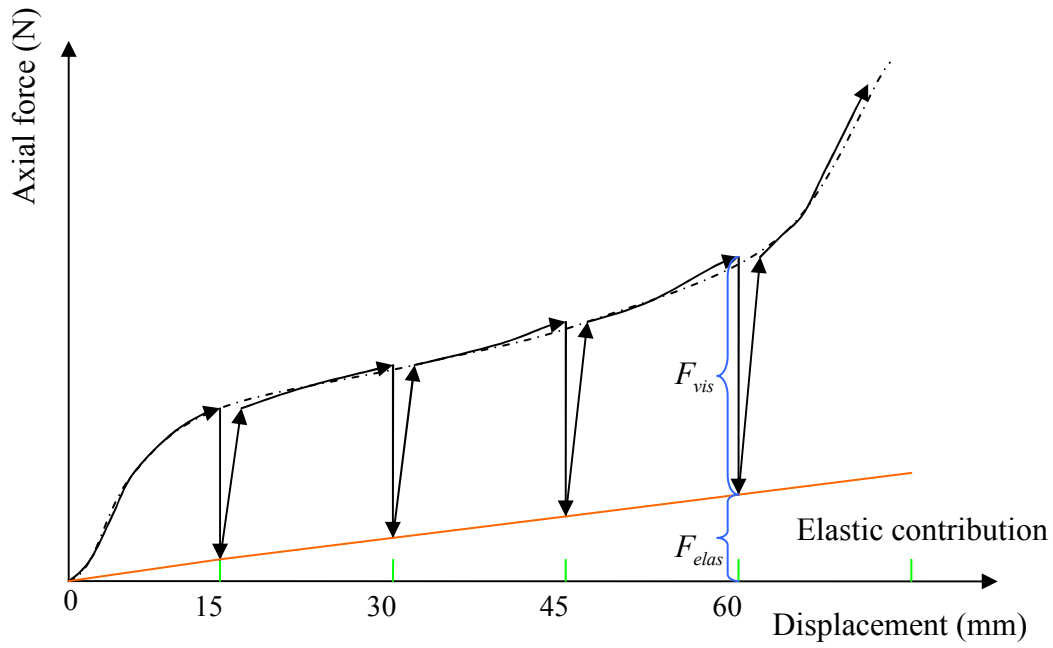

Figure 2.5. Schematic of the crosshead force versus displacement from PF relaxation tests. F_{vis} is the viscous force needed to shear a composite sheet, while F_{elas} is the elastic contribution. The dashed line is the result of a PF test without relaxation, while the solid orange line represents the elastic contribution.

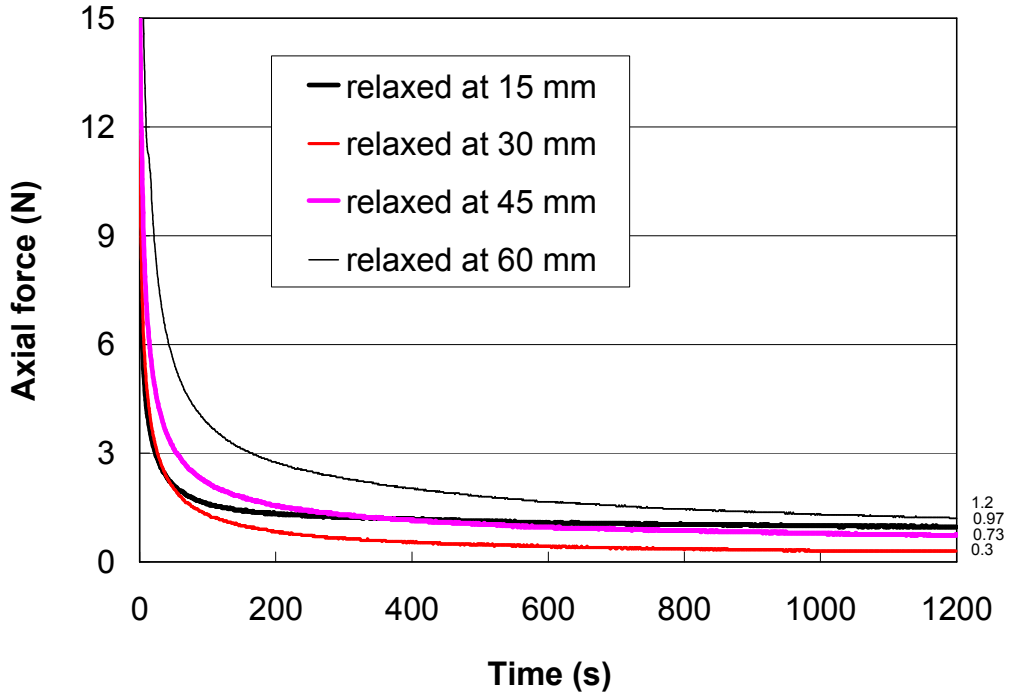

Figure 2.6. A typical result from stress relaxation tests for prepregs. The relaxing force recorded at 15, 30, 45 and 60 mm for a period of 1200 seconds. The values of relaxed force are 0.3N, 0.97N, 0.73N and 1.2 N respectively.

2.3.3 Shear behaviour in bias extension tests

The bias extension (BE) test is another popular method for characterising the in-plane shear properties of continuous fibre-reinforced composites [20, 29]. Unlike picture frame tests, BE tests are less sensitive to misalignment due to freer boundary conditions but samples undergo various deformation mechanisms, such as intra-ply slip, in addition to shear. Specimens were cut into the shape shown in Figure 2.7(a), which comprises regions A, B and C. If intra-ply shear is the dominant deformation mechanism, then region A can be equivalent to the tested area of a picture frame test, and region B undergoes shear at half the rate of region A. Region C remains un-sheared during the test.

The trapezium shape of the clamp area is to hold the tows at the border of regions C and B so as to eliminate any tow slip in region C. The aspect ratio λ (l_{BE} to w_{BE}) must be at least 2 in order for all three regions to exist. Increasing the value of λ would increase the area of region A. The sample was clamped using grips shown in Figure 2.8 in such a way that all tows in the warp and weft directions were initially orientated at $\pm 45^{o}$ to the loading direction. Jagged surfaces on the grips were used to clamp samples effectively in order to reduce the possibility of slipping without inducing fibre damage.

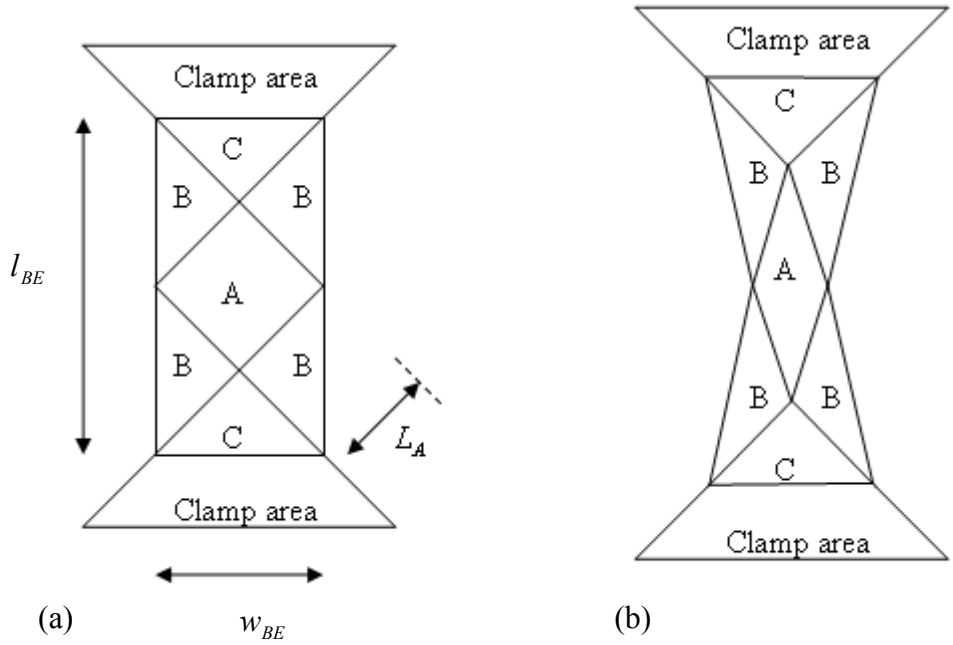

Figure 2.7. Schematic of an idealised sample used in BE tests with an aspect ratio $\lambda = l_{BE}/w_{BE} = 2$ where l_{BE} and w_{BE} are the initial length and width of the test sample. The tested area is divided into 3 regions, region A, B and C. L_A is the side length of region A. (a) un-sheared specimen (b) sheared specimen.

(a) (b)

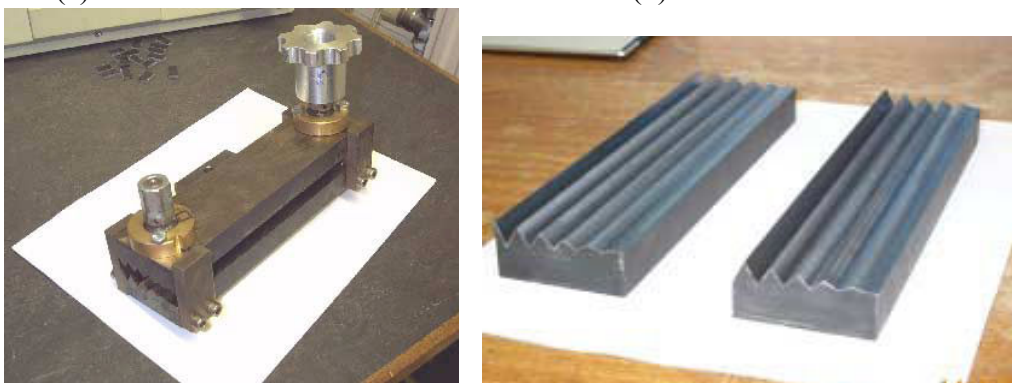

Figure 2.8. (a) Photographs of the clamps used, (b) geometry of jaws on the clamping surfaces which was originally proposed by Potter [29].

A photograph of a BE test is shown in Figure 2.9. The lower clamp was attached to the base of a Universal Testing machine, while the upper clamp was connected to a load cell. The test procedure is similar to PF tests described in the previous section. The axial force versus the displacement at various rates was recorded by a PC. To obtain data of shear force versus shear angle, as region A is considered equivalent to the tested area of a picture frame test Equations (2.5) and (2.6) apply, where F_{PF} and d_{PF} correspond to the axial force and the displacement of the crosshead and L_{PF} is the side length of region A (L_A). To ensure validity of Equation (2.6), a time-consuming visual analysis based on video clips taken by a digital camera during the tests was used to measure the actual shear angle in region A versus the crosshead displacement. The shear angle was measured using AutoCAD on images saved from the video clips at various displacements. For all experiments three repeats were performed for each condition to assess variability of the test data. If investigation of temperature dependence was required, an oven was used.

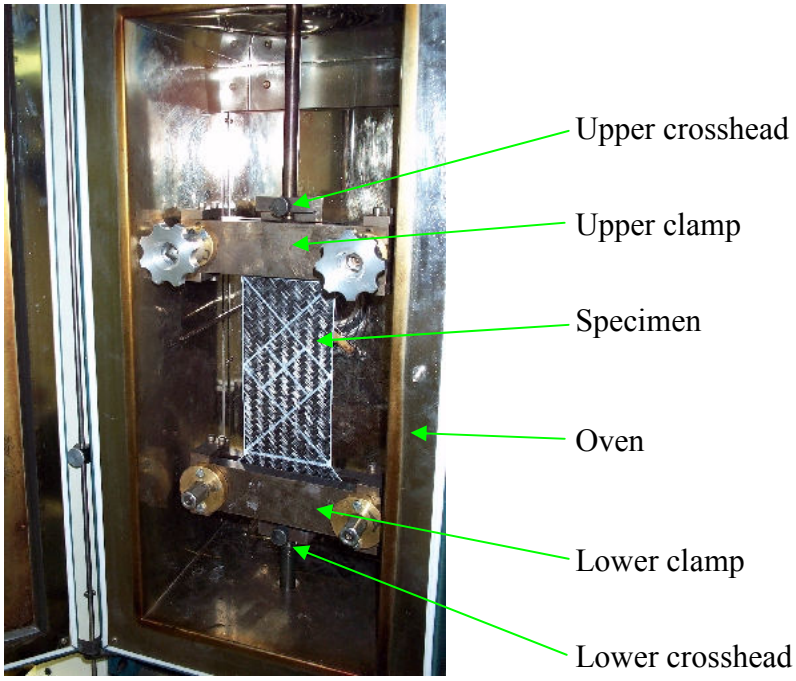

Figure 2.9. BE test rig. Marking lines were used to illustrate regions A, B and C, and also to measure the shear angle at the centre of the specimen.

2.3.4 Bending behaviour in 3-point bending tests

Three-point flexural tests were performed using British Standard tests (BS EN ISO 14125: 1998) for HexPly® M21 UD prepreg to investigate whether a new bending model developed in Chapter 4 can capture the bending resistance of viscous composites. The specimen is comprised of 3 layers with the same fibre direction. Specimen dimensions are 42x15x0.84 mm (length x width x thickness). Tests were performed at room temperature at 3 speeds, 2, 100 and 500 mm/min. Instead of elastic behaviour, plastic deformation is of interest, and hence calculations and expression of results described in the standard document were not applied. However, to reduce effects of the test geometry, specimen dimensions were those recommended by the standard. A schematic

of the test is shown in Figure 2.10. The two supporting rollers with radii $R_2 = 2$ mm are fixed at the base of a Universal Testing machine, while the loading roller with a radius of $R_1 = 5$ mm is connected to a load cell attached to the crosshead. The applied force versus displacement (deflection) was measured. In order to obtain a symmetric bending shape, great care must be taken during laying the specimen on the supporting rollers.

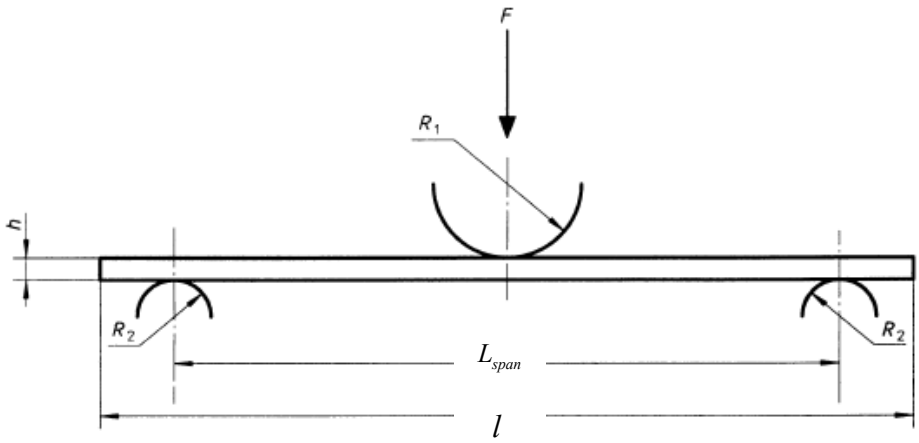

Figure 2.10. Three-point loading arrangement, where F is the force applied to the specimen, h is the specimen thickness (=0.84 mm), l (=42 mm) and L_{span} (=34 mm) are respectively specimen length and span, R_1 and R_2 are the radii of loading and supporting rollers respectively. Reproduced from BS EN ISO 14125: 1998.

If tests were conducted at elevated temperatures, an environmental chamber was used to enclose the whole testing rig. Three repeats were performed for each condition to assess the reproducibility of experiments.

2.3.5 Bending behaviour in buckling tests

Experimental measurements on the bending resistance of viscous continuous fibre-reinforced composites were also made by means of a large-displacement buckling test at various displacement rates and temperatures. The buckling test has been used previously to study the buckling behaviour of dry textiles [30], and has some advantages over 3-point bending tests, such as use of thin and flexible samples and elimination of deformation under self weight. In this test method, the bending behaviour is expressed as the axial force versus the displacement parallel to the applied force. Specimens were cut into a rectangular shape comprised of testing and clamped regions. The length of the clamped region was 25mm, and the tested region was 50x50mm. In order to obtain significant measured forces, a specimen was made of three UD prepreg plies with different fibre orientations and was subjected to pressure using a press for about 30 minutes at an uncontrolled room temperature. The experimental setup is shown in Figure 2.11. The setup consists of a specimen and upper and lower clamps which are made of aluminium.

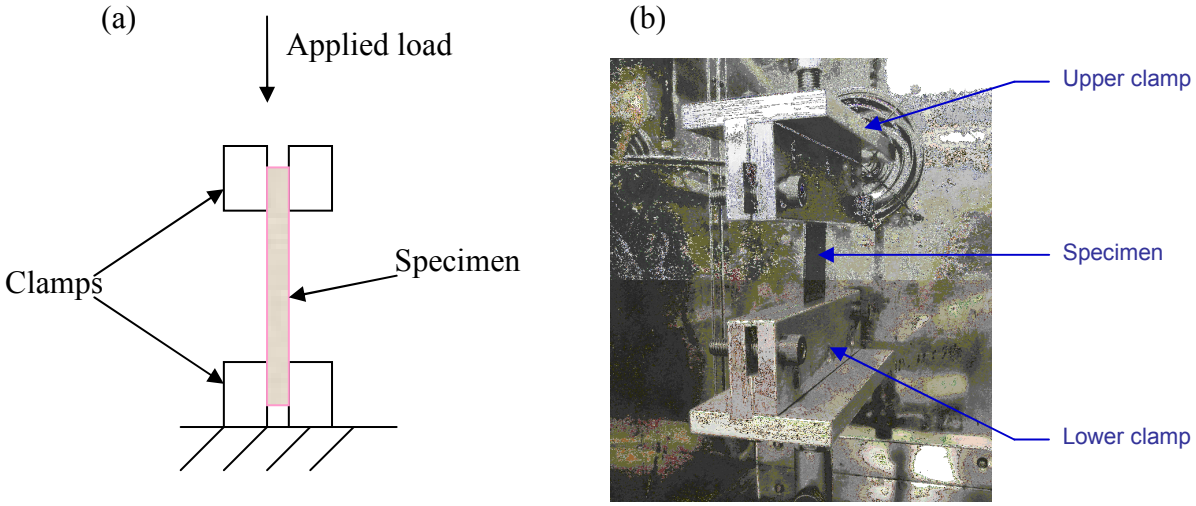

Figure 2.11. (a) Layout of a buckling test and (b) photograph of experimental setup.

The axial force and displacement of the crosshead were measured using a Universal Testing machine through a PC, at various temperatures and crosshead displacement rates. The specimen was mounted in the clamps with great care to avoid any misalignment which could lead to defects, such as unsymmetrical bending shapes, wrinkles or a vee-shape. During testing, the lower clamp was fixed, while the upper clamp was attached to a load cell mounted on the crosshead. The upper clamp moved downwards until a pre-determined displacement was reached. To ensure a repeatable bending shape of the sample, the specimen was compressed by a displacement of 1 mm prior to testing, and then a mode I deformed shape was initiated by manual displacement of the fabric in order to obtain a uniform deformed curve across the specimen. For all experiments three repeats for each condition were performed to assess variability.

2.4 Formability characterisation experiments

2.4.1 Overview of methodology

Figure 2.12 shows a schematic of a formability characterisation experiment. This method is called stamp forming, also known as matched-die moulding. A pair of matched metal moulds, punch (male tool) and die (female tool) was mounted in a press which supplies pressure during forming. A small gap was maintained when the moulds were closed. During forming, the blank was forced to conform to the punch and was pressurised on its periphery with a blank-holder. Both stamping process and cure can take place at either ambient or elevated temperature as punch, blank-holder and die can be heated. Sufficient pressure and temperature were maintained by the press and heaters during component curing to maintain the formed shape. Once the component can maintain its shape, it was demoulded.

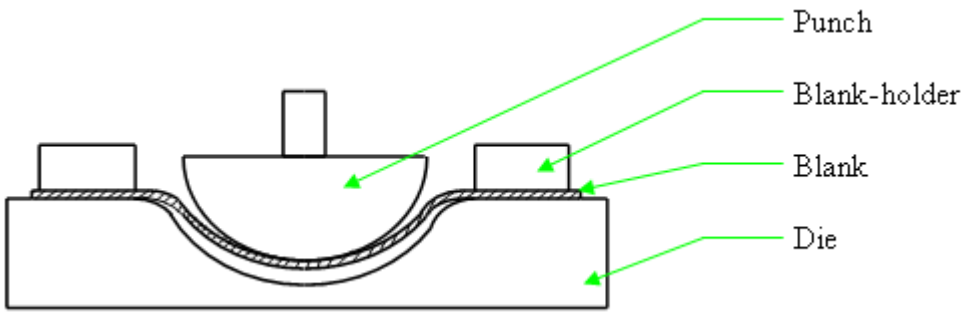

Figure 2.12. Schematic of formability characterisation method.

The punch and die can be many shapes, such as hemisphere and helicopter pilot helmet (Figure 2.13). Processing conditions include forming rate, temperature and blank-holder force profile. Formability characterisation

experiments can be performed to optimise these three processing parameters mainly, ultimately aiming to enable one to produce defect-free parts.

(a)  (b) 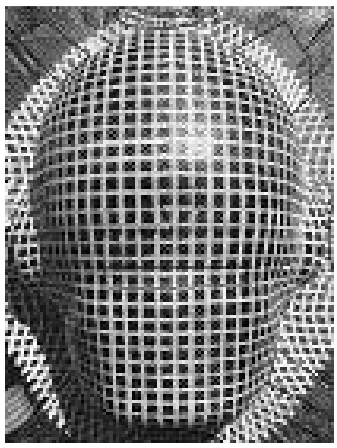

Figure 2.13. Two different shapes of formed component. (a) hemisphere (b) helicopter pilot helmet. Grids of white lines were marked using a template prior to forming.

2.4.2 Hemisphere forming

Isothermal hemisphere forming experiments were carried out using a dedicated up-stroking hydraulic press with integral cartridge heaters in the punch and die. During forming the cartridge heaters were monitored by a controller through thermocouples to maintain required temperatures. Figure 2.14 shows the experimental layout without a blank-holder, involving punch, die and infra-red heater. The moulds are made of aluminium. A blank-holder also with an integral heater was used, shown in Figure 2.15, consisting of two aluminium plates which can apply pressure to the periphery of the sample through four springs at each corner. The spring stiffness is 6.33 N/mm. Spring compression was measured using a digital calliper to ensure the required pressure. A sample sheet was cut into a square, with corners cut off if the specimen was too large.

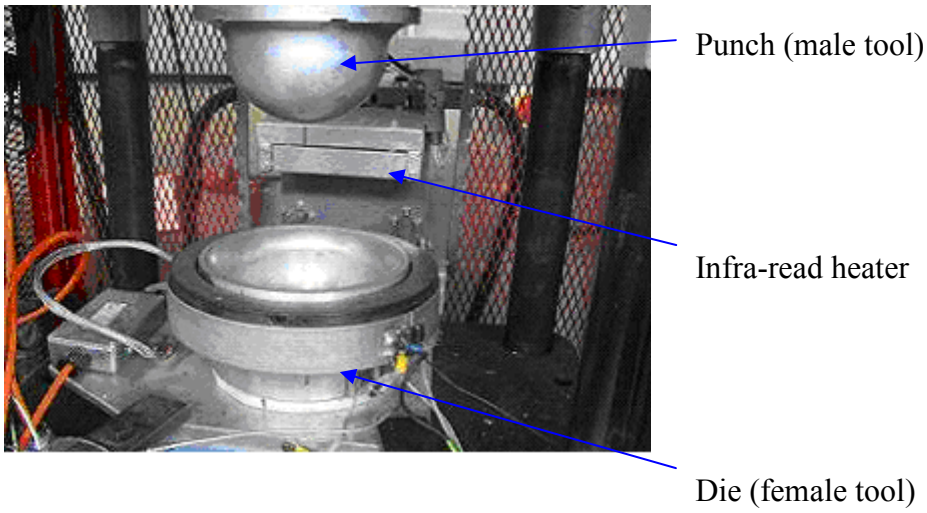

Figure 2.14. Photograph of hemisphere forming experiment setup but without a blank-holder. Punch radius is 60mm.

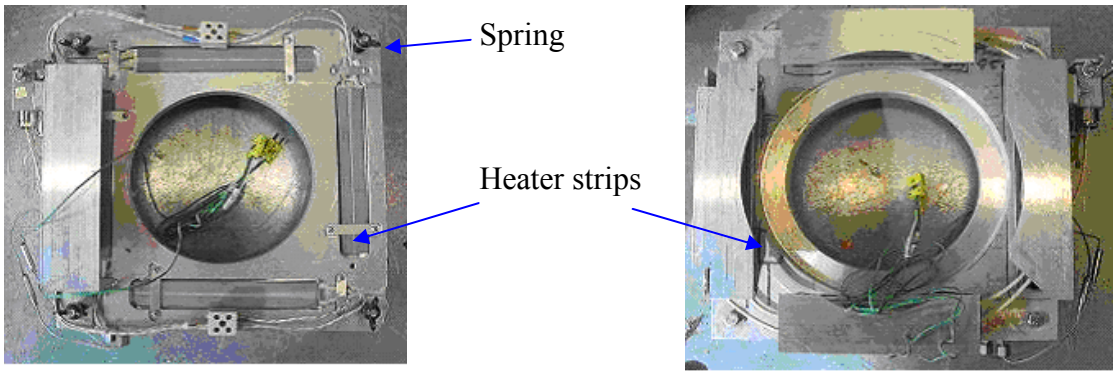

Figure 2.15. Photographs of a blank-holder with the upper plate (left) and the lower plate (right). Four heater strips are built-in around the four edges for each plate.

Prior to testing, mould release agent was applied to the tool surfaces to prevent the specimen from sticking to tools. Next, all heaters were switched on to heat up the tools. Tool temperatures were monitored by thermocouples. Once the equipment was at the required temperature, the specimen sheet was laid between the upper and lower plate of the blank-holder with great care to avoid any misalignment. This process of clamping specimens needed to be fast to

avoid heat loss. The blank-holder together with the sample sheet was then placed onto the female mould. The specimen was then heated using the infra-red heater automatically shuttled in from the back of the rig. The specimen was heated for 5 minutes to reach the required temperature, monitored by a thermocouple. Then the tools were closed to form the hemisphere with a speed of approximately 133.3 mm/min. Samples were then left inside the tools for 1 hour at 150 ^{o}C to cure. Once cured, the hemisphere was demoulded.

2.5 Optical microscopy

In order to investigate deformation mechanisms during bending, some optical microscope images were taken to observe the internal structure of the deformed specimens from buckling tests described in Section 2.3.5. Although the procedure has been well described in the literature [31, 32] the technique is presented again briefly here. There are two main steps for the process.

The first one is to make specimens with good surface quality for image acquisition. All deformed prepregs were cured in a hot air oven after deformation in buckling tests before removal from the clamps. These cured prepregs were cut into pieces with a length of approximately 25mm and a width of 20mm. Two lines for each piece were marked beforehand for cutting, one for guiding the cut and another to locate the intended cross-section. These pieces were held on the detachable bases of plastic pots using epoxy adhesive, with the intended cross-section facing upwards. Polyester casting resin mixed with Butanox catalyst and accelerator were then poured into the pots and left to cure at room temperature for more than 5 hours. Once casting resin was cured,

the specimens were demounted and cut on both surfaces to a thickness of about 14 mm. To make the two surfaces parallel, coarse polishing papers were used. The grinding operation was performed using Strues® DAP-7 machine equipped with an automatic holder (Strues® Pedemin-S) with 240 rpm motor speed. To obtain a polished surface of good quality, at least four waterproof abrasive papers with increasing grit number (eg. 240, 600, 1200 and 4000 grit) were used for grinding for between 5 and 30 minutes. If the quality of specimen surfaces does not fulfil the requirement, 1 μm alumina paste consisting of 20% by volume of powder and the balance of water on a flocked wheel was used for further grinding.

The second step is to take images of these specimen discs under a Zeiss Axiolab optical microscope equipped with a CCD camera connected to a PC for image acquisition. There are four magnifications available, 5x, 10x, 20x and 50x. Selection depends on features of interest in different regions. Image analysis software, Aphelion™ , assisted in taking micrographs from the camera. A graticule was used to calibrate each image. A typical micrograph is shown in Figure 2.16.

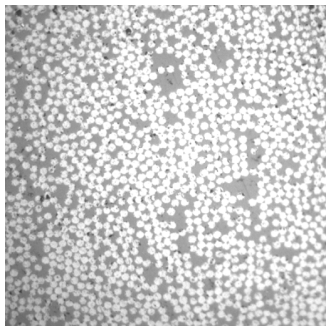

Figure 2.16. Typical microscopic image. Circular spots in white colour are fibres, while other regions are composite resin, casting resin and voids.

Chapter 3 Predictive modelling of composite viscosities

3.1 Introduction

Continuous fibre-reinforced composites (CFRC) comprised of inextensible fibres aligned in an incompressible fluid are highly anisotropic with principle directions along and perpendicular to the fibres. A CFRC is often assumed to be a continuum. A continuum theory of the mechanics of the CFRC in an elastic state was developed by Spencer and termed as an 'ideal fibre-reinforced model'(IFRM) [33, 34]. The continuum approach ignores any further micromechanics, although the microstructure dictates two local fibre directions with unit vectors $\boldsymbol{a}(\boldsymbol{x},t)$ and $\boldsymbol{b}(\boldsymbol{x},t)$ for biaxial CFRCs where all vector and tensor components are referred to in a Cartesian coordinate system with position coordinates x_i (i =1,2,3). This implies that neither detailed considerations of the interactions between individual fibres and the matrix nor the relations of the mechanical properties between the composite and its constituents are considered.

The IFRM has more than nine model parameters, which would require a large number of experiments to determine. Hence, it is difficult to apply this model to practical examples, unless some assumptions, such as incompressibility and fibre-inextensibility, are made to simplify the model. Composite materials can be treated as either a linear viscous fluid (analogous to isotropic Newtonian fluid) or a non-linear viscous fluid. Although approximately linear viscous behaviour has been found in some unidirectional fibre-reinforced composites, others exhibit non-linearity. Rogers [35] suggested a convenient and intrinsic

three-dimensional linear form consisting of only two model parameters for viscous uniaxial CFRC, as shown in Equation (3.1).

$$\boldsymbol{\tau} = 2\eta_T \mathbf{D} + 2(\eta_L - \eta_T)(\mathbf{AD} + \mathbf{DA}) \quad \textbf{(3.1)}$$

where $\boldsymbol{\tau}$ is the extra stress tensor, **D** is the rate of deformation tensor (with components D_{ij}), **A** is dyadic product of $\boldsymbol{a}$, and η_L and η_T, are the composite viscosities of the viscous composite, named longitudinal (LV) and transverse (TV) viscosity respectively. Derivations of this form from IFRM can be referred to Appendix 3.A. LV can be referred to as the resistance of the fibres to shear along the fibre direction, while TV is the resistance of the fibres to shear transverse/perpendicular to the fibre direction. LV and TV can be interpreted as shown in the schematic of Figure 1.10.

A large amount of work on experimental methods and the development of analytical, empirical and numerical models have been carried out and are available in the literature [21, 36-69], as reported for example by Harrison et al. [11], and to date the reasons for large discrepancy in results remain unclear. It has been suggested that LV and TV may depend on the fibre volume fraction, matrix viscosity, and fibre arrangement. A review of previous work is presented in Section 3.2. The key objectives in this chapter are to develop a fully predictive model for these two rheological parameters and attempt to explain the discrepancies in the previous work. Experimental measurements from the literature were used to validate the TV and LV models. These two viscosities are also important for the bending and shear models and will be employed in Chapters 4 and 5. Development of the TV and LV models is

presented in Sections 3.3 and 3.4, followed by validation and discussion of results.

3.2 Review of previous work

3.2.1 Theoretical modelling

Much modelling work has been published on determining the longitudinal and transverse viscosities [19, 47, 51, 53, 67-70]. Some models were developed to estimate the shear viscosity of composites with fibres of low aspect ratio and volume fraction [71]. The Maron-Pierce equation can reasonably model the rheological behaviour as a function of particle content of a wide range of materials [72, 73]. In order to model the shear viscosity of high volume fraction composites with fillers/fibres of large aspect ratio, Binding [69] suggested the following expressions to represent upper and lower bounds:

$$\frac{\eta_L}{\eta_m} = \frac{1 - v_f}{\left(1 - \sqrt{1.1 v_f}\right)^2} \qquad \text{upper bound}$$

$$\frac{\eta_L}{\eta_m} = \frac{1 - v_f}{\left(1 - 1.1 v_f\right)^2} \qquad \text{lower bound} \qquad \textbf{(3.2)}$$

where v_f is the fibre volume fraction, η_m is the viscosity of the polymer matrix. Assumptions in theoretical models reviewed in this section will be stated later. Experimental results for high aspect ratio glass fibre-polypropylene composites with 0.25 volume fraction at 200^{o}C using a capillary rheometer, were found to lie between these two bounds. Experimental measurements using dynamic linear oscillatory tests for a nylon fibre-reinforced golden syrup composite at 20^{o}C have extremely good agreement with the upper bound [60].

Measurements using steady shear linear pull-out tests for the nylon fibre-reinforced golden syrup composite at 25^{o}C show that there is good agreement with the upper bound at low fibre volume fraction, with increasing discrepancy as the fibre volume fraction increases [62]. Goshawk and Jones [62] also found that the Christensen transverse viscosity model [67] gives much lower predictions at all fibre volume fractions and the discrepancy increases with increasing volume fraction.

The Christensen models [67] are semi-empirical models estimating the effective longitudinal and transverse shear viscosities for an aligned fibre suspension. The forms of the models were constructed empirically to cover the full range of the fibre volume fraction through two extremes of fibre concentration, the classical dilute suspension conditions and the very concentrated conditions for a hexagonal arrangement of fibres. The empirical forms of the Christensen models are shown in Equations (3.3)and (3.4).

$$\frac{\eta_L}{\eta_m} = \frac{\left(1 + 0.96 v_f\right)}{\left(1 - 0.97 v_f\right)^{1/2} \left(1 - 1.1 v_f\right)^{1/2}} \quad \textbf{(3.3)}$$

$$\frac{\eta_T}{\eta_m} = \frac{\left(1 - 0.21 v_f\right)}{\left(1 - 0.65 v_f\right)^{3/2} \left(1 - 1.1 v_f\right)^{3/2}} \quad \textbf{(3.4)}$$

Dynamic linear oscillatory tests show that predictions from the Christensen models underestimate and deviate from measurements as the fibre volume fraction increases [60]. The reason for this could be due to fibre entanglement, which is likely to increase with increasing fibre volume fraction. None of the theoretical models account for fibre entanglement, instead they assume fibres to be straight and rigid during shear deformation, and therefore only shear

deformation of the matrix fluid is considered; tension, compression, torsion or bending of fibres due to entanglement are neglected. By this argument, model predictions of LV and TV would be lower than experimental measurements and the difference would increase with fibre volume fraction.

The Christensen TV model makes similar predictions to the Coffin model [68], but the Christensen LV model gives lower values, as Coffin's micromechanical analysis suggests that the longitudinal and transverse viscosities are equal. The relations of the Coffin model for determining the effective longitudinal and transverse viscosities are simple and easily derived, and are shown in Equation (3.5).

$$\eta_L = \eta_T = K\eta_m \tag{3.5}$$

where K is a factor that amplifies the effective shear viscosity of the assembly compared to the viscosity of the fluid due to a magnification in the fluid deformation rate by the presence of fibres. K is determined by considering the kinematics of adjacent rigid fibres interacting with the viscous fluid matrix in states of shear deformation with no slip conditions at the fluid-fibre interface, shown in Equation (3.6)).

$$K = \frac{1}{1 - \sqrt{1.1v_f}} \tag{3.6}$$

There is reasonably good agreement between the Coffin model and the experimental results of Binding [69]. To support the equality in LV and TV, Coffin [68] quoted linear oscillatory shear test results by Wheeler and Jones [59] for a carbon fibre Golden Syrup composite with 0.6 volume fraction. Measurements by Groves and Stocks [57] who performed rotational oscillatory

dynamic testing (see Section 3.2.2.2) for a carbon/polyaromatic thermoplastic composite with a fibre volume fraction of 0.6 showed that the LV and TV are approximately equal (the TV is consistently slightly higher) at a range of shear rates from 0.01 to 1 s^{-1}. Groves et al. [74] who performed experiments with a slightly modified technique for two composites, 60% carbon fibre volume fraction in a polyetheretherketone matrix and 35% glass fibre volume fraction in polypropylene, obtained the same results, consistently slightly higher in TV.

Nonetheless, experimental results by Scobbo and Nakajima [55] who performed oscillatory tests in simple shear on two different thermoplastic composites showed that the LV was 10% higher than the TV, whilst a value of 30% was suggested by Cogswell [75]. Empirical relations based on finite element results by Coffin [68] also show that the LV is greater than the TV at a fibre volume fraction ranging from 0.2 to 0.78. Dykes et al.[66] who performed vee-bending tests for unidirectional glass/polypropylene composites with different lay-ups and a fibre volume fraction of 0.35 found that LV > TV for all the temperatures and forming speeds investigated. Results from Sengupta and Mukhopadhyay [76] also showed that LV is greater than the TV for carbon fibre/polypropylene composites with fibre volume fractions 0.13, 0.24 and 0.35.

Measurements of Stanley and Mallon [77] who performed steady shear linear pull-out tests for APC-2 (60% by volume carbon fibre/PEEK) at a shear rate of 0.01 s^{-1} showed that the ratio of LV to TV is approximately 2.5. Interestingly, Roberts and Jones [60] suggest (Nylon-Syrup) that LV > TV for v_f<0.55, LV

= TV for v_f =0.55 and LV < TV for v_f >0.55. However, experimental measurements (Nylon-Syrup) by Goshawk and Jones [62] found that LV<TV for all v_f.

Pipes [70, 78] developed constitutive relations for the prediction of the LV and TV for an oriented assembly of discontinuous fibres suspended in both a Newtonian fluid and a power-law fluid with finite yield stress. Even though the paper referred to discontinuous fibres, the analysis for both LV and TV models does not involve any assumptions of discontinuity of fibres, so that the theory may also be applied to continuous fibres. The approach developed obtains the resulting fluid motion from the imposed fibre kinematics and then determines directly the effective properties of the composite assuming that the applied shearing stress in the composite and average shearing stress in the fluid are equal. The constitutive relations can be expressed as

$$\frac{\eta_L}{\eta_m} = \frac{\left(2 - \sqrt{1.1 v_f}\right)}{2\left(1 - \sqrt{1.1 v_f}\right)} \qquad \textbf{(3.7)}$$

$$\frac{\eta_T}{\eta_m} = \frac{1}{\left(1 - \sqrt{1.1 v_f}\right)} \qquad \textbf{(3.8)}$$

Harrison [19] proposed a relation for the prediction of the LV for a unidirectional composite with a square fibre packing under picture frame shear. Fibres are assumed to be uniformly distributed cuboids, and are rigid compared with the matrix which is incompressible. The model was developed by considering the shearing deformation in two different regions within a unit cell,

between the fibres and outside the fibres. The relation is shown in Equation (3.9).

$$\eta_L = \eta_{btw}\left[\frac{L_f \cos\theta\left(L_f + g_o\right)}{\cos\theta\left(L_f + g_o\right)^2 - L_f\left(L_f + g_o\right)}\right] + \eta_{ots}\left[\frac{1}{\cos\theta} - \frac{L_f}{L_f + g_o}\right] \quad \textbf{(3.9)}$$

where L_f is the side length of the square cross-section of fibres, g_o is the initial gap between fibres prior to shear (a function of the fibre volume fraction), θ is material shear angle, η_{btw} and η_{ots} which can be Newtonian or non-Newtonian are the viscosities of the matrix fluid sheared at the simple shear strain rates in two different regions, the region of shearing resins between fibres and the other region of shearing resins outside the fibres. By setting θ=0, the model predicts similar results to the Christensen [67] and Coffin [68] models.

In order to show clearly the potential accuracy of the LV and TV models, the assumptions are summarised in Table 3.1, which includes those of newly developed models in Sections 3.3 and 3.4. Derivations for Coffin, Pipes and Harrison models were based on the same approach (Points 15&17), force equilibrium (i.e. equating the applied shearing stress to average shearing stress in the fluid), which is a simple solution. However, the resin flow is generally in two directions (Point 16), especially during transverse shearing. Hexagonal fibre packing may be closer to the real fibre configuration than square packing, although it is more complicated for model derivations. As such, Christensen models may be preferred to these three models. In order to simplify some integrations in derivations, Christensen derived asymptotic relations for TV and LV at two extremes of fibre packing (zero and maximum for hexagonal),

by equating the rate of dissipation energy for the overall composite to that dissipated for shearing of matrix fluids. Based on the results at these two extremes, Christensen developed TV and LV models semi-empirically to cover the full range of fibre volume fractions. The approach thus is thought to be an approximation method and non-fully predictive. Since a fully predictive and accurate model is required for optimisation, the Christensen's approach will be modified to develop new TV and LV models in Sections 3.3 and 3.4, by solving the integrations to give the full range of fibre volume fractions (instead of the two extreme fibre volume fractions). The Binding model based on imposed fibre kinematics only provides upper and lower bounds for the LV model. Harrison's LV model is shear-angle dependent (Point 13), which is very useful in modelling picture frame shear. However, Harrison LV yields a severe sudden increase when the shear angle reaches a certain value which depends highly on the value of fibre initial gap (determined by the assumed fibre packing). Beyond this shear angle, the 1st term of Equation (3.9) becomes negative, which is inappropriate.

Table 3.1 Summary of assumptions and features of all theoretical models in this chapter.

No.	Assumptions and features	Binding LV	Christensen TV	Christensen LV	Coffin TV	Coffin LV	Pipes TV	Pipes LV	Harrison LV	New TV	New LV
1	Negligible composites mass	Yes	Yes	Yes	Yes	Yes	Yes	Yes	Yes	Yes	Yes
2	All fibres with the same dimensions	Yes	Yes	Yes	Yes	Yes	Yes	Yes	Yes	Yes	Yes
3	Un-deformable / rigid fibres	Yes	Yes	Yes	Yes	Yes	Yes	Yes	Yes	Yes	Yes
4	unidirectional, parallel uniformly spaced fibres	Yes	Yes	Yes	Yes	Yes	Yes	Yes	Yes	Yes	Yes
5	No slip conditions	Yes	Yes	Yes	Yes	Yes	Yes	Yes	Yes	Yes	Yes
6	No structure reorganisation of fibres	Yes	Yes	Yes	No	No	No	No	No	Yes	Yes
7	No fibre rotation during shear	Yes	Yes	Yes	No	No	No	No	Yes	Yes	Yes
8	Fibres are assumed to form compacted layers parallel to the shearing planes	Yes	No	No	Yes	Yes	Yes	Yes	Yes	No	No
9	Fibre packing	Hexagonal	Hexagonal	Hexagonal	Square	Square	Square	Square	Square	Hexagonal	Hexagonal
10	Incompressible fluid	No	Yes	No	No	No	No	No	No	Yes	No
11	Newtonian / Non-Newtonian fluid	Newtonian	Newtonian	Newtonian	Newtonian	Newtonian	Newtonian	Newtonian	Both	Newtonian	Newtonian
12	Fibre cross-section	Circular	Circular	Circular	Square	Square	Circular	Circular	Square	Circular	Circular
13	Shear-angle dependent	No	No	No	No	No	No	No	Yes	No	No
14	Fully predictive	No	No	No	Yes	Yes	Yes	Yes	Yes	Yes	Yes
15	Energy approach	No	Yes	Yes	No	No	No	No	No	Yes	Yes
16	Directions of resin flow allowed	Only x	x and y	Only x	Only x	Only x	Only x	Only x	Only x	x and y	Only x
17	Derivations based on	Fibre kinematics (fibre spacing and diameter)	Fibre kinematics + rheological behaviour	Fibre kinematics + rheological behaviour	Fibre kinematics (fibre spacing and diameter)	Fibre kinematics (fibre spacing and diameter)	Fibre kinematics (fibre spacing and diameter)	Fibre kinematics (fibre spacing and diameter)	Fibre kinematics + rheological behaviour	Fibre kinematics + rheological behaviour	Fibre kinematics + rheological behaviour
18	Accounting for fibre entanglement	No	No	No	No	No	No	No	No	No	No

3.2.2 Experimental measurements

On the experimental side, various methods have been designed and performed to measure both TV and LV, such as dynamic testing using either rotational [54-58] or linear [55, 59-61] oscillatory experiments, steady shear linear 'pull-out' experiments [62, 77], Vee-bending experiments [63-66] and picture frame tests [21]. Squeeze flow experiments [36-53] also have been used to measure the TV of viscous polymer composites.

3.2.2.1 Squeeze flow experiments

Much attention has been paid to the squeeze flow method [36-51] for characterising the TV of viscous composites. In squeeze flow experiments, the test specimen, in the form of a rectangular sheet, is placed between two parallel impermeable platens with the lower platen fixed. A normal force is applied to the upper platen. During experiments, either a constant force is applied and the displacement versus time is measured, or alternatively, a constant displacement rate is applied and the force versus time is measured. Such industrial testing devices are known as parallel plate plastometers or squeeze plate viscometers [79, 80]. A schematic of squeeze flow testing setup is shown in Figure 3.1. The test can be performed using a standard mechanical testing machine. Equation (3.10) [51] was used to interpret the TV for a composite with a Newtonian fluid.

$$\eta_T = \frac{-F}{h'}\left(\frac{h^3}{8L_p w_p^3}\right) \tag{3.10}$$

where h is the thickness of the composite, $h^{'} = dh/dt$, L_p is the platen length along the fibre direction and $2w_p$ is the platen width transverse to the fibre direction.

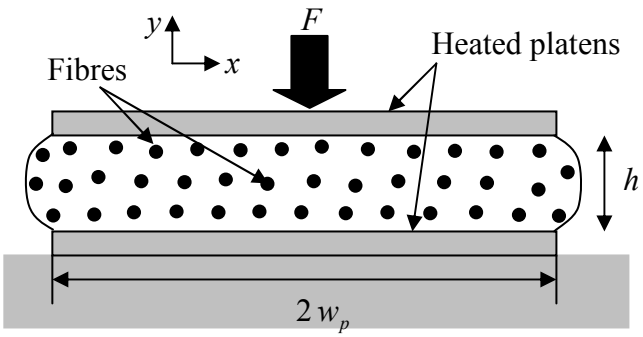

Figure 3.1. Squeeze flow testing setup. $2w_p$ and h are the plate width and specimen height respectively. F is the applied force on the upper plate through a testing machine. The upper plate is pressed downwards and the reaction force is measured as a function of h. The sample is squeezed out from between the plates during the experiment. Reproduced from [81].

This testing method has some advantages due to its mechanical simplicity, inclusion of fibres without the danger of attrition, capability of testing at very high shear rates and temperatures and the ease of testing high-viscosity materials [36]. Besides that, it is also a technique to characterise the rheological behaviour of viscous composites.

In the parallel plate plastometer, measurements for the case of constant applied force can be used to investigate the rheological properties of the specimen, while those for the case of the constant applied displacement rate can be used to determine the viscosity dependence on shear rate. Although unsteady shear

flows are unavoidable in squeeze flow experiments, the flow rates are usually low enough so that quasi-steady state solutions can be applied in the theoretical analysis. This creeping flow assumption was assessed to be valid by Shuler and Advani [51] who showed that the Reynolds number was smaller than unity, indicating steady state flow conditions. Two testing cases, constant pressed area and constant volume of the specimen, are available by making different cross-sectional areas of specimens. The former case applies if the cross-sectional area of the specimen is equal or bigger than that of the platens, while the latter applies if the cross-sectional area of the specimen is small enough so that no resin is squeezed out of the platens during experiments. The former case was adopted by Shuler and Advani [51] and Harrison [82].

It is necessary to ensure that the main flow deformation must be transverse to fibres. Some research on the squeeze flow behaviour of unidirectional fibre-reinforced thermoplastic composites that were treated as transversely isotropic materials have been performed [47, 48, 51, 52]. Experimental results on these materials showed that the resulting squeeze flow deformation is strictly perpendicular to the fibre direction. This could be explained by the high ratio of extensional viscosity in the fibre direction, which is infinite in the case of continuous reinforcements, to the TV. This two-dimensional flow phenomenon was confirmed by Shuler and Advani [51] using a flow visualisation technique. Therefore, if there is no resin percolation out of the fibre bed, then the resin in these composites can be regarded as incompressible anisotropic fluids with an effective shear viscosity transverse to the fibre direction. Experimental results

from Goshawk et al. [53] show that the squeeze flow experiment has high repeatability.

Harrison et al. [82] performed some squeeze flow tests using square platens with 40x40, 60x60, 80x80 and 115x115 mm of glass/polypropylene unidirectional composites with 0.35 fibre volume fraction at a temperature of 180^{o}C. Experimental results suggest that the TV is length and temperature dependent. Temperature dependence confirms that the TV is a function of the matrix viscosity, whereas length dependence might need to be investigated further. The problem of length dependence might be analogous to investigation of end effects of samples. The aspect ratio (length to width and length to thickness) may be required to be sufficiently large so as to eliminate end effects. However, theoretical models from the literature, including two models presented in the next two sections, do not encounter the problems of end effects as the fibres in composites are continuous and the whole composite is regarded as a continuum, which means that the aspect ratio is infinity. Similar work on the study of geometry effects, such as fibre length dependence and fibre shape, were done earlier [51, 69]. Binding [69] who used a capillary rheometer for glass fibre-polypropylene composites with 0.25 volume fraction and with different aspect ratios at 200^{o}C, suggested that the LV was length independent and the effect of fibre shape seems insignificant. However, experimental results from transverse squeeze flow tests by Shuler and Advani [51] show that the influence of fibre diameter on TV is not negligible.

3.2.2.2 Dynamic testing

Dynamic testing measures the response of a material to small-amplitude oscillatory shear to determine its viscoelastic behaviour. It has been widely used to test isotropic materials but may also be able to characterise the shear flow of continuous fibre-reinforced composites [56, 83].

Rotational oscillatory experiments

Dynamic testing with small strain rotational oscillation [56, 57] has been used to characterise the rheology of composite materials at various temperatures. For the tests at elevated temperatures, the rheometer temperature was measured at the centre of the lower disc platen, and an inert nitrogen atmosphere was used in a hot gas oven to ensure polymer stability throughout the measurement. A pair of parallel circular disc platens with rotation or oscillation about the cylindrical axis can be used to avoid misaligning the original position of fibres in the planar laminated ply specimens. A schematic of the testing setup for measuring TV is shown in Figure 3.2. LV is measured by loading the UD composite with the fibre direction along the shearing direction.

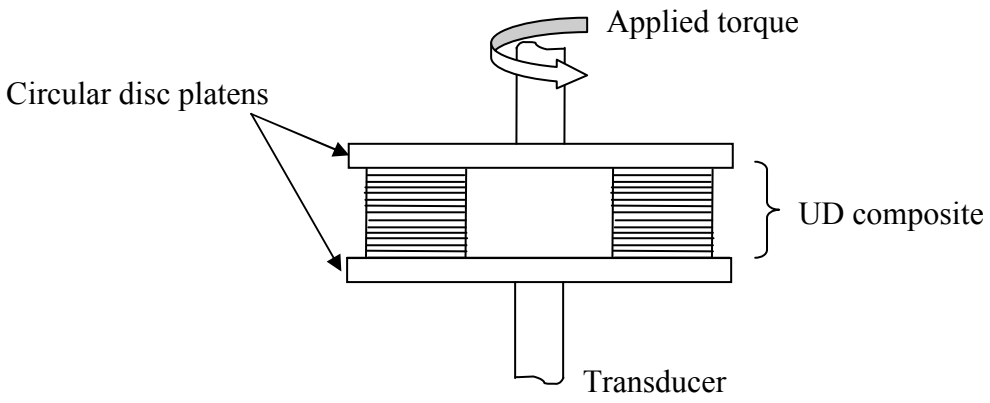

Figure 3.2. Schematic of dynamic testing with small strain rotational oscillation measuring TV. The fibre direction is transverse to the shearing direction.

As the balance of a single off-centre specimen is not easy to control [83], a symmetrical pair of off-centre specimens were used and loaded in place using a template. Rogers [35] also suggested that dynamic measurements for the longitudinal/transverse shear moduli can be made with this modification to ordinary rotational rheometers. Note that the fibre orientation of a composite laminate should be the same for both off-centre specimens in each test, due to the dependence of the phase angle on the fibre orientation. The accuracy of the subsequent analysis may be therefore reduced by the mean phase angle when a sample with a mixed fibre orientation is used. A problem that might be unavoidable is the preferential loss of matrix polymer due to squeezing when the matrix is melted between the platens, which would cause an increase in the fibre volume fraction of the sample. Complex viscosity (η^*) and dynamic viscosity (η') can be calculated by the relations shown in Eqs (3. 11) and (3. 12) respectively.

$$\eta^* = G^* / \omega \qquad \textbf{(3. 11)}$$

where G^* is the complex modulus which can be calculated by the torque and strain amplitude vectors from the maximum shear stress and shear strain, ω is the angular frequency.

$$\eta' = \eta^* \sin \vartheta \qquad \textbf{(3. 12)}$$

where ϑ is the phase angle which can be used to calculate the in-phase storage modulus (G') and the quadrature loss modulus (G'') by assuming linear viscoelasticity with a sinusoidal response for an isotropic specimen. The moduli G' and G'' are expressed as functions of ω to represent the dynamic response and strain amplitude in an isotropic case to establish linearity of the

strain response. In the case of an anisotropic response along and transverse to the fibre direction, the torque and phase are expressed as a function of strain amplitude which suggests a linear strain response.

Results using this technique by Groves [56] present some interesting information. At low shear rates, composites with Newtonian polymers show clearly non-Newtonian behaviour. Groves speculated that this is caused by the elastic contribution of the fibres. This phenomenon was also observed in experimental measurements of Roberts and Jones [60] for a nylon/Golden Syrup composite with fibre volume fractions of 0.3, 0.4, 0.5, 0.6 and 0.7 in linear oscillatory dynamic testing. If this is true, then theoretical models for the LV and TV need to consider elastic effects. To date, no theoretical models can prove that the composite viscosities are non-Newtonian for composites with Newtonian matrix. However, Goshawk and Jones [62] who performed steady shear linear pull-out tests for a nylon/Golden Syrup Newtonian fluid with 0.2, 0.4 and 0.6 fibre volume fractions showed that both composite viscosities were independent of shear rate. Investigation of effects of the resin contribution reveals that the ratio of the composite viscosity to the resin viscosity is less than 1 at high shear rates, agreeing with the suggestion of Groves [56] that intraply flow of the matrix polymer as well as interply flow in the resin rich layers must exist. No theoretical models take this into account. As expected, the sample thickness was shown to have little effect on the composite viscosity by investigating the number of laminate plies for carbon fibre composites in cross ply orientation. Results also showed that composites with shorter fibres (using smaller platen diameters) have a higher composite viscosity. This point

was discussed in Section 3.2.2.1, where it was suggested that this effect is due to end effects.

Linear oscillatory tests

Due to the highly anisotropic nature of continuous fibre-reinforced composite materials, a more direct method of measuring dynamic data for the longitudinal/transverse shear moduli is linear oscillation along and transverse to the fibre direction [59]. The apparatus, shown in Figure 3.3, is a linear oscillator. Two parallel platens with the lower plate oscillating linearly at a given frequency and amplitude are used to contain the sample. The lower plate provides the linear oscillatory motion to shear the sample, while another one provides the vertical motion to set the appropriate gap. The upper plate is constrained by leaf springs. A record of the resulting motion of the upper plate is made during measurements. The dynamic viscosity is output from a computer which converts the measured displacements of the top/bottom plates by transducers to amplitude and phase-lag data.

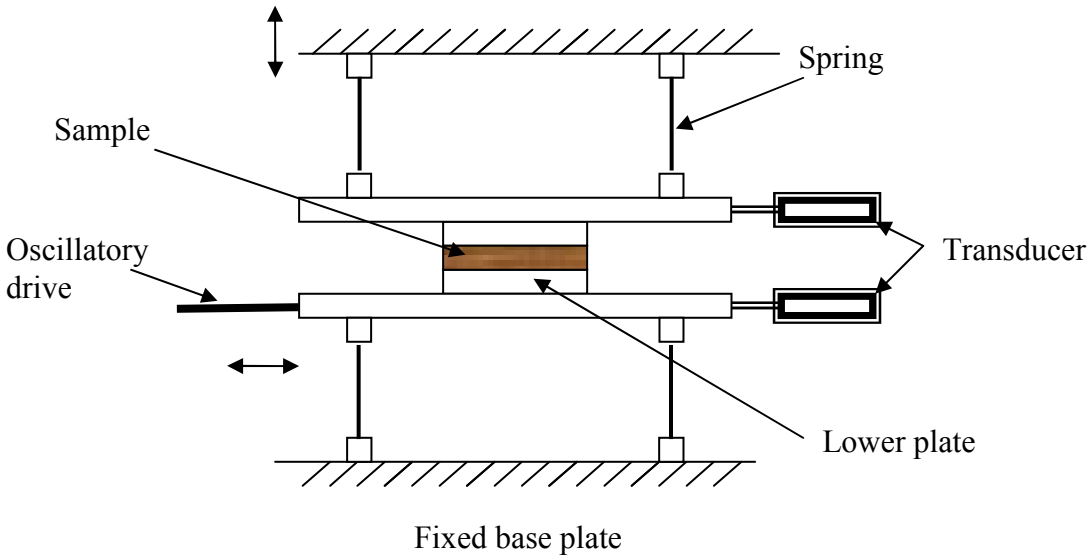

Figure 3.3. Schematic of linear oscillator. Reproduced from [59].

Derivation of the theory for the linear oscillatory test is similar to that for the rotational oscillatory viscometer which is based on linear viscoelasticity as given by Walters [84]. The dynamic viscosity and rigidity can be derived as shown in Eqs (3. 13)) and (3. 14)) respectively.

$$\eta' = -\frac{S\upsilon \sin c_p}{\upsilon^2 - 2\upsilon \cos c_p + 1} \quad \textbf{(3. 13)}$$

where υ denotes the amplitude ratio, c_p is the phase-lag, and S is defined by Equation(3. 15)).

$$G' = \frac{\omega S\upsilon(\cos c_p - \upsilon)}{\upsilon^2 - 2\upsilon \cos c_p + 1} \quad \textbf{(3. 14)}$$

where ω is the frequency.

$$S = \frac{g_p(k_{leaf} - \omega^2 M_{up})}{L_a L_b \omega} \quad \textbf{(3. 15)}$$

where g_p is the gap between the platens, k_{leaf} is the restoring constant of the leaf springs, L_a and L_b are the dimensions of the plate and M_{up} is the mass of the upper plate. These relations can be used to characterise the TV and LV at various frequencies.

An assumption in dynamic testing that the dependence of the dynamic viscosities on fibre volume fraction has the same form as that for the steady shear viscosities may restrict this test method to apply to certain material types. For example, usually the Cox-Merz rule is used to convert the complex viscosity measured in dynamic tests to a steady shear viscosity for most polymers, but this may not be suitable for some polymers, such as Boger fluids, cross-linked or gelled systems [18]. Investigation of sample thickness by

Roberts and Jones [60] using this technique showed that dynamic response was independent of the thickness for thickness > 3mm, which contradicts the results from Groves [56] using rotational dynamic testing. Variability of this technique also needs to be addressed. Discrepancies in studies of dynamic shear moduli still remain unclear as the source of the elastic response is not yet fully understood. Contributory factors could be fibre type, fibre entanglement, fibre twisting, fibre misalignment, or interfacial effects between fibres [60].

3.2.2.3 Steady shear linear 'pull-out' experiments

In the dynamic testing method, measurements of the LV and TV are frequency-dependent. This dependency increases with fibre volume fraction [60]. A relatively simple testing method, steady shear linear 'pull-out', was designed by Goshawk and Jones [62] to measure the LV and TV. A schematic of this method is shown in Figure 3.4.

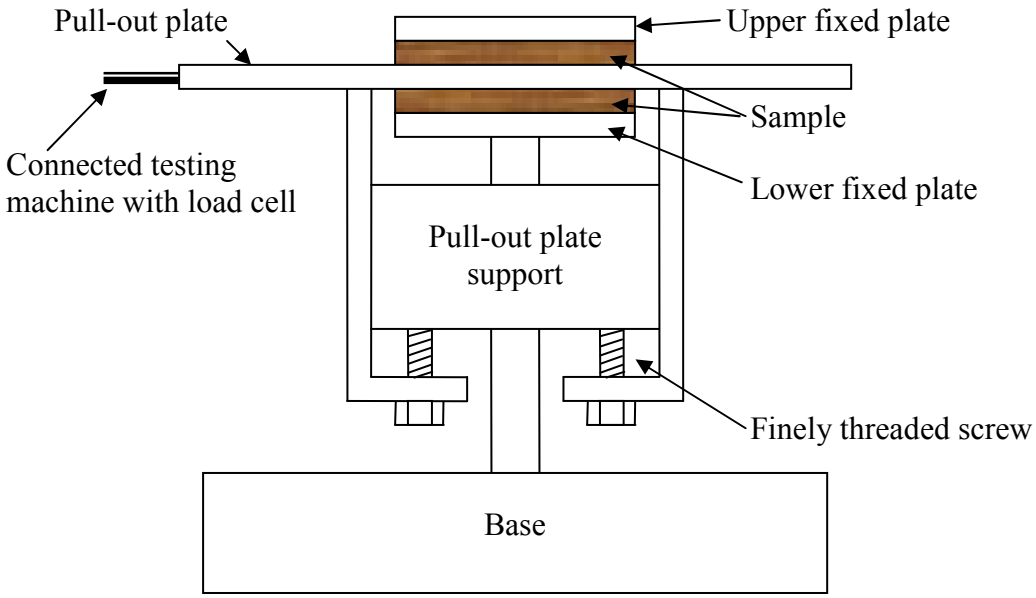

Figure 3.4. Schematic of the setup of steady shear linear 'pull-out' experiments.

One end of the pull-out plate is connected to a testing machine. During the test, a constant force is applied to the pull-out plate which moves unidirectionally along its length to shear the upper and lower samples; the displacement versus time is measured, from which the velocity of the pull-out plate can be determined. Then the viscosity measured is

$$\eta = \frac{F_{pull} h}{2 A_{cont} v_{pull}} \tag{3. 16}$$

where F_{pull} is the pull-out force, v_{pull} is the velocity of the pull-out plate, h the composite thickness, and A_{cont} is the contact area between the plates and samples.

Recently, Stanley and Mallon [77] characterised the LV and TV for a thermoplastic composite APC-2, 0.6 volume fraction carbon fibre/polyetheretherketone (PEEK), using a method with a similar principle to Figure 3.4; only the control unit and alignment (adjustment) device differ. Although this test method has the advantages of simple setup and a straightforward approach to interpret measurements, some careful considerations have to be taken to ensure validity of measurements. A monitoring mechanism, such as a flow visualisation technique used by Shuler and Advani [51], may be needed to ensure that effect of fluids flowing out of the fibre bed during testing is negligible, which can cause a change in fibre volume fraction, and most importantly to make sure no slip conditions occurred between the samples and plates. Although no visualisation monitoring for slip conditions during the test was used, the results of Stanley and Mallon [77] showed that the pull-out-force remained relatively constant up to a certain

displacement and then decreased, indicating the start of slip at the composite-platen interface. The relatively constant force together with the constant pull-out velocity ensures that a constant viscosity can be measured, and also implies a simple shear deformation through the sample thickness which was supported by images taken from deformed samples. Results of Goshawk and Jones [62] for a nylon/Golden Syrup composite with 60% fibre volume fraction showed that hardly any shear occurred within the fibre layer for the longitudinal case, i.e. slip occurred, but more shear occurred for the transverse case although slip was evident.

It is also necessary to consider the effect of the sample dimensions, i.e. end effects. Stanley and Mallon [77] suggested that a critical fibre length could exist for this type of experiment by investigating samples with various lengths but constant width and height. Below this critical value, results for both LV and TV cases were not influenced by the fibre length. The longer fibres tended to prevent the composite from shearing, which was thought to be due to the effect of fibre entanglement. To eliminate end effects, a systematic study on optimum dimensions, length, width and height, is needed. A shear thinning effect was evident and a limiting value for the shear rate to prevent slipping might exist [77]. It is noteworthy that substantial fibre reorientation can occur during transverse shearing [62], which could affect the local fibre concentration and even the fibre packing. In other words, fibres may re-arrange during transverse shearing. This effect may also increase fibre entanglement during shearing, where Stanley and Mallon [77] believed that the degree of fibre entanglement was magnified when using larger samples.

3.2.2.4 Vee-bending experiments

A vee-bending experiment [63, 66] may be used to obtain LV and TV. In practice, it is analogous to a 3-point bending experiment. The bending jig is mounted on a testing machine. Applied loads are produced by the punch which is connected to a load cell. In the test, the sample is subjected to a predetermined displacement of the crosshead. The output, force versus displacement, is analysed using the viscous bending model described in [66] (which will be reviewed briefly in Section 4.2.2).

Dykes et al.[66] performed tests for unidirectional glass/polypropylene composites with different lay-ups and a fibre volume fraction of 0.35 at various temperatures and rates. They found that the material had viscoelastic behaviour, showing an asymptotic decay in applied load with time, which is not considered by any theoretical models. It was also found that the material's elasticity was increased as the forming temperature was decreased. Shear thinning and rate-dependence were observed in the measurements. It was suggested that a mathematical relationship linking LV and TV might exist due to a similarity between the ratio of TV/LV and the ratio of transverse-to-longitudinal elastic moduli for various composite materials. Measurements from vee-bending tests [66] disagreed with theoretical predictions of Binding [69], Pipes [70] and Christensen [67]. However, in terms of the ratio of TV/LV, there was good agreement between measurements and the ratio of (Pipes TV/Binding LV), and the ratio of (Christensen TV/Binding LV), which reiterates that a mathematical relationship between LV and TV might exist.

3.2.2.5 Picture frame tests

McGuiness and O'Bradaigh [21] used a picture frame test to characterise the TV and LV for cross-plied laminates of unidirectional carbon fibre/PEEK composite at various rates and temperatures. The description of this test method is presented in Chapter 2. The output, force versus displacement, together with continuum mechanics models described in [21] which treats the composite material as an anisotropic fluid with inextensible constraint in the fibre direction, was used to interpret the LV and TV.

Reasonably good agreement was observed for TV between the picture-frame experiment results and squeeze flow measurements by Shuler and Advani [51]. However, McGuiness and O'Bradaigh [21] compared the results with published data from tests involving torsional rheometry (as in 3.2.2.2) with the same material and concluded that picture-frame shear testing is more appropriate for three reasons. Firstly, slip conditions may occur in the torsional tests which rely on surface loading to produce in-plane shear. Secondly, as the torsional experiments involve small-amplitude shear, shearing of the resin-rich layers (the layer with lower fibre volume fraction) due to slip conditions could provide a significant contribution to the overall shear in torsion. Thirdly, a 'size-effect' that both sets of tests used different specimen dimensions may exist. It may be necessary to investigate end effects in order to produce comparable measurements between different test methods. A picture frame test itself has some limitations and some careful considerations when using it are needed, such as sample alignment and boundary conditions. Further discussions on picture frame tests are presented in Chapter 5.

3.2.3 Discussion

Results from the literature described above are shown in Figure 3.5 and Figure 3.6 for longitudinal and transverse viscosities respectively. As all theoretical models discussed in this chapter are based on Newtonian fluids, the composite viscosities are normalised by matrix viscosities. Model predictions are calculated using Equations (3.3)-(3.9) based on the maximum fibre packing fraction for a hexagonal arrangement, except for the Harrison model which assumes square packing. The materials, testing temperatures and rates are given in the legends. Some fibres are different in type and diameter. APC-2 is a thermoplastic carbon fibre/polyetheretherketone (PEEK) composite. Most abbreviations can be easily interpreted from the preceding sections.

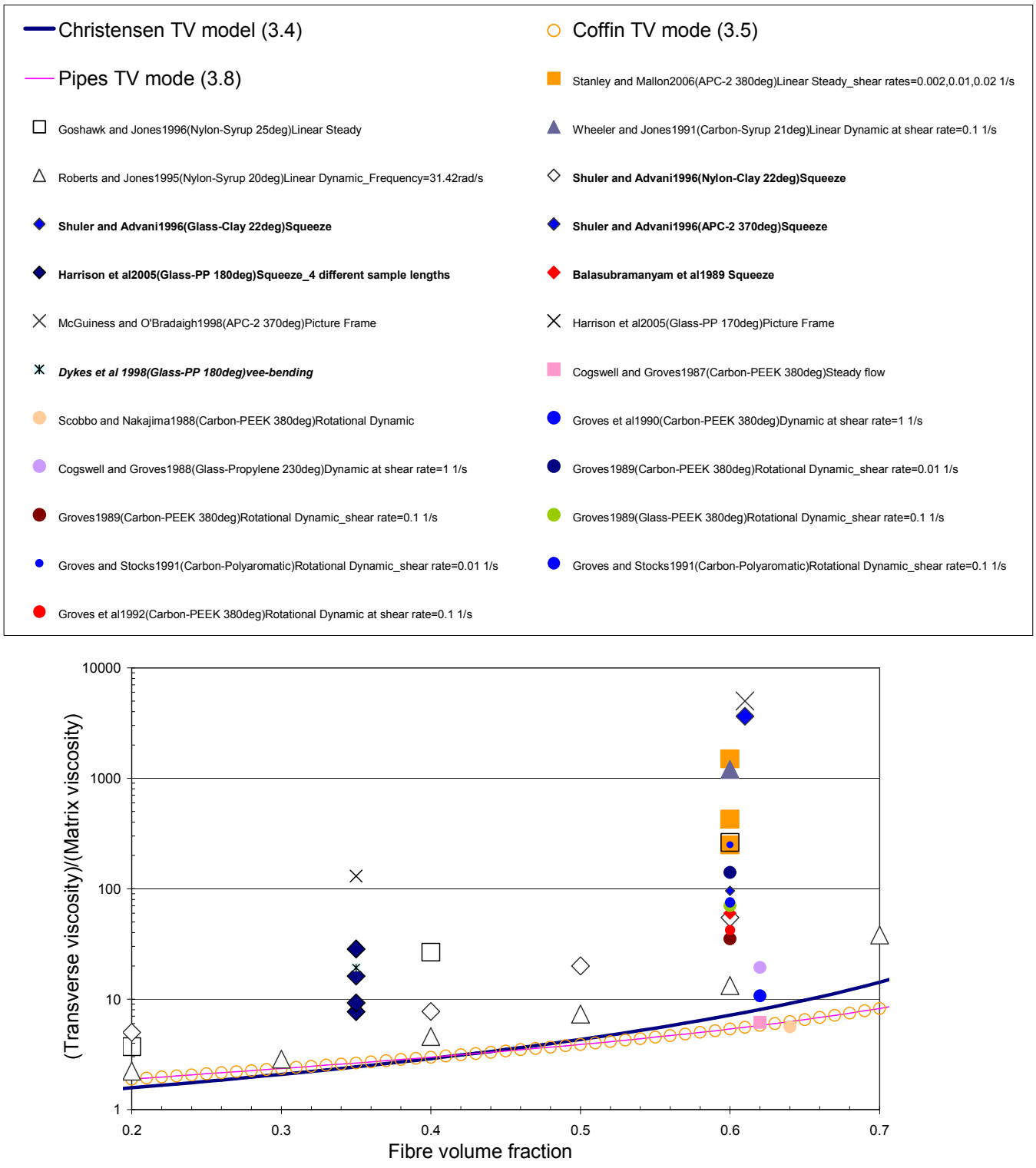

Figure 3.5. Data showing ratio between transverse and matrix viscosities versus fibre volume fraction from a number of different experiments and micro-mechanical models. The investigation and material are given in the legends: eg. Linear Steady=Linear steady shear pull-out and Linear Dynamic=Linear oscillatory dynamic test. The testing temperature and rate are also shown.

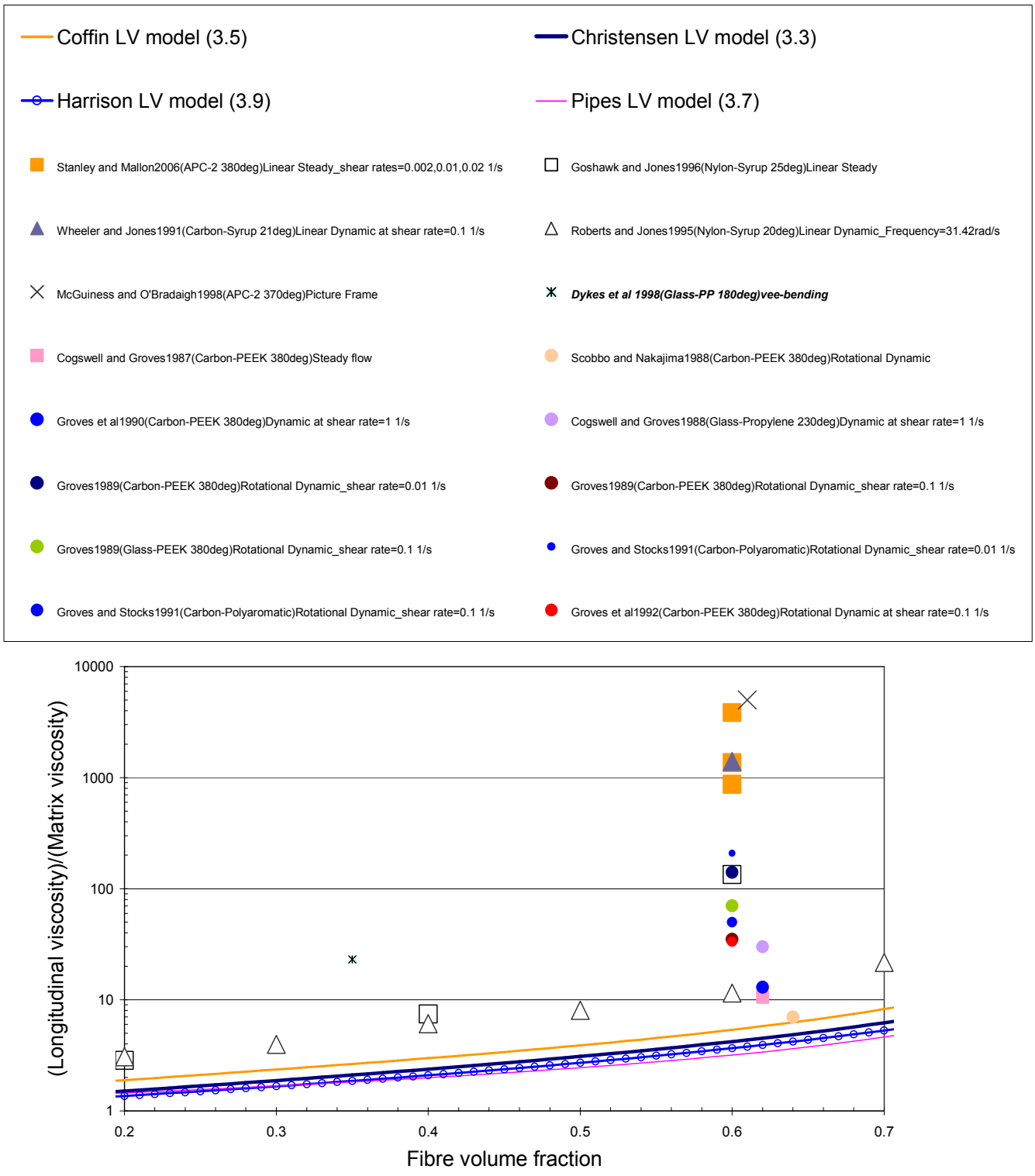

Figure 3.6. Data showing ratio between longitudinal and matrix viscosities versus fibre volume fraction from a number of different experiments and micro-mechanical models. The interpretation of the legends is same as Figure 3.5.

Most polymers in these materials investigated are non-Newtonian, thus the data collected in Figure 3.5 and Figure 3.6 should rate-dependent and temperature-dependent, i.e. depends on testing conditions. For dynamic testing, data are obtained at some specific rate and matrix viscosity used for normalisation is the value at the steady state due to the lack of detailed matrix viscosity in the published papers, and hence for shear thinning composites variation in experiment values for different rates would be less. For squeeze flow experiments, the values at the steady state for composite and matrix viscosities were adopted.

At first glance all data collected in Figure 3.5 and Figure 3.6 differ enormously based on testing methods, material types and experimental conditions, especially at higher volume fractions. McGuiness and O'Bradaigh [21] reported that a difference is up to three orders of magnitude in comparisons between picture frame and torsional rheometry techniques, and believed that this could be due to slip conditions and a large contribution of shearing of the resin-rich layers in torsional tests, and different sample dimensions tested. One can easily observe from Figure 3.5 and Figure 3.6 that the difference is increased with fibre volume fraction. For example in Figure 3.5, comparing linear steady testing by Goshawk and Jones [62] with linear dynamic testing by Roberts and Jones [60], the differences are 40%, 83% and 95% respectively for fibre volume fractions 0.2, 0.4 and 0.6. The trend also can be found in Figure 3.6 for the longitudinal case. One may speculate that a composite with higher fibre contents would have more effects from fibre entanglement, misalignment, twisting and fibre contact, which could produce fibre bending, torsion and dry

friction between solid fibres. This kind of phenomenon is not represented by any of the models.

From Figure 3.5 and Figure 3.6, the difference between model predictions and measured viscosities is up to three orders of magnitude. For the transverse case, theoretical models agree very well and provide a good approximation for the lower bound of measured values, whereas LV models only agree reasonably well, but the highest predictions (Coffin model) still underestimate the lower bound. All theoretical models do not account for non-ideal arrangement of fibres (such as fibre entanglement, misalignment and twisting) and fibre contact, instead they assume fibres are straight and rigid during shearing with a resin film consistently between fibres. This has neglected effects of fibre properties, such as elastic behaviour and fibre geometry which will be investigated later. By this argument, model predictions would indeed be lower than measurements and the difference would increase with fibre volume fraction.

At this stage it is very difficult to tell which test method or model can better capture the shear viscosities of a composite. Instead, investigations into some aspects, such as fibre geometry, matrix viscosity (non-Newtonian effects) and fibre packing, can be attempted.

3.2.3.1 Investigation of geometry effects

As discussed above, fibre geometry or dimensions could affect the shear behaviour through elastic deformation of fibres. Shuler and Advani [51] reported that a composite of smaller fibre diameter has higher TV, which was thought to be due to the fact that the fibres with smaller diameter have a larger ratio of surface area to volume. To support this, TV at a fibre volume fraction of 0.6 versus fibre diameter is plotted in Figure 3.7. Even though there is large scatter in data due to different testing methods and shear rates, the trend that TV decreases with fibre diameter is evident. In practice, it may be more realistic and reasonable to compare results from one testing method, like squeeze flow experiments performed by Shuler and Advani [51]. A strong trend can be observed, although there are only 3 points (diamonds with different colours).

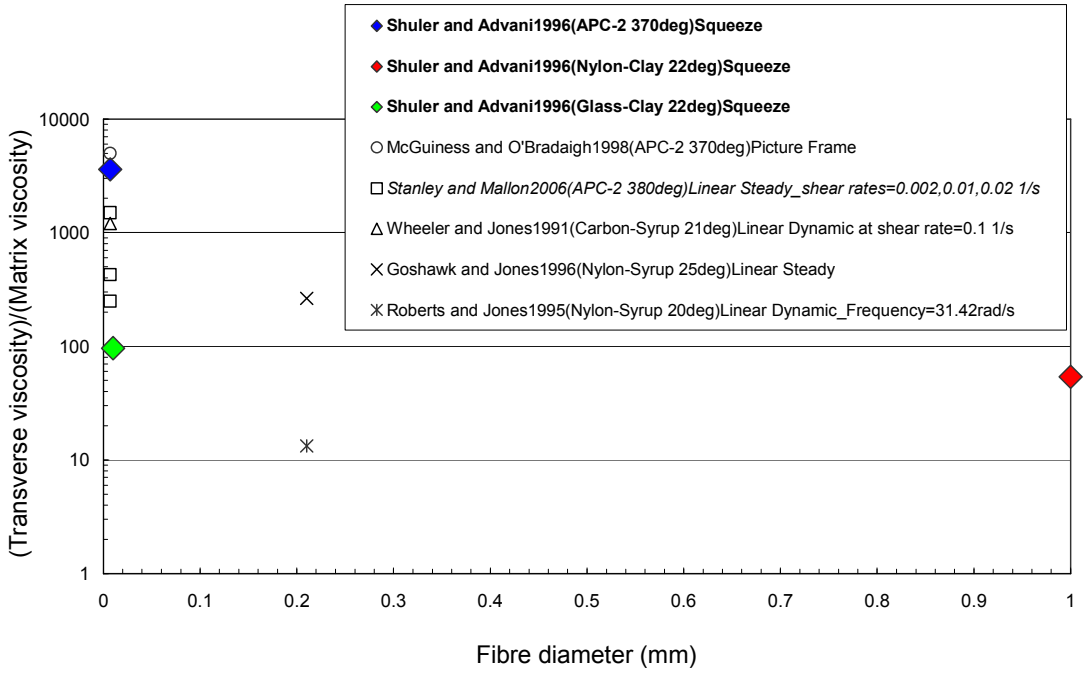

Figure 3.7. Plot of the ratio between transverse and matrix viscosities versus fibre diameter. The interpretation of the legends is same as Figure 3.5.

It may be necessary to consider that fibre shape could vary along the fibre length. This can affect the shear deformation rate across the whole composite, as the resin film thickness is a function of position within the composite sheet. This may be a contributory factor to the variability of experimental data. Another issue about effects of sample geometry relates end effects, and this should be studied within the development of a test method.

3.2.3.2 Investigation of matrix viscosity

Roberts and Jones [60] reported that the composite viscosities depend linearly on the matrix viscosity for fibre volume fractions 0.2, 0.4 and 0.6 based on linear oscillatory dynamic testing. This means that the change in matrix viscosity during shear deformation would result in a change in the composite viscosities. Two factors, shear rate and temperature, are most influential on the matrix viscosity. These rate and temperature dependences may be used to explain the high variation in rotational dynamic testing data and other characterisation techniques. Even for the same testing method, values vary due to the rate dependence (see Figure 3.5 and Figure 3.6, data from Stanley and Mallon linear steady testing). As discussed in Section 3.2.2.2, non-Newtonian behaviour of matrix resin defines the rheological behaviour of the composite. To clarify the difference between characterisation techniques and then to decide which one might be better to obtain more accurate composite viscosities, a matrix resin with less sensitivity to rate and temperature should be used. This is important in validation of theoretical models if they assume idealised Newtonian behaviour for the matrix viscosity.

3.2.3.3 Investigation of fibre packing

All model predictions except for Harrison's model in Figure 3.5 and Figure 3.6 are based on hexagonal fibre packing. All theoretical models need to be derived based on certain geometrical assumptions, such as regular fibre packing during shearing deformation. This allows determination of the shear strain rate field. Model predictions based on square and hexagonal packing shown in Figure 3.8. Predictions based on a square packing are consistently higher than those based on hexagonal throughout the fibre volume fraction range. This is attributed to the fact that the fibre gap for square packing is smaller than that for hexagonal for all fibre volume fractions, and hence the shear strain rate is higher. The difference increases with fibre volume fraction.

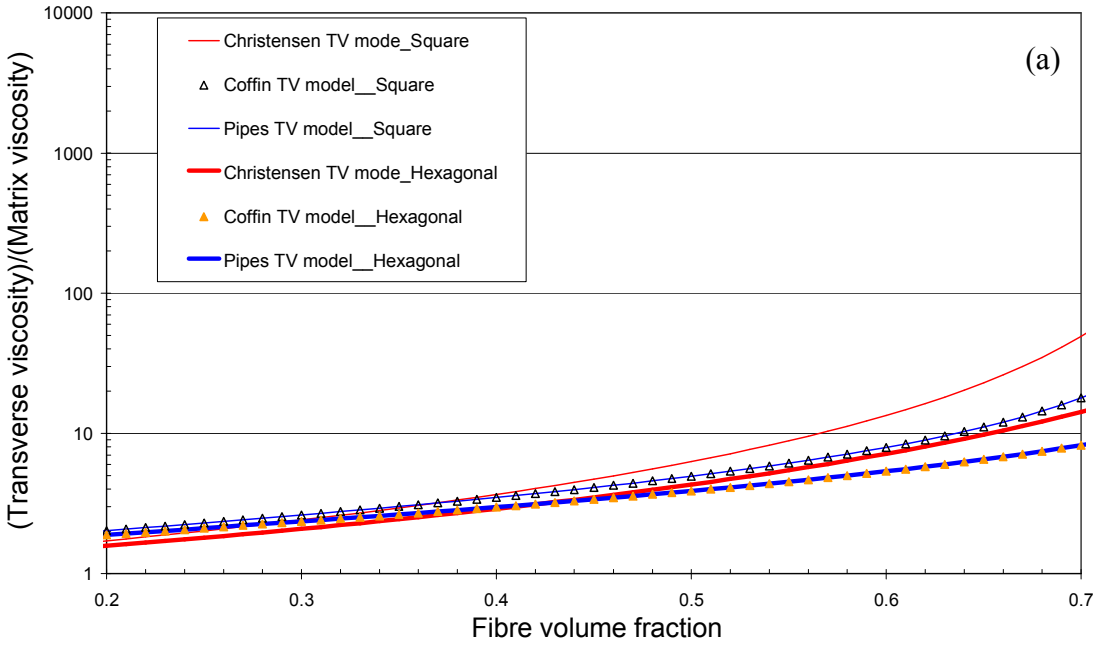

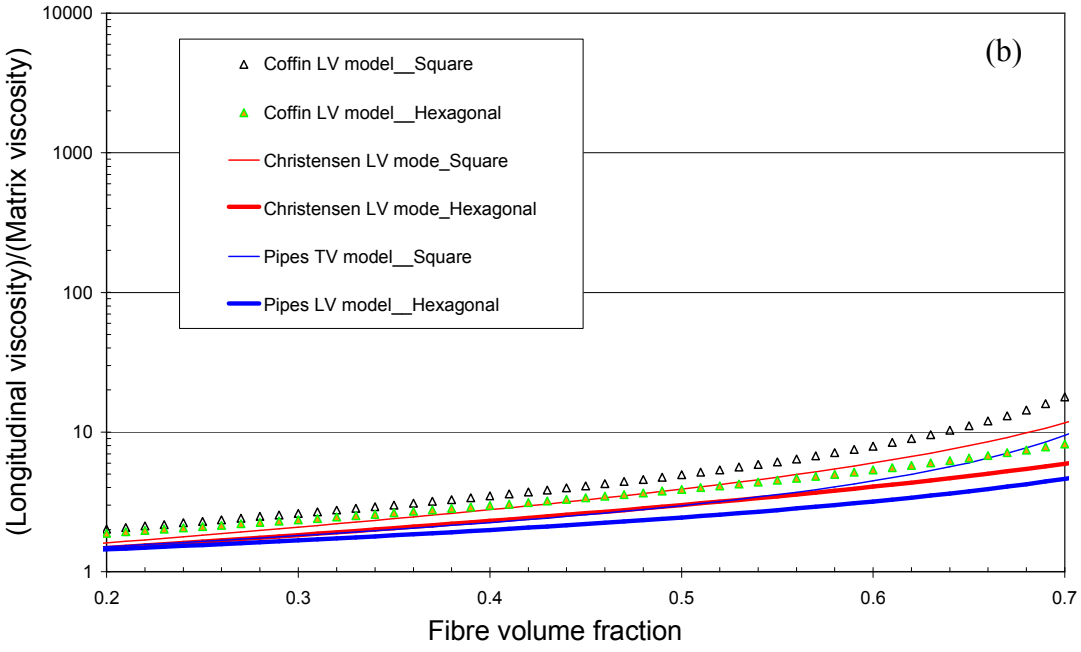

Figure 3.8. Model predictions based on hexagonal and square fibre packings. (a) Transverse (b) Longitudinal.

3.2.4 Summary

Theoretical models and characterisation techniques to determine LV and TV were reviewed. The results and conclusions of previous studies were compared and analysed systematically, leading to some interesting observations, such as the ratio of TV/LV and its mathematical relationship, shear-angle dependence, effects of non-Newtonian matrix, fibre packing, viscoelastic effects and end effects.

The results from theoretical models and experiments were plotted for evaluation for both LV and TV. Data are highly scattered; model predictions underestimate the measurements but are close to the lower bound of experiment data. The discrepancy is found to increase with fibre volume fraction. Investigation of matrix viscosity shows that composite viscosities are shear rate and temperature dependent, which explain some of the variation in data, as some data were obtained at different rates and temperatures, even for the same test method and material. This means that it is necessary to develop TV and LV models for non-Newtonian fluids. Certainly, variability of the characterisation technique itself could also be one of contributory factors in the scatter of data. Both TV and LV based on square fibre packing are consistently higher than those based on hexagonal packing for all fibre volume fractions, and the difference increases with fibre volume fraction.

In addition to the above issues, possible reasons for large amount of scatter in the data may be summarised as follows:

1. Elastic effects from fibres

2. Viscoelasitc effects from matrix
3. Non-ideal fibre arrangement, fibre entanglement, fibre twisting and fibre misalignment
4. Fibre stiffness and bending rigidity
5. End effects (different sample dimensions for compared test results)
6. Intraply flow of the resin and interply flow in the resin rich layers (leading to non-uniform or inhomogeneous shear through the thickness)

Christensen [67], Coffin [68] and Pipes [70] models predict both LV and TV, while Harrison's [19] model only predicts LV. Binding's [69] model predicts an upper and lower bound for LV. Coffin's model suggests that LV=TV, however Christensen's and Pipes's models propose TV>LV for all fibre volume fractions which is supported by linear steady shear pull-out testing by Goshawk and Jones [62]. However, most experimental data collected in this literature review shows that the ratio of LV to TV is between 1 and 2.5. Roberts and Jones [60] suggest that the ratio may be a function of the fibre volume fraction. This could lead to speculation that a mathematical correlation linking these two composite viscosities might exist, which was first proposed by Dykes et al. [66] from vee-bending tests.

When the LV is analysed using picture frame shear, the structure of a composite material, such as fibre gap and packing, may be reorganised with respect to the shear angle. Hence LV could be shear-angle dependent. As such, Harrison [19] proposed a relationship to account for the shear-angle

dependence. However, Harrison LV model was not yet validated by any picture frame shear results.

On the experimental side, a number of test methods have been used to measure the TV and LV, such as linear or rotational dynamic testing, linear steady pull-out experiments, vee-bending and picture frame tests. The squeeze flow test is a popular method, but only measures TV. This technique is well developed by Shuler and Advani [51] through important investigations on testing conditions, such as rate, creeping flow assumption and 2-D transverse flow deformation using a visualisation technique. Harrison et al. [81] used this method to suggest that TV was length-dependent. This could prompt the importance of investigation of end effects of this characterisation technique. None of the characterisation techniques reviewed in this chapter investigated end effects.

Dykes et al. [66] using vee-bending experiments found that viscoelastic effects are evident and the material's elasticity increases as the forming temperature decreases. Groves [56] who performed rotational dynamic testing found that at low shear rates, composites with a Newtonian matrix showed non-Newtonian behaviour, which was thought to be due to the elastic contribution of fibres. So far no theoretical models can account for non-Newtonian behaviour and elastic effects. Elastic behaviour of LV and TV may be due to tension, compression, torsion or bending of fibres which could be caused by fibre contact and non-ideal arrangement of fibres within the composite. This argument may explain why all theoretical models underestimate the measured viscosities and the difference increases with fibre volume fraction.

Experimental data from the literature show that TV decreases with fibre diameter, which was thought by Shuler and Advani [51] to be due to the fact that the fibres with smaller diameter have a larger ratio of surface area to volume, hence shear strain rate is decreased.

Although the development of an accurate characterisation technique for measuring LV and TV is still in its infancy, an attempt may be made to decide which methods should be preferred based on the information described in the preceding sections. Rotational dynamic testing is only able to provide isotropic measurements [59] and slip conditions may very likely occur for surface loading to produce in-plane shear [21]. In contrast, linear dynamic testing is a much more direct means of obtaining data. However, measurements from dynamic testing are highly frequency dependent, particularly at higher fibre volume fractions. Moreover, an assumption involved in dynamic testing that the dependence of the dynamic viscosities on fibre volume fraction has the same form as that for the steady shear viscosities, may limit its application for certain materials. Therefore, linear steady pull-out test may be preferred to dynamic testing. For vee-bending, the complexity of the apparatus and theoretical interpretation could affect accuracy and limit its application. Squeeze flow experiments were shown to be length-dependent. The picture frame test is sensitive to the material tested and subject to high variability [25]. Linear steady pull-out tests from Goshawk and Jones [62] were further developed by Stanley and Mallon [77] to assure no slip conditions and linear velocity gradient through the sample thickness. Therefore, the linear steady pull-out test [77] appears to be the best among those described in this section.

However, in order to clarify the discrepancies between all test methods and theoretical models, a benchmarking exercise would be highly desirable.

3.3 Modelling of transverse viscosity

This section develops a new TV model. Most of the analysis follows the method in the Christensen model [67] and are re-described here for completeness.

Figure 3.9 shows a hexagonal fibre arrangement with circular fibres and a reduced unit cell. Axis 1 is in the fibre direction (out of page) and axes 2 and 3 are parallel to x and y. Applying a velocity of Λ to the top fibre of Figure 3.9(b), transverse to the fibre direction (along the 2 axis), then the normal and tangential components of relative velocity of two fibre cylinders are respectively given by:

$$v_n = \frac{1}{2}\Lambda \quad \text{and} \quad v_t = \frac{\sqrt{3}}{2}\Lambda . \tag{3.17}$$

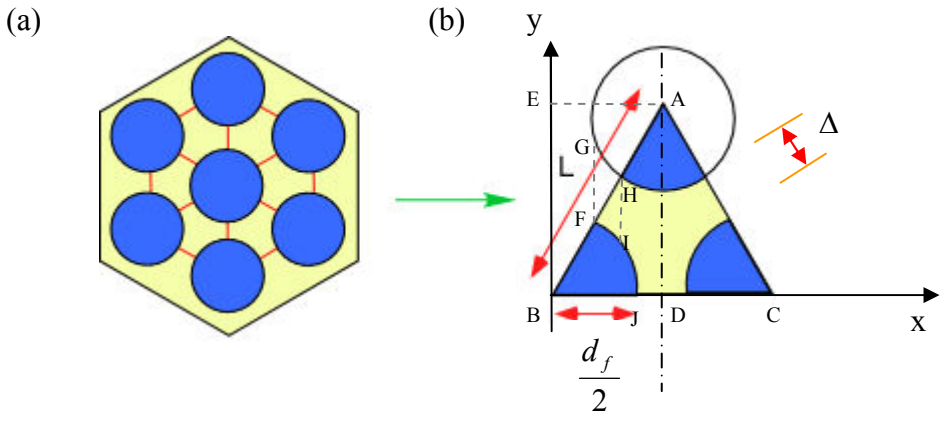

Figure 3.9. (a) Hexagonal fibre arrangement with circular cross-section fibres and (b) a reduced unit cell, where Δ, d_f and L are minimum fibre gap, fibre diameter and side

length of the reduced unit cell respectively. A 2-D coordinate system with its origin B is fixed at the centre of the fibre at the left bottom.

Assuming a state of shear strain rate caused by the applied velocity, the bulk rate of deformation tensor can be determined as

$$(\mathbf{D})_{\text{bulk}} = \begin{bmatrix} 0 & 0 & 0 \\ 0 & 0 & \dfrac{\Lambda}{\sqrt{3}\left(d_f + \Delta\right)} \\ 0 & \dfrac{\Lambda}{\sqrt{3}\left(d_f + \Delta\right)} & 0 \end{bmatrix} \tag{3. 18}$$

where d_f is the fibre diameter and Δ is the minimum fibre gap which can be determined by the fibre volume fraction (v_f) through

$$\Delta = d_f\left(\sqrt{\frac{\pi}{2\sqrt{3}v_f}} - 1\right) \tag{3. 19}$$

For the equivalent homogeneous fluid under this rate of deformation, the rate of dissipation of energy is

$$P = \frac{\Lambda^2 \eta_{32}}{2\sqrt{3}} \tag{3. 20}$$

where η_{32} is the effective transverse viscosity.

In the matrix fluid, a lubrication approximation is applied to the thin annulus of fluid between two nearly touching fibre cylinders. By taking an infinite, uniform sheet of fluid as shown in Figure 3.10, one surface of fluid sheet (the upper surface) is given a motion relative to the other (the bottom surface). Thereafter, the rate of deformation tensor will be derived in terms of velocity components expressed in a rectangular Cartesian coordinate system.

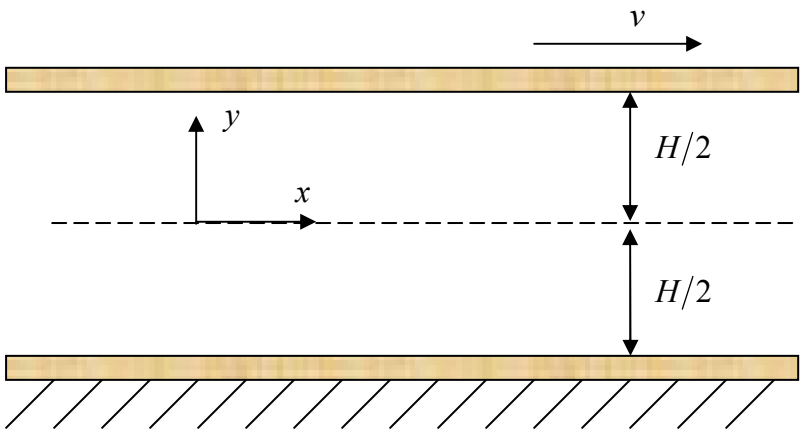

Figure 3.10. Schematic of two plates filled with fluids between, where the bottom is fixed and the upper is allowed to move. H is the thickness of fluid film between two fibres. The two plates can be any shapes, such as circular. Hence H is a function of position x.

The incompressibility condition in a rectangular Cartesian coordinate system yields

$$\frac{\partial v_x}{\partial x} + \frac{\partial v_y}{\partial y} = 0 \qquad \textbf{(3. 21)}$$

With the incompressible flow assumption and constant viscosity, the Navier-Stokes equations for an incompressible Newtonian fluid can be written in a vector form as

$$-\nabla p + \eta_m \nabla^2 v + F_{body} = \rho_m \left[\frac{\partial v}{\partial t} + (v \cdot \nabla) v \right] \qquad \textbf{(3. 22)}$$

where ∇p is a pressure gradient arising from normal stresses, η_m is the matrix viscosity, F_{body} represents other body forces such as gravity and centrifugal force and ρ_m is the matrix density.

Under creeping flow conditions with negligible body forces, the equations of motion in a rectangular Cartesian coordinate system become

$$-\frac{\partial p}{\partial x}+\eta_m \nabla^2 v_x = 0 \quad \textbf{(3. 23)}$$

and

$$-\frac{\partial p}{\partial y}+\eta_m \nabla^2 v_y = 0 \quad \textbf{(3. 24)}$$

The assumptions

$$v_y << v_x \text{ and } \frac{\partial^2 v_x}{\partial x^2} << \frac{\partial^2 v_x}{\partial y^2} \quad \textbf{(3. 25)}$$

can be shown to be valid for $x/H >> 1$. Hence the equations of motion can be re-derived as

$$\frac{\partial^2 v_x}{\partial y^2} = \frac{1}{\eta_m}\frac{\partial p}{\partial x} \text{ and } \frac{\partial p}{\partial y} = 0 \quad \textbf{(3. 26)}$$

The effect from the tangential component of velocity was neglected in the Christensen TV model, whilst it is included in the new developed TV model, which will be discussed in Section 3.5. Hence from this point the derivation is different from the Christensen TV model. Using boundary conditions

$$v_x = \pm\frac{v_t}{2} \text{ and } v_y = \pm\frac{v_n}{2} \text{ at } y = \pm\frac{H}{2}, \quad \textbf{(3. 27)}$$

then Equations (3. 21) and (3. 26) can be integrated to fulfil these boundary conditions giving

$$v_x = \frac{3}{2}\left(\frac{v_n}{H}\right)\left(\frac{4y^2}{H^2}-1\right)x + \frac{v_t}{H}y \quad \textbf{(3. 28)}$$

and

$$v_y = -\frac{3}{2}\left(\frac{v_n}{H}\right)\left(\frac{4y^3}{3H^2} - y\right) \tag{3. 29}$$

By using Equations (3. 28) and (3. 29), the rate of deformation tensor is

$$\mathbf{D} = \begin{bmatrix} \frac{3}{2}\left(\frac{v_n}{H}\right)\left(\frac{4y^2}{H^2} - 1\right) & \frac{6xyv_n}{H^3} + \frac{v_t}{2H} & 0 \\ \frac{6xyv_n}{H^3} + \frac{v_t}{2H} & -\frac{3}{2}\left(\frac{v_n}{H}\right)\left(\frac{4y^2}{H^2} - 1\right) & 0 \\ 0 & 0 & 0 \end{bmatrix} \tag{3.30}$$

The rate of dissipation of energy per unit volume is given by

$$P_u = \eta_m D_{ij} D_{ij} \tag{3.31}$$

where D_{ij} is the component of the rate of deformation tensor.

Using Equation (3.30), the rate of energy dissipated in the fluid (Equation (3.31)) can re-written as

$$P_u = \eta_m \left[\frac{9}{2}\left(\frac{v_n}{H}\right)^2 \left(\frac{4y^2}{H^2} - 1\right)^2 + 2\left(\frac{6xyv_n}{H^3} + \frac{v_t}{2H}\right)^2 \right] \tag{3.32}$$

Integrating over the half fibre gap gives

$$\int_0^{H/2} P_u dy = \eta_m \left[\frac{6}{5}\left(\frac{v_n}{H}\right)^2 H + 3\left(\frac{v_n}{H}\right)^2 \frac{x^2}{H} + \frac{v_t^2}{4H} + \frac{3xv_n v_t}{2H^2} \right] \tag{3.33}$$

Using the lubrication approximation, the dimension H is taken to be a function of x in accordance with the gap between fibres in Figure 3.9. The total rate of energy dissipated in the reduced unit cell is given by

$$P = 2\eta_m \int_a^d \left[\frac{6}{5}\left(\frac{v_n}{H}\right)^2 H + 3\left(\frac{v_n}{H}\right)^2 \frac{x^2}{H} + \frac{v_t^2}{4H} + \frac{3xv_n v_t}{2H^2} \right] dx \tag{3.34}$$

where a and d are the endpoints of the interval, corresponding to points F and D respectively, and given by Equations

$$a = d_f/4 \text{ and } d = \left(d_f + \Delta\right)/2 \tag{3.35}$$

Using Equation (3. 17), Equation (3.34) can be re-written as

$$P = \frac{\eta_m}{2}\int_a^d \left[\frac{6\Lambda^2}{5H} + \frac{3\Lambda^2 x^2}{H^3} + \frac{3\Lambda^2}{4H} + \frac{3\sqrt{3}x\Lambda^2}{2H^2}\right]dx \tag{3.36}$$

Equating Equations (3. 20) and (3.36) would determine the effective transverse viscosity η_{32} as

$$\eta_{32} = \sqrt{3}\eta_m \int_a^d \left[\frac{6}{5H} + \frac{3x^2}{H^3} + \frac{3}{4H} + \frac{3\sqrt{3}x}{2H^2}\right]dx \tag{3.37}$$

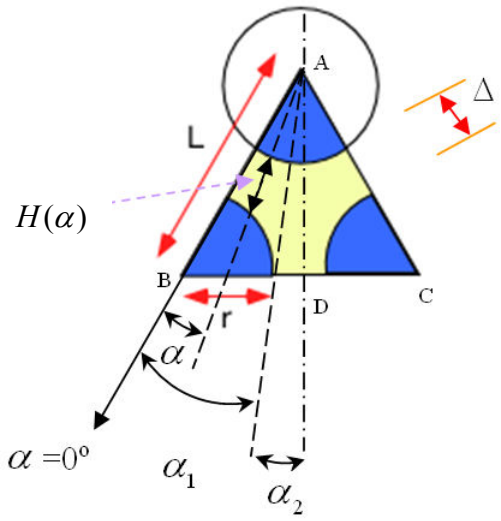

Figure 3.11. The reduced unit cell where a polar coordinate system with its pole A is fixed at the centre of the upper fibre.

In order to ease integration of Equation (3.37), a polar coordinate system is applied (see Figure 3.11). Dimension H is taken to be a function of α in accordance with the gap between fibres, then Equation (3.37) becomes

$$\eta_{32} = 6\sqrt{3}\eta_m \left[\int_0^{\alpha_1} \left(\frac{2}{5H_1} + \frac{x^2}{{H_1}^3} + \frac{1}{4H_1} + \frac{\sqrt{3}x}{2{H_1}^2} \right) dx + \int_{\alpha_1}^{\frac{\pi}{6}} \left(\frac{2}{5H_2} + \frac{x^2}{{H_2}^3} + \frac{1}{4H_2} + \frac{\sqrt{3}x}{2{H_2}^2} \right) dx \right] \quad \textbf{(3.38)}$$

with a geometrical approximation

$$x = \frac{\alpha}{4}\left[2d_f + \Delta + H\right] \quad \textbf{(3.39)}$$

and then

$$dx = \frac{d\alpha}{4}\left[2d_f + \Delta + H\right] \quad \textbf{(3.40)}$$

Then Equation (3.38) becomes

$$\eta_{32} = \frac{3\sqrt{3}\eta_m}{2} \left[\begin{array}{l} \int_0^{\alpha_1} \left(\frac{2}{5H_1} + \frac{\alpha^2\left(2d_f + \Delta + H_1\right)^2}{16{H_1}^3} + \frac{1}{4H_1} + \frac{\sqrt{3}\alpha\left(2d_f + \Delta + H_1\right)}{8{H_1}^2} \right) \left(2d_f + \Delta + H_1\right) d\alpha \\ + \int_{\alpha_1}^{\frac{\pi}{6}} \left(\frac{2}{5H_2} + \frac{\alpha^2\left(2d_f + \Delta + H_2\right)^2}{16{H_2}^3} + \frac{1}{4H_2} + \frac{\sqrt{3}\alpha\left(2d_f + \Delta + H_2\right)}{8{H_2}^2} \right) \left(2d_f + \Delta + H_2\right) d\alpha \end{array} \right] \quad \textbf{(3.41)}$$

Note that the term $\frac{2}{5H} + \frac{\alpha^2\left(2d_f + \Delta + H\right)^2}{16H^3}$ is associated with the normal component of velocity, v_n, while $\frac{1}{4H} + \frac{\sqrt{3}\alpha\left(2d_f + \Delta + H\right)}{8H^2}$ is associated with tangential component, v_t. We can make predictions from these two separate contributions so as to investigate the effect of the tangential component of velocity which was assumed negligible in the Christensen TV model.

The fibre gap $H(\alpha)$ in the polar coordinate system can be shown to be

$$H_1(\alpha) = L\cos\alpha - \frac{d_f}{2} - \sqrt{\left(L\cos\alpha\right)^2 + \frac{{d_f}^2}{4} - L^2} \quad \textbf{(3.42)}$$

for $0 < \alpha < \alpha_1$ and

$$H_2(\alpha) = L\sin 60^o \sec(\alpha - 30^o) - \frac{d_f}{2} \tag{3.43}$$

A combination of Equations (3.41), (3.42) and (3.43) predicts the transverse viscosity.

3.4 Modelling of longitudinal viscosity

This section develops a novel LV model. For hexagonal fibre packing, the geometry of Figure 3.9 and the equation (3. 19) still hold. The approach is based on the idea of the Christensen LV model [67] and follows similar methodology to modelling transverse viscosity in the preceding section. The difference between the Christensen LV model and the new model is that a polar coordinate system was used to solve integration of Equation (3.51).

By applying a velocity of Λ to the top fibre of Figure 3.9, along the fibre direction and assuming a state of shear strain rate caused by the velocity, then the bulk rate of deformation tensor can be determined as

$$(\mathbf{D})_{\text{bulk}} = \begin{bmatrix} 0 & 0 & \dfrac{\Lambda}{\sqrt{3}(d_f + \Delta)} \\ 0 & 0 & 0 \\ \dfrac{\Lambda}{\sqrt{3}(d_f + \Delta)} & 0 & 0 \end{bmatrix}. \tag{3. 44}$$

For the equivalent homogeneous fluid under this rate of deformation, the rate of dissipation of energy is

$$P = \frac{\Lambda^2 \eta_{31}}{2\sqrt{3}} \tag{3. 45}$$

where η_{31} is the effective longitudinal viscosity.

In the matrix fluid, under the lubrication approximation the treatment shown in Figure 3.10 still applies. The rate of deformation tensor in shear caused by the velocity Λ is given by:

$$\mathbf{D} = \begin{bmatrix} 0 & 0 & \frac{\Lambda}{2H} \\ 0 & 0 & 0 \\ \frac{\Lambda}{2H} & 0 & 0 \end{bmatrix}. \quad \textbf{(3. 46)}$$

The rate of dissipation of energy per unit volume is given by Equation (3.31). Using Equation (3. 46), the rate of energy dissipated in the fluid gives

$$P_u = \frac{\eta_m}{2}\left(\frac{\Lambda}{H}\right)^2. \quad \textbf{(3. 47)}$$

Integrating over the fibre gap gives

$$\int_0^H P_u dy = \frac{\eta_m \Lambda^2}{2H}. \quad \textbf{(3. 48)}$$

Using the lubrication approximation, the dimension H is taken to be a function of x in accordance with the gap between fibres in Figure 3.9. The total rate of energy dissipated in the reduced unit cell is given by

$$P = \int_a^b \frac{\eta_m \Lambda^2}{2H_1(x)} dx + 2 \times \left[\int_b^c \frac{\eta_m \Lambda^2}{2H_1(x)} dx + \int_c^d \frac{\eta_m \Lambda^2}{2H_2(x)} dx \right] \quad \textbf{(3. 49)}$$

where b and c are the endpoints of the interval, corresponding to points I and J respectively, and given by:

$$b = \frac{d_f + 2\Delta}{4} \text{ and } c = d_f/2 \ . \quad \textbf{(3.50)}$$

Equating Equations (3. 45) and (3. 49) determines the effective longitudinal viscosity η_{31} as

$$\eta_{31} = \sqrt{3}\eta_m \left[\int_a^b \frac{1}{H_1(x)} dx + \int_b^c \frac{2}{H_1(x)} dx + \int_c^d \frac{2}{H_2(x)} dx \right]. \tag{3.51}$$

As a polar coordinate system is used to ease integration of Equation (3.51), the derivation from this point is different from that of the Christensen LV model. In polar coordinates (see Figure 3.11), the dimension H is taken to be a function of α in accordance with the gap between fibres, an approximation

$$dx = \frac{d_f}{2} d\alpha + \frac{H}{2} d\alpha \tag{3.52}$$

is taken, and the fibre gap $H(\alpha)$ between fibres in the polar coordinate system are given by Equations (3.42) and (3.43). Therefore, Equation (3.51) becomes

$$\eta_{31} = 2\sqrt{3}\eta_m \left[\int_0^{\alpha_1} \frac{d_f}{2H_1(\alpha)} d\alpha + \int_{\alpha_1}^{\frac{\pi}{6}} \frac{d_f}{2H_2(\alpha)} d\alpha \right] + \frac{\sqrt{3}\pi\eta_m}{6} \tag{3.53}$$

A combination of Equations (3.53), (3.42) and (3.43) predicts the longitudinal viscosity.

3.5 Results, validation and discussion

As fibre diameter appears in new TV and LV models, investigation of effects of fibre diameter was performed and showed no effects. The fibre diameter used in new model predictions is 5 microns. As the new TV and LV models are developed based on the Christensen's model, it is necessary to investigate their differences by comparisons. The first term of Equation (3.41) arises from the normal velocity component, while the second term from the tangential velocity

component. Figure 3.12 shows the normalised TV versus fibre volume fraction predicted by the new model with the normal and tangential velocity components, and compared with predictions by the Christensen's model. It is shown that the normalised TVs caused by these two velocity components are approximately equal, and well agree with the Christensen TV model within the variability of experimental data from the literature, but both terms are slightly higher than Christensen model at lower fibre volume fractions and slightly lower at higher volume fractions. Christensen [67] argues that for a hexagonal fibre packing, more energy dissipation is caused by the normal velocity component of relative velocity between two fibres due to higher order velocity gradients than by the tangential component and relative rotation motion between the fibres. This means that just the normal velocity component is considered in the Christensen model, so it is understandable for it to agree with the new TV model with one component. Hence, the tangential component might not be neglected during transverse shearing. Figure 3.12 also shows that the new TV model predictions are higher than Christensen model predictions at all fibre volume fractions by up to a factor of 2.5. Figure 3.13 shows the normalised LV versus fibre volume fraction for Christensen LV model, new LV model and Binding lower and upper bound models. Christensen model predictions are closer and approximately equal to the Binding lower bound for all volume fractions. The new LV model predictions agree Christensen and Binding lower bound models very well, although they are slightly lower at higher fibre volume fractions.

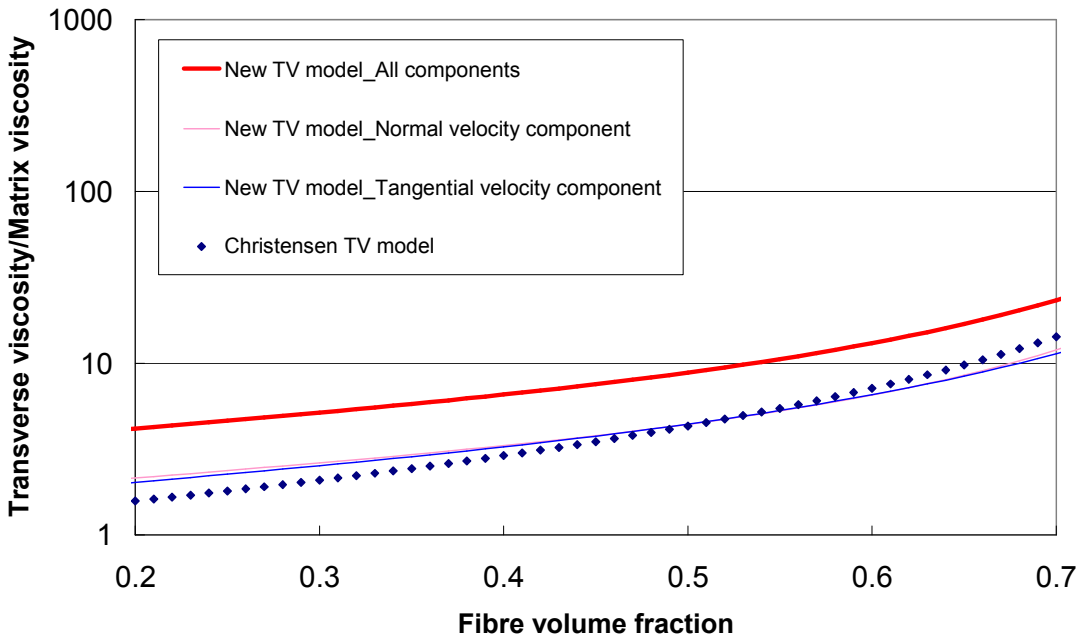

Figure 3.12. Comparisons between Christensen TV model and the new TV model with two components.

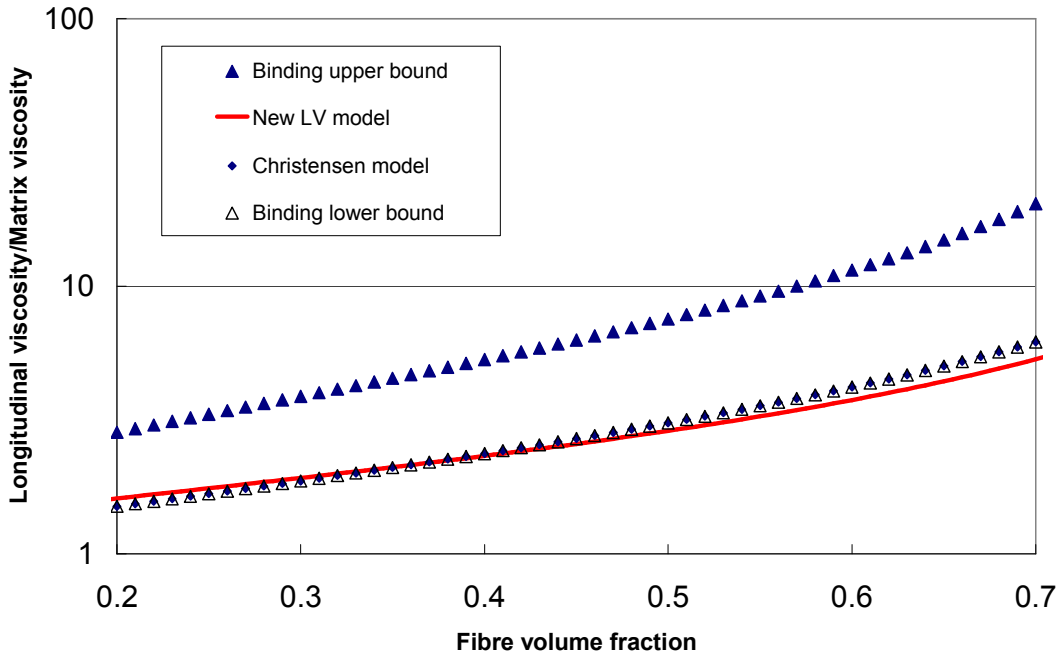

Figure 3.13. Comparisons between Christensen LV model, the new LV model and Binding upper and lower models.

It is expected [67] that the values of both the normalised TV and LV should satisfy two extreme cases, the dilute and highest concentration of fibre-

reinforced fluids, i.e. $v_f = 0$ for fluids without reinforcements and $v_f = 0.9069$ for close hexagonal fibre packing. At $v_f = 0$, the values of both the normalised TV and LV should be 1. All theoretical models fulfil this condition using Equations (3.2)-(3.9), and the values for new TV and LV models tend to 1 at low fibre volume fractions. TV and LV model predictions at the highest fibre volume fraction are close to those from Christensen (e.g. there is only 1.4% difference between Christensen's and new LV model at $v_f = 0.9069$).

Although dramatic scatter is found in experimental data from the literature, they may be used to evaluate the new models for reference by plotting the lower and upper bounds from Figure 3.5 and Figure 3.6, in Figure 3.14. Figure 3.14 (a) shows that the TV model predictions lie between the lower and upper bounds of experimental data, except at a fibre volume fraction of 0.7. Particularly, the model predictions agree well with squeeze flow data at lower volume fractions and with linear dynamic testing at higher volume fractions. For the longitudinal case, the new LV model predictions underestimate the lower bound of experimental data, shown in Figure 3.14 (b). It is notable that the Binding upper bound model predicts linear dynamic data extremely well. However, within variability of experimental data collected, the new TV and LV models have reasonably good agreement. The reason for the underestimation may be due to the lack of elastic contributions in models, or non-ideal organisation of fibres within composite materials, which was discussed in Section 3.2.

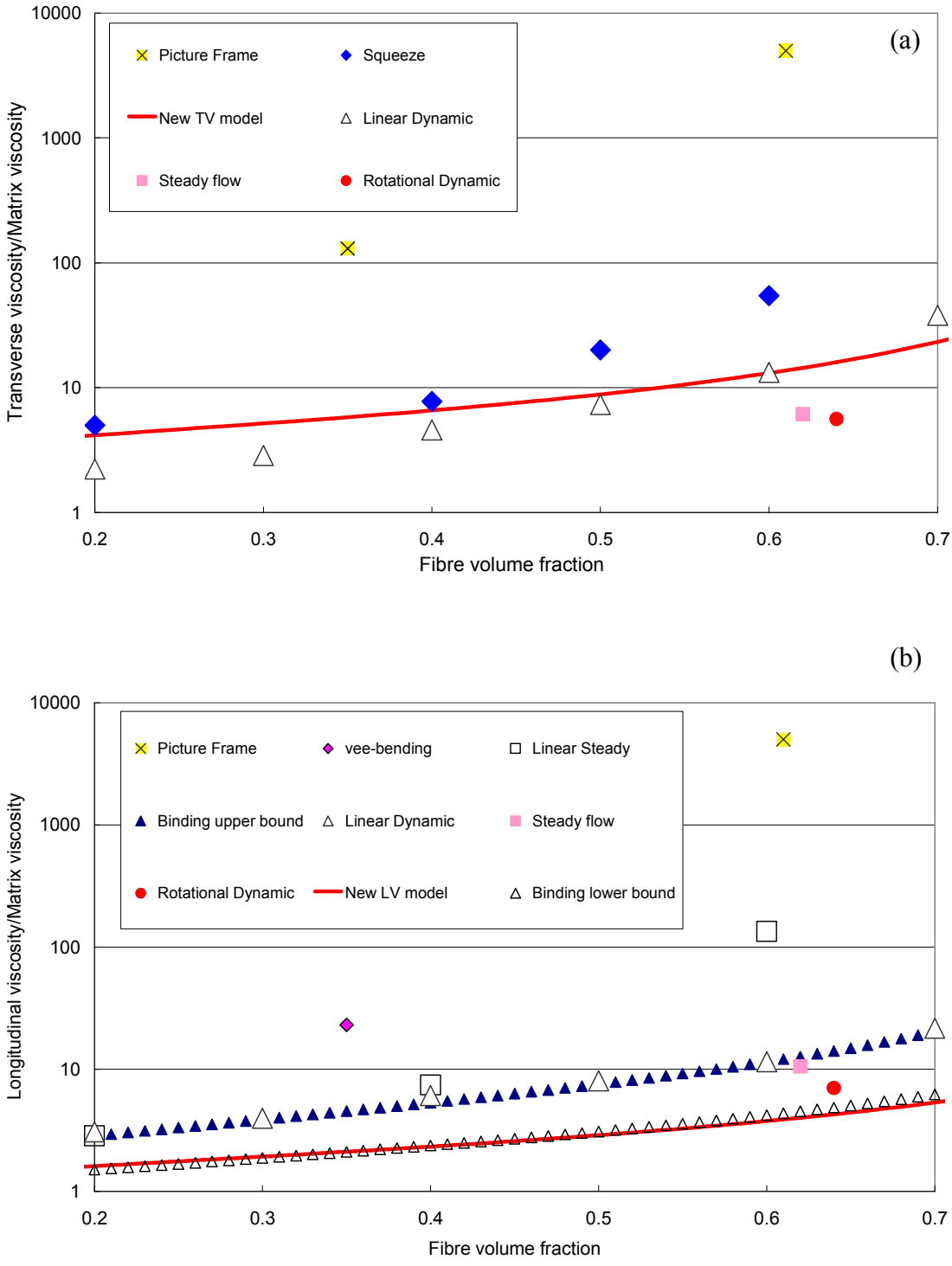

Figure 3.14. Comparisons between experimental data and new model predictions (a) Transverse (b) Longitudinal.

3.6 Conclusions

Theoretical models available in the literature (Binding LV upper/lower bound, Christensen TV/LV, Coffin TV/LV, Pipes TV/LV and Harrison LV) have been reviewed. As the resin flow between fibres is generally in two or three directions during shearing, Christensen models are preferred. However, Christensen models were developed semi-empirically. Therefore, fully predictive models based on Christensen for TV and LV were developed in this chapter, and evaluated against experimental data collected from the literature. The new models show reasonably good agreement within the variability of experimental results, although only TV model predictions lie between the lower and upper bounds of test results. It is suggested that a benchmarking characterisation programme would be desirable to investigate the discrepancies between data collected using different test methods.

These two models will be applied further in developing bending and shear models in Chapters 4 and 5.

Chapter 4 Bending behaviour of viscous composites

4.1 Introduction

Much work has been performed on studying reinforcement deformations during composites forming, such as [85, 86] . A number of deformation mechanisms, such as inter-fibre shear, fibre bending, fibre crimping/straightening and slip [85], may occur. It is widely accepted that the key deformation mechanisms during forming of composite sheets are in-plane shear and out-of-plane bending. In-plane (or intra-ply) shear deformation was always considered to be the dominant mechanism [10, 85] and a lot of work has been done, both experimental and theoretical [19, 21], and is discussed further in Chapter 5. Often in simulations of three-dimensional forming operations, especially over double-curvature or complex geometrical shapes, out-of-plane bending is not taken into account in order to simplify the analysis. However, bending behaviour might also be important for the formability of viscous textile composites into complex geometries in some circumstances, such as forming at higher rates [87]. A good initial understanding of this deformation mechanism may therefore be important for simulating forming processes [88]. Furthermore, in-plane and out-of-plane fibre/tow are subject to bending deformation during buckling, which may lead to wrinkling. At present the modelling and characterisation of the bending behaviour of viscous composites still remains unresolved, although some efforts primarily for dry textiles have been made [63, 89-94]. Two measurement systems, Kawabata Evaluation System (KES) [95] and Fabric Assurance by Simple Testing

(FAST) [96], have been widely used to characterise the low-stress bending behaviour for dry fabrics. However, as KES equipment is not widely available and FAST is based on the linear elastic assumptions, an alternative testing method, a buckling test, which may have some advantages (such as the capacity to show rate and temperature dependence) over other methods, was attempted in this study. A preliminary theoretical bending model, in which the composite sheet is treated as an orthotropic continuum, was also developed to predict the experimental measurements using material parameters such as fibre volume fraction and matrix rheology as input data, and to further study bending behaviour in composites forming.

This chapter starts with a brief review on related work, followed by two main sections, experimental study using a buckling test and development of an analytical bending model. Finally, some conclusions are drawn based on experimental and model work.

4.2 Review of related work

4.2.1 Experimental characterisation

KES fabric bending (KES-FB) tests [95] are concerned with measuring applied moments by applying a prescribed pure bending curvature to a fabric sheet mounted in a vertical plane, i.e. measuring the moment-curvature relationship. Errors in KES-FB results are caused mainly by sample alignment and mounting, requiring care to obtain repeatable results [97]. The development of KES-FB method can be dated back to the early 1930s [98] and since then there was a long history of designing an appropriate clamping system for assuring pure bending conditions and maintaining uniform curvature throughout the sample [95, 99-104]. This uses sophisticated apparatus, able to provide a complete description of fabric bending behaviour including bending rigidity and hysteresis as a function of curvature, i.e. offering a continuous stress-strain relation. However, the working principles and set-up are relatively complicated and expensive, limiting its application and availability.

In contrast, the measurement principle of the FAST system [96] is much simpler. A FAST bending tester is based on the principle of Peirce's cantilever test [98] which measures fabric deformation under its own weight. This cantilever method involves a rectangular strip of fabric on a horizontal platform being pushed slowly forward with no slippage to project as a cantilever horizontally until the tip of the cantilever touches a plane with a inclined angle of 41.5^{o} (deflection angle) to the horizontal. Then the cantilever length is measured. The measured length is used to establish a measure of the

interaction between the fabric bending rigidity and weight, and hence the bending rigidity, based on linear elastic beam theory [98]. This linear elastic assumption restricts the FAST bending test method from being applied to viscous polymer composites. Some other testers, such as the ASTM standard test [105] and the Shirley bending length tester [106], are also based on the principle of the cantilever method. Apart from the cantilever method, some other test methods, such as the folded loop method [107, 108] and hanging loop methods [98] (e.g. heart loop and pear loop methods), were also used to measure fabric bending length under self-weight. Again they are based on linear elastic theory. The flat loop method and the cantilever method for some materials are British Standard tests, such as rubber or plastic coated fabrics (BS EN 1735: 1997) and nonwoven textiles (BS EN ISO 9073-7: 1998).

Banks et al. [109] used the ASTM standard test [105] to measure the flexural rigidity to assess drapability for the design of a new low-cost woven glass/epoxy prepreg. As this standard test is unable to measure the rate dependence of prepreg, the sample was advanced in small increments with a 30-second delay between increments to allow for time-dependent behaviour. Test results showed that the bending stiffness was sensitive to the matrix viscosity, indicating the important role of the matrix resin in the bending behaviour of a prepreg. As mentioned above, the calculations of the flexural rigidity from the measured bending length are based on linear elastic theory. Thus, experimental measurements of Banks et al. [109] are unable to fully represent the bending behaviour of a viscous prepreg in respect of rate

dependence and reorganisation of the internal structure during the course of bending deformation.

A buckling test method, similar to that used in this chapter, was originally designed to measure plate and shell buckling of dry fabrics [30, 99]. It is well-known that the plate (or a solid strut or beam with a sufficiently high aspect ratio) buckles when the compression load reaches a certain value [30, 99, 110, 111]. The load at this value is referred to the buckling load and the total compression at the buckling load is called buckling compression [30]. Recently, Kocik et al. [112] applied this buckling test to measure the bending rigidity of flat textiles which is believed to be of importance for handling. Elastic theory together with the analysis of the elastic buckling of the rods is applied to determine the bending rigidity from experimental measurements of axial compression force versus displacement. This may not be appropriate for viscous composite materials due to rate dependency. Moreover, the maximum force (the buckling load) was used to calculate the maximum bending moment which was believed to occur at this buckling point, and hence to determine the bending rigidity. The bending rigidity obtained was based on very small curvatures and automatically assumed to be constant within buckling compression. This crucial assumption might not be accurate, as the curvature across the sample was not measured. For viscous composites forming with double-curvature, bending rigidity at higher curvatures is usually required, which means that the analysis of the bending behaviour may lie beyond the buckling compression (higher displacement), i.e. post buckling. However,

when the test results of Kocik et al. [112] were compared with those obtained by the FAST system, a linear correlation was found.

4.2.2 Theoretical modelling

There are many works on theoretical modelling of the bending behaviour of dry textiles reported in the literature, based on various methods, such as phenomenological models [113], energy approaches [114, 115] and linear elastic beam theory [116]. Elastic theory may be valid for dry textiles, but is not suitable for composites due to the presence of a viscous fluid matrix. Fibres are much less deformable and more rigid compared to the fluid matrix, which means that deformation of the composite is due mainly to deformation of the fluid matrix. Polymers used in composites generally behave in a highly viscoelastic manner. As a result, elastic theory is invalid. Very little work on viscous textile composites has been reported. Martin et al. [63] developed a viscous fluid beam bending model with a plane strain assumption, based on the 'ideal fibre-reinforced model'(IFRM) developed by Spencer [33, 34]. The viscous thermoplastic composite sheet was treated as an incompressible Newtonian fluid reinforced by a single family of inextensible fibres. Predictions of the beam bending model were compared with experimental results of vee-bending tests (see Chapter 3, Section 3.2.2.4), but showed disagreement in terms of both the shape and magnitude of force curves of punch load versus displacement at various temperatures. Hence it was argued that the beam bending model was only valid for small deflection. However, one of reasons for this disagreement might be the assumptions of the kinematic model for the shape of a composite sheet formed to a vee-bend. The kinematic

model accounted for deformation of the composite sheet along the length based on tool geometries, from which the shear strain rate was determined. If the shear strain rate captures inaccurately the rate of change of deformation within the composite during bending, the resultant shear stress across the deforming composite sheet would not be well determined, leading to different shapes of the force curve between predictions and tests.

4.2.3 Implementation in forming simulations

It may be crucial to incorporate bending behaviour into composite forming simulation, particularly for rate and temperature dependent polymer composites. Some approaches were used to account for the bending behaviour in finite element simulations, such as constant flexural rigidity (with no rate and temperature dependence) by Cartwright et al. [117] and an asymmetric axial modulus for the bending rigidity by Yu et al. [118].

Cartwright et al. [117] considered the bending behaviour of viscous composites using a calibration factor (bending factor) in finite element simulations using PAM-FORM software. The bending factor, between 0 and 1, was defined as flexural rigidity divided by the stiffness based on the fibre direction modulus and ply thickness. Flexural rigidity was measured by conducting the ASTM standard test [105]. Due to the viscous effect of the resin, the deflection of the composite cantilever was time-dependent. The deflection first increased quickly and then tended to a constant value which was assumed to be the effective deflection used to determine the flexural rigidity. Matrix viscosity was ignored. This approach may be more valid for dry textile simulations.

Recently, Yu et al. [118] proposed an asymmetric axial model based on elastic beam theory due to its ease of implementation into finite element simulations. For a solid beam, the compressive modulus is generally assumed to be equal to the tensile modulus. Obviously this assumption is invalid for flexible textiles. An asymmetric factor, the ratio of the compression modulus to the tensile modulus, was utilised to introduce an asymmetric axial modulus for the bending rigidity of the textile, to account for the flexible bending behaviour. This asymmetric factor was determined experimentally by the cantilever method. This approach was proven to be successful by conducting a cantilever deflection test and simulation in the bias direction. However, it may not be valid for viscous composites for several reasons, such as the viscous effect of the resin (rate and temperature dependence), fabric architecture and different deformation mechanisms compared to elastic beams (such as fibre slipping/sliding, crimping/stretching and discontinuous stress distribution through thickness). Nevertheless, a theoretical model which can predict the asymmetric factor would significantly improve predictive capability of this approach for forming simulations.

4.3 Experimental characterisation

4.3.1 Introduction

This section presents experimental characterisation of the bending behaviour of viscous composite materials, HexcelPly® M21 and 8552 UD prepregs (see Section 2.2.2 for details), by means of a large-displacement buckling test. The test method is described in Section 2.3.5. The buckling test is adopted in this research due to some potential advantages over other bending test methods, including ease of investigation of rate and temperature dependence, which are shown in Sections 4.3.5 and 4.3.6. A preliminary study on optimum specimen dimensions presented in Appendix 4.A suggests that symmetric sample dimensions of 50x50 mm may be considered as the optimum dimensions for a buckling test.

For large deformation, different deformation mechanisms may co-exist or be present at different stages. Hence, the force curve may be divided into different regions to model these deformation mechanisms. Investigation of bending shape is essential for the theoretical modelling to analyse both the amount and rate of change of deformation during bending. Both are presented at Sections 4.3.3 and 4.3.4, following explanations of advantages/disadvantages of the buckling test method. As we know, most fibres are usually not at 0^o to the bending axis during forming to a double-curvature components, i.e. the bending stiffness could be a function of the fibre orientation relative to the bending axis. Moreover, investigation of effects of fibre orientation (lay-up) may offer some insight in development of a bending model for woven textile

composites. Therefore, different fibre orientations to the loading direction, $0/0/0^o$, $0/90/0^o$ and $+45/0/-45^o$, were investigated and were used in evaluating a preliminary bending model (Section 4.4.5). Investigation of experimental reproducibility shown in Appendix 4.B may be important for improving the characterisation method and for providing an explanation for the difference between test results and model predictions.

To develop an accurate bending model, deformation mechanisms must be well understood. As such, some aspects, such as viscoelasticity, variation in thickness along the sample length and effects of micro-buckling, are also studied.

4.3.2 Advantages/disadvantages of characterisation method

There are a number of advantages of using this characterisation method (Section 2.3.5) which may be summarised as follows:

1. Simple and cheap. The experimental set-up is very simple so as to reduce the characterisation cost.
2. Very thin and flexible samples can be characterised, compared with standard 3-point and 4-point bending tests.
3. It is relatively easy to investigate rate and temperature dependence, compared with the cantilever method and KES-FB.
4. The curvature along the length is more uniform, compared with 3-point and vee-bending tests.
5. It is able to provide a continuous stress-strain relationship (unlike the cantilever method).

However, a number of disadvantages can be anticipated, including:

1. Sample misalignment. Great care must be taken during clamping samples to avoid any misalignment.
2. The method has not yet been standardised for composites. In contrast, 3-point and 4-point bending tests have been standardised and are widely used for various (solid) materials.
3. It is relatively difficult to investigate end effects as symmetric bending shape of the prepreg sheet highly depends on sample dimensions. The sheet with a large aspect ratio tends to acquire an asymmetric bending shape (severe wrinkles).
4. Pre-buckling has to be introduced in order to prevent asymmetric bending shapes. This is done by compressing the sample by 1 mm displacement prior to testing.
5. Sample thickness might be reduced significantly near clamps and this cannot be controlled accurately, hence influencing boundary conditions.

4.3.3 Interpretation of buckling curves

According to Clifford [119] and observations on experimental data, buckling may consist of 3 stages: 'elastic'/'plastic' buckling and a transition zone, see Figure 4.1. At the 1st stage, fibre layers within the composite probably behave like leaf springs and hence pure 'elastic' buckling may be assumed to be the sole deformation mechanism, showing a straight line in the buckling curve. Due to the presence of polymer matrix, fibres may be held stiffly (restricted from slipping relative to each other) and bent about the same neutral axis, leading to an elastic beam bending behaviour. Hence, elastic theory may be

applicable at this stage. Up to a certain point, as fibres are less deformable than the polymer matrix, the energy required for 'elastic' deformation is mainly stored as strain energy. The strain energy may reach a limit so that the composite tends to 'plastic' deformation, i.e. fibres start to slip relative to one another, then fibres start to bend about their own neutral axes. Hence, the main energy dissipation at this stage (i.e. the 3rd stage) would be shearing of matrix resin. The 2nd stage is a mixture of 'elastic' and 'plastic' buckling, i.e. the transition stage between the 'elastic' and 'plastic' buckling. At the transition region, some fibres are bent about their own neutral axes whilst some bend about the neutral axis of the sample. An energy minimisation approach might be required to predict the deformation behaviour in the transition region. The 'elastic' and 'plastic' terminologies are used here to emphasise the similarity between the buckling deformation behaviour of viscous composites and that of metal samples.

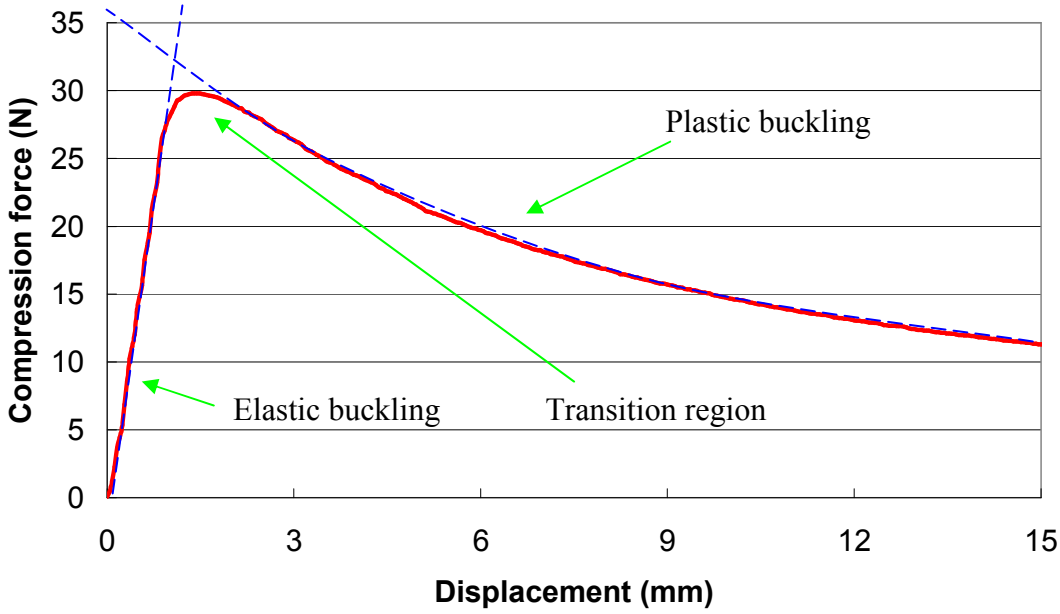

Figure 4.1. Typical experimental curve from buckling tests for a UD prepreg, illustrating three zones of buckling behaviour.

4.3.4 Investigation of bending shape

In order to determine the shear strain field within the sample during bending and hence the shear strain rate, it is necessary to know the bending shape during buckling tests. According to basic mechanics of solids considerations [110], the bending shape for a thin beam with clamped conditions in buckling should follow a cosine curve. Some photos were taken during buckling tests for UD and woven prepregs, with two typical photographs shown in Figure 4.2. Using image analysis based on the UTHSCSA image tool [120], the bending shapes measured were fitted with cosine curves for both the UD and woven prepregs, shown in Figure 4.3. This shows that the cosine bending shape is a reasonable approximation.

(a) (b)

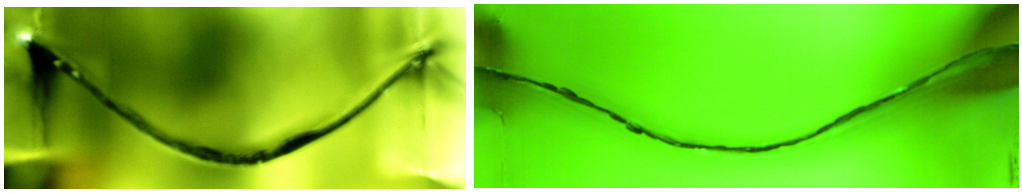

Figure 4.2. Photographs of bending shapes taken during buckling tests (a) UD prepreg at 7 mm displacement (b) woven prepreg at 3 mm displacement.

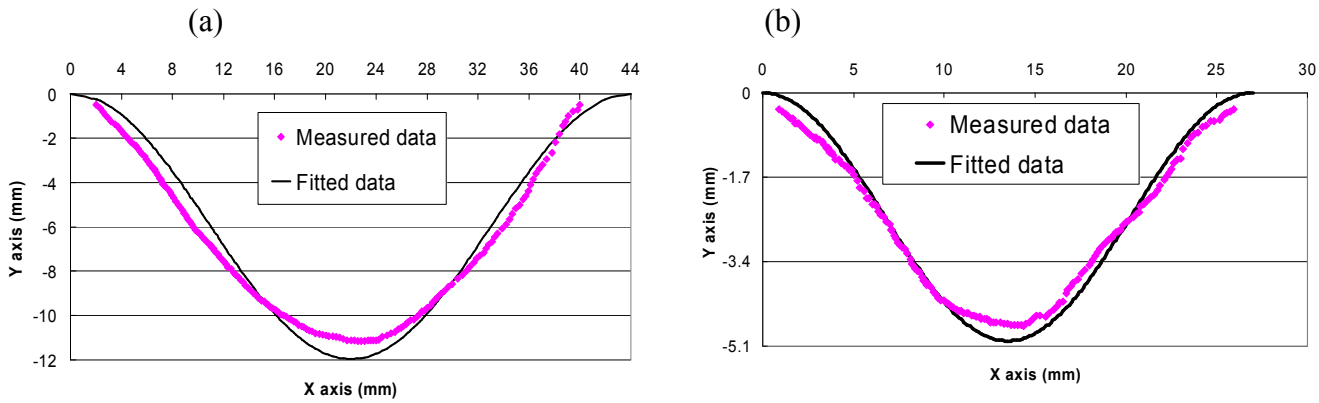

Figure 4.3. The bending shapes from photos in Figure 4.2 are fitted by cosine curves (a) $y = 5.98[\cos(0.14x) - 1]$ **for UD prepreg (b)** $y = 2.5[\cos(0.23x) - 1]$ **for woven prepreg.**

4.3.5 Rate dependence

Due to the viscous behaviour of epoxy matrix, the bending behaviour is rate dependent, which is shown in Figure 4.4. Samples with 3 layers ($0/0/0^{o}$) were cut into 50x50 mm and tested at room temperature and various displacement rates, 4.4, 10, 30, 100 and 300 mm/min respectively. Figure 4.4 shows that there is no clear rate effect up to 30 mm/min, but the results at 300mm/min may suggest that these two UD prepregs have high rate dependence at higher rates. To investigate the relationship between the bending behaviour and rate further, axial forces at 8 mm displacement are plotted against the displacement rate in Figure 4.5. Note that the axial force for each rate is the average of 3 repeats. Figure 4.5 shows that the bending resistance for these two materials may depend linearly on the testing rate.

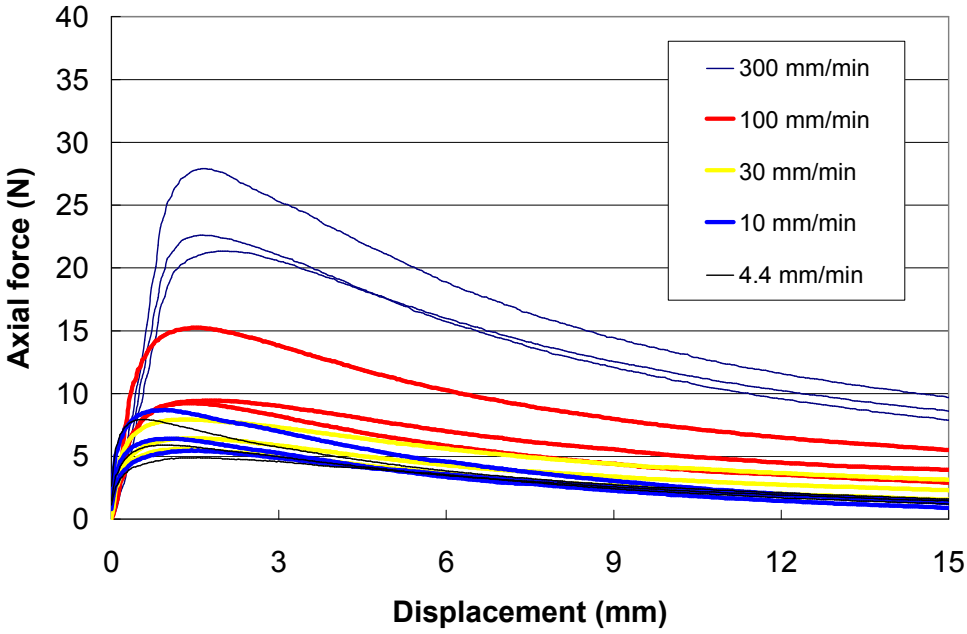

(a)

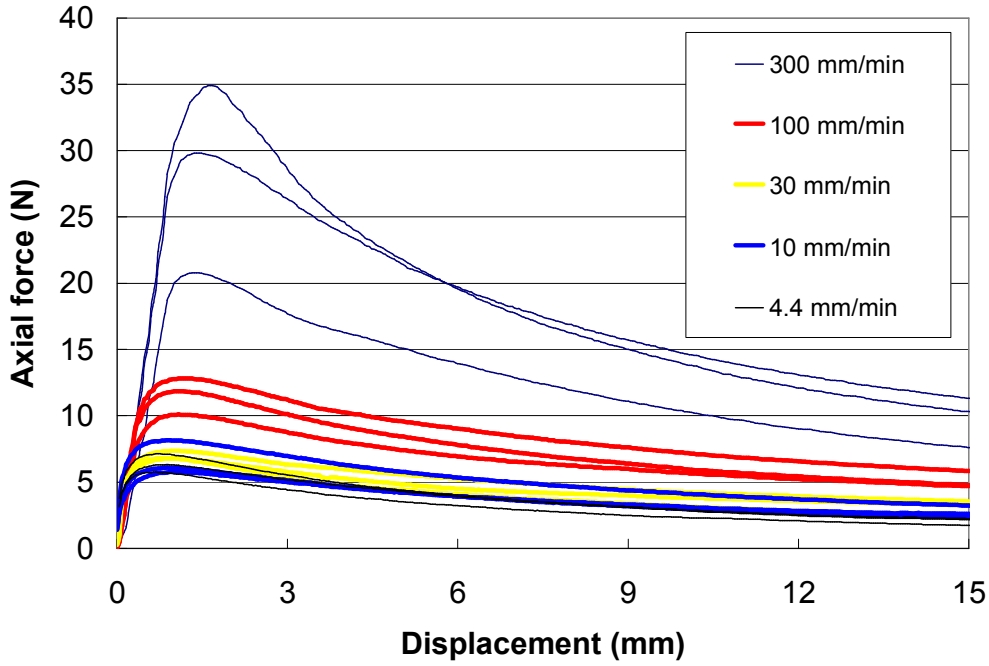

(b)

Figure 4.4. Bending test results for 50x50mm samples with 0/0/0° lay-ups, performed at room temperature and various displacement rates, 4.4, 10, 30, 100 and 300 mm/min respectively. (a) HexPly® 8552 (b) HexPly® M21.

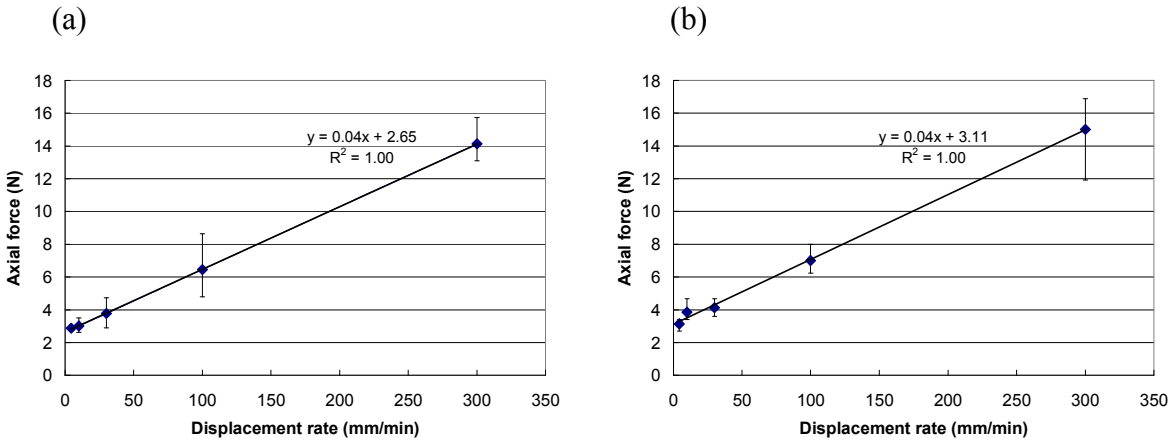

Figure 4.5. Axial force versus displacement rate at 8mm displacement. Data are from Figure 4.4 and the force value is the average of three repeats for each displacement rate, including error bars for maximum and minimum values. (a) HexPly® 8552 (b) HexPly® M21.

4.3.6 Temperature dependence

To investigate the temperature dependence of the bending behaviour, bending tests for materials HexcelPly® M21 and 8552 UD prepregs were performed with three repeats at a displacement rate 30mm/min and various temperatures, room temperature (RT), 60, 80, 110 and 150 ^{o}C respectively. The results are shown in Figure 4.6. For both materials, the force curve is reduced significantly with increasing temperature. For example, the axial force is 4.13 N at room temperature and 8 mm displacement for material HexcelPly® M21 UD prepreg but it is 0.447 N at 60 ^{o}C, a reduction of 89%. Moreover, the axial force at room temperature is more than 10 times larger than at 80 ^{o}C or higher. The reason is the reduction in resin viscosity with increasing temperature, such as indicated in Figure 2.2.

It is also notable that for material HexcelPly® 8552 UD prepreg the bending behaviour (the force magnitude) is approximately the same within the reproducibility of the test method for 80, 110 and 150 ^{o}C, whereas for material HexcelPly® M21 UD prepreg this applies only for 110 and 150 ^{o}C. The cause can be explained by the rheological data at such high temperatures. For example, for resin HexcelPly® 8552 the resin viscosity is fairly low and similar for 80 and 110 ^{o}C, whereas for resin HexcelPly® M21 the viscosity at 80 ^{o}C is much higher than at higher temperatures.

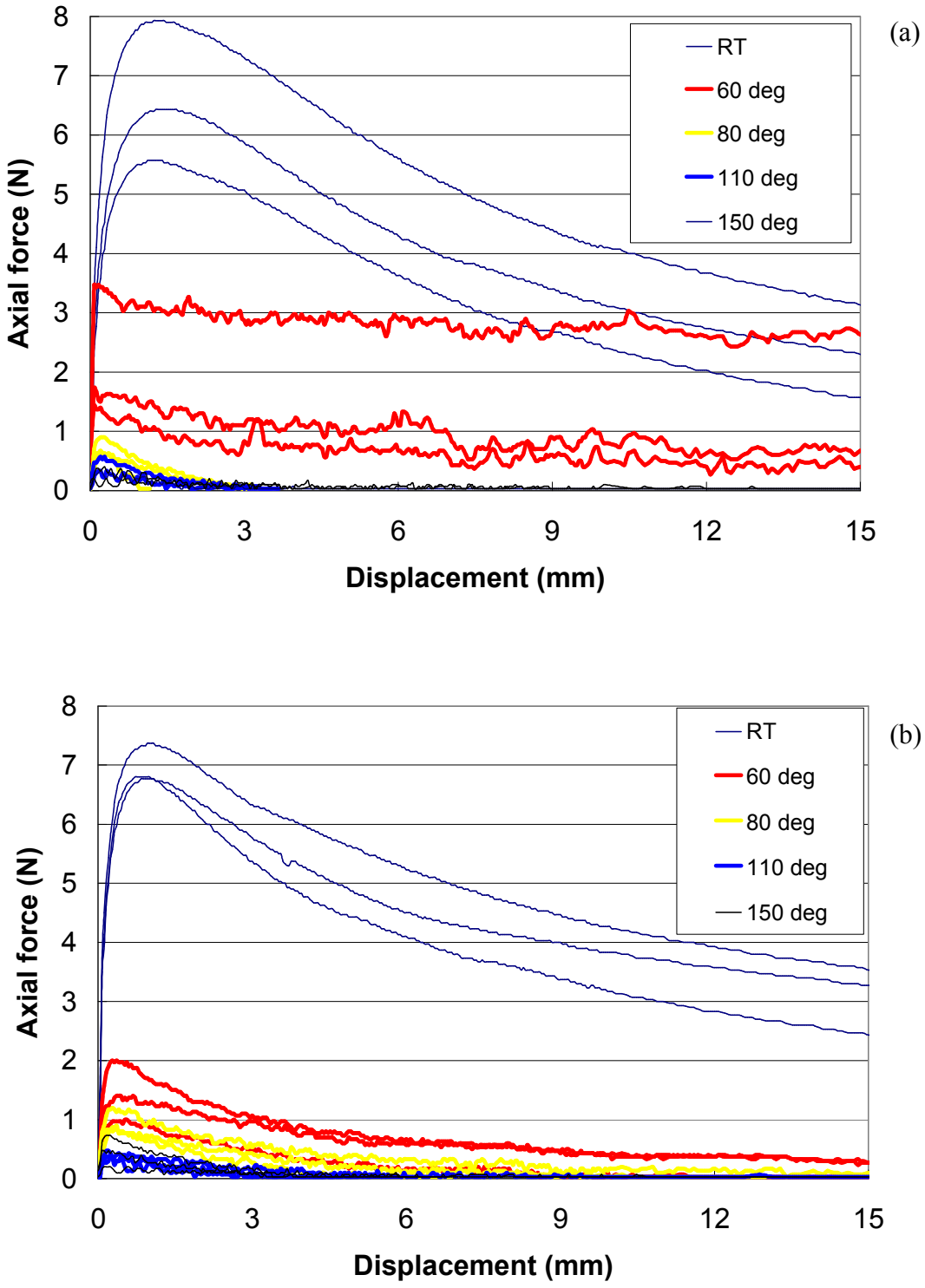

Figure 4.6. Bending test results for 50x50mm samples with 0/0/0° lay-ups, performed at 30 mm/min displacement rate and various temperatures, room temperature (RT), 60, 80, 110 and 150 °C respectively. (a) HexPly® 8552 (b) HexPly® M21.

4.3.7 Effects of lay-up (fibre orientation)

To investigate the effects of lay-up with different fibre directions to the loading direction, buckling tests were performed at room temperature and a displacement rate of 10 mm/min using 50x50mm 3-ply samples with different lay-ups, $0/0/0^o$, $0/90/0^o$ and $+45/0/-45^o$. Test results for material HexPly® 8552 UD prepreg shown in Figure 4.7(a) show that the force curves of the $0/90/0^o$ sample are similar to those for the $+45/0/-45^o$ sample, but the force is about half of those for the $0/0/0^o$ sample. However, the extent of effects of lay-up may be influenced by the matrix used in UD prepregs, by comparing the force curves at the same fibre orientation for these two UD prepreg. For material HexPly® M21 UD prepreg, Figure 4.7(b) shows that the bending behaviour is significantly influenced by lay-up. For example, at 8mm displacement, the force for the sample with $0/0/0^o$ is about 1.5 times that for the sample with $0/90/0^o$ and about 4 times that for the sample with $+45/0/-45^o$. The modulus of the fibres plays an important role in the prepreg stiffness according to the analysis of off-axis elastic constants of a laminate [121]. As the angle of fibre orientation increases, the effective axial modulus of the prepreg sheet along the loading direction decreases, and hence the bending resistance to axial compression reduces. On the whole, the trend of reducing the applied force for both materials is the same, i.e. the force curve for the $0/0/0^o$ lay-up is the highest, followed by the $0/90/0^o$ lay-up, with $+45/0/-45^o$ lay-up requiring the lowest force.

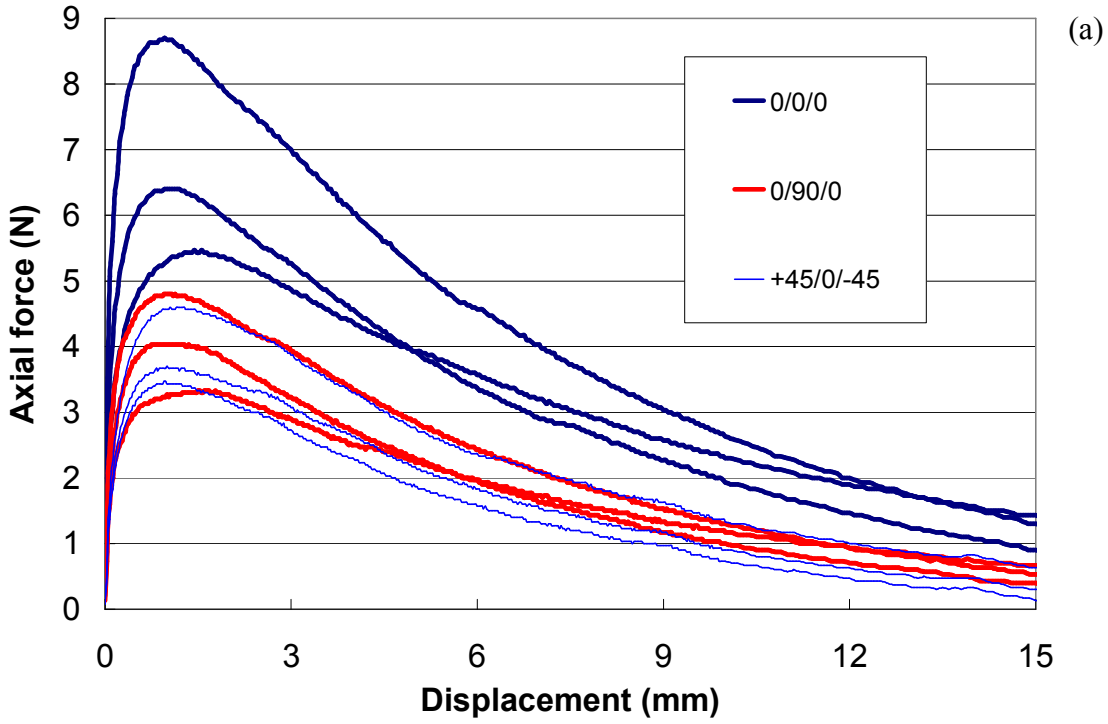

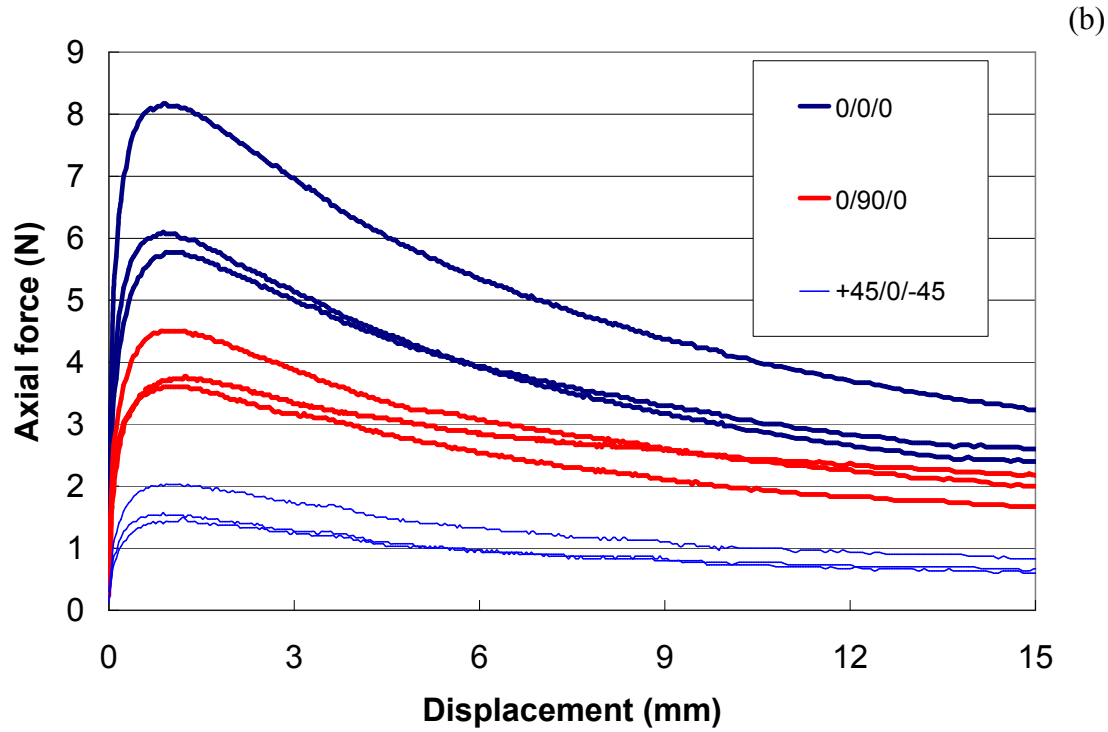

Figure 4.7. Bending test results at room temperature and 10 mm/min displacement rate using 50x50mm 3-ply sample with different lay-ups, 0/0/0°, 0/90/0° and +45/0/-45°. (a) HexPly®8552 UD prepreg (b)HexPly®M21 UD prepreg.

4.3.8 Investigation of viscoelastic behaviour

The viscoelastic behaviour of UD prepregs during bending was investigated by performing stress relaxation tests. The material used was carbon/epoxy UD prepreg (HexPly® M21). Material details are in Section 2.2.2. Tests were performed to final displacements of 1, 3, 5, 7, 9 and 11 mm at a displacement rate of 10 mm/min. Different samples were used for each test. Each sample has 3 plies with the fibres along the loading direction (i.e. $0/0/0^{o}$). Three repeats were performed for each displacement. A stress relaxation test was performed by stopping the crosshead at fixed displacements, then measuring the decay in force with time over 180 s. A detailed description of the test method is presented in Section 2.3.2. Experimental results are shown in Figure 4.8. Only the middle curve of three repeats for each displacement is shown. The initial value of the force at time 0 s is the force observed when the crosshead stops at a fixed displacement. The force drops significantly over a short time and then relaxes slowly over 180 s towards a steady-state value that would be the elastic contribution. For convenience, the proportion of the elastic contribution is approximated to the relaxed steady-state value at time 180 s divided by the initial force at time 0 s. The elastic contributions for relaxation displacements 1, 3, 5, 7, 9 and 11 mm are 19%, 21%, 33%, 12%, 21% and 22% respectively. There is no obvious correlation between the relaxation displacement and elastic contribution.

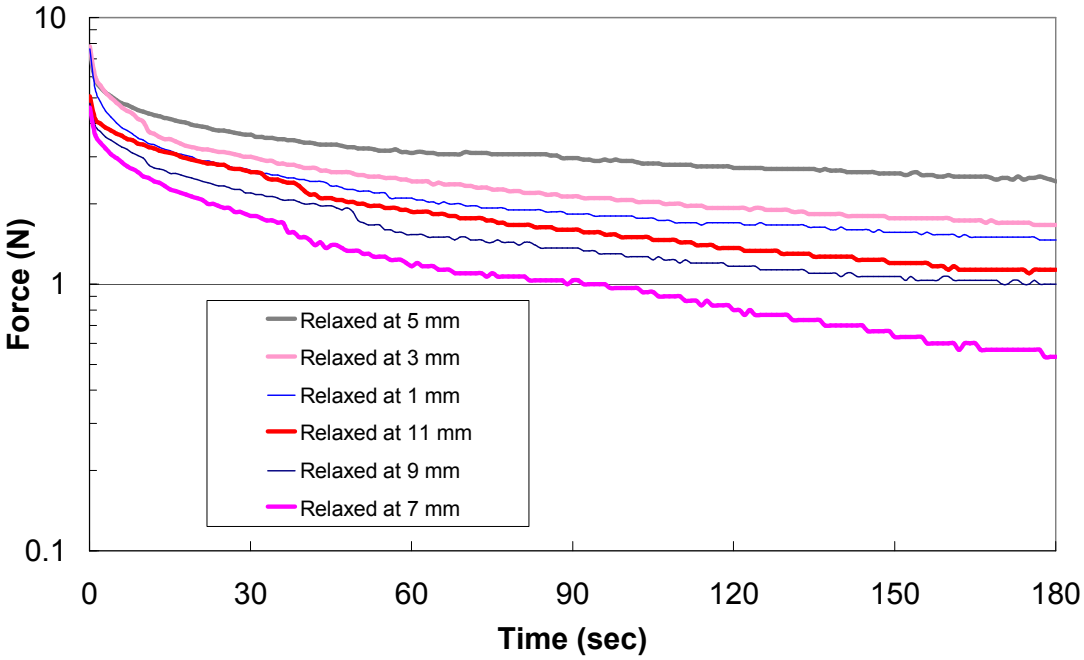

Figure 4.8. Force relaxation recorded at room temperature at different final displacements 1, 3, 5, 7, 9 and 11 mm for a period of 180 s using different samples.

The force relaxation curve can be fitted by the standard linear solid (SLS) model using least squares, shown in Equation (4.1).

$$F = \frac{k_1 dwh}{l(k_1 + k_2)}\left[k_2 + k_1 e^{-t(k_1+k_2)/\eta_{dash}}\right] \quad \textbf{(4.1)}$$

where F is the relaxing force at time t at a fixed displacement d. l, w and h are length, width and thickness of the prepreg respectively, k_1, k_2 and η_{dash} are spring stiffness and dashpot viscosity respectively.

The fitted values of these constants by using least squares are shown in Table 4.1. Figure 4.9 shows a typical example of a fitted curve, indicating that the SLS model can be well fitted to the experimental curves. The elastic constants of the SLS model, shown in Table 4.1, decrease monotonically with the final displacement. This probably means that the elastic contribution decreases as

the bending curvature of the prepreg increases, which contradicts the expectation based on elastic beam theory. This implies that during buckling tests the prepreg is not bent like an elastic beam, and hence elastic beam theory may not be suitable to predict the elastic contribution. However, typical bending diagrams registered on the Kawabata bending tester for textile yarns (KES-FB) [122] shows that the bending rigidity decreases as the bending curvature increases, which agrees with the results from Table 4.1 as the bending rigidity is proportional to elastic constants. Therefore, modelling approaches for textiles may be suitably applied to predict the elastic contribution.

In conclusion, the bending model might need to account for the elastic behaviour of UD prepregs which may be predicted using modelling approaches for textiles. This was not yet considered in the bending model developed in Section 4.4.5.

Table 4.1. List of constants for the SLS model at various relaxed displacements.

Displacement (mm)	k_1 (MPa)	k_2 (MPa)	Dashpot viscosity(MPa.s)	Relaxation time(sec)
1	8.58	2.78	94.88	8.36
3	2.92	1.07	43.32	10.86
5	1.66	1.05	32.14	11.85
7	0.74	0.16	17.25	19.15
9	0.60	0.20	17.07	21.51
11	0.52	0.18	18.42	26.27

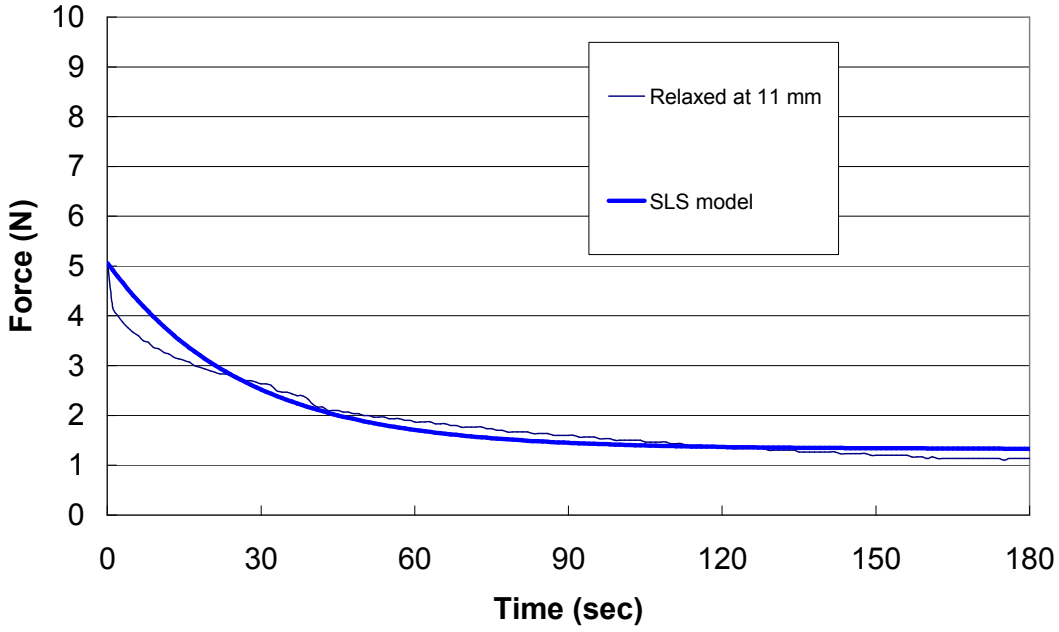

Figure 4.9. The SLS model is fitted into the experimental results of force at 11 mm displacement.

4.3.9 Investigation of sample thickness using optical micrograph

Buckling tests for 7 different samples of 50x50mm were performed at room temperature with a displacement rate of 30 mm/min. The material used was HexPly® M21 carbon/epoxy UD prepreg. Material details are in Section 2.2.2. All samples were cured at 150°C for 1 hour in the oven after deformation before removal from the clamps. Figure 4.10 shows measurements of sample thickness along the sample length using a digital calliper. The measured thickness is normalised by the mean thickness. It is shown that the sample becomes thicker at ends and thinner at the middle after deformation, and the pattern is slightly asymmetric. It is evident that the variation in thickness along the sample length becomes more significant after bending. This might be caused by fibre reorganisation and delamination, i.e. localised out-of-plane

buckling of fibres, observed on the inner surface of deformed samples shown in Figure 4.11(a). This has been investigated further by taking optical micrographs from deformed samples. Figure 4.11(b) shows a cavity formed from the localised buckling of fibres through the cross-section. Localised buckling can cause the thickness to increase locally, and this is thought be the main cause of variation in sample thickness along the length.

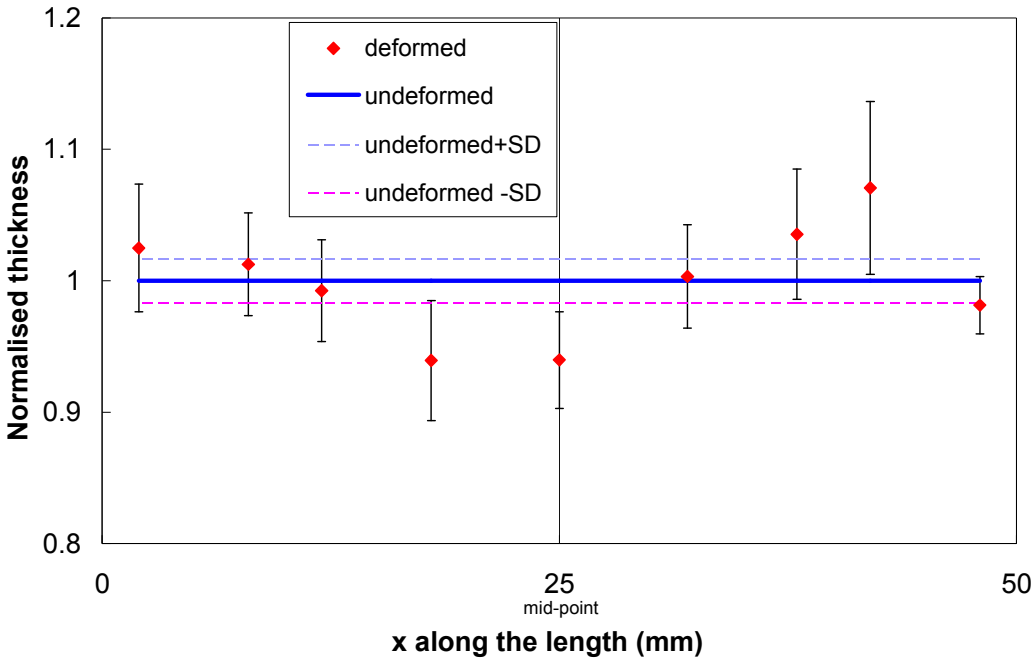

Figure 4.10. Normalised thickness along the sample length. The sample length is in the loading direction. The error bars show the standard deviation (SD). These measurements were made from 7 cured samples from bending tests at room temperature, 10 mm displacement and 30 mm/min displacement rate.

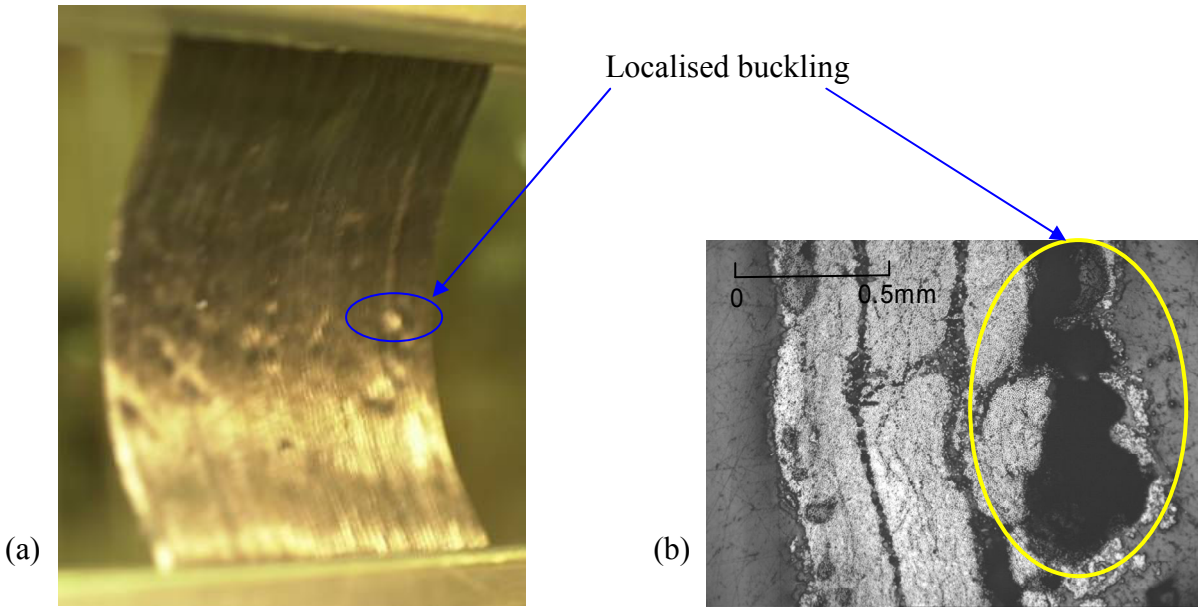

Figure 4.11. Localised buckling on the inner surface of a deformed sample. (a) photograph of deformed sample; (b) optical micrograph on the cross section of a deformed sample at 10 mm displacement.

4.3.10 Effects of micro-buckling

Micro-buckling of fibres was observed during bending (Section 4.3.9). It is necessary to investigate whether there is a significant energy contribution from micro-buckling during bending.

Figure 4.12 shows a schematic of micro-buckling. σ_n is the normal stress to debond the interface of fibres and epoxy (the direction of σ_n is normal to the surface of the prepreg sheet), while σ_s is the shear stress during shearing between fibres and epoxy at the debonding point P. σ_n is not rate dependent and instead depends on the bond strength of the fibre and epoxy, whereas σ_s is rate dependent due to shearing of resin at this point.

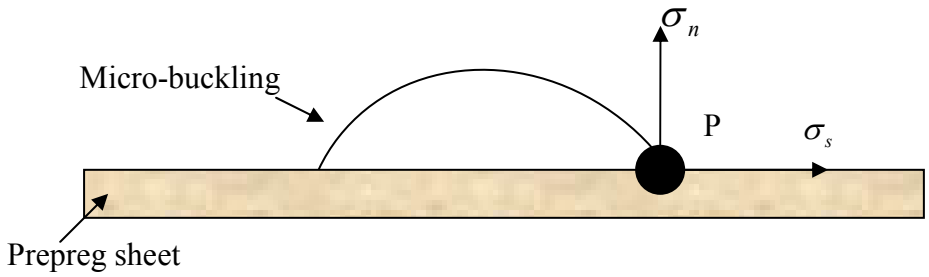

Figure 4.12. Schematic of micro-buckling with normal/shear stresses at the debonding region. σ_n and σ_s are the normal stress and shear stress at the debonding point A.

Figure 4.13 shows a schematic of a transverse tensile strength test. The work done by the external force F is equal to the work done by σ_n and σ_s (if just one crack occurred during the test). Therefore,

$$\sigma_n \leq \frac{F}{wh} \tag{4.2}$$

where w and h are width and thickness of the composite in the tested region.

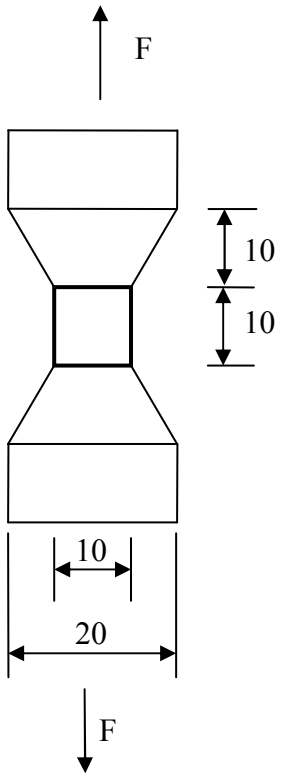

Figure 4.13. Schematic of transverse tensile strength test on a sample with a dog bone shape. Unit for dimensions is mm. The tested area is 10x10 mm (w x l). Sample thickness is 0.89 mm.

Assuming the micro-buckle (appearing like bubbles on the inner surface of the sample, see Figure 4.11) is a dome with radius R_{dome} and thickness h_{dome}, and the normal stress σ_n is uniformly distributed on this micro-buckle (bubble), then the energy dissipated during formation of the micro-buckle is approximated to:

$$W = \sigma_n \times \pi \times R_{dome}^2 \times h_{dome} \quad \textbf{(4.3)}$$

From Equations (4.2) and (4.3),

$$W \le \frac{F}{wh} \times \pi \times R_{dome}^2 \times h_{dome} \quad \textbf{(4.4)}$$

To obtain F in Equation (4.4), five transverse tensile strength tests were performed at room temperature with different displacement rates using the Universal Testing machine. The samples were cut into a dog bone shape, as shown in Figure 4.13. Figure 4.14 shows the experimental results from transverse tensile strength tests. The results are summarised in Table 4.2.

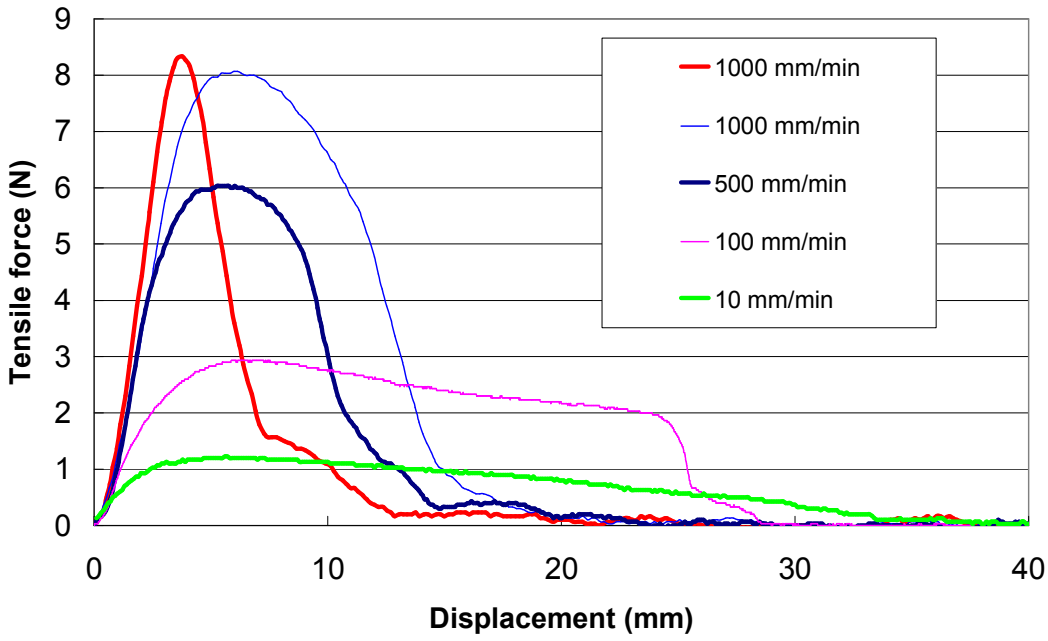

Figure 4.14. Tensile force versus displacement from transverse tensile strength tests at room temperature with various displacement rates.

Table 4.2. Results from transverse tensile strength tests.

Displacement rate (mm/min)	Max. force (N)	Cross-sectional area (mm^2)	σ_n (KPa)	Max. energy for a micro-buckle (mJ/bubble)
10	1.23	12.24	100	0.177
100	2.93	11.03	266	0.468
500	6.03	11.04	546	0.963
1000	8.06	10.49	769	1.356
1000	8.33	12.54	665	1.172

The energy required for bending a sample at 10 mm displacement and 30 mm/min is the area under the experimental force curve (Figure 4.15). It approximates to 50.1 m J

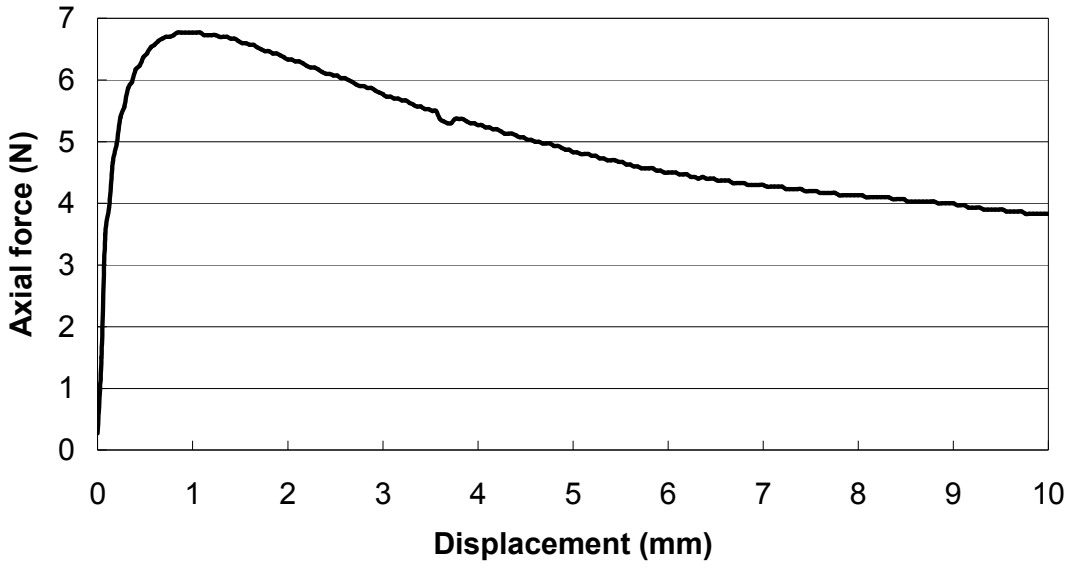

Figure 4.15. Experimental results from bending tests performed at room temperature and 30 mm/min displacement rate with a sample of 50x50 mm.

By the results from relaxation tests in Section 4.3.8, the elastic contribution is up to 33%. Hence, there would be 50.1*(1-33%) = 33.6 mJ due to viscous deformation. If it is assumed that all remaining energy dissipation is due to micro-buckling, then there would be 33.6/1.356 = 25 micro-bubbles. By observations on the inner surface of deformed samples, there are approximately 5 to 10 such micro-bubbles. This means that considerable energy due to micro-buckling is dissipated during bucking tests. Therefore, it may be necessary to take effects of micro-buckling into account in the bending model. However, this effect has not yet been incorporated into the bending model developed in Section 4.4.5.

4.3.11 Summary

A test method, characterising the rate and temperature dependence of the bending of viscous composites, has been used. The method has several advantages over other bending test methods, such as simplicity of experimental set-up and capability of characterising the rate and temperature dependence. A series of tests with various displacement rates were performed to investigate the rate dependence and showed that the bending resistance for two UD materials tested may depend linearly on the testing rate. Due to the reduction in resin viscosity with increasing temperature, the axial force is reduced significantly when the sample is heated up to 60 ^{o}C or higher. The investigation of effects of lay-up shows that the sample with more fibres along the loading direction has a higher stiffness.

Some effort related to development of a bending model has been performed. Relaxation tests suggest that a bending model might need to account for the viscoelastic behaviour of UD prepregs. The variation in thickness along the sample length becomes more significant after bending, which is thought to be due to localised out-of-plane buckling of fibres, i.e. micro-buckling. A simple estimation of the energy contribution from micro-buckling during bending was attempted and suggests that micro-buckling may be a source of energy dissipation during bending and should be considered in the bending model.

4.4 Theoretical modelling

4.4.1 Introduction

For many engineering materials, it is accurate to assume the bending rigidity (defined as the ratio of applied bending moment per unit width to curvature) to be constant. However, some materials, such as viscous textile composites, generally have non-linear bending behaviour. The fibres in a composite are high in tensile stiffness and generally assumed to be rigid and inextensible, leading to considerable freedom of motion for fibres relative to one another, within the viscous polymer matrix. Due to this mobility, viscous composites behave more flexibly and have a lower bending rigidity than corresponding solid composites. This is supported by Popper's study [123] on the effects of fibre interactions on the bending behaviour of cotton textiles. Therefore, for viscous polymer composites non-linearity in the bending behaviour may be caused by inter-fibre shearing deformation associated with fibre movement during bending. As a result, development of a bending model for viscous composites must consider fibre/matrix interaction, which is represented by composite viscosities (longitudinal and transverse viscosities studied in Chapter 3). That is, in order for double-curvature composite forming to accommodate out-of-plane bending, inter-fibre shearing may occur so that bending stiffness could be correlated to the axial viscosity of the viscous composite sheet, or transverse viscosity depending on the angle of the bending axis and fibre orientation.

As per interpretation of buckling curves in Section 4.3.3, theoretical modelling was carried out for different buckling stages to account for the different deformation mechanisms, 'elastic' and 'plastic' buckling, which are presented in Sections 4.4.4 and 4.4.5 respectively. Finally predictions based on a combination of 'elastic' and 'plastic' buckling models were made. Following these, an evaluation of the bending model is presented in sections, 4.7, 4.9 and 4.8.

4.4.2 Prediction of bending shape

According to the theory of buckling of struts [110], the deflected shape of a sample with a boundary condition of built-in ends is a cosine curve. Experimental observations in Section 4.3.4 also show that for composite samples the bending specimen shape can be fitted by a cosine function, shown in Equation (4.5).

$$y = a\left[\cos(bx) - 1\right] \tag{4.5}$$

where a and b are fitted coefficients of the function. The coefficient b can be related to the sample length (l) and the displacement (d) of a buckling test by $b = 2\pi/(l-d)$, hence Equation (4.5) can be re-written as

$$y = a\left[\cos\left(\frac{2\pi x}{l-d}\right) - 1\right]. \tag{4.6}$$

An assumption that the prepreg thickness (h) is constant is made, in Section 4.4.3, hence a parallel cosine curve to Equation (4.6) is needed to represent another surface of the prepreg sheet, which can be shown as

$$y_2 = a\left[\cos\frac{2\pi\left(x_2 - \dfrac{h\tan\psi}{\sqrt{\tan^2\psi+1}}\right)}{l-d} - 1\right] - \frac{h}{\sqrt{\tan^2\psi+1}} \tag{4.7}$$

where $\tan\psi$ is the slope of the curve at the coordinate of x_2. The detailed derivation of Equation (4.7) is presented in Appendix 4.C.

The sample length can be determined by

$$l = \int_{x_1}^{x_2}\sqrt{1+\left(\frac{dy}{dx}\right)^2}\,dx \tag{4.8}$$

Where x_1 and x_2 are the coordinates of two ends of the cosine curve along the horizontal axis which equal 0 and ($l-d$) respectively.

By a combination of Equations (4.6) to (4.8), the fitted coefficient a with respect to the displacement can be obtained. It was determined using a numerical method (Simpson's rule) due to difficulties in obtaining an analytical solution from integration of Equation (4.8).

4.4.3 Assumptions in the bending model

Several assumptions used to simplify the model are shown below:

1. Viscous fluid is incompressible.
2. Fibres are inextensible
3. Fibres are unidirectional and parallel.
4. Composite viscosities from the ideal fibre-reinforced fluid model are applicable in the analysis.

5. The prepreg thickness remains constant during bending (i.e. resin within the composite is not squeezed out)
6. Velocity gradient through the prepreg thickness is linear.
7. There is a no slip condition at clamps.
8. Deformation along the sample width is uniform.
9. Elastic contribution at the stage of 'plastic' deformation is assumed negligible (although it was shown up to 33% in Section 4.3.8). This will be investigated in future modelling.
10. Effects of sample weight can be neglected.

4.4.4 Modelling of 'elastic' buckling

4.4.4.1 Method 1: Pseudo spring stiffness equivalence

By the stress-strain relationship, compressive stress (σ_c) applied to the prepreg during buckling may be related to compressive strain (ε_c) as

$$\sigma_c = E_{eff}\varepsilon_c \tag{4.9}$$

where E_{eff} is the effective elastic modulus and the compressive stress and strain can be expressed as follows

$$\sigma_c = \frac{F}{wh} \tag{4.10}$$

where F is the applied force in a buckling test, w and h are width and thickness of the composite, and

$$\varepsilon_c = \frac{d}{l} \tag{4.11}$$

where d and l are the displacement and composite length.

A combination of Equations (4.9) to (4.11), gives

$$F = \frac{E_{eff} wh}{l} d = k_{eq} d \tag{4.12}$$

where k_{eq} is the equivalent spring stiffness of the prepreg during compression.

k_{eq} would be overestimated if E_{eff} were predicted by the Rule of Mixtures ($E_{eff} = v_f E_f + (1 - v_f) E_m$, where v_f=0.5 for M21 UD prepreg, E_f=294GPa and E_m=0 as $E_m << E_f$), shown in Figure 4.16(a). Therefore, a linear function ($y = cx$) is fitted to all experimental curves, shown in Figure 4.16. It is found that the transition region (2nd region in Figure 4.1) is wider for a lower displacement rate (Figure 4.16(b)), which means that there is no pure 'elastic' buckling region (1st region in Figure 4.1). Namely, 'plastic' deformation occurs at the start together with 'elastic' deformation. Nevertheless, as a whole all results at different rates can be fitted well by a straight line, shown in Figure 4.16, where k_{eq} = 30 N/mm.

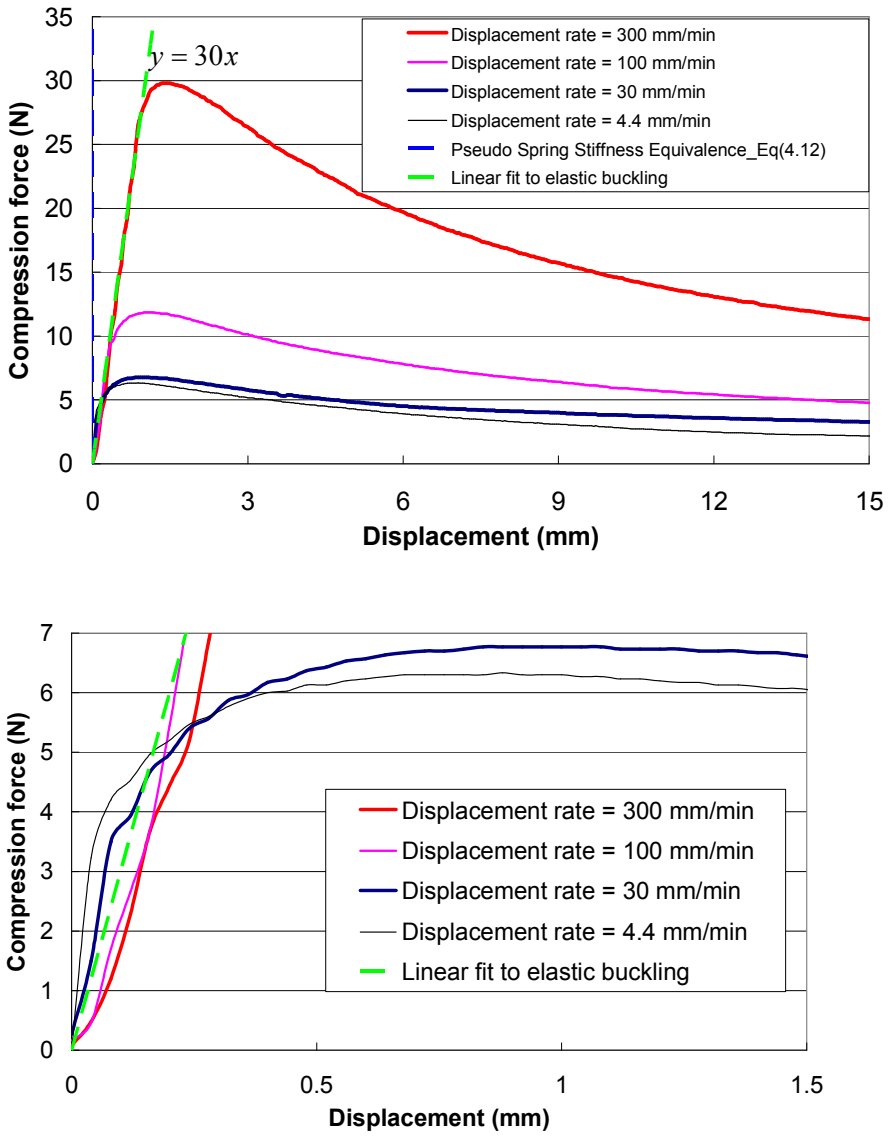

Figure 4.16. (a) A linear function is used to fit all experimental curves for M21 UD prepregs at different rates for the 1st region ('elastic' buckling). (b) Smaller scale to (a).

4.4.4.2 Method 2: An energy approach

The approach described in this section follows exactly the formulations in [111]. During 'elastic' buckling, energy formulation of buckling may be given by:

$$U_e - W_{ext} - W_P = 0 \qquad \textbf{(4.13)}$$

where W_{ext} is the work done by external loads, W_P is the potential energy of the in-plane loads due to deflection and may be neglected in a buckling test, and U_e is the strain energy due to elastic deformation of the prepreg and may be formulated as in Equation (4.14) using classical laminate theory [111].

$$U_e = \frac{1}{2}\iint\{\zeta_{11}\left(\frac{\partial u_x}{\partial x}\right)^2 + 2\zeta_{12}\frac{\partial u_x}{\partial x}\frac{\partial u_y}{\partial x} + \zeta_{22}\left(\frac{\partial u_y}{\partial y}\right)^2 \tag{4.14}$$

$$+2\left(\zeta_{16}\frac{\partial u_x}{\partial x}+\zeta_{26}\frac{\partial u_y}{\partial y}\right)\left(\frac{\partial u_x}{\partial y}+\frac{\partial u_y}{\partial x}\right)+\zeta_{66}\left(\frac{\partial u_x}{\partial y}+\frac{\partial u_y}{\partial x}\right)$$

$$-\xi_{11}\frac{\partial u_x}{\partial x}\frac{\partial^2 u_z}{\partial x^2}-2B_{12}\left(\frac{\partial u_y}{\partial y}\frac{\partial^2 u_z}{\partial x^2}+\frac{\partial u_x}{\partial x}\frac{\partial^2 u_z}{\partial y^2}\right)$$

$$-2\xi_{16}\left[\frac{\partial^2 u_z}{\partial x^2}\left(\frac{\partial u_x}{\partial y}+\frac{\partial u_y}{\partial x}\right)+2\frac{\partial u_x}{\partial x}\frac{\partial^2 u_z}{\partial x\partial y}\right]$$

$$-2\xi_{26}\left[\frac{\partial^2 u_z}{\partial y^2}\left(\frac{\partial u_x}{\partial y}+\frac{\partial u_y}{\partial x}\right)+2\frac{\partial u_y}{\partial y}\frac{\partial^2 u_z}{\partial x\partial y}\right]$$

$$-\xi_{22}\frac{\partial u_y}{\partial y}\frac{\partial^2 u_z}{\partial y^2}-4\xi_{66}\frac{\partial^2 u_z}{\partial x\partial y}\left(\frac{\partial u_x}{\partial y}+\frac{\partial u_y}{\partial x}\right)$$

$$+\varsigma_{11}\left(\frac{\partial^2 u_z}{\partial x^2}\right)^2+2\varsigma_{12}\frac{\partial^2 u_z}{\partial x^2}\frac{\partial^2 u_z}{\partial y^2}$$

$$+\varsigma_{22}\left(\frac{\partial^2 u_z}{\partial y^2}\right)^2+4\left(\varsigma_{16}\frac{\partial^2 u_z}{\partial x^2}+\varsigma_{26}\frac{\partial^2 u_z}{\partial y^2}\right)\frac{\partial^2 u_z}{\partial x\partial y}$$

$$+4\varsigma_{66}\left(\frac{\partial^2 u_z}{\partial x\partial y}\right)^2\}dxdy$$

where ζ_{ij}, ξ_{ij} and ς_{ij} are the stiffness constants and can be expressed by engineering constants, u_x, u_y and u_z are respectively the displacements along

x, y and z in a Cartesian coordinate system. u_z is the out-of-plane deflection of the laminate.

For a UD prepreg, the stretching-bending coupling terms ξ_{ij} are zero (symmetric laminate), and the terms containing only the in-plane displacement u_x and u_y can be reduced to a constant C (pure bending). Moreover, for the case of orthotropic, prepreg yields $\varsigma_{16} = \varsigma_{26} = 0$ and the differentiation of u_z with respect to y equals to zero according to the assumption 8 (uniform deformation along the sample width), so the strain energy can be simplified to:

$$U_e = \frac{1}{2}\iint\left[\varsigma_{11}\left(\frac{\partial^2 u_z}{\partial x^2}\right)^2\right]dxdy + C\,. \tag{4.15}$$

The stiffness constant ς_{ij} is given by:

$$\varsigma_{ij} = \frac{1}{3}\sum\left(h_k^3 - h_{k-1}^3\right)\left(Q_{ij}\right)_k \tag{4.16}$$

where h_k and $\left(Q_{ij}\right)_k$ are the thickness and reduced stiffness matrix of the k^{th} layer of the laminate. Therefore, the stiffness constant ς_{11} of a UD prepreg with a thickness of h can be obtained:

$$\varsigma_{11} = Q_{11}h^3 \Big/ 12 \tag{4.17}$$

where Q_{11} is

$$Q_{11} = \frac{E_L}{1 - \frac{E_T}{E_L}\nu_{LT}^2} \tag{4.18}$$

where E_L and E_T are respectively longitudinal and transverse Young's moduli, and ν_{LT} is the longitudinal Poisson ratio. Due to $E_T << E_L$ for a UD prepreg with partially-cured epoxy at room temperature, $Q_{11} \approx E_L$. E_L may be estimated by the Rule of Mixtures.

By a combination of Equations (4.6) and (4.16), the strain energy can be obtained and hence the compression force required for 'elastic' buckling:

$$F = \frac{\partial U_e}{\partial d} = (12\pi + 24)\pi^3 w\varsigma_{11} a^2 (l-d)^{-4} \tag{4.19}$$

where w is the sample width.

From equations (4.17) and (4.18), one may have

$$w\varsigma_{11} = Q_{11} \times \frac{wh^3}{12} = Q_{11} \times I_{eq} \tag{4.20}$$

where I_{eq} is the equivalent second moment of area.

The upper bound of predicting I_{eq} may be calculated as the second moment of area for the whole rectangular cross section, i.e.

$$I_{eq} = \frac{wh^3}{12} \tag{4.21}$$

where all fibres are bending about the same neutral axis.

For the lower bound, I_{eq} may be estimated from each individual fibres bending at their own axes [122],

$$I_{eq} = \frac{\pi d_f^4}{64} \times N_f \tag{4.22}$$

where d_f is the fibre diameter, N_f is the total number of fibres on the cross-section. Therefore, the equation for the compression force to predict 'elastic' buckling may be written as

$$F = \frac{\partial U_e}{\partial d} = (12\pi + 24)\pi^3 a^2 (l - d)^{-4} Q_{11} I_{eq} \tag{4.23}$$

with the upper/lower bounds for I_{eq} shown in Equations (4.21) and (4.22) respectively.

4.4.4.3 Results and discussion

Predictions of 'elastic' buckling based on Method 2 (an energy approach) are orders of magnitude different from experimental results. Predictions based on Method 2 need to be multiplied by factors of 0.041 and 3500 (upper and lower bounds respectively) to match the experimental data, as shown in Figure 4.17. It is shown that predictions based on the upper bound of the second moment of area I_{eq} are much higher than measurements, while those based on the lower bound are much lower. This could be that the effective bending modulus is overestimated (E_{eff} in Equation (4.11) and Q_{11} in Equation (4.23)). However, it is also speculated that not all fibres are bending about the same neutral axis, i.e. a small amount of fibres might slip relative to each other and bend about their own neutral axes. In other words, the prepreg sheet does not bend like a solid beam. Hence, prediction of the degree of fibre slipping during 'elastic' buckling is required to estimate the overall second moment of area for the cross-section of the prepreg sheet, and hence the bending rigidity. Due to small

deformation during 'elastic' buckling, shear energy from fibre slipping would be negligible, compared to elastic deformation of the fibres. Therefore, it is reasonable to assume this region to be pure 'elastic' buckling (see the interpretation of buckling curves in Section 4.3.3). A predictive model for the bending rigidity is needed to predict 'elastic' buckling more accurately.

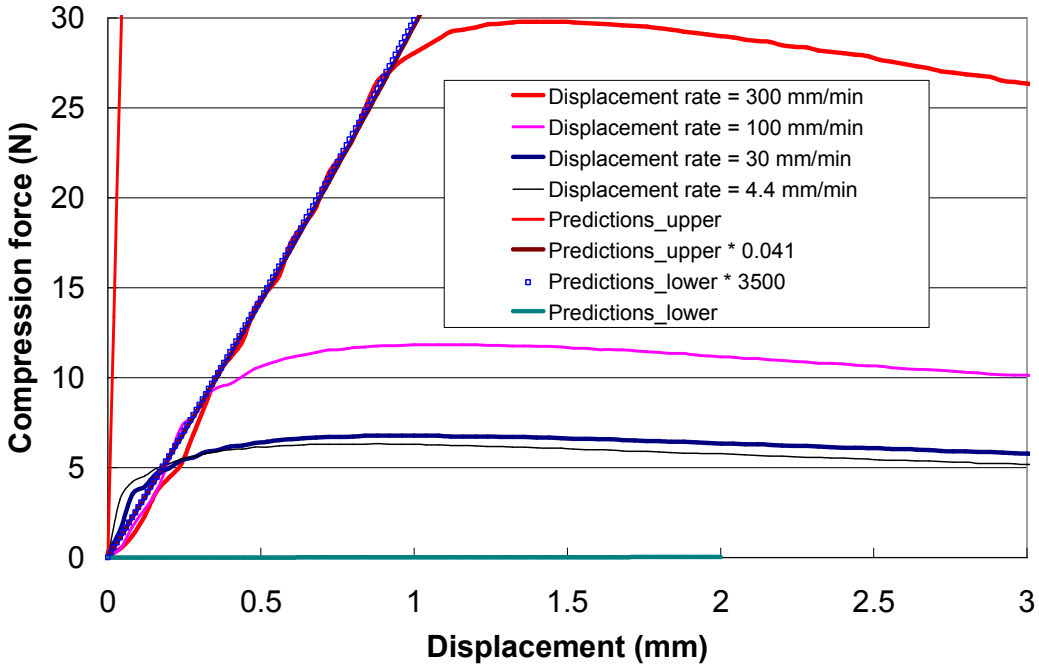

Figure 4.17. Comparing experimental results with predictions of elastic buckling based on an energy approach using Equation (4.23) with lower/upper bounds for I_{eq} shown in Equations (4.21) and (4.22) respectively, where v_f =0.5 for M21 UD prepreg, E_f =294GPa and E_m =0 as $E_m << E_f$. Artificial factors, 0.041 and 3500, were used to illustrate how much theory differs from measurements.

4.4.5 Modelling of 'plastic' buckling

If a fibre-reinforced composite is assumed to be a continuum, fibres can be considered as being continuously distributed throughout the material. A

continuum theory of the mechanics of the continuous fibre-reinforced composite (CFRC) in a solid or elastic state was developed by Spencer and termed as an 'ideal fibre-reinforced model'(IFRM) [33, 34]. A number of works on the modelling of viscous composites are based on the IFRM [19, 21, 22, 35, 124-129]. An attempt of modelling of bending behaviour of viscous composites in a buckling test is made in this chapter based on the IFRM which is reviewed briefly in Appendix 3.A.

4.4.5.1 Determination of rate of deformation tensor

To obtain rate of deformation tensor (Equation (3.A.2)), the velocity field must be determined first. The bending shape of the prepreg during a buckling test can be represented and predicted using a cosine function, see Sections 4.3.4 and 4.4.2. As a cosine curve can be divided into 4 quadrants within the period of 0 to 2π, the analysis focuses on one quarter of a prepreg sheet. Figure 4.18 shows a schematic of deformation of a one-quarter segment of the prepreg sheet at a certain displacement d. Two offset quarter cosine curves representing the upper and lower surfaces of a prepreg sheet are divided into 2 elements with an arc length of Δl. As fibres are along the loading direction and assumed to be inextensible, the arc length of every fibre layer is constant during bending, i.e. OA = O'A' = AB = A'B' = Δl = constant. Points O and O' are fixed during buckling tests as no slip conditions at clamps are assumed. From the assumption of unidirectional and parallel fibres, if AA'' and BB'' are normals to the upper and bottom surfaces of the prepreg defined by these two cosine curves, then AA'' = BB'' = prepreg thickness h. Therefore, the arc lengths A'A'' and B''B' are the displacements of the elements OAA'O' and

ABB'A' respectively at a crosshead displacement of d, relative to their corresponding counterparts points A and B.

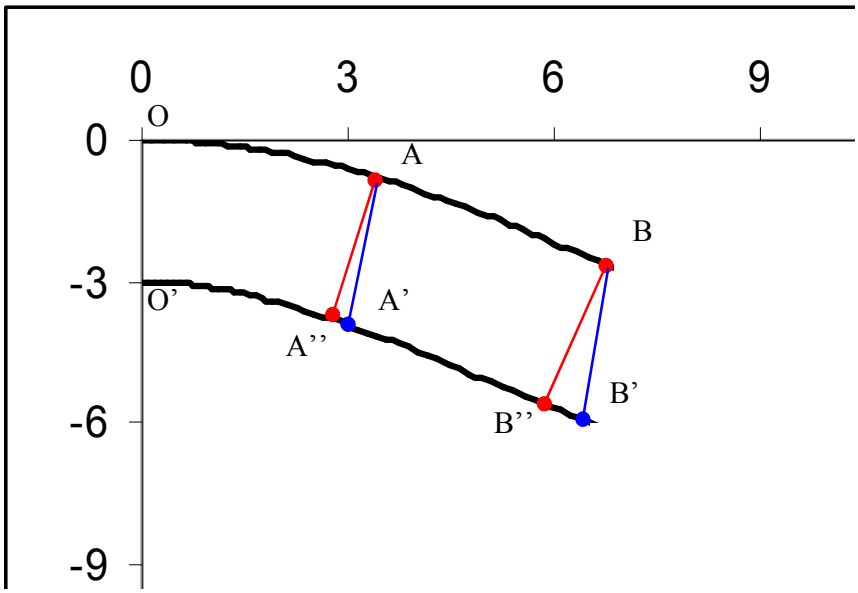

Figure 4.18. Schematic of deformation of one-quarter prepreg sheet (OBB'O') at a certain displacement (d). This segmented sheet is divided into two elements, OAA'O' and ABB'A'.

The relative velocities between the upper and bottom surfaces of the prepreg for these two elements may be approximately equal to the average velocities during the time period t (where the test time $t = d/\dot{d}$ if a constant displacement rate $\dot{d}$ is applied). Then the relative velocity between the upper and bottom surfaces for element OAA'O' is

$$v_{rel} = \text{A'A''}/t \tag{4.24}$$

This is the average velocity over the time period t. Element ABB'A' has an analogous form. It is noted that here v_{rel} is the relative velocity of particle A' relative to its counterpart A. The relative velocity of particles along O'A' increases from 0 at point O' to v_{rel} at point A'. That is, more elements would

improve the accuracy. To obtain an accurate relative velocity, the time period t is divided into a number of time steps Δt. The relative velocity for element n can be obtained,

$$v_e = \frac{\Delta_e}{\Delta t} \tag{4.25}$$

where Δ_e is the difference in displacement of element i in one time step Δt.

A material coordinate system, X_i, is considered with X_1 attached to the fibre direction, X_2 perpendicular to the fibre direction through the prepreg thickness and X_3 normal to the plane of X_1X_2 which is across the prepreg width. It is assumed that during bending the prepreg thickness remains constant and deformation along the prepreg width is homogeneous. Therefore, the velocity field for element n gives

$$v_1 = \frac{\Delta_e}{\Delta t} \tag{4.26}$$

$$v_2 = 0 \tag{4.27}$$

$$v_3 = 0 \tag{4.28}$$

Finally, Equations (4.26)-(4.28) can be used to find the rate of deformation tensor for element n,

$$\mathbf{D} = \begin{bmatrix} 0 & \frac{\Delta_e}{2h\Delta t} & 0 \\ \frac{\Delta_e}{2h\Delta t} & 0 & 0 \\ 0 & 0 & 0 \end{bmatrix} \tag{4.29}$$

which satisfies the incompressibility condition given by Equation (3.A.4).

4.4.5.2 Model formulation

The rate of work done by the external force applied to the prepreg sheet is related to the stress power of this deforming prepreg through the relationship

$$F\dot{d} = A_e h(\sigma_{ij} D_{ij}) \tag{4.30}$$

where F is the external force applied the prepreg (axial compression force in a buckling test), $\dot{d}$ is the rate of the crosshead displacement along the loading direction, A_e is the surface area of element n, h is the thickness of the composite, σ_{ij} and D_{ij} are respectively stress tensor and the rate of deformation tensor presented in the preceding sections. This argument was originally presented by McGuiness [130] in relation to a picture frame test to model shear behaviour of composites and was applied by Harrison [19] to develop a multi-scale energy model to predict the in-plane shear behaviour of viscous textile composites, which is further developed in Chapter 5. Applying a plane stress condition (i.e. $\sigma_{13} = \sigma_{23} = \sigma_{33} = 0$), a combination of Equations (3.A.12), (3.A.20) and (4.29) can be used to determine the scalar product of the stress power $\sigma_{ij} D_{ij}$ for each element,

$$\sigma_{ij} D_{ij} = \frac{\eta_L \Delta_e^2}{h^2 \Delta t^2} \tag{4.31}$$

If the prepreg sheet along the length is divided into n elements, a sum of the stress power dissipated in each element would give the total power per unit volume dissipated in the prepreg sheet at a crosshead displacement of d. Thus, using Equation (4.30), at a displacement rate of $\dot{d}$ the applied axial force (F) in a buckling test can be predicted by

$$F = \frac{\eta_L}{\dot{d}\,h} \sum_{e=1}^{n} \frac{A_e \Delta_e^2}{\Delta t^2} \tag{4.32}$$

4.5 Model predictions for a buckling test

A model combining the 'elastic' buckling model (Section 4.4.4) and the 'plastic' buckling model (Section 4.4.5) is used to predict buckling test results. As development of bending model is still in its infancy, artificial factors, 0.041 and 2 for 'elastic' and 'plastic' respectively, are applied to make predictions conform to experimental results, shown in Figure 4.19. Predictions for 'elastic' and 'plastic' buckling have an intersection at point A which may be the ideal transition point from pure 'elastic' to pure 'plastic' deformation. In practice, the transition would not be a critical point, instead there exists a smooth transition region where is a mixture of 'elastic' and 'plastic' deformation. Predictions on this transition region remain unknown.

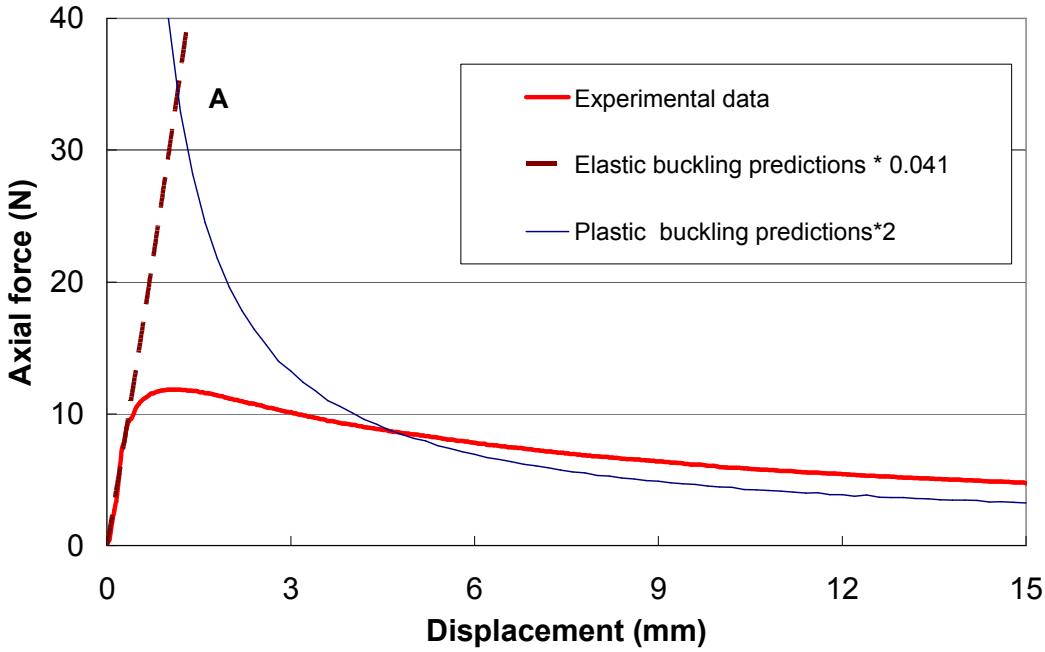

Figure 4.19. Model predictions for a typical buckling test result, axial force versus displacement, for a 50x50x0.89mm sample at room temperature and 100 mm/min displacement rate by combining elastic/plastic buckling models. An energy approach (Section 4.4.4.2) is used to predict elastic buckling, while plastic buckling predictions are based on New-LV model and matrix rheology data Ply®M21 shown in Table 2.1.

4.6 Effects of longitudinal viscosity models

A longitudinal viscosity model is applied to account for effects of fibres on matrix viscosity along the fibre direction during bending, which is reflected in the model presented in the previous section in Equation (4.32). Several theoretical LV models are available in the literature [19, 67-70] and a fully predictive one (New-LV model) has been developed in Chapter 3. To investigate effects of the longitudinal viscosity on the bending model, Harrison's, Christensen's and New-LV models are used to make predictions, as shown in Figure 4.20. Predictions based on theoretical models are steeper at

lower displacements and are lower at higher displacements than experimental results. Differences between predictions based on Harrison's, Christensen's and New-LV models with Newtonian fluid shows longitudinal viscosity might be a dominant parameter in the bending model. The disagreement might be due to micro-buckling in that micro-buckles might compensate some shear strain caused by compressive stress on the outer fibre layers at higher curvature. Hence, some energy would be dissipated by micro-buckling rather than shearing between fibres within the prepreg. By the results from relaxation tests (Section 4.3.8), elastic contribution is up to 33%, which may be considered in the bending model. It can be concluded that a longitudinal viscosity model plus a micro-buckling model and elastic consideration should be combined to ensure predictions to agree with experimental measurements.

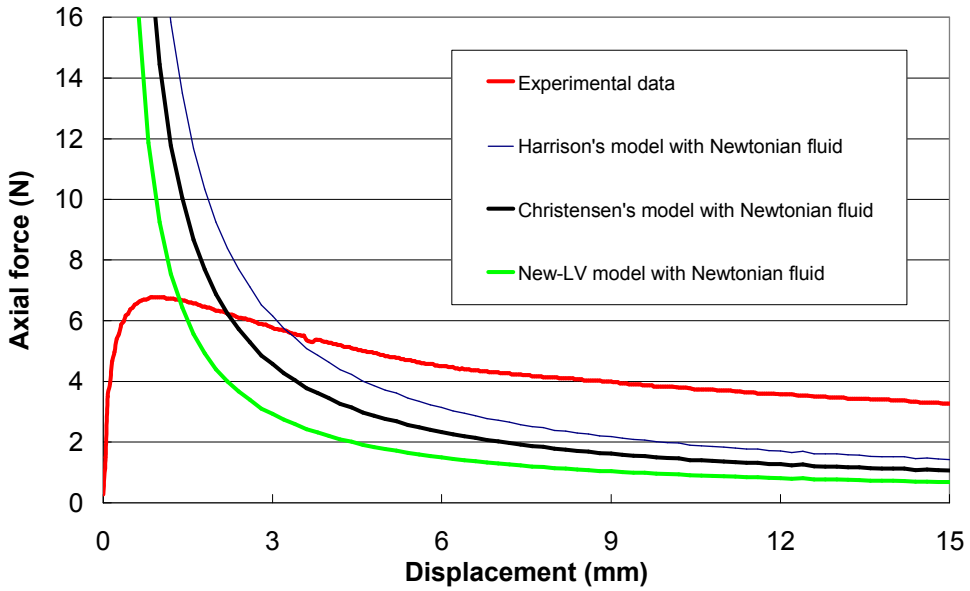

Figure 4.20. Model predictions for buckling test results, axial force versus displacement, for a 50x50x0.89mm Ply® M21 sample at room temperature and 30 mm/min displacement rate based on different theoretical models of longitudinal viscosity with Newtonian fluid. Newtonian fluid viscosity is 340000 Pa.s which is the plateau value of actual rheology data provided by Hexcel Composites (see Chapter 2).

4.7 Evaluation of bending model for rate dependence

Experimental measurements at different displacement rates on buckling tests reveal that the bending behaviour of viscous 3-ply Ply®M21 UD prepregs is rate dependent, see Section 4.3.5. As such, it is necessary to investigate the rate dependence of the bending model. The rate dependence of the model is reflected mainly in the rate of deformation tensor in Equation (4.29) and the displacement rate $\dot{d}$ in Equation (4.32), and also rate-dependent matrix viscosity in the LV model. Model predictions based on New-LV model (LV model developed in Chapter 3) and matrix rheology data shown in Table 2.1 were made to compare with experimental results at 3 displacement rates, 30, 100 and 300 mm/min, shown in Figure 4.21. An artificial factor of 2 was applied for each rate to produce closer predictions. Reasonably good agreement is observed for higher rates, 100 and 300 mm/min. Underestimations of model predictions decrease with increasing rate. The reason for underestimations could be due to effects of micro-buckling which was discussed in Section 4.6. As a whole, the bending model can reasonably capture the trend of the rate dependence of the bending behaviour, if an artificial factor is included.

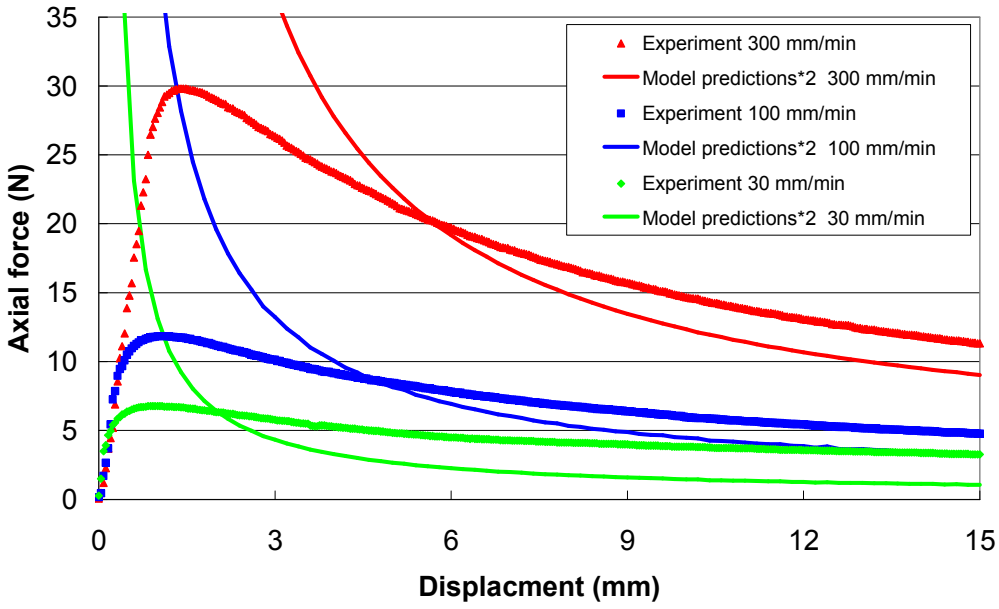

Figure 4.21. Comparisons between model predictions and experimental measurements at 3 displacement rates, 30, 100 and 300 mm/min at room temperature for 3-ply Ply®M21 UD prepregs in buckling tests. Model predictions are based on New-LV model and matrix rheology data shown in Table 2.1.

4.8 Evaluation of bending model on effect of fibre orientations

Model predictions for different fibre orientations, $0^o/0^o/0^o$ and $0^o/90^o/0^o$, were made to compare with experimental measurements at room temperature and 10 mm/min displacement rate for 3-ply Ply®M21 UD prepregs from buckling tests, shown in Figure 4.22. For each ply, the angle of the shearing direction is same as that of fibre orientation, then the shear stress exerted on this ply can be resolved into parallel and transverse to the fibre direction, in which longitudinal and transverse viscosities are employed. The predictions are based on longitudinal and transverse viscosity models (LV and TV) developed in Chapter 3 and matrix rheology data in Table 2.1. It is assumed that the deformation mechanisms occurring in $0^o/0^o/0^o$ prepregs are the same as those in

$0^o/90^o/0^o$ prepregs, i.e. the Equation (4.29) for the rate of deformation tensor still holds. Equation (4.32) for the axial force is applied except that the transverse viscosity is used for the middle layer accounting for 90^o fibre orientation. As discussed in Chapter 3, the newly developed viscosity models show that the TV is greater than the LV for all fibre volume fractions. This means that bending model predictions for $0^o/90^o/0^o$ prepregs are greater than those for $0^o/0^o/0^o$ prepregs, which contradicts the experimental measurements, see Figure 4.22. There might be two possible reasons. Firstly, if the bending model is correct, then the ratio of the TV and LV may be inaccurate. Disagreement among published studies on the ratio exists, as reported in Chapter 3. Secondly, if the viscosity models are correct (i.e. TV > LV for all fibre volume fractions), then the bending model might be incorrect and the rate of deformation tensor must be re-derived.

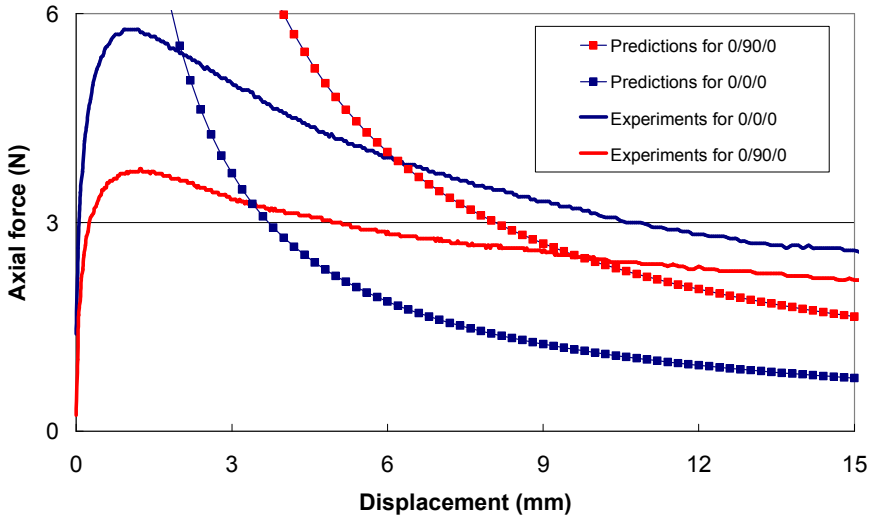

Figure 4.22. Comparisons between model predictions and experimental measurements at different fibre orientations, $0^o/0^o/0^o$ and $0^o/90^o/0^o$ at room temperature and 10 mm/min displacement rate for 3-ply Ply®M21 UD prepregs in buckling tests. Model predictions are based on New-TV model (new transverse viscosity model developed in Chapter 3), New-LV model and matrix rheology data in Table 2.1.

4.9 Validation of bending model using a standard 3-point test

4.9.1 Experimental results

To validate the bending model, a series of standard 3-point bending tests were performed at 3 different rates using 3-ply Ply®M21 UD prepregs. Detailed descriptions of the tests can be found in Section 2.3.4. For all experiments three repeats were performed to assess the reproducibility of the test method. Experimental results, load versus deflection at the middle of the specimen, are shown in Figure 4.23. The force curves may be interpreted in the same way as that of buckling tests: three regions of 'elastic' deformation, transition and 'plastic' deformation. The 'elastic' deformation region becomes more evident as the rate increases. It is speculated that at higher rates, at the beginning of bending, higher shear stress may be required for shearing of neighbouring fibres, i.e. fibres are held by matrix resin more tightly and hence the specimen deforms more like a solid (less slip between fibres). Thus it tends to more 'elastic' deformation (i.e. less 'plastic' deformation) as the speed increases. More undulations at some regions were observed for 100 mm/min. This may be due to slip and stick conditions between the specimen and rollers. It is noteworthy that both the shape and the magnitude of the force curves are rate dependent, which means that deformation mechanisms occurring during bending could be different at different rates. This makes a standard 3-point test for viscous composite materials more complicated in characterising the bending behaviour than a buckling test. This could be due to different boundary conditions, free and clamped, in these two characterisation methods.

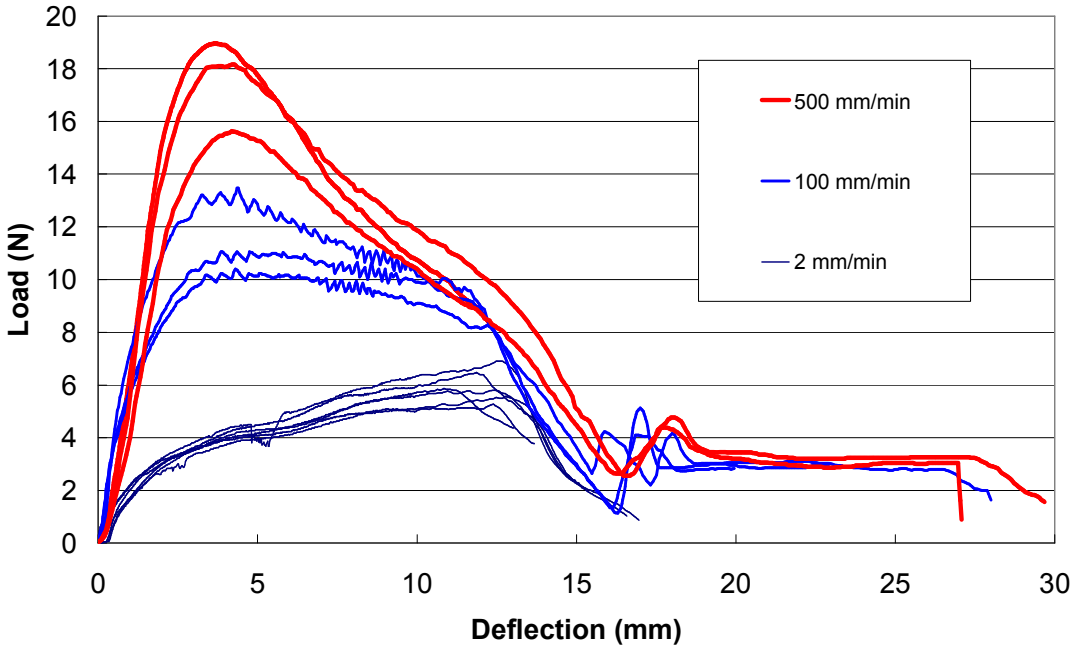

Figure 4.23. Experimental results of standard 3-point bending tests at room temperature for 3-ply Ply®M21 UD prepregs at 3 displacement rates, 2, 100 and 500 mm/min.

4.9.2 Model predictions

According to solid mechanics [111], the shape function for a 3-point bending test may follow

$$y = -c\left(3L_{span}^2 x - 4x^3\right) \tag{4.33}$$

where L_{span} is the span and c is a constant of this shape function at a displacement of d. Note that $0 \le x \le L_{span}/2$ where $L_{span} = 34$ mm. To verify this assumption, some images taken during tests were fitted using Equation (4.33). The fitting procedure is the same as Section 4.3.4. A typical result is shown in Figure 4.24. It is shown that Equation (4.33) can reasonably predict the bending shape in a standard 3-point bending test.

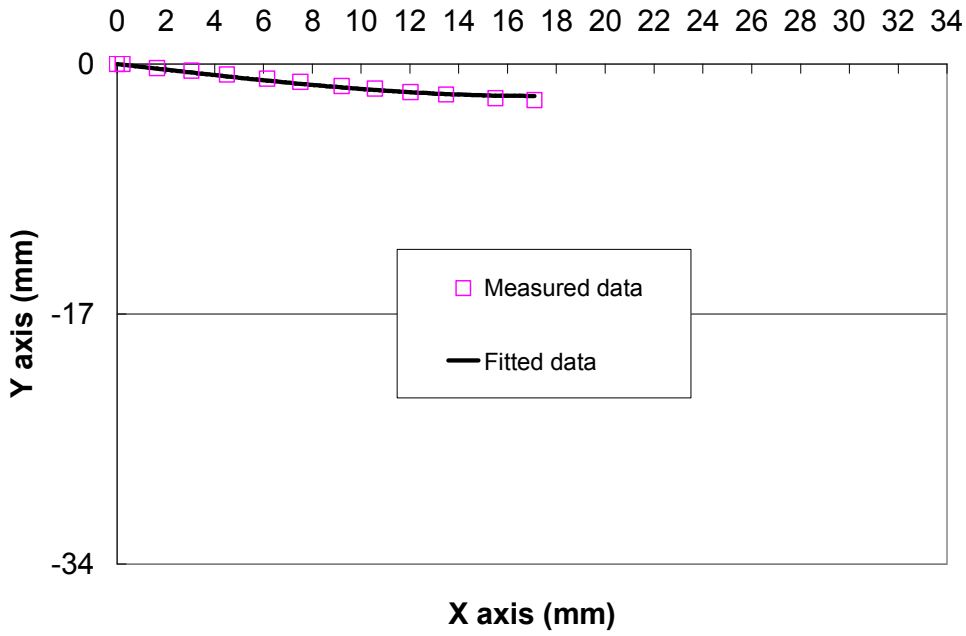

Figure 4.24. A typical fitted result for the bending shape for 3-ply Ply®M21 UD prepregs at a displacement of 2 mm at 2 mm/min displacement rate by Equation (4.33), which yields $y = -5.53 \times 10^{-5} \times \left(3L_{span}^2 x - 4x^3\right)$.

The bending shape is symmetric at the middle point of the specimen (the loading point). This point can then be regarded as a fixed condition, like a clamped condition in a buckling test. Thus the shape function (Equation (4.33)) need to be transformed to a different coordinate system so that the procedure of determination of the rate of deformation tensor can be applied, similarly to Section 4.4.5.1. The transformed bending shape at a displacement of d is

$$y = c\left(3L_{span}^2\left(-x + \frac{L_{span}}{2}\right) - 4\left(-x + \frac{L_{span}}{2}\right)^3\right) - d \qquad \textbf{(4.34)}$$

which replaces the Equation (4.5) to determine the rate of deformation tensor. For the same assumptions described in Section 4.4.3, Equations (4.29) and (4.32) still hold. Therefore, predictions based on the New-LV model for

'plastic' deformation are made to compare with experimental measurements from Figure 4.23 at three rates, shown in Figure 4.25. In order to obtain higher magnitude, model predictions are multiplied by artificial factors, 6, 15 and 200 for displacement rates 500, 100 and 2 mm/min respectively. Figure 4.25 shows that the bending model can only predict the force shape at the highest rate. The force shape and magnitude of model predictions are lower and completely different from the test results. It was thought that various deformation mechanisms could coexist during the test at lower rates. However, this phenomenon reveals that deformation mechanisms occurring in a characterisation method should be similar to those in composites forming in terms of bending behaviour. A characterisation method is basically designed to measure the deformation mechanisms (in the form of energy or force) to characterise the forming behaviour (such as bending) during a forming process. Therefore, it may be necessary to study what deformation mechanisms could possibly occur during bending of a composite material involved in any forming process, so as to judge which characterisation method is most representative of the actual bending behaviour.

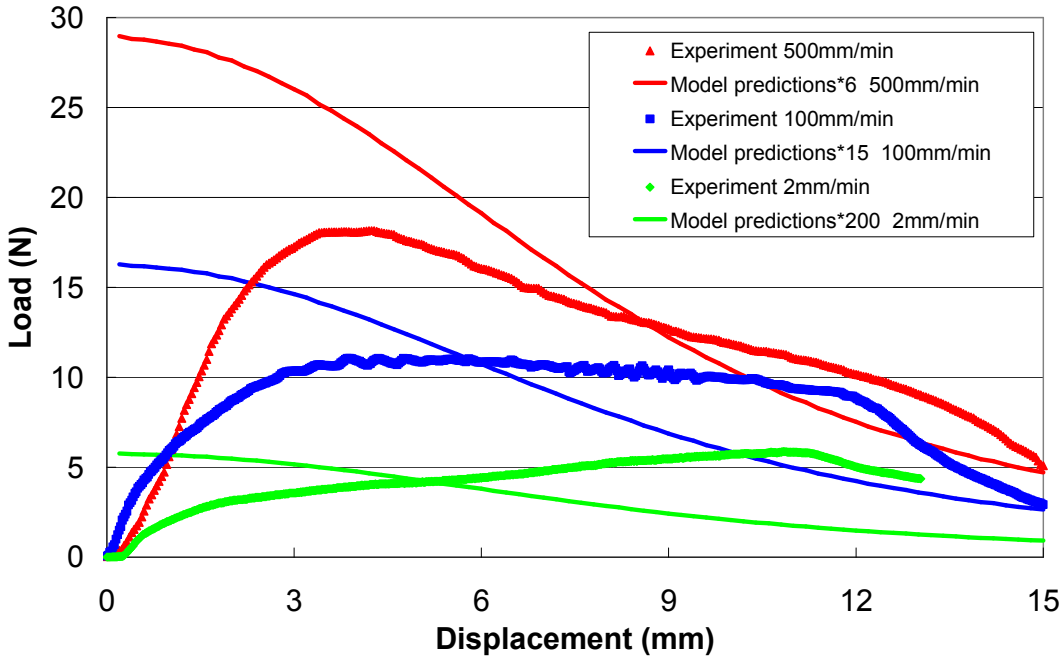

Figure 4.25. Comparisons between model predictions and experimental measurements at 3 displacement rates, 2, 100 and 500 mm/min at room temperature for 3-ply Ply®M21 UD prepregs. Model predictions are based on New-LV model and matrix rheology data in Table 2.1.

4.10 Conclusions

This chapter studies the bending behaviour of viscous composites during forming by experimental characterisation and modelling. Experimental measurements were made by utilising a large-displacement buckling test due to its advantages over other bending test methods, such as ease of applying different rates and temperatures to investigate the importance of viscous matrix resin. However, the method certainly has some disadvantages, such as clamped boundary conditions which may make the analysis of the method more complex. Experimental results show that the bending behaviour of viscous composite is rate and temperature dependent.

A simple bending model was developed to further understand the bending behaviour of viscous composites during forming. The buckling curve may be divided into 3 regions in terms of deformation mechanisms, 'elastic'/'plastic' buckling deformation and their combination (transition). The bending model was developed by considering separately 'elastic'/'plastic' buckling deformation but ignoring the transition region. Two methods for predicting 'elastic' buckling were attempted, suggesting that a predictive model for the bending rigidity is needed. Modelling 'elastic' buckling was based on a pseudo spring stiffness equivalence or classical elastic laminate beam theory, while modelling 'plastic' buckling was based on the uniaxial continuum theory for ideal fibre-reinforced fluids. A cosine bending shape was shown to be valid by experimental observations and used to estimate the shear strain of fibre layers of a prepreg sheet, and hence to estimate energy during 'elastic' buckling and shear energy during 'plastic' buckling. Comparisons between experimental measurements and model predictions showed that both modelling approaches need to be developed further as artificial factors were required in order for the models to match experimental data. Nevertheless, the shape of buckling curves was moderately captured by both modelling approaches, apart from predictions for the transition region from pure 'elastic' to 'plastic' deformation. Comparisons for model predictions based on several theoretical models of longitudinal viscosity showed that longitudinal viscosity was an important parameter in the bending model. It was also suggested that a simple micro-buckling model might account for local changes of fibre arrangement and volume fraction and hence longitudinal viscosity during bending. Elastic

contribution has not yet been considered in the bending model during 'plastic' buckling, although it was shown to be up to 33%.

Evaluation of the bending model for rate dependence showed that the trend of the rate dependence of the bending behaviour can be captured reasonably. The bending model was applied to predict experimental measurements by 3-point bending tests, showing that disagreement was found for lower rates but reasonable qualitative agreement for the highest rate. However, it was argued that disagreement might be due to the fact that deformation mechanisms occurring in 3-point bending tests may not be the same as in the large-displacement buckling test. Evaluation of effects of fibre orientations showed that the bending model together with the new longitudinal viscosity model developed in Chapter 3 was unable to predict the bending behaviour for different fibre orientations.

Chapter 5 Shear behaviour of viscous composites

5.1 Introduction

In-plane shear (or intra-ply shear) and out-of-plane bending are essentially considered as the key deformation mechanisms occurring during composites forming, although various deformation mechanisms could simultaneously co-exist, such as inter-fibre shear, fibre bending, fibre crimping/straightening and slip [85]. Much work has been performed on studying reinforcement deformations during composites forming [85, 86]. Study of the bending behaviour of viscous polymer composite materials is reported in Chapter 4, while the in-plane shear behaviour will be the focus of the current chapter. Much work, using both experimental characterisation and theoretical modelling, has concentrated on in-plane shear which is always considered to be the dominant mechanism [10, 85]. This will be reviewed in Section 5.2. The objectives of this study are to understand further the material characterisation methods of shear especially for viscous polymer textile composites and to develop a fully predictive model to replace costly and time-consuming material characterisation tests. Experimental study measurements will be used to validate the shear model. The current work on predictive modelling is a complementary component of a shear model (the multi-scale energy model, MSEM) developed by Harrison [19], which turns the MSEM into a fully predictive model. Even though temperature dependence is an important aspect for polymer composites, the work in this chapter focuses mainly on room temperature as shear test methods have not yet been standardised. Once the

shear behaviour at room temperature is fully understood, temperature dependence can be considered.

This chapter starts with a brief review of previous work on the in-plane shear behaviour, including experimental characterisation and theoretical modelling. Following that, it is split into three areas, experimental study, theoretical modelling and validation on various aspects, such as rate dependence, weave architecture etc.

5.2 Review of previous work

5.2.1 Experimental characterisation

Experimental methods, such as direction shear force measurement (the Treloar shear apparatus), picture frame and bias extension tests, have been used widely in the textile industry to measure the shear behaviour of fabrics. The Treloar apparatus involves two clamps which hold the fabric on two edges along and perpendicular to the fibre direction. One clamp is fixed while to the other a direct shear force is applied along the fibre direction, with lateral tension exerted through either suspending a mass [131] or a light spring [132]. This work was developed further by Kawabata [133] and led to the Kawabata Evaluation System for Fabrics (KES-F) [95] which is commercially available for measuring low-stress mechanical properties of textiles. However, work on the KES-F by Hu and Zhang [134] suggested that the specimen was not subjected to pure and uniform shear, by showing a non-uniform distribution of the shear strain using finite element analysis. As KES-F was initially designed

for apparel fabrics, only small shearing angles up to 8^o can be applied [135], whereas textile composites could obtain maximum shear angles of over 50^o [86]. Furthermore, the KES-F equipment is very expensive and not widely available.

The detailed descriptions of picture frame and bias extension test methods were reported in Sections 2.3.2 and 2.3.3 respectively. Both methods are currently being studied and widely used to characterise textile composites. For further understanding and to standardise the test methods for composite materials, some research groups among the international composites community established benchmark exercises for bias extension and picture frame tests using dry textile composites [26, 28, 136]. Picture frame tests of each group were performed at room temperature but for different frame lengths, different fabric lengths and different crosshead speeds. To eliminate effects of frame length and fabric length, three approaches were attempted to normalise the data, normalised by the frame length or the fabric area, or by using an energy method [20, 137]. It was noticed that the best agreement was observed by using Peng's energy normalisation method [137], but some deviations can still be found. These deviations could be due to rate dependence. If the fabric is rate-dependent, the crosshead speed should be also normalised as suggested by Harrison et al. [20] to compare the results at a comparable speed. Otherwise, all tests should be performed at the same rate of change of material shear angle. Further studies are still underway to standardise the shear test methods to obtain more accurate and appropriate material properties, in terms of both rate and temperature dependence.

The uniaxial bias extension test method has been used extensively for both dry textiles and composite materials [20, 29, 138-143], including unidirectional prepregs [29]. Potter [29] performed bias extension tests using cross-plied stacks of unidirectional prepregs and found a heterogeneous shear profile especially on the edges of the specimen. The same phenomenon was observed by Harrison et al. [19]. It was observed from photographs that the shear strain was not uniformly distributed and that the deformation primarily occurred in those regions with relatively low fibre volume fraction between the tows. Some fibres within the prepreg may tend to form a tow-like bundle which would have a higher composite viscosity (e.g. longitudinal viscosity) than neighbouring regions, i.e this tow-like bundle has a higher resistance to shear. Thus, the phenomenon of non-uniform shear can be observed on unidirectional prepregs and on textile composites. Fibre buckling and wrinkling were also observed. Potter postulated a hypothesis that the overall deformation may be controlled by some misaligned tows rather than fibre locking, and that compressive loads could be induced, leading to buckling being initiated and propagated.

Investigation of picture frame and bias extension tests by Harrison et al. [20] suggested that a lower bound of the shear behaviour could be obtained by the bias extension test due to inter-tow slip which offers a lower energy mode of deformation, while a upper bound of the shear behaviour could be found by the picture frame test due to the more severe boundary conditions. These two extremes may be useful for optimisation studies based on forming simulation techniques, especially for textile composites forming where shear deformation is assumed to be dominant.

5.2.2 Theoretical modelling

There are numerous work performed on modelling the fabric deformation of dry textiles [131, 133, 142, 144-151]. However, theories developed from these studies may not be applicable directly to viscous polymer composites due to resin flow present during composites deformation. Certainly neither is the classical elastic theory for solid mechanics appropriate due to highly anisotropic nature of viscous fibre-reinforced composites. A well-known continuum theory, the 'ideal fibre-reinforced model' (IFRM) developed by Spencer [33, 34], is specialised in modelling the deformation of fibre-reinforced materials, with a kinematic constraint of inextensibility along fibre directions and an assumption of material incompressibility. These theoretical works are reviewed in Appendix 3.A. A number of rheological models, including Newtonian models, power law viscous models and shear rate dependent Kelvin type material models, were developed by McGuinness et al. [22] within the framework for constitutive modelling established by Spencer and first applied to the modelling of composite forming processes by Rogers [35, 152]. The rate of deformation tensor derived by McGuinness et al. [22] assumed a uniform shear deformation at any point across the picture-frame sample sheet, which may limit its validity to macro-scale (component scale). However, heterogeneous shear profiles were observed on various textile composites (including both viscous and dry composites) by Harrison et al. [19] and on unidirectional prepregs by Potter [29]. In other words, the shear strain rate must be considered separately at different regions, tow (yarn) region, inter-tow (inter-yarn) region and tow crossovers. The rate of deformation tensor accounting for this was first derived by Harrison et al. [19] to predict the in-

plane shear behaviour of viscous textile composites. Nevertheless, the shear strain rate at these different regions had to be determined from experimental measurements on heterogeneous shear profiles (called tow kinematics) from deformed materials. As such, a theoretical model is attempted in this chapter to predict the tow kinematics, allowing Harrison's shear model to be fully predictive. Harrison's shear model is reviewed in detail in Section 5.4.2.

In McGuinness's models [22, 130], the rate of work applied to the picture frame apparatus was equated to the integration of the stress power per unit volume over the specimen volume. Subsequently the integrand was assumed to be constant throughout the sheet, i.e. the extra stress tensor and rate of deformation tensor are uniform throughout the material. Apparently this is not valid due to heterogeneous shear deformation across the sheet. However, this may be valid for Harrison's shear model as the stress power is considered separately at tow and inter-tow regions, if the extra stress tensor and rate of deformation tensor are uniform at these two regions. However, this assumption has not yet been verified.

5.3 Experimental characterisation

5.3.1 Introduction

Some characterisation methods have been suggested for measuring the in-plane shear behaviour of textile composites, as reviewed in Section 5.2.1. For example, the picture frame and bias extension tests have been widely used to produce a trellis in-plane shearing mode in textile composites. Peng et al. [137]

suggested that the picture frame test was a better way to obtain pure shear behaviour of woven composites as it could produce a uniform shear deformation state in the composite sheet. Harrison et al. [20] suggested that deformation produced by the picture frame test may be closer to that occurring during typical forming operations. There could be various complicated deformation mechanisms involved in bias extension, such as intra-ply slip [20], though it has some advantages, such as simplicity of the experimental procedure and relative insensitivity to fibre misalignment. Based on these considerations, the main focus of the study in this section will be the picture frame test. Materials used are automotive prepregs which were described in Section 2.2.3.

5.3.2 Effect of boundary conditions

As the test boundary condition is a critical factor in obtaining reliable data [22, 153, 154], two boundary conditions were investigated, clamped (four edges of PF are clamped) and pinned (three co-linear pins through the tows at each clamping edge provide the shear force to the material sheet during testing). For both clamping mechanisms (boundary conditions) no slippage is assumed to occur during shear. Thus, the clamping mechanisms are not taken into account in the shear model described in Section 5.4. Loose pinning conditions of the sample edges could lead to failure to introduce the desired kinematics, while the tightly clamped case may induce significant tension in the fibre direction even if there is a small degree of misalignment [153, 155]. However, one important requirement is that the shear deformation should be uniform, pure and in-plane shear, i.e. wrinkle free. It had been found that the pinned case is

more suitable for Twintex (a pre-consolidated 2x2 twill weave, glass/polypropylene thermoplastic textile composite) [20]. Therefore, three PF tests for each boundary condition were performed using automotive prepreg. Slight wrinkling occurred in only one test for the clamped cases, whereas serious wrinkling happened at the start of all tests for the pinned case (see Figure 5.1). The deformation is no longer uniform and in-plane pure shear beyond the onset of wrinkling. This suggests that the clamped case should be used in the PF tests for the automotive prepreg. Although uniform and in-plane pure shear deformation can be achieved for the clamped case, care must be taken to avoid any misalignment as the clamped edges could induce fibre/tow stretch and consequently tension. It has been shown theoretically [153] that the stretch in the fibre direction increases monotonically as the shear angle increases, and is amplified by the degree of misalignment. This would no longer lead to reliable measurements.

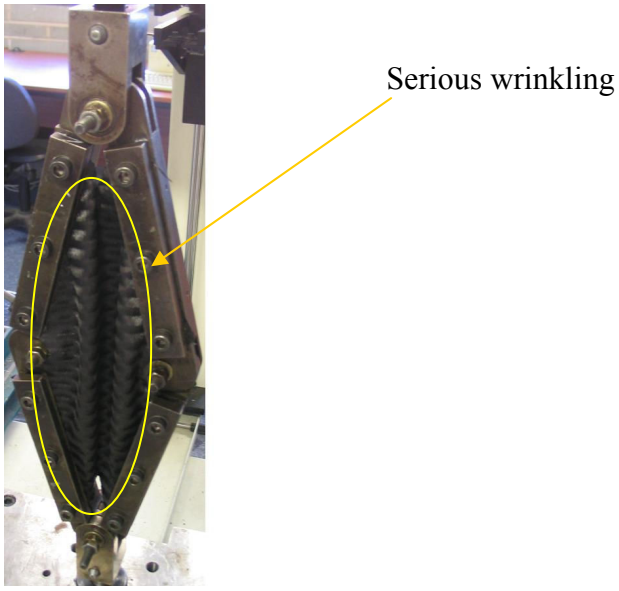

Figure 5.1. Serious wrinkling occurred in all tests for the pinned case.

5.3.3 Influence of direction of shear deformation

There are two directions of shear deformation, positive and negative. It is necessary to consider the dependence on shearing direction due to its practical significance, since the composite material would be sheared in different directions at different locations when deforming into complex curvature components [22]. A positive shearing deformation is defined with the warp fibre directions at an angle of + 45^{o} with the axis of loading, as viewed from the front of the PF apparatus. PF test results for a 8-harness satin weave (glass fibre fabric reinforced PA-12) showed that the force required to shear the composite sheet in positive shear was nearly double the corresponding force in negative shear, but no effect was observed for a 1/3 Crowfoot weave (glass fibre fabric reinforced Nylon) [22]. To investigate its influence for automotive prepreg, three tests for each case were performed. The results shown in Figure 5.2 suggest that the direction of shearing deformation for this prepreg has a negligible effect on PF measurements, compared with the reproducibility of PF tests (see Section 5.3.5). This may imply that weave pattern is the key to the influence of direction of the shearing deformation, suggesting that both shearing directions should be tested for a material prior to obtaining reliable data.

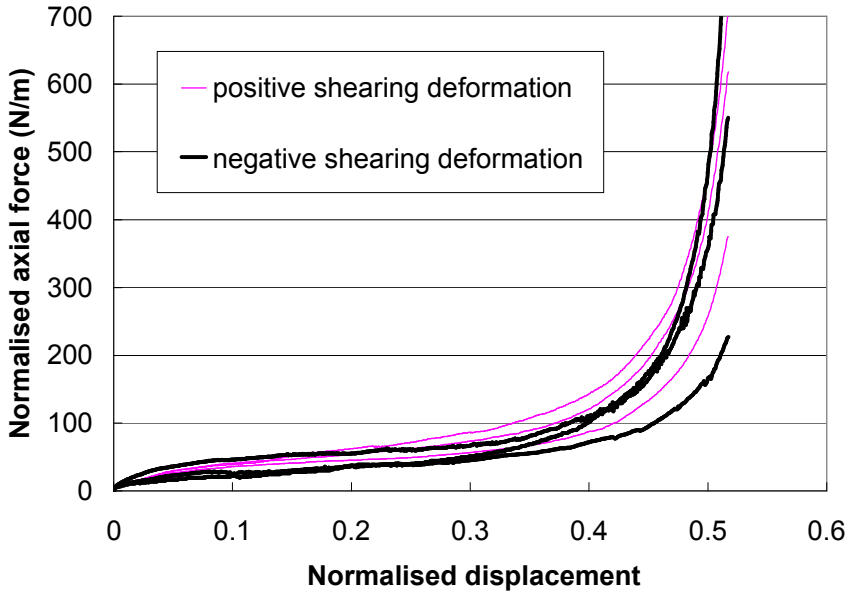

Figure 5.2. The PF results with different directions of the shearing deformation, positive and negative shearing deformation respectively. Note that PF results are normalised by the side length of the picture frame [20], e.g. the normalised displacement equals to the recorded displacement divided by the side length.

5.3.4 Influence of tow-meander

Ideally, the tows of specimens in the weft direction are straight and perpendicular to those in the warp direction. However, in practice, the tows are not exactly straight and perpendicular to each other, as shown in Figure 5.3(a). Such specimens would not align the fibres perfectly along and perpendicular to the clamping edges of the frame. As a result, tensile strain is introduced in the tows [156]. Due to high tensile modulus of the fibres, large variations in tensile stress would then be produced, which would lower the accuracy of test data. Some work has been carried out to investigate the influence of tension on the shear behaviour of textiles during picture frame shearing [149, 151, 157-160]. To reduce effects of tensile strain induced by clamping misaligned fibres,

Lebrun et al. [161] proposed a specimen shape such that only small portions of its length, close to the hinges of the frame, were clamped, instead of clamping the whole length by the clamping bars. It was found that the influence of tension was significantly reduced but wrinkling occurred when the locking angle was reached. However, further understanding on the effect of tension on the shear behaviour could give some insight on forming a wrinkle-free part as this may be similar to the tension introduced by a blank-holder into the tows during composite forming [149]. Chang et al. [155] investigated effects of tow misalignment (tows misaligned to the picture frame by an angle of 2.5^{o}) on deformation under a microscope using a dry satin weave fabric, and found that misalignment caused a significant difference in tow deformation behaviour with tows either being under compression or tension, which highlights the importance of alignment of tows in the picture frame test. As shown in Figure 5.3(a), the tows in the weft direction are not perpendicular to those in the warp direction on material roll of automotive prepreg. In order to investigate the influence of tow-meander, three tests were performed with samples taken directly off-the-roll and another three were for the material straightened to improve tow alignment (i.e. straightened to align the tows in the warp and weft directions). From Figure 5.3 (b), the results for off-the-roll specimens are much higher than those for the case of straightened specimens, and show poor reproducibility. This suggests that test specimens should be straightened prior to testing in order to reduce the influence of tow-meander on test data, for both shear and formability characterisation experiments.

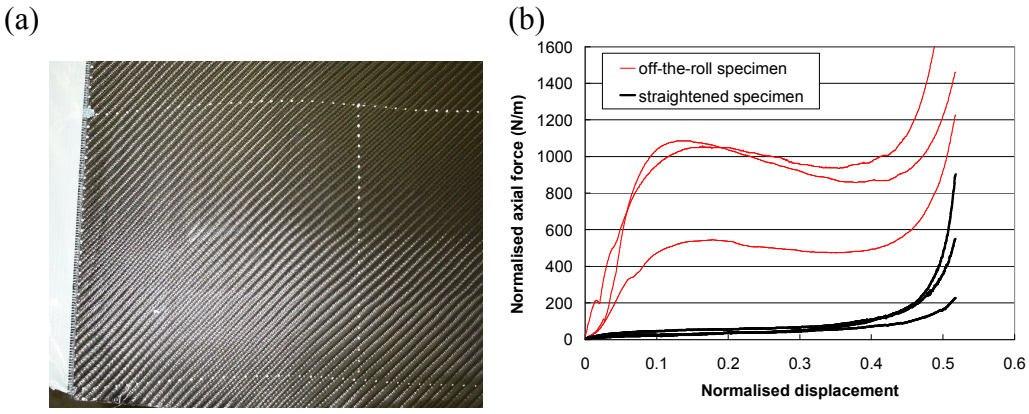

Figure 5.3. (a) The profile of tows in the warp and weft direction in the material roll of automotive prepreg. (b) PF results with the cases of tow-meander and straightened specimens.

5.3.5 Experimental reproducibility

Experimental errors involved during the tests may be due to material variability [162] or misalignment induced by cutting material sheets from the material roll, aligning sheets, clamping of the material, sample misalignment etc. A small degree of misalignment (5^{o}) is sufficient to cause a high variability of experimental data [143]. This echoes the suggestion made in Section 5.3.4 that the specimen should be straightened prior to testing to have the degree of misalignment under control. Chen et al. [143, 163] noticed that repeatable data could be obtained from a fabric that had been sheared multiple times without removal from the frame (so called 'mechanical conditioning'), but the loads were only half that of the fabric without conditioning. Mechanical conditioning may make misaligned tows due to tow-meander straighten and consequently be loose in the frame. Furthermore, permanent compaction of the tows, which become thinner with larger gaps after conditioning, could be induced and hence

the measured shear behaviour may no longer represent the actual forming behaviour of the composite [150]. Figure 5.4 shows the PF results for automotive prepreg at three normalised crosshead speeds. Some PF tests were discarded due to premature wrinkling. The reproducibility of PF tests at each speed is fairly low. From Figure 5.4, the variability can be estimated as approximately 50% (= (maximum-minimum)/average). This variability should be taken into account in the validation of a theoretical model.

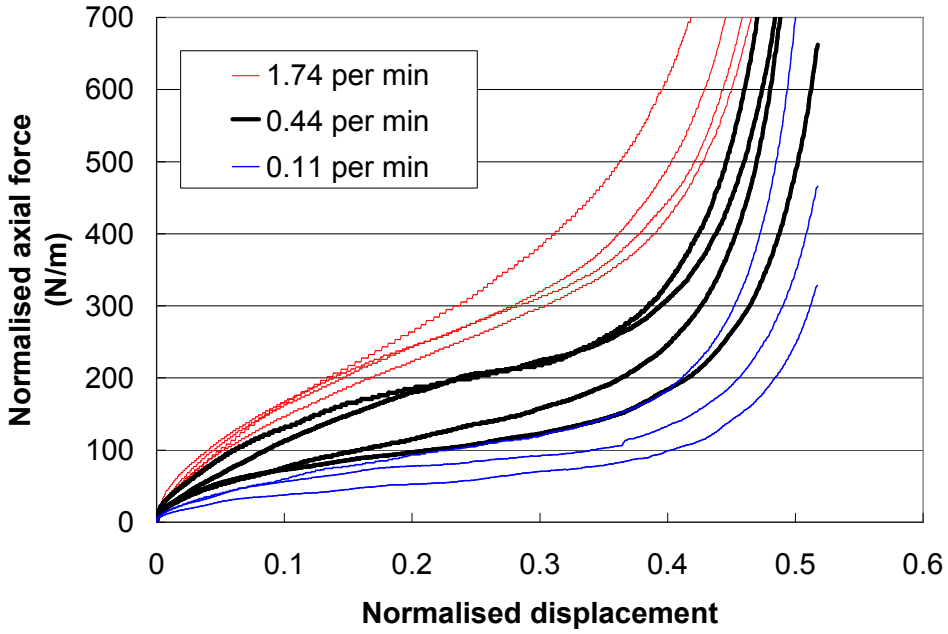

Figure 5.4. PF test results for automotive prepreg at different normalised crosshead speeds (speed/side length) to investigate the reproducibility of experiments.

5.3.6 Investigation of aging effects

The partially cured epoxy resin in prepregs is curing continuously, no matter what temperature it is stored at. Hence, the material must be stored in a freezer to slow down the curing process. However, the material roll might be thawed and refrozen many times as cutting material was performed for experiments at different times. Each time the prepreg is exposed at room temperature, the curing process would progress further. As a result, the aging of prepreg may affect shear force data.

In order to investigate the effect of aging, a number of PF tests on automotive prepreg with different aging times, 2 hours, 4 days and 6 days respectively, were performed. The aging time is the time that the material is thawed and kept at room temperature. The results shown in Figure 5.5 for the aging time of 4 days increase by 140% compared to those for 2-hour aging time, whereas those for the 6-day aging time increase by 300%. This means that the aging process has a significant effect on the shear resistance of prepregs, which implies that there may be some uncertainty in comparisons between model predictions and experimental data. This would also suggest that comparable measurements must be taken from the same batch, i.e. exactly same aging history.

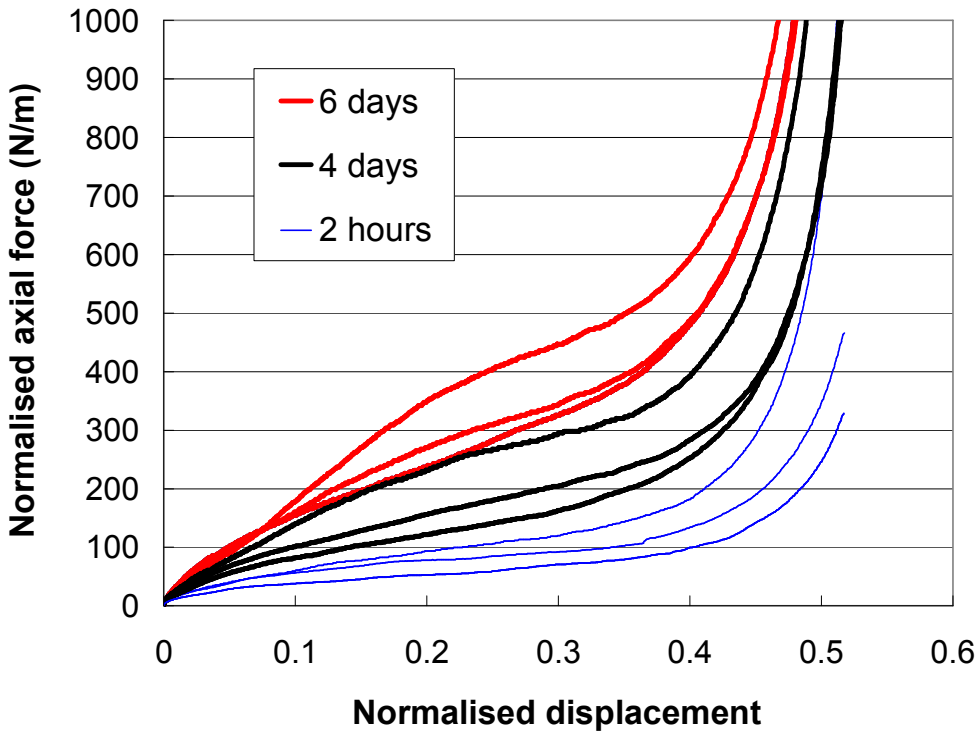

Figure 5.5. Aging tests with three different aging times, 2 hours, 4 days and 6 days respectively, in PF tests for automotive prepregs. Tests were performed at room temperature with a displacement rate of 0.11 min^{-1}.

5.3.7 Investigation of viscoelastic behaviour

The viscoelastic behaviour of viscous composites during in-plane shearing may be investigated by performing stress relaxation tests. The main aim of this study is to investigate if the elastic contribution during shearing a viscous composite sheet is considerable. The material used was automotive prepreg. Material details are in Section 2.2.3. A stress relaxation test was performed by stopping the crosshead at a fixed displacement then measuring the decay in force with time. A detailed description of the test method is presented in Section 2.3.2. The force was recorded for 1200 seconds when the PF rig

stopped at displacements of 15, 30, 45 and 60 mm respectively. According to Section 2.3.2, the relaxed force is the elastic contribution to the total axial force. Experimental results are shown in Figure 5.6. The initial value of the force at time 0 s is the force observed when the crosshead stops at a fixed displacement. The force drops significantly over a short time and then relaxes slowly over 1200 s towards a steady-state value that would be the elastic contribution. For the purpose of convenience, the proportion of the elastic contribution is approximated to the relaxed steady-state value at time 1200 s divided by the initial force at time 0 s. Therefore, the elastic contributions for relaxation displacements 15, 30, 45 and 60 mm are 6.6%, 1%, 1.7% and 2% respectively. There is no obvious correlation between the relaxation displacement and elastic contribution. According to Section 2.3.2, the elastic contribution can be plotted together with viscous contribution, as shown in Figure 5.7. It is shown that the elastic contribution during in-plane shearing is negligible. The same conclusion was drawn previously for Twintex (a pre-consolidated 2x2 twill weave, glass/polypropylene thermoplastic textile composite) [19].

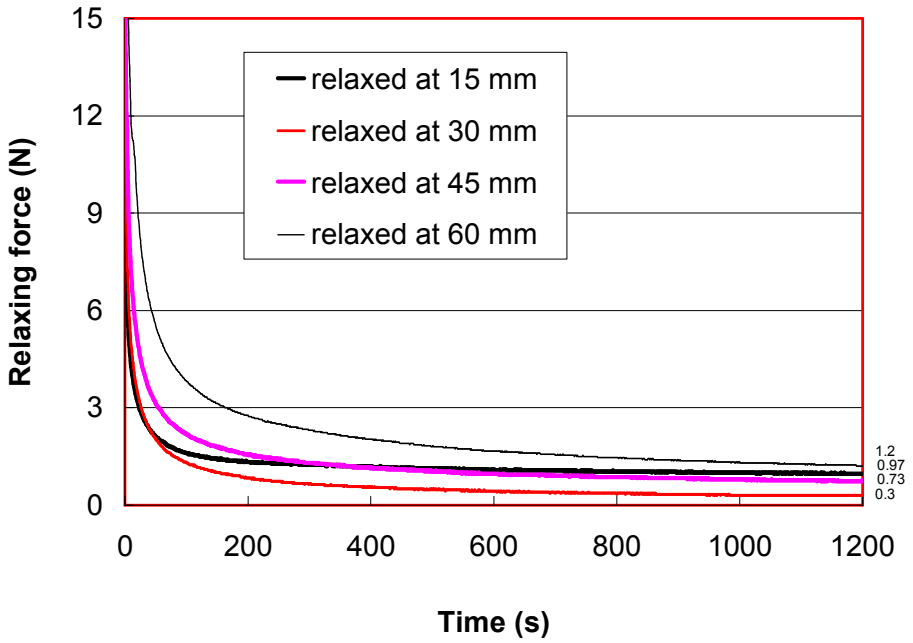

Figure 5.6. The relaxing force recorded at 15, 30, 45 and 60 mm for a period of 1200 seconds. The values of relaxed force are 0.3N, 0.97N, 0.73N and 1.2 N respectively.

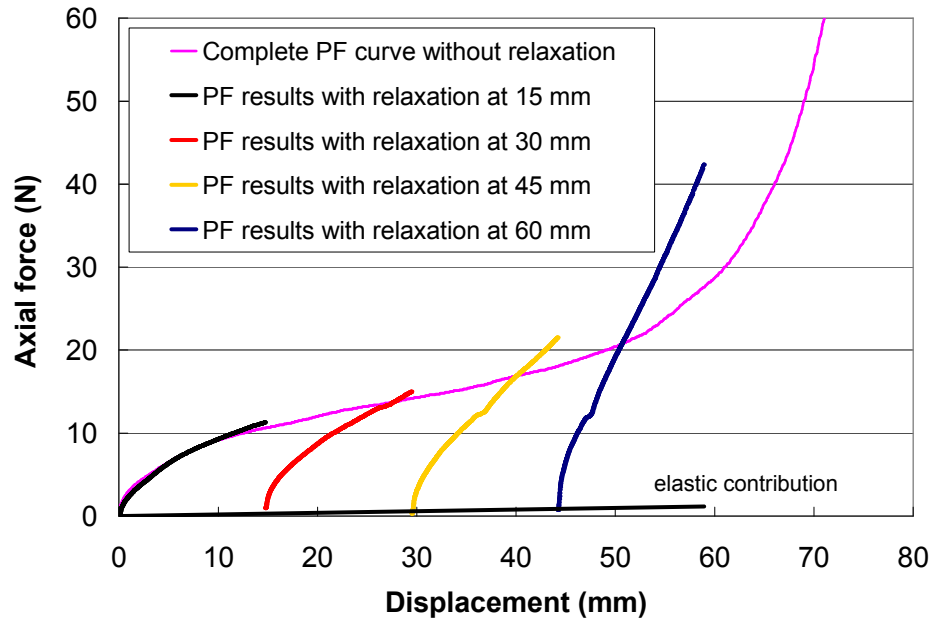

Figure 5.7. PF results from relaxation tests which were performed at room temperature at a displacement rate of 63.1 mm/min. The force decay was measured at 4 displacements, 15, 30, 45 and 60 mm respectively, and at each displacement the relaxing forces were recorded, shown in Figure 5.6. The discrepancy between complete PF results and PF results with relaxation tests was thought to be due to the variability of tests.

5.4 Theoretical modelling

5.4.1 Introduction

Little analytical modelling work on the in-plane shear behaviour of viscous composite materials is reported in the literature, although much effort has been carried out using numerical methods primarily for dry textiles [154, 164]. Analytical modelling is of interest in the current research in terms of not only its economical computation but also its fully predictive capability based on information provided by material suppliers. As such, uniaxial continuum theory developed by Spencer [33, 34] and Rogers [35, 152, 165] was applied by McGuiness [22] and Harrison [19] to establish shear models for viscous composites. Harrison's shear model [19], the multi-scale energy model (MSEM), is developed further here to be a fully predictive model, and is reviewed in detail in the next section (Section 5.4.2). The MSEM was originally developed to predict the shear behaviour of composite sheets, as induced by picture frame tests. The model evaluation was made on two different materials by comparing predictions with experimental results from in-plane shear tests, picture frame test and bias extension test [19]. Good agreement from these comparisons encouraged further development of the model. In order for the MSEM to require less experimental input, an energy minimisation method has been attempted to predict the meso-scale tow kinematics of the heterogeneous shear strain profile, which previously was obtained by time-consuming experimental measurements [19, 166]. Success in modelling the tow kinematics was verified by experimental measurements on formed hemispheres. The structure of this section is as follows. Firstly, the

MSEM developed by Harrison [19] is reviewed. Following that, measurements of the tow kinematics from formed hemispheres were performed. The tow-kinematics model based on an energy minimisation approach is presented in Section 5.4.4, and finally validated by comparing with experimental measurements on hemispheres.

5.4.2 Review of Multi-Scale Energy Model

The multi-scale energy model (MSEM) predicts shear force as a function of shear angle and angular shear rate using an energy summation approach for viscous textile composites [19]. The input data of the MSEM can be obtained from manufacturers' material geometry, textile architecture, fibre volume fraction and matrix rheology. The model has been described in detail previously [19] and so only a brief review is given here.

It has been found that heterogeneous shear occurs for a variety of textile materials, such as prepregs, thermoplastic composites and dry fabrics with different fibre volume fractions [19, 29]. Figure 5.8 shows an example. The initially continuous white lines were drawn prior to shear tests. All lines became discontinuous after tests. This indicates that shear deformation is not uniform across the composite sheet and the deformation occurs mainly in the inter-tow regions, which suggests that shear energy is dissipated at inter-tow regions, in addition to intra-tow regions and tow crossovers. Such observations have motivated the use of a novel two-phase material model structure to analyse the energy dissipation within viscous textile composites. These meso-scale kinematics have important consequences for the deformation occurring

during shear, both within tow and inter-tow regions, and also between tow crossovers. The rate of deformation tensor must be derived separately for both the tow and inter-tow regions and a further dissipative energy term must be derived to account for viscous energy loss at the tow crossovers. Shear force can then be predicted from the shear energy dissipated at crossovers and tow/inter-tow regions respectively.

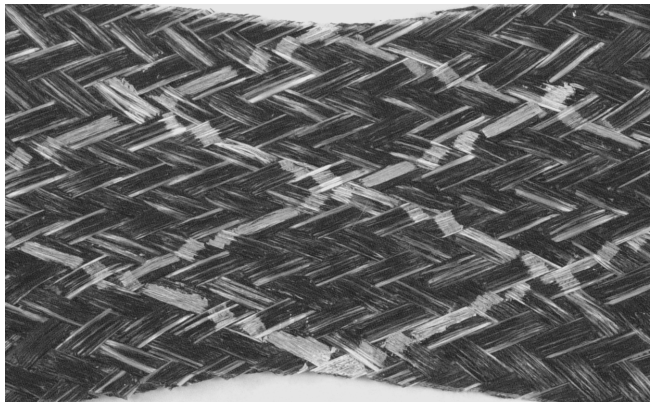

Figure 5.8. Example of non-uniform shear deformation occurring across a textile composite. This sample is a 2x2 twill weave glass/polypropylene thermoplastic composite from a bias extension test at 180^{o}C. Reproduced from [19].

In the MSEM, a textile composite is modelled as two distinct superposed layers, each comprised of parallel tows and isotropic matrix fluid between tows. The tow was modelled as a uniaxial ideal fibre reinforced fluid. The MSEM was then based on a combination of three parts, crossover energy, tow energy and inter-tow energy. The model for the energy dissipated at tow/inter-tow regions [130] used uniaxial continuum theory [35, 127, 129, 167] together with longitudinal/transverse viscosity micro-mechanical models [67, 68]. The uniaxial continuum theory was reviewed in Appendix 3.A.

5.4.2.1 Crossover model

Assuming that at crossovers the gap between the top and bottom of tows is filled with viscous fluid, the energy dissipated at a crossover is due to the shearing of this thin fluid layer. The velocity field between tows at crossovers is calculated by analysing the in-plane kinematics of tow deformation during shear. Using the velocity field and matrix film thickness, the shear strain rate in the matrix film separating tows at crossovers can be estimated. From these calculations an estimate of the rate of energy dissipation can be determined due to shear between tow crossovers.

To obtain the total energy dissipated at one crossover, the area of the crossover is divided into small elements, as shown in Figure 5.9.

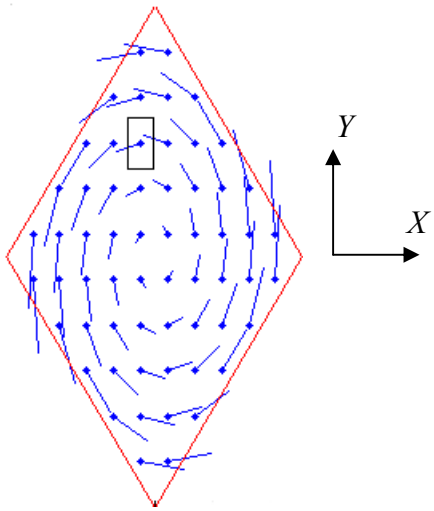

Figure 5.9. Schematic of relative velocity field at the crossover. Vector lines represent the magnitude and direction of relative velocities, while a rectangle drawn on one of the points represents a small element. Reproduced from [19].

The relative velocity at the centre of each element can be calculated from Equation (5.1).

$$\vec{v}_{rel} = \{(\dot{\gamma}_{tow} - \dot{\theta})(1-\sin\theta)Y\}\hat{i} + \{(\dot{\theta} - \dot{\gamma}_{tow})(1+\sin\theta)X\}\hat{j} \quad \textbf{(5.1)}$$

where θ, $\dot{\theta}$ and $\dot{\gamma}_{tow}$ are material shear angle, angular rate and the simple shear strain rate of the tow respectively, $\hat{i}$ and $\hat{j}$ are unit vectors in the local Cartesian reference system, X and Y are the coordinates expressed in the global Cartesian reference system.

The relative velocity is assumed to be constant across the element. Given the film thickness of the viscous fluid layer between two elements of top and bottom tows, the shear strain rate can be calculated. With the polymer viscosity, the shear stress acting on this element can then be calculated, and then the shear force required to shear the element, and hence the energy dissipated at this element. The total energy required to shear one crossover over a small time step can be obtained from the summation of the energy of elements.

From the geometry of crossover, the displacement increment of the corner point in the Y direction (see Figure 5.9) Δd can be easily obtained. Therefore, the force contribution due to shearing at crossovers can be determined by differentiating the total energy with respect to the displacement increment Δd.

5.4.2.2 Tow/inter-tow shear model

A relationship [130] that the rate of work of the force F applied to the picture-frame apparatus by the testing machine is equal to the stress power ($\sigma_{ij} D_{ij}$)

multiplied by the volume of the deforming material, is shown in Equation (5.2).

$$F\dot{d} = L_{PF}^2 h(\sigma_{ij} D_{ij}) \tag{5.2}$$

where $\dot{d}$ is the displacement rate of the picture frame crosshead, L_{PF} is the side length of the picture frame, h is the thickness of the composite sheet, σ_{ij} and D_{ij} are the stress tensor and the rate of deformation tensor respectively. The constitutive equation for the stress tensor derived by Rogers [35] using the Ideal Fibre Reinforced Newtonian Fluid continuum theory is:

$$\sigma_{ij} = -p\delta_{ij} + Ta_i a_j + 2\eta_T D_{ij} + 2(\eta_L - \eta_T)(a_i a_k D_{kj} + a_j a_k D_{ki}) \tag{5.3}$$

for a Cartesian coordinate system. The Cauchy stress comprises of three terms which are an arbitrary hydrostatic pressure ($-p\delta_{ij}$), an arbitrary tension stress in the fibre direction ($Ta_i a_j$) and the deviatoric stress (τ_{ij}), where δ_{ij} and the unit vector **a** denote the unit tensor and the local fibre direction respectively, and η_L (longitudinal viscosity) and η_T (transverse viscosity) are the two tow viscosities in this model, which describe the dynamic interaction occurring between fibres and matrix on a micro-scale (studied in Chapter 3). The rate of deformation tensor (D_{ij}) derived in [19] is:

$$2D_{ij} = \begin{bmatrix} 0 & (\dot{\theta}_{tow}\sec^2\theta_{tow} - \dot{\theta}\tan\theta\tan\theta_{tow}) & 0 \\ (\dot{\theta}_{tow}\sec^2\theta_{tow} - \dot{\theta}\tan\theta\tan\theta_{tow}) & -2\dot{\theta}\tan\theta & 0 \\ 0 & 0 & 2\dot{\theta}\tan\theta \end{bmatrix} \tag{5.4}$$

where θ and $\dot{\theta}$ are the material shear angle and angular rate respectively, θ_{tow} and $\dot{\theta}_{tow}$ are the tow shear angle and angular rate respectively. θ_{tow} is a

function of θ and can be either measured from meso-scale tow kinematics of formed parts or predicted using the energy minimisation method, studied in the following sections. Note that this equation can apply not only to the tow regions but also the inter-tow regions.

In Equation (5.2), F has a combination of contributions from the tow and inter-tow regions. Thus, the combined contribution from the tow and inter-tow regions can be re-written as.

$$F\dot{d} = w_{tow} h \sigma_{ij}^{t} D_{ij}^{t} + (l_{uc} - w_{tow}) q h \sigma_{ij}^{m} D_{ij}^{m} \tag{5.5}$$

where w_{tow} and ($l_{uc} - w_{tow}$) are the initial width of the tow and inter-tow regions respectively, t and m are the superscripts to indicate the tow and inter-tow regions respectively, q is a constant related to the weave architecture indicating that in viscous woven textile composites the actual contact area between two adjacent tows at the inter-tow regions is discontinuous. Using Equations (5.3) and (5.4) together with a plane stress condition (i.e. $\sigma_{13} = \sigma_{23} = \sigma_{33} = 0$), the stress power for the tow and inter-tow regions can be derived as shown in Equations (5.6) and (5.7) respectively.

$$\sigma_{ij}^{t} D_{ij}^{t} = 4\eta_T \dot{\theta}^2 \tan\theta + \eta_L \dot{\gamma}_{tow}^2 \tag{5.6}$$

$$\sigma_{ij}^{m} D_{ij}^{m} = 4\eta_m \dot{\theta}^2 \tan\theta + \eta_m \dot{\gamma}_{m}^2 \tag{5.7}$$

where $\dot{\gamma}_{tow}$ and $\dot{\gamma}_{m}$ are simple shear strain rate at the tow and inter-tow regions. By substituting Equations (5.6) and (5.7) into (5.5), the force contributions from the tow and inter-tow regions can be determined.

5.4.3 Experimental measurements of tow kinematics

The tow kinematics can be measured from formed components, such as hemispheres or picture frame samples or bias extension tests. In this section, the tow kinematics were measured from hemispheres. Figure 5.10 shows an illustration of measuring tow kinematics from a hemisphere using AutoCAD. The hemisphere was formed at room temperature and a speed of 133.3 mm/min using automotive prepreg. The experimental procedure and material details were reported in Chapter 2. Grids of white lines marked using a template prior to forming were used to measure material shear angle and tow kinematics. The material shear angle θ and the tow shear angle θ_{tow} were measured and plotted in Figure 5.11.

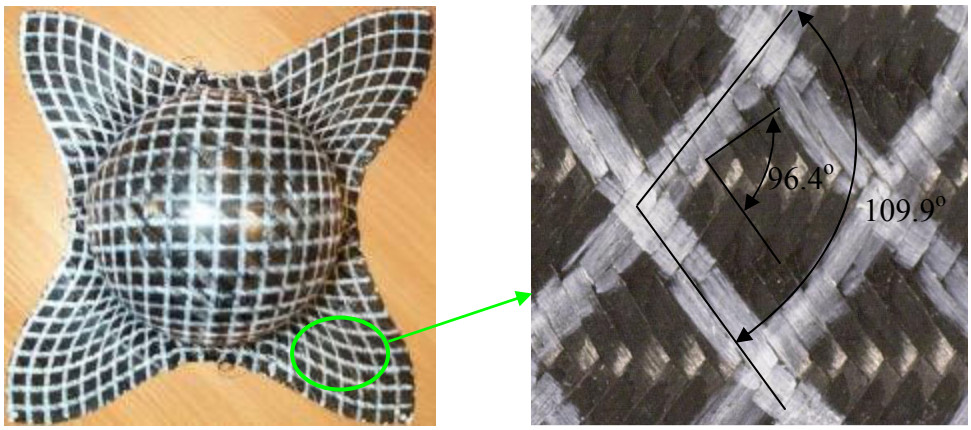

Figure 5.10. Illustration of measuring tow kinematics from a formed hemisphere.

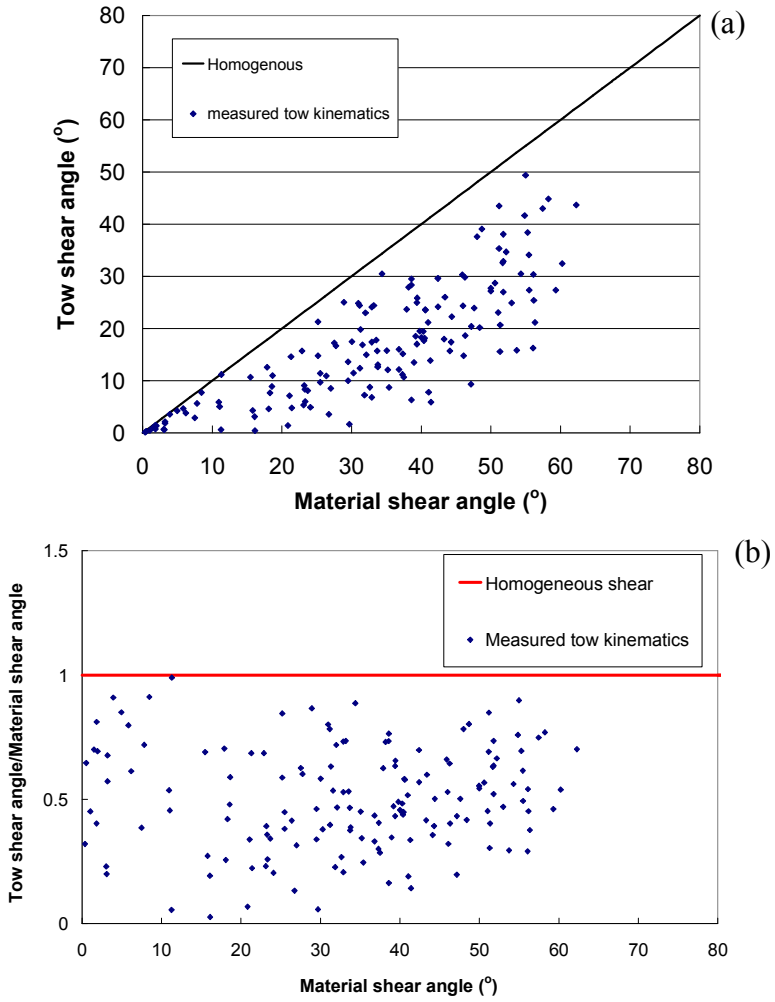

Figure 5.11. Measured tow kinematics for automotive prepreg from hemisphere forming experiments. (a) Raw data of tow shear angle versus material shear angle. (b) Normalised tow shear angle versus material shear angle, where tow shear angle is divided by material shear angle.

Measurements are highly scattered. This is thought to be due to some important factors, such as material variability and variation in friction conditions between the blank and tools. The material variability was found to be significant for a pre-impregnated carbon/epoxy satin weave textile and a commingled glass/polypropylene fabric [162]. However, the material variability and the experimental variability of hemisphere forming tests are currently assumed to

be negligible when making tow-kinematics measurements. Figure 5.11 shows that approximately homogeneous shear deformation can occur at low shear angles, less than 10^o, whereas tow shear deformation is about a half of the bulk material at higher shear angles (e.g. at shear angle 40^o, tow shear angle is half, 20^o). If tow-kinematics measurements are applied in the MSEM to make predictions, then measured data need to be fitted by an appropriate function to capture the behaviour at different shear angles. In previous studies [19], predictions are based on measured tow kinematics where measured data were fitted by a polynomial. Figure 5.11 will be used for the purpose of evaluating the tow-kinematics model presented in Section 5.4.4.

5.4.4 Predictive modelling of tow kinematics

A tow-kinematics model (TKM) is developed in this section to model the heterogeneous shear strain profile which occurs during in-plane shearing of a viscous composite, based on an energy minimisation method.

The actual tow kinematics are predicted by minimising the energy generated due to in-plane tow shear, in-plane inter-tow shear and crossover shear. For example, a low degree of in-plane tow shear ($\dot{\theta}_{tow} << \dot{\theta}$) generates a relatively small amount of energy due to in-plane shearing of tows but a relatively large energy contribution due to in-plane inter-tow shear and crossover shear. Alternatively, a high degree of in-plane tow shear ($\dot{\theta}_{tow} \approx \dot{\theta}$) generates a relatively large amount of energy due to in-plane shearing of tows but a relatively small energy contribution due to in-plane inter-tow shear and

crossover shear. The amount of energy dissipated by the in-plane tow shear, predicted by Equation (5.8), is directly related to the longitudinal viscosity of the tows, η_L. The amount of energy dissipated by inter-tow regions, Equation (5.9), and crossovers, Equation (5.10), is directly related to the matrix viscosity, η. The tow angular shear rate, $\dot{\theta}_{tow}$, determines the in-plane shear rate of the tow and inter-tow regions as well as the crossover shear rate. Thus, by increasing $\dot{\theta}_{tow}$ from 0 to $\dot{\theta}$ (material angular shear rate) the minimum energy dissipation during any small angular increment can be determined. In this way the tow angular shear rate corresponding to minimum energy can be determined. The process is demonstrated in Figure 5.12. Calculations were made for automotive prepreg using the following experimental parameters: temperature = 23°C, θ=30°, material shear angular velocity $\dot{\theta}$=0.0026 rad/s, the tow shear angle for this step θ_{tow} = 15°.

$$W_{tow} = l_{uc} w_{tow} h \eta_L \Delta\theta \dot{\theta}^{-1} \left(\dot{\theta}_{tow} \sec^2 \theta_{tow} - \dot{\theta} \tan\theta \tan\theta_{tow} \right)^2 \quad \textbf{(5.8)}$$

where W_{tow} is the energy due to in-plane tow shear during a small angular increment $\Delta\theta$, l_{uc}, w_{tow} and h are the initial length of a unit cell, initial width of the tow and the thickness of the composite sheet respectively, θ_{tow} and $\dot{\theta}_{tow}$ are tow shear angle and angular rate respectively.

$$W_{inter-tow} = l_{uc} \left(l_{uc} - w_{tow} \right)^{-1} hq \eta_m \Delta\theta \dot{\theta}^{-1} \left(l_{uc} \dot{\theta} - w_{tow} \dot{\theta}_{tow} \sec^2 \theta_{tow} + w_{tow} \dot{\theta} \tan\theta \tan\theta_{tow} \right)^2 \quad \textbf{(5.9)}$$

where $W_{inter-tow}$ is the energy due to in-plane inter-tow shear during a small angular increment $\Delta\theta$ and q is a factor accounting for weave architecture.

$$W_{cross} = \sum A_e \eta_m \Delta\theta \left(\dot{\theta} h_{cross} \right)^{-1} \left(D_{12} - \dot{\theta} \right)^2 \left[\left(1 + \sin^2\theta\right)\left(X^2 + Y^2\right) + 2\sin\theta\left(X^2 - Y^2\right) \right] \quad \textbf{(5.10)}$$

where W_{cross} is the energy due to in-plane shear between tow crossovers during a small angular increment $\Delta\theta$, A_e is the surface area of the element, h_{cross} is the thickness of resin film between tow crossovers, D_{12} is the component of the rate of deformation tensor shown in Equation (5.4), X and Y are the coordinates expressed in the global Cartesian reference system shown in Figure 5.9.

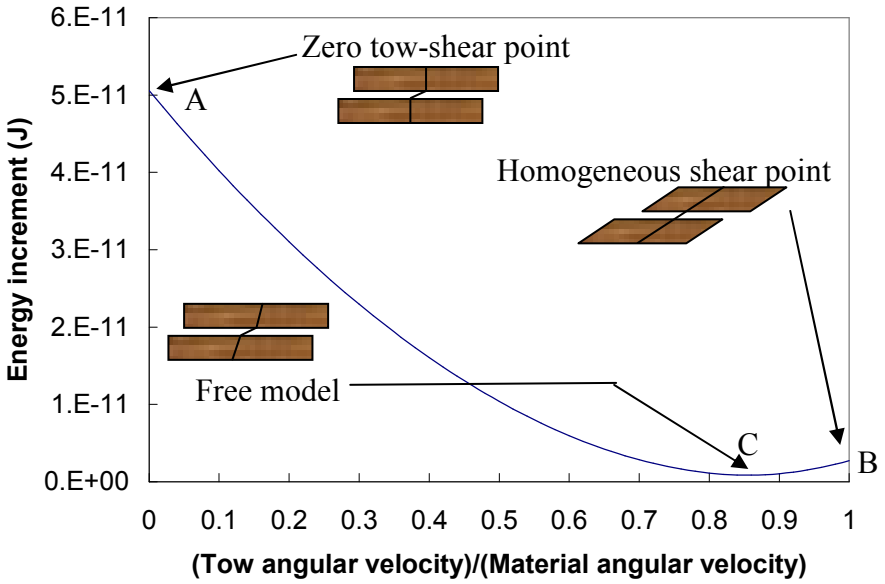

Figure 5.12. Schematic of energy minimisation method to predict the tow kinematics.

Point A in Figure 5.12 is the zero tow-shear point where tows are effectively rigid, i.e. there is no shear energy dissipation in the tow regions, whereas point B is the homogeneous shear point where the shear strain rate is the same across the composite sheet, i.e. there is no shear energy contributions from crossover regions and the tow region has its maximum contribution of shear energy. If there is no constraint imposed, i.e. free model, the minimum of energy

contributions from crossovers and tow/inter-tow regions (point C) would yield the actual tow angular velocity and tow shear angle. Therefore, from Figure 5.12, $\dot{\theta}_{tow}$ can be predicted by minimising the total energy increment by using golden section search, which is at point C. By increasing the material shear angle (θ), the corresponding $\dot{\theta}_{tow}$ and θ_{tow} can be determined, which induces a form of θ_{tow} versus θ, i.e. predicted tow kinematics.

5.4.5 Validation of tow-kinematics model

The TKM developed in the preceding section can be validated using experimental measurements reported in Section 5.4.3, shown in Figure 5.13. The measured data shown in Figure 5.11 were divided into several points and re-plotted using the error bars indicating the standard deviation of the data. The points are mean values within a small interval. The longitudinal viscosity (LV) developed in Chapter 3 was used in the TKM. Matrix rheology data (HexPly® M47) used in automotive prepreg was characterised in Section 2.3.1. The comparison shown in Figure 5.13 shows that the predicted tow kinematics are much higher than average measurements, giving homogenous shear profile. The discrepancy between predictions and measurements is thought to be due mainly to the accuracy of some parameters of the MSEM, such as TV, LV and weave architecture. The TKM was developed based on the in-plane simple shear of crossover, tow and inter-tow regions. Therefore, it is speculated that the LV used in predicting in-plane tow shear energy might not accurately capture the micro-mechanical interactions between fibres within the tow, presuming the crossover model and the rate of deformation derived in (5.4) to

be accurate. In practice the fibre gap within the tow during in-plane shear may vary, i.e. be a function of the material shear angle, whereas it is assumed to be constant in the LV model in Chapter 3. Hence, a sensitivity study on the effect of LV on the TKM was performed, shown in Figure 5.13. It is shown that the modified LV can improve the predictions of tow kinematics, where the LV was multiplied by a factor of 50. Reasonable agreement was found as the predictions lie approximately between error bars. However, effects of transverse shear of tows (tow squeezing) are not yet considered, which may influence energy dissipations in the TKM and more profoundly affect the in-plane geometry of tows.

One may conclude that the LV model developed in Chapter 3 needs to be developed further to capture the actual micro-mechanical behaviour of composites, so as to improve the tow-kinematics model. Nevertheless, in the following sections, LV model will not be multiplied by any factor to predict shear force.

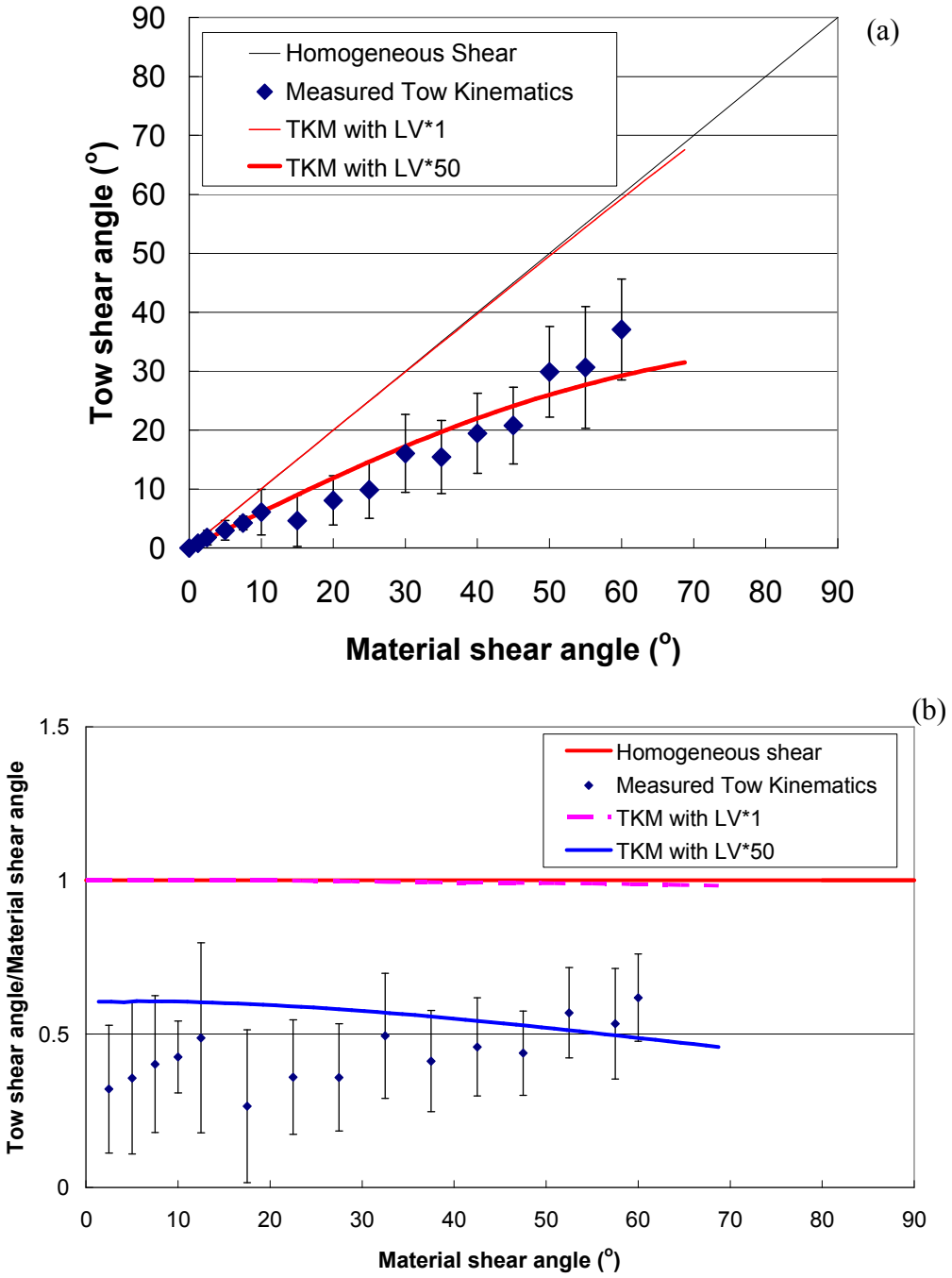

Figure 5.13. Predicted tow kinematics by the MSEM using the tow-kinematics model. TKM and LV stand for the tow-kinematics model and longitudinal viscosity respectively. The error bars indicate the standard deviation. (a) tow shear angle versus material shear angle (b) Normalised tow shear angle versus material shear angle.

5.5 Evaluation of shear model for rate dependence

Experimental measurements at different rates on PF tests show that the shear behaviour of automotive prepreg is rate dependent, see Figure 5.4. As such, it is necessary to investigate whether the shear model can accurately predict rate-dependent forming behaviour. Model predictions based on New-LV and New-TV models (LV and TV models developed in Chapter 3) and the tow-kinematics model developed in Section 5.4.4 were made to compare with experimental results from picture frame tests at room temperature and 3 normalised displacement rates, 0.11, 0.44 and 1.74 min^{-1}, shown in Figure 5.14. Matrix rheology data (HexPly® M47) was reported in Section 2.3.1. The Carreau-Yasuda model was used in the MSEM to fit rheology data of resin to capture the rate-dependent behaviour of the polymer. Only one result for each displacement rate was chosen to represent PF results. The lowest force curve was chosen as being the least influenced by misalignment. Figure 5.14 shows that the shear model is rate sensitive and the force predictions at all rates are lower than PF tests at lower shear angles, but increase rapidly towards higher shear angles. According to [19], the simple shear flow in the MSEM is dominant below a certain shear angle, after which squeeze flow becomes dominant. Since LV is associated with the simple shear flow and TV with the squeeze flow, the comparisons in Figure 5.14 suggest that LV may be underestimated but TV overestimated. The results from validation of the tow-kinematics model reported in Section 5.4.5 and from validation of the LV model using experimental measurements presented in Chapter 3 also suggest that LV may be underestimated. However, the TV model was reported to lie well between the lower and upper bounds of test results. It is speculated that

effects of the locking angle on the squeeze flow might need to take into account. Locking angle refers to the angle where the tows in the prepreg are no longer able to rotate but compress on each other as the prepreg is further sheared. When the locking angle is reached, the neighbouring tows come into contact and consequently are squeezed and the tow width becomes thinner, if wrinkling has not yet occurred (in-plane shearing deformation). As a result, the shear strain profile should account for squeeze flow at the locking angle, and hence the rate of deformation tensor and the tow-kinematics model should be modified.

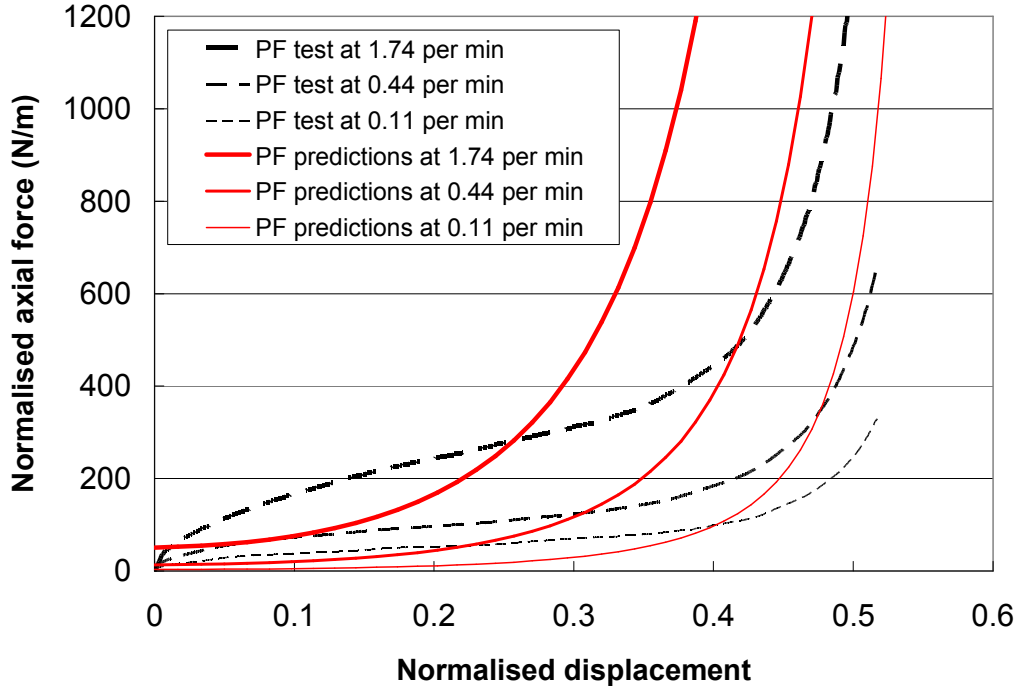

Figure 5.14. Comparisons between model predictions and experimental measurements at room temperature and 3 normalised displacement rates, 0.11, 0.44 and 1.74 min^{-1} for automotive prepreg in picture frame tests. Model predictions are based on the tow-kinematics model, New-LV model and matrix rheology data for HexPly® M47 shown in Table 2.1.

5.6 Evaluation of shear model for weave architecture

Many weave patterns are of interest in the current research due to different formability over various processing conditions, ranging from 1x1 plain weave to 4x4 twill weave, and to 1/4 satin weave. Experimental studies on formability of viscous composites with different weave patterns showed that plain weaves were more formable than twill weaves (automotive prepregs) on pilot helmet forming experiments [168], and aerospace prepregs were slightly less formable than automotive prepregs on hemisphere forming experiments [169]. Material details for plain weaves, automotive and aerospace prepregs were reported in Section 2.2.3. However, the conclusions might not be definitive as other material parameters vary between the materials and could be influential on formability [170], such as tow spacing, tow geometry and fibre volume fraction. Experimental measurements using picture frame tests on two commingled glass/polypropylene woven fabrics, plain weave and 1/3 satin weave, differed by up to a factor of 2 and the discrepancy increased with increasing shear angle [171]. This observation is interesting and may suggest that the weave pattern has an effect on the squeeze flow and the locking angle, which are important in the MSEM and TKM as discussed in Section 5.5. Picture frame test results on 3 dry glass fabrics also showed that weave pattern had effects on the shear behaviour, with the plain weave being least compliant, the twill weave having the highest shear resistance and 4-harness satin in the middle [172, 173]. Moreover, comparisons of picture frame tests between plain weave (material codes: M47/42%/193P/CHS-3K) measured by Evans [174] and automotive prepreg from Section 5.3 showed effects of weave architecture.

A factor, q, was used in the shear model to account for the weave architecture related to the actual discontinuous contact area between two adjacent tows at the inter-tow regions in woven textile composites. This allows the shear energy at inter-tow regions to be calculated by the proportion of the actual contact area within the unit cell. The q factor is defined as: (actual contact area within one unit cell)/(unit cell length x sheet thickness). It ranges from 0 to 1. However, the calculation of contact area depends on the accuracy of the assumption of the tow path along the fibre direction. The tow path is currently assumed to be sinusoidal. If the role of weave patterns is shown to be influential in the MSEM or TKM, then more accurate geometric descriptions of weave patterns would be required, such as the work by McBride et al. [142] and Souter [149]. In the sensitivity study, q is equal to 0.001, 0.38 and 0.999. Figure 5.15 shows that the shear model is insensitive to the value of q. This is because the energy contribution from the inter-tow region is tiny compared with other regions, which means that the effect of weave pattern cannot be modelled accurately by the MSEM. This deficiency of the shear model could be due to inaccurate modelling of inter-tow shear deformation, or inaccurate predictions of the tow kinematics. Therefore, improving the tow-kinematics model is believed to be the key to incorporating effects of weave pattern into the MSEM.

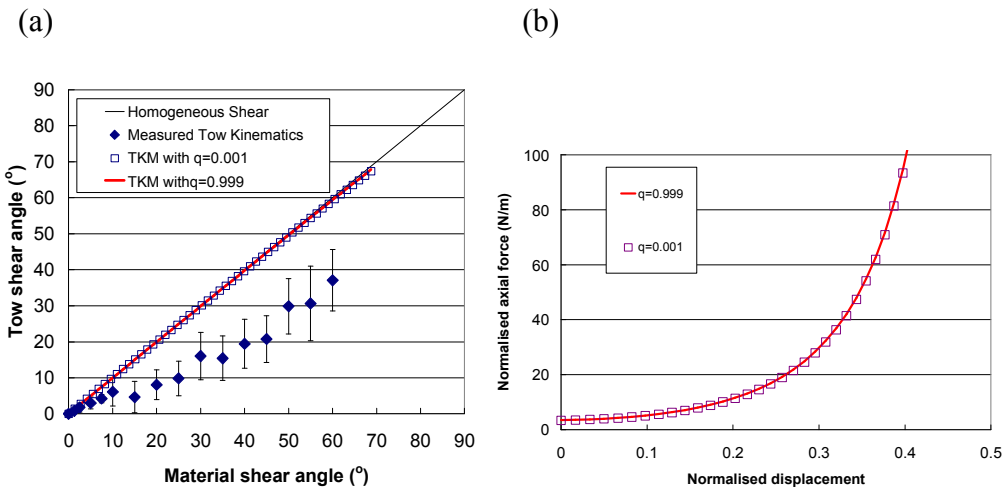

Figure 5.15. Predictions of tow kinematics and force versus displacement in (a) and (b) respectively, at a normalised displacement rate of 0.11 min^{-1} for automotive prepreg sheet, with two extreme q factors, 0.001 and 0.999. Model predictions were based on the tow-kinematics model (TKM), New-LV model and matrix rheology data for HexPly® M47 in Table 2.1.

5.7 Evaluation of shear model on unidirectional prepreg

The continuum theory used in the shear model was originally for uniaxial/biaxial non-woven fibre-reinforced composites. A brief review was presented in Appendix 3.A. It is straightforward to use the MSEM to predict the in-plane shear behaviour for UD prepregs by ignoring terms of crossover and inter-tow regions. However, in experiments cross-plied (i.e. 0/90°) specimens were used in order to balance the picture frame rig during shearing. Hence, inter-ply shear is modelled by the crossover model, i.e. only the contribution from inter-tow regions is ignored in the MSEM. Strictly speaking, model predictions now should be closer to experimental measurements as the material structure is more similar to the theory and fewer assumptions are made

due to no inter-tow contributions. By setting the initial width of the tow and inter-two regions (l_{uc} and w_{tow} in Equation (5.5)) equal to the side length of the picture frame (L_{PF}), the MSEM can be used to model the in-plane shear behaviour of UD prepregs. The sample thickness in the MSEM is doubled for two layers of UD prepregs. Model predictions based on New-LV model (LV model developed in Chapter 3) and matrix rheology data in Table 2.1 were made to compare with experimental results at room temperature and 3 normalised displacement rates, 0.07, 1.38 and 5.52 min^{-1}, as shown in Figure 5.16. As expected, homogenous shear was predicted by the TKM, i.e. simple shear rate of tows equals to the material shear angular rate. Therefore, in this case the accuracy of the TKM discussed in the previous sections would not affect the accuracy of model predictions. Figure 5.16 shows that the discrepancy between model predictions and experimental measurements below a certain displacement (simple shear flow is dominant) is decreased with increasing rate, while the discrepancy above a certain displacement (squeeze flow is dominant) is increased with increasing rate. As discussed in Section 5.5, LV and TV are associated with the simple shear flow and squeeze flow. Therefore, according to discussion in Section 5.4.5, the factor multiplying LV is not a simple constant but shear-angle-dependent and rate-dependent. Moreover, a parabolic factor as a function of the shear angle was shown to improve the shear model in force magnitude and shape at low rates [25]. Therefore, development of LV and TV models which are a function of the shear angle and rate may be the key to improving the MSEM.

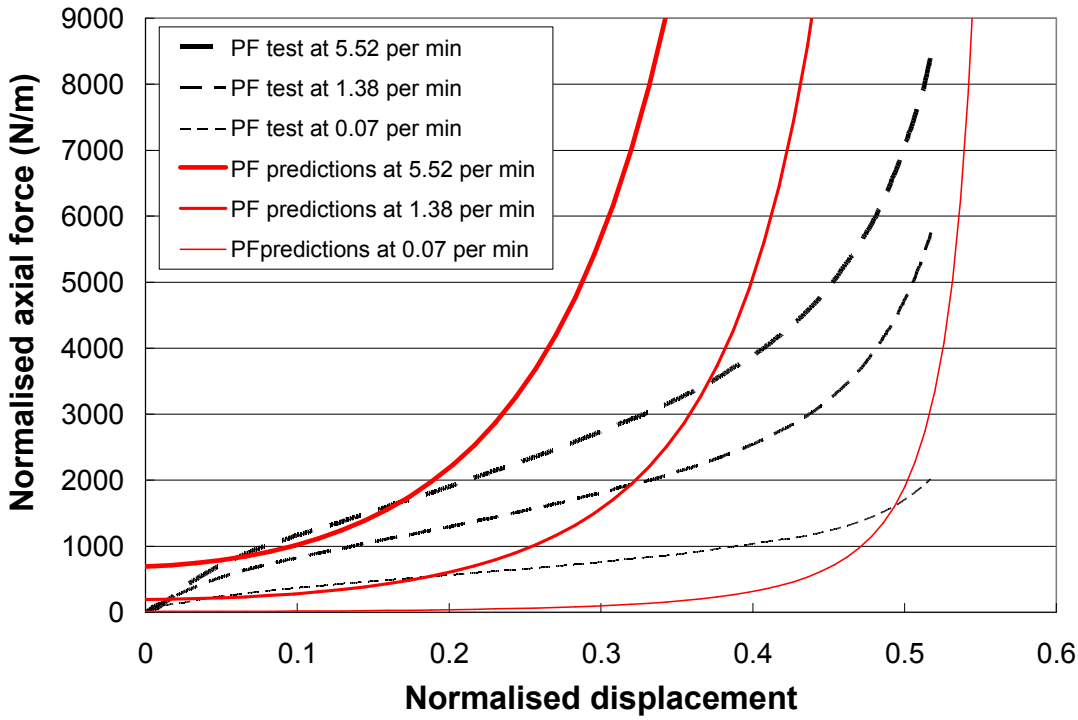

Figure 5.16. Comparisons between model predictions and experimental measurements at room temperature and 3 normalised displacement rates, 0.07, 1.38 and 1.74 min^{-1} for HexPly® M21 UD prepregs in picture frame tests.

5.8 Evaluation of shear model using bias-extension tests

The Bias Extension (BE) test is another popular method of characterising the in-plane shear properties of composites. It has some advantages compared with the picture frame test [20], such as less vulnerable to boundary conditions due to tension in the fibre direction. The detailed description of a bias extension test was reported in Section 2.3.3. The MSEM was originally developed to predict the shear behaviour of composite sheets, as induced by picture frame tests. In order for the model to predict BE results, a normalisation technique is adopted from [20]. Model predictions are based on the procedure described in Section 5.5. The highest force curve was chosen for each displacement rate to represent

test results as inter-tow slippage may give an underestimation. Figure 5.17 shows comparisons between model predictions and experimental measurements at various rates. The observations are almost the same as those in Section 5.5 except that the difference between model predictions and measurements decreases as the rate increases. This might be due to the fact that at higher rates higher shear energy dissipation would be required such that tows tend to slip, according to the minimum energy approach. Figure 5.17 also shows that the difference between model predictions and measurements is larger comparing to Figure 5.14. This is believed to be due to inter-tow slippage.

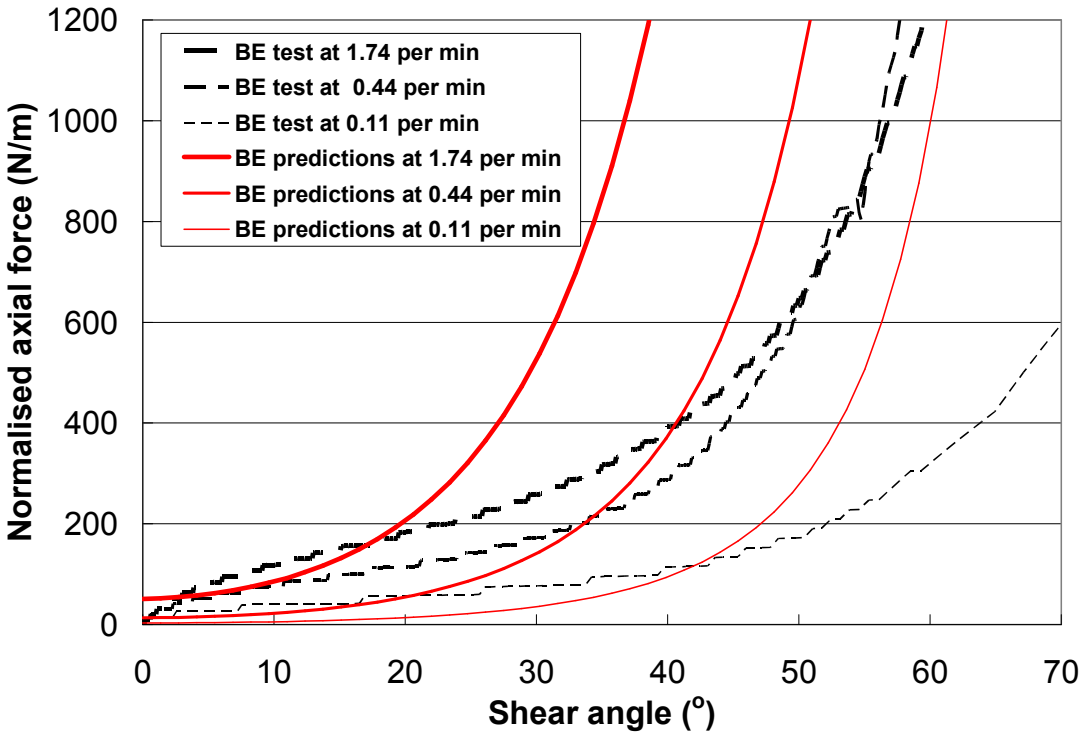

Figure 5.17. Comparisons between model predictions and experimental BE measurements for automotive prepreg at room temperature and 3 normalised displacement rates, 0.11, 0.44 and 1.74 min^{-1} for automotive prepregs in bias extension tests. Model predictions are based on the tow-kinematics model, New-LV and TV models, and matrix rheology data for HexPly® M47 in Table 2.1.

5.9 Conclusions

The in-plane shear behaviour of viscous polymer composites was studied in this chapter using both experimental tests and theoretical modelling. The picture frame and bias extension tests are widely used methods. However, these methods are not yet standardised within the composites community. In order to obtain more reliable data, some experimental and material aspects were investigated, such as boundary conditions and reproducibility of experiments, tow-meander and prepreg aging effects. A clamped boundary condition was suggested for a thermoset prepreg in picture frame tests, in contrast with a pinned condition for a thermoplastic prepreg from the literature [20]. Even under this condition, relatively poor reproducibility of the experimental method was observed. Investigation of tow-meander in the automotive prepreg suggested that test specimens should be straightened prior to testing in order to obtain more repeatable and reliable measurements, for both shear and formability characterisation experiments. Aging effects due to curing of the epoxy resin are unavoidable. Experimental measurements revealed that aging has a significant impact on the shear behaviour and suggested that for obtaining comparable measurements specimens should be taken from the same batch possessing exactly the same aging history. Investigation on the influence of direction of shearing deformation showed a negligible effect for the automotive prepreg within the experimental variability, in contrast with more significant effect suggested in the literature for some dry fabrics [22]. Relaxation tests on the automotive prepreg using picture frame tests suggested that the elastic contribution during in-plane shearing is

negligible, which justifies development of a shear model based on resin rheological behaviour.

On the modelling side, the current work builds on the multi-scale energy model, MSEM, developed by Harrison [19]. A complementary model, the tow-kinematics model (TKM), was developed using an energy minimisation approach. It was based on pure in-plane shear energy dissipated in crossover, tow and inter-tow regions; effects of squeeze flow have not yet been considered. The TKM has been implemented successfully in the MSEM, and validated using experimental measurements made on formed hemispheres, which suggested that the longitudinal viscosity (LV) model could be the key to improving predictive capability of the TKM and LV may be a function of the shear angle.

Comparisons between model predictions and experimental measurements from picture frame tests for the automotive prepreg showed that the shear model based on the TKM was rate-dependent and disagreed with experimental data, which suggests that the LV may be underestimated and effects of locking angle and the squeeze flow should be considered. Comparisons of experimental picture frame test results for prepregs with different weave styles showed a measurable effect. However, a sensitivity study of the MSEM on weave pattern showed a negligible effect, suggesting that the effect of weave pattern has not yet been modelled accurately. The shear model initially developed for woven composites from the literature was modified to predict the shear behaviour for unidirectional (UD) prepregs. Disagreement between model predictions and

experimental measurements from picture frame tests for HexPly® M21 UD prepregs was found again, suggesting that LV and TV models could be a function of the shear angle. Evaluation of the shear model using bias extension tests suggested that the effect of inter-tow slippage may be significant.

Chapter 6 Discussion and conclusions

6.1 Introduction

The work presented in this thesis is concerned with the deformation behaviour of viscous polymer composites during forming into complex shapes. In order for forming simulations to be accurate and to be useful for design optimisation of composites structures, fundamental deformation mechanisms must be understood and advanced material models are required. These predictive models can then be employed and incorporated into finite element simulations for composites forming. Simulations of formed components can be analysed as to the importance of the various deformation mechanisms to decide which material parameters are most important. For instance, the bending behaviour may be negligible at some process conditions, and so could be ignored to save computational effort. In this thesis, experimental validation was performed for each stage of model development.

6.2 Discussion

6.2.1 Micro-mechanical modelling

Micro-mechanical modelling of fibre-matrix-fibre interaction was attempted to predict the rheological behaviour for viscous unidirectional polymer composites during shearing along and transverse to the fibre direction, i.e. longitudinal and transverse viscosities. This is the fundamental deformation behaviour at a micro level during composites forming. These micro-scale composite viscosity models served as input parameters for forming behaviour

models at larger scales, in particular at meso-scale (tow/yarn level), as implemented in the bending and shear models. The accuracy of the bending and shear models relies on the composite viscosity models, emphasizing the importance of the work. The LV and TV models were developed based on a number of assumptions, such as material incompressibility, fibre inextensibility, and hexagonal fibre packing. When the models were applied to practical situations, some model assumptions may become influential. Using fibre packing as an example, composites with different weave patterns may have different fibre arrangements within their tows, such as square, hexagonal, or a combination. The LV and TV models assume that hexagonal fibre packing persists during composites deformation, which is obviously a simplification. Also both models do not include a change of fibre packing during deformation, and this effect cannot be incorporated easily. In future this assumption could be treated as a material parameter for inputs in the models. Experimental validation of the models showed that TV model predictions were in good agreement with measurements collected from the literature, but slight underestimation of LV model predictions was observed. The difference is partially due to the differences between model predictions and experimental measurements in material constituents, material geometries, such as fibre diameter and packing. The causes were also thought to be due to non-ideal fibre arrangements, such as fibre entanglement, twisting and misalignment, in which effects of fibre type and stiffness would become highly prominent. Therefore, application of knowledge on modelling of dry fabrics to this issue is believed to be helpful and may be used to model effectively the elastic contributions.

6.2.2 Bending behaviour study

A 3-point bending test has been used widely to measure flexural properties and has been standardised for numerous solid materials but not for viscous fibre-reinforced composites. In 3-point tests a very thin and flexible specimen may bend under its own weight and may not adopt the same shape as fibres bent in a double-curvature component. Among the textiles community, two measurement systems, Kawabata Evaluation System (KES) and Fabric Assurance by Simple Testing (FAST), are used widely for experimental characterisations. However, a continuous stress-strain relationship cannot be obtained from such systems; neither can various rates and temperatures be applied easily. Therefore, a large-displacement buckling test was developed to characterise bending behaviour. Moreover, the buckling test is currently thought to be a good avenue to study the buckling behaviour and the onset of wrinkling during forming. Further efforts, though, are required to standardise the test method.

The rate and temperature dependence, which are major characteristic properties of viscous polymer composites, was successfully measured by the buckling test. The bending resistance at room temperature for two unidirectional prepregs was found to be linearly dependent on the rate, while it was reduced significantly at higher temperatures. This stresses the importance of rheological behaviour of resin flow between fibres during bending deformation. Reproducibility of the test method was poor and was found to depend on the rate and material type, which highlights the need to standardise the test

procedure. To improve reproducibility, optimum specimen dimensions should be used and different dimensions may be appropriate for different rates and temperatures.

A material model was developed to predict the bending behaviour for viscous polymer composites, and was validated using experimental measurements from buckling and 3-point tests in terms of the rate dependence and fibre orientations. The bending model was comprised of two stages of deformation, pre-buckling and post-buckling. Elastic deformation was thought to be the main mechanism at the pre-buckling stage ('elastic buckling'), while viscous shear deformation was focused on at the post-buckling stage ('plastic buckling'). The pre-buckling stage is believed to be important for study of wrinkling formation, whereas the post-buckling phase would currently be of more interest for the bending behaviour during composites forming. As such, the bending model and its validation concentrated on the post-buckling stage. Micro-mechanical LV and TV models discussed in the preceding section were two essential input parameters for this bending model, and dominated the accuracy of model predictions. The bending model with the LV model underestimated experimental measurements for unidirectional prepregs at all rates, but was capable of capturing the trend of the rate-dependent behaviour. The causes may be attributed to underestimation of the LV and negligence of effects of micro-buckling which was observed on micro-images. Micro-buckling could cause fibre re-arrangement locally during bending and subsequently affect the local fibre volume fraction and the LV. Thus, a micro-buckling model should be considered in the bending model. Experimental

validation of effects of fibre orientations showed poor agreement, suggesting that the ratio of LV to TV should be greater than 1. This once again emphasizes the importance of developing accurate composite viscosity models.

6.2.3 Shear behaviour study

To date no internationally-accepted standard test has been established for characterising the shear behaviour of viscous polymer composites. Within the composites community, picture frame and bias extension tests are preferred, due to simplicity of experimental setup, low cost, wide availability and more importantly existence of a region of pure and uniform shear. In this thesis, experimental work which concentrated on picture frame tests may contribute towards efforts of standardisation of the shear characterisation method, and was used to validate a viscous shear model. A standard test procedure would specify the boundary condition (clamped or pinned) for different materials to induce pure and uniform shear, and specify an appropriate way for specimen handling prior to testing to reduce uncertainty due to material variability. A systematic study on a number of groups of materials (different weave patterns and matrix resins) on various test conditions would be constructive for the standardisation process. In the present study, experimental measurements show that shear resistance increases with increasing the shear rate, whereas it decreases significantly when the temperature is increased to 60^{o}C. It was observed that measurements at 80, 110 and 150^{o}C are similar to those at 60^{o}C.

A tow-kinematics model (TKM) based on an energy minimisation method was developed to predict the shear profile within and between tows for a viscous

composite, which is a complementary model to a shear model (the multi-scale energy model, MSEM) adapted from the literature. Validation of the TKM using experimental measurements on formed hemispheres suggested that the LV was the key to accuracy, which echoes the suggestions from the bending study. As deformation was assumed to be in-plane, only in-plane shear energy contributions were considered in the energy minimisation approach. However, transverse shear of tows through the thickness (equivalent to tow squeezing) may make some contributions to the total energy. Also tow squeezing would reduce the width of tows, which could change the in-plane kinematics of tows and consequently the shear profile across the material. This may explain why the tow shear starts to increase at a certain material shear angle (about 45^{o} observed from measurements).

The TKM was implemented successfully into the MSEM and shear predictions were made for viscous composites, and validated using experimental results obtained from picture frame and bias extension tests for different materials, at various rates and temperatures. The shear model is currently not able to make predictions for materials with different weave patterns. It was suggested that the TKM may play an important role in energy contributions from different regions, as the TKM determines the shear strain distribution and hence energy dissipation due to the different deformation mechanisms. Experimental validation of the shear model also suggested that the composite viscosities could be a function of the material shear angle. During shearing, the fibre gap and arrangement of tows change with material shear angle. This suggests that the LV and TV models must be re-derived to accommodate fibre re-orientation

during shearing. Poor agreement on temperature dependence led to speculations that deformation mechanisms at elevated temperatures during in-plane shear may be different from those at room temperature, with the polymer possibly behaving like a lubricant at higher temperature so that its rheological behaviour is no longer dominant. At this point studies on modelling of dry fabrics and lubrication theory might be relevant.

6.3 Major conclusions

This section summarises the significant conclusions drawn from this study.

1. Longitudinal and transverse viscosity models, fibre-matrix-fibre micro-mechanical interaction behaviour at the micro-scale (fibre level), accounting for the shear flow behaviour along and perpendicular to the fibre directions, were developed. Experimental validation showed that the transverse viscosity model predictions lay well within experimental measurements collected from the literature, whereas longitudinal viscosity model predictions were slightly below experimental measurements.

2. A large-displacement buckling test was proposed to characterise the out-of-plane bending deformation of polymer composites, showing some advantages over other methods, such as simplicity of set-up and the ability to measure rate and temperature dependence. Experimental observations showed that the bending shape was a cosine curve, and the bending behaviour was viscoelastic.

3. A simple bending model, based on the ideal fibre-reinforced model (IFRM) and elastica theory, was developed to facilitate further understanding of the bending behaviour of viscous composites during forming. Validation using experimental measurements showed that the

shape of buckling curves was captured, whereas artificial factors were used in order for the force magnitude to be matched. It was proposed that a simple micro-buckling model might account for local changes of fibre arrangement and volume fraction and hence longitudinal viscosity during bending, whereas predicting the longitudinal viscosity accurately was believed to be the key to improving the model efficiently.

4. Experimental evaluations using both the buckling test and the standard 3-point bending test showed that the bending model could capture reasonably the rate-dependent behaviour, if artificial factors were allowed. However, the model was unable to predict the effect of fibre orientations.

5. Experimental investigations using a picture frame test suggested that a clamped boundary condition rather than a pinned condition should be used for thermoset prepreg, and the test specimen should be straightened prior to testing to reduce the degree of tow-meander such that measurements are more repeatable and reliable, for both shear and formability characterisation experiments. Aging history of curing epoxy resin was shown to be important, especially when obtaining comparable measurements. Influence of direction of the shearing deformation was found to be negligible for the prepreg used.

6. The predictive capability of the multi-scale energy model was improved by incorporating a tow-kinematics model. This was developed based on an energy minimisation method to predict the heterogeneous shear profile which was previously obtained from experimental measurements. Evaluation using measurements from formed hemispheres suggested that predicting accurately the longitudinal viscosity could be the key to improving the tow-kinematics model.

7. Whilst the combined tow kinematics and shear model could accurately predict the shape of the picture-frame shear force curve, relatively poor agreement was found from experimental validation on the effect of rate,

temperature and weave pattern on shear force. The causes were discussed in detail in Chapter 5.

6.4 Recommendations for future work

From the major conclusions presented in the preceding section, additional investigations in a number of areas would be beneficial. A summary of these is presented below.

In terms of the composite (longitudinal and transverse) viscosities, future work could include the following.

1. Both longitudinal and transverse viscosity models were developed by assuming that all the deformation mechanisms are due to viscous shear, i.e. ignoring elastic mechanisms. However, some experimental findings showed non-linear viscoelasticity for some polymer composites. Validation of this assumption would be beneficial. In addition more accurate fibre packing models might be required to account for complex (realistic) fibre orientations. A statistical factor may be considered to account for non-uniform fibre distribution across the composite cross-section, incorporating resin-rich regions and irregular fibre packing (square, hexagonal or combinations).
2. As rheological behaviour of most polymers in composites is non-Newtonian, predictive capability of the composite models for non-Newtonian fibre-reinforced fluids is desired in order to capture accurately rate and temperature dependence. In practice, some fibres might come into contact during composites shear deformation. In this case dry fibre-to-fibre friction should be considered. The composite viscosity models should be re-derived to capture the actual micro-mechanical behaviour during shearing of viscous composites, so as to

improve the shear and tow-kinematics models. The composite viscosity is likely to be a function of the material shear angle, and this should be considered within future studies.

3. For some complex weave architectures, the composite viscosity model may need to be modified to account for tension, compression, bending and torsion of fibres due to non-ideal arrangement of fibres within a composite, such as fibre entanglement, misalignment, twisting and bending. Further understanding of the ratio of TV to LV is crucial. Development of a mathematical relationship linking TV and LV based on material parameters may be useful.
4. Investigation of effects of fibre diameter could be helpful in understanding the discrepancy between developed models and experimental results. A benchmarking characterisation programme is needed to clarify the discrepancies between test methods. A more accurate test method should be developed by investigating experimental aspects, such as end effects, sample shape and dimensions, and elimination of slipping between the specimen and platens (no-slip conditions).

Recommendations for future research on study of the bending behaviour of viscous polymer composites are listed as follows.

1. It is necessary to investigate effects of boundary conditions and to explore what clamping conditions may be most appropriate.
2. Elastic behaviour during plastic buckling has not yet been considered, which could make a significant contribution to the force magnitude. It may be necessary to investigate whether sample weight contributes to bending behaviour of viscous composites. This has been proven to be important in modelling of deformation for dry textiles. An energy minimisation approach could be used to predict the transition region in

buckling curves where it is a mixture of elastic deformation of fibres and shearing of matrix resin.

3. To develop a bending model for woven composites, the tows may be modelled as UD composites, similarly to the shear model described in this thesis. During deformation, mechanisms in woven composites may be different from those in UD composites due to factors such as tow crimp and interactions at crossovers.
4. Wrinkling formation through fibre/tow buckling might be studied based on the buckling test and the bending model.

Future work on the shear behaviour of viscous polymer composites is identified below.

1. Further investigation on the test methods (picture frame and bias extension) is constructive in order to establish a standard test procedure for characterising the in-plane shear behaviour of viscous polymer composites at both room and elevated temperatures. Effects of boundary conditions (clamping mechanisms) may need to be considered in the shear model, if experimental measurements are used for validation.
2. Effects of transverse shear of tows (tow squeezing) on the tow-kinematics models have not yet been considered, which may influence energy dissipation in the model and more profoundly affect the in-plane geometry of tows. Effects of tow locking on squeeze flow might need to take into account, as this influences the shear strain profile at high shear angles and hence the rate of deformation tensor and the tow-kinematics model.
3. Further understanding of the actual deformation mechanisms and fibre-fibre micro-mechanical interactions for polymer composites during in-plane shear at elevated temperatures is required. Lubrication theory

may be employed to model the flow behaviour of polymer melts and studies on shear modelling of dry textiles may be relevant.

4. The modelling of inter-tow region and the assumed tow paths should be re-considered so that the shear model can make more accurate predictions for different weave patterns.
5. Effects of material variability on material structure, geometry and local fibre volume fraction may need to be considered in the shear model, which could allow the distribution in shear force data to be predicted. This would allow the influence of variability in each of the input parameters to be established, thus informing materials design.

References

1. Kelly, A. Concise encyclopaedia of composite materials. 1994, Oxford: Pergamon Press.
2. Chawla, K.K., *Reinforcements*. Composite Materials: Science and Engineering, ed. K.K. Chawla. 1998, New York: Springer-Verlag.
3. Matthews, F.L. and R.D. Rawlings, *Composite Material: Engineering and Science*. 1994, Oxford: Chapman & Hall.
4. http://www.hexcel.com/NR/rdonlyres/230A6C2A-FDFA-4EC7-B048-E4EB28E3BC8C/0/PrepregTechnology1.pdf, *Hexcel Composites.* Last accessed: 13th December, 2007.
5. http://www.fibrecote.com/pabo6.html, Last accessed: March, 2006.
6. http://www.c2-composites.demon.co.uk/frames/manufacture.htm, *C2 Composites, Devon, UK.* Last accessed: 13th December, 2007.
7. Wakeman, M.D. and J.-A.E. Manson, *Chapter 6: Composites manufacturing - thermoplastics*. Design and manufacture of textile composites, ed. A.C. Long. 2005, Cambridge: Woodhead Publishing Limited.
8. http://www.tech.plym.ac.uk/sme/MATS324, *Faculty of Technology, University of Plymouth.* Last accessed: 13th December, 2007.
9. Chun, H.J., K.S. Ryu, and H.J. Byun, *Predictions of elastic properties of multiaxial warp knitted fabric composites.* Key Engineering Materials, 2004. **261-263**: p. 1499-1504.
10. Sutcliffe, M.P.F., et al. *A comparison of Simulation Approaches For Forming of Textile Composites*. in *5th International ESAFORM Conference on Materials Forming*. 15-17th April 2002. Krakow, Poland, P.311-314.
11. Harrison, P. and M.J. Clifford, *Rheological behaviour of pre-impregnated textile composites*. Design and manufacture of textile composites, ed. A.C. Long. 2005, New York: CRC Press.
12. http://www.hexcel.com/NR/rdonlyres/B3F3476E-44CE-4B3C-ABF2-8E7F4C251778/0/HexPly_M47_eu.pdf, *Hexcel Composites.* Last accessed: 13th December, 2007.
13. http://www.hexcel.com/NR/rdonlyres/3656E480-DB4D-4AD8-B42E-BB4A766C18D1/0/HexPly_M21_us.pdf, *Hexcel Composites.* Last accessed: 13th December, 2007.
14. http://www.hexcel.com/NR/rdonlyres/9229D78D-51BC-4460-9248-CC256BC6B6A4/0/HexPly_8552.pdf, *Hexcel Composites.* Last accessed: 13th December, 2007.
15. http://www.torayusa.com/cfa/pdfs/T800SDataSheet.pdf, Last accessed: 13th December, 2007.
16. http://www.hexcel.com/NR/rdonlyres/5659C134-6C31-463F-B86B-4B62DA0930EB/0/HexTow_AS4.pdf, *Hexcel Composites.* Last accessed: 13th December, 2007.
17. Spoelstra, A.B., G.W.M. Peters, and H.E.H. Meijer, *Chemorheology of a Highly Filled Epoxy Compound.* Polymer Engineering and Science, 1996 **36** (16): p. 2153-2162.

18. http://www1.cems.umn.edu/courses/chen8102/Cox-Merz.pdf, *Department of Chemical Engineering and Materials Science, University of Minnesota.* Last accessed: May, 2005.
19. Harrison, P., et al., *A constituent-based predictive approach to modelling the rheology of viscous textile composites.* Composites: Part A, 2004. **35**: p. 915-931.
20. Harrison, P., M.J. Clifford, and A.C. Long, *Shear characterisation of viscous woven textile composites: a comparison between picture frame and bias extension experiments.* Composites Science and Technology, 2004. **64**: p. 1453-1465.
21. McGuiness, G.B. and C.M. O'Bradaigh, *Characterisation of thermoplastic composite melts in rhombus-shear: the picture frame experiment.* Composites: Part A, 1998. **29**(A): p. 115-132.
22. McGuiness, G.B. and C.M. O'Bradaigh, *Development of rheological models for forming flows and picture-frame shear testing of fabric reinforced thermoplastic sheets.* Journal of Non-Newtonian Fluid Mechanics, 1997. **73**: p. 1-28.
23. Boisse, P., B. Zouari, and A. Gasser, *A mesoscopic approach for the simulation of woven fibre composite forming.* Composites Science and Technology, 2005. **65**: p. 429-436.
24. Zhu, B., T.X. Yu, and X.M. Tao, *An experimental study of in-plane large shear deformation of woven fabric composite.* Composites Science and Technology, 2007. **67**: p. 252-261.
25. Wang, J., Harrison, P., Long, A.C. and Clifford, M.J. *Prediction and Characterisation of the Shear Behaviour of Viscous Woven Textile Composites*. in *The 8th International Conference on Flow Processes in Composite Materials (FPCM8)*. 2006. Douai, France.
26. Cao, J., et al. *A cooperative benchmark effort on testing of woven composites*. in *7th International ESAFORM Conference on Materials Forming*. 2004. Trondheim, Norway.
27. Lomov, S.V., T.Z. Stoilova, and I. Verpoest. *Shear of woven fabrics: Theoretical model, numerical experiments and full field strain measurements*. in *7th International ESAFORM Conference on Materials Forming*. 2004. Trondheim, Norway.
28. Gorczyca-Cole, J.L., J. Chen, and J. Cao, *Chapter 13: Benchmarking of composite forming modelling techniques*. Composites forming technologies, ed. A.C. Long. 2007, Cambridge: Woodhead Publishing Limited.
29. Potter, K., *Bias extension measurement on cross-plied unidirectional prepreg.* Composites: Part A, 2002. **33**: p. 63-73.
30. Dahlberg, B., *Part II: Buckling.* Journal of Textile Research, 1961: p. 94-99.
31. Crookston, J.J., *Prediction of elastic behaviour and initial failure of textile composites, Ph.D. Thesis*. 2004, University of Nottingham, UK.
32. Gil, R.G., *Forming and consolidation of textile composites, Ph.D. Thesis*. 2003, University of Nottingham, UK.
33. Spencer, A.J.M., *Deformation of Fibre-reinforced Materials*. 1972, Oxford: Clarendon Press.
34. Spencer, A.J.M., *Continuum theory for Strongly anisotropic solids*, in *CISM Courses and Lectures No. 282, Spinger-Verlag*. 1984: New York.

35. Rogers, T.G., *Rheological characterisation of anisotropic materials.* Composites, 1989. **20**(1): p. 21-27.
36. Leider, P. and R. Bird, *Squeeze flow between parallel disks. I: Theoretical analysis.* Ind. Eng. Chen. Fundarn., 1974. **13**(4): p. 336-341.
37. Advani, S.G. and E.M. Sozer, *Constitutive laws and their characterisation*. Processing Modelling in Composites Manufacturing, ed. S.G. Advani. 2002, New York: Marcel Dekker Incorporated.
38. Leider, P., *Squeeze flow between parallel disks. II: Experimental results.* Ind. Eng. Chen. Fundarn., 1974. **13**(4): p. 342-346.
39. Brindley, G., J. Davies, and K. Walters, *Elastico-viscous squeeze films. part 1.* JNNFM, 1976. **1**: p. 19-37.
40. Brindley, G., J. Davies, and K. Walters, *Elastico-viscous squeeze films. part 2, superimposed rotation.* JNNFM, 1976: p. 259-275.
41. Grimm, R., *Squeeze flows of polymeric liquids.* AIChE, 1978. **24**(3): p. 427-439.
42. Tadmor, Z. and C.G. Gogos, *Principles of Polymer Processing*. 1979, New York: John Wiley and Sons.
43. Shrodikar, P. and S. Middleman, *Lubrication flows in viscoelastic liquids. i. squeezing flow between approaching parallel rigid planes.* Rheology, 1982. **26**(1): p. 1-17.
44. McClelland, M. and B. Finlayson, *Squeezing flow of elastic liquids.* JNNFM, 1983. **13**: p. 181-201.
45. Phan-Thien, N. and R. Tanner, *Viscoelastic squeeze -film flows-Maxwell fluids.* Fluid Mech., 1983. **129**: p. 265-281.
46. McClelland, M. and B. Finlayson, *Squeezing flow of highly viscous polymers.* Rheology, 1988. **32**(2): p. 101-133.
47. Balasubramanyam, R., R.S. Jones, and A.B. Wheeler, *Modelling transverse flows of reinforced thermoplastic materials.* Composites, 1989. **20**(1): p. 33-37.
48. Barnes, J.A. and F.N. Coggwell, *Transverse flow processes in continuous fibre-reinforced thermoplastic composites.* Composites, 1989. **20**(1): p. 38-42.
49. Jones, R.S. and R.W. Roberts, *Ply re-orientation in compression.* Composites Manufacturing, 1991. **2**(3/4): p. 259-266.
50. Wheeler, A.B. and R.S. Jones, *Numerical simulation of fibre reorientation in the consolidation of a continuous fibre composite material.* Composites Manufacturing, 1995. **6**(3/4): p. 263-268.
51. Shuler, S.F. and S.G. Advani, *Transverse squeeze flow of concentrated aligned fibres in viscous fluids.* Non-Newtonian Fluid Mech., 1996. **65**: p. 47-74.
52. Wang, E.L. and T.G. Gutowski, *Laps and gaps in thermoplastic composites processing.* Composites Manufacturing, 1991. **2**: p. 30-39.
53. Goshawk, J.A., V.P. Navez, and R.S. Jones, *Squeezing flow of continuous fibre-reinforced composites.* Non-Newtonian Fluid Mech., 1997. **73**: p. 327-342.
54. Cogswell, F.N. and D.J. Groves. *The melt rheology of continuous fibre reinforced structural composite materials*. in *Xth International Congress on Rheology*. 1988. Sydney.

55. Scobbo, J.J. and N. Nakajima. *Dynamic mechanical analysis of molten thermoplastic/continuous graphite fibre composites in simple shear deformation*. in *21st International Society for the Advancement of Materials and Process Engineering (SAMPE-21) Technical Conference*. September, 1989. Atlantic city, New Jersey.
56. Groves, D.J., *A characterisation of shear flow in continuous fibre thermoplastic laminates.* Composites, 1989. **20**(1): p. 28-32.
57. Groves, D.J. and D.M. Stocks, *Rheology of thermoplastic-carbon fibre composite in the elastic and viscoelastic states.* Composites Manufacturing, 1991. **2**(3/4): p. 179-184.
58. Cogswell, F.N., *Thermoplastic Aromatic Polymer Composites*. 1992, Oxford: Butterworth-Heinemann Ltd.
59. Wheeler, A.B. and R.S. Jones, *A characterisation of anisotropic shear flow in continuous fibre composite materials.* Composites Manufacturing, 1991. **2**(3/4): p. 192-196.
60. Roberts, R.W. and R.S. Jones, *Rheological characterisation of continuous fibre composites in oscillatory shear flow.* Composites Manufacturing, 1995. **6**(3/4): p. 161-167.
61. Jones, R.S. and R.W. Roberts, *Anisotropic shear flow in continuous fibre composites.* Composites, 1994. **25**: p. 171-176.
62. Goshawk, J.A. and R.S. Jones, *Structure reorganization during the rheological characterisation of continuous fibre-reinforced composites in plane shear.* Composites: Part A, 1996. **27A**: p. 279-286.
63. Martin, T.A., D. Bhattacharyya, and I.F. Collins, *Bending of fibre-reinforced thermoplastic sheets.* Composites Manufacturing, 1995. **6**: p. 177-187.
64. Martin, T.A., et al., *Bending of Continuous Fibre-Reinforced Thermoplastic sheets*. Composite Sheet Forming, ed. D. Bhattacharyya, Pipes, S.G. 1997, Amsterdam: Elsevier.
65. Mander, S.J., *Roll forming of fibre reinforced thermoplastic composites, Ph.D. Thesis*. 1998, University of Auckland: New Zealand.
66. Dykes, R.J., T.A. Martin, and D. Bhattacharyya, *Determination of longitudinal and transverse shear behaviour of continuous fibre-reinforced composites from vee-bending.* Composites: Part A, 1998. **29**(A): p. 39-49.
67. Christensen, R.M., *Effective viscous flow properties for fibre suspensions under concentrated conditions.* Journal of Rheology, 1993. **37**(1): p. 103-121.
68. Coffin, D.W., R.B. Pipes, and P. Simacek, *First-order approximations for the effective shearing viscosities of continuous-fiber suspensions.* Journal of Composite Materials, 1995. **29**(9): p. 1180-1196.
69. Binding, D.M., *Capillary and contraction flow of long-(glass) fibre filled polypropylene.* Composites Manufacturing, 1991. **2**(3-4): p. 243-252.
70. Pipes, R.B., *Anisotropic viscosities of an orientated fibre composite with a power law matrix.* Composite Materials, 1992. **26**(10): p. 1536-1552.
71. Quemada, D., *Rheology of conce trated disperse systems and minimum energy dissipation principle.* Rheol Acta, 1977. **16**: p. 82-94.

72. Kitano, T., T. Karaoka, and T. Shirota, *An empirical equation of the relative viscosity of polymer melts filled with various inorganic fillers.* Rheol Acta, 1981. **20**: p. 207-209.
73. Metzner, A.B., *Rheology of suspensions in polymeric liquids.* Rheology, 1985. **29**: p. 739-775.
74. Groves, D.J., A.M. Bellamy, and D.M. Stocks, *Anisotropic rheology of continuous fibre thermoplastic composites.* Composites 1992. **23**(2): p. 75-80.
75. Cogswell, F.N., *The experience of thermoplastic structural composites during processing.* Composites Manufacturing, 1991. **2**(3/4): p. 208-216.
76. Sengupta, P.K. and D. Mukhopadhyay, *Dynamical mechanically study on unidirectional carbon fibre-reinforced polypropylene composites.* Applied Polymer Science, 1994. **51**: p. 831-840.
77. Stanley, W.F. and P.J. Mallon, *Intraply shear characterisation of a fibre reinforced thermoplastic composite.* Composites: Part A, 2006. **37**: p. 939-948.
78. Pipes, R.B., et al., *A Constitutive Relation for the Viscous Flow of an Oriented Fibre Assembly.* Composite Materials, 1991. **25**: p. 1204-1217.
79. Dienes, G. and H. Klemm, *Theory and application of the parallel plate plastometer.* Applied Physics, 1946. **17**: p. 459-471.
80. Oka, S., *Chapter 2*. Rheology, ed. F.R. Eirch. 1960, New York: Academic Press.
81. Harrison, P., T. Haylock, and A.C. Long. *Measurement of the Transverse and Axial Viscosities of Continuous Fibre Reinforced Composites*. in *8th International ESAFORM Conference on Materials Forming*. 2005. Cluj-Napoca, Romania.
82. Harrison, P., Haylock, T. and Long, A.C. *Measurement of the Transverse and Axial Viscosities of Continuous Fibre Reinforced Composites*. in *8th International ESAFORM Conference on Materials Forming*. 2005. Cluj-Napoca, Romania.
83. Groves, D.J., A.M. Bellamy, and D.M. Stocks. *Isotropic and anisotropic shear flow in continuous fibre thermoplastic composites*. in *Proc. 3rd European Rheology Conference*. 3-7th September 1990. Edinburgh.
84. Walters, K., *Rheometry*. 1975: Chapman and Hall. pp 125-127.
85. Long, A.C., et al., *Characterizing the processing and performance of aligned reinforcements during preform manufacture.* Composites: Part A, 1996. **27**(A): p. 247-253.
86. Long, A.C., et al. *Experimental analysis of fabric deformation during forming of textile composites*. in *5th International ESAFORM Conference on Materials Forming*. 2002. Krakow, Poland.
87. Wang, J., et al. *Energy Analysis of Reinforcement deformations during Viscous Textile Composite Forming*. in *10th International ESAFORM Conference on Materials Forming*. 2007. Zaragoza, Spain.
88. Young, M. and R. Paton. *Diaphragm forming of resin pre-impregnated woven carbon fibre materials*. in *IMEA Conference*. 23-26 September 2001. Melbourne, Australia: Institute of Engineering Materials.

89. Abbott, N.J., *The measurement of stiffness in textile fabrics.* Journal of Textile Research, 1951. **21**: p. 435-444.
90. Livesey, R.G. and J.D. Owen, *Cloth stiffness and hysteresis in bending.* J. Textile Inst., 1964. **55**: p. T516-T530.
91. Grosberg, P. and G.M. Abbott, *Measurement of fabric stiffness and hysteresis in bending.* Journal of Textile Research, 1966. **36**: p. 928-930.
92. Zhou, N. and T.K. Ghosh, *On-line measurement of fabric bending behaviour --Part III: dynamic considerations and experimental implementation.* Journal of Textile Research, 1999. **69**(3): p. 176-184.
93. Shi, F., J. Hu, and T. Yu, *Modeling the creasing properties of woven fabrics.* Journal of Textile Research, 2000. **70**(3): p. 247-255.
94. Hu, J. and S. Chung, *Bending behaviour of woven fabrics with vertical seams.* Journal of Textile Research, 2000. **70**(2): p. 148-153.
95. Kawabata, S., *The standardisation and analysis of hand evaluation*. 2nd ed. 1986, Osaka, Japan: The Textile Machinery Society of Japan.
96. *Instructional Manual for Fabric Assurance by Simple Testing*. 1990: CSIRO Division of Wool Technology, Australia.
97. Mahar, T.J., R.C. Dhinggra, and R. Postle, *Measuring and interpreting low stress mechanical and surface properties, Part 1: precision of measurement.* Journal of Textile Research, 1987. **57**(6): p. 357-369.
98. Peirce, F.T., *The 'handle' of cloth as a measurable quantity.* Journal of Textile Institute, 1930. **21**: p. T377-416.
99. Eeg-Olofsson, T., *Some mechanical properties of visous rayon fabrics.* Journal of Textile Institute, 1959. **50**: p. T112-132.
100. Livesey, R.G. and J.D. Owen, *Cloth stiffness and hysteresis in bending.* Journal of Textile Institute, 1964. **55**(10): p. T516-530.
101. Owen, J.D., *An automatic cloth-bending-hyteresis tester and some of its applications.* Journal of Textile Institute, 1966. **57**(9): p. T435-438.
102. Abbott, N.J. and P. Grosberg, *Measurement of fabric stiffness and hysteresis in bending.* Journal of Textile Research, 1966. **36**(10): p. 928-930.
103. Owen, J.D., *An improved manually operated cloth-bending hysteresis tester.* Journal of Textile Institute, 1967. **58**(11): p. 589-591.
104. Isshi, T., *Bending tester for fibres, yarns and fabrics.* Journal of Textile Machinery Society of Japan, 1957. **3**(2): p. 48-52.
105. *Textiles-Yarns, Fabrics, General Test Methods*, in *ASTM Annual Book of Standard, 1987, Vol. 07.01*
106. *Shirley Developments Catalogue No. 6*. 1991: Shirley Developments Ltd, Manchester, UK.
107. Stuart, I.M. and K. Baird, *A new test for bending length.* Journal of Textile Research, 1966. **36**(1): p. 91-93.
108. Cassidy, T., et al., *The stiffness of knitted fabrics: a new approach to the measurement of bending Part 1: development.* International Journal of Clothing Science and Technology, 1991. **3**(5): p. 14-19.
109. Banks, R., et al., *Development of a new structural prepreg: characterisation of handling, drape and tack properties.* Composite Structures, 2004. **66**: p. 169-174.

110. Fenner, R.T., *Instability and the Buckling of Struts and Columns*. Mechanics of Solids, ed. R.T. Fenner. 1993, Florida: CRC Press.
111. Berthelot, J.-M., *Buckling of Laminate or Sandwich Beams and Plates*. Composite materials: mechanical behaviour and structural analysis, ed. F.F. Ling. 1998: Springer-Verlag New York, Inc.
112. Kocik, M., et al., *Evaluating the Bending Rigidity of Flat Textiles with the Use of an Instron Tensile Tester.* FIBRES & TEXTILES in Eastern Europe, April/June 2005. **13**(No. 2(50)): p. 31-34.
113. Lahey, T.J. and G.R. Heppler, *Mechanical modelling of fabrics in bending.* Applied Mechanics, 2004. **71**: p. 32-40.
114. Grieber, M.T. and P.M. Taylor, *The bending behaviour of fabrics: An energy appoach.* Mathematics and Computers in Simulation, 1996. **41**: p. 579-586.
115. Choi, K.F. and S.K. Tandon, *An energy model of yarn bending.* Journal of Textile Institute, 2006. **97**(1): p. 49-56.
116. Realff, M.L., M.C. Boyce, and S. Backer, *A micromechanical model of the tensile behaviour of woven fabric.* Journal of Textile Research, 1997. **67**(6): p. 445-459.
117. Cartwright, B.K., et al. *Some proposed experimental tests for use in finite element simulation of composite forming*. in *12th International Conference on Composite Materials (ICCM-12)*. 5-9th July, 1999. Paris, France.
118. Yu, W.R., et al., *Analysis of flexible bending behaviour of woven preform using non-orthogonal constitutive equation.* Composites: Part A, 2005. **36**: p. 839-850.
119. Clifford, M.J., *Column buckling experiment*, in *Structural Mechanics*. 1981, Department of civil and municipal engineering, University College London: London.
120. http://ddsdx.uthscsa.edu/dig/itdesc.html, *University of Texas Health Science Centre in San Antonio.* Last accessed: 17th August, 2008.
121. Hull, D. and T.W. Clyne, *Chapter 5: Elastic deformation of laminates*. An Introduction to Composite Materials, Second Edition. 1996: Cambridges University Press.
122. Long, A.C., *Chapter 1*. Design and manufacture of textile composites, ed. A.C. Long. 2005, Cambridge: Woodhead Publishing Limited.
123. Popper, P., *The effect of friction and fibre mobility on the bending and unbending behaviour of cotton structures, Ph.D. Thesis*. 1966, Massachusetts Institute of Technology, US.
124. Hull, B.D., T.G. Rogers, and A.J.M. Spencer, *Theoretical analysis of forming flows of continuous fibre resin systems.* Flow and Rheology in Composite Manufacturing, 1994: p. 203-256, Ch.10, Ed.Advani S.G.,Pipes R.B.,Elsevier,Amsterdam.
125. McGuinness, G.B. and C.M. O'Bradaigh, *Effect of perform shape on buckling of quasi-isotropic thermoplastic composite laminates during sheet forming.* Composites Manufacturing, 1995. **6**(3-4): p. 269-280.
126. Murtagh, A.M. and P.J. Mallon. *Shear characterisation of unidirectional and fabric reinforced thermoplastic composites for pressforming applications*. in *10th International Conference on Composite Materials (ICCM-10)*. August, 1995. Whistler,Canada.

127. Rogers, T.G., ed. *Shear characterisation and inelastic torsion of fibre reinforced materials*. Inelastic Deformation of Composite Materials, ed. G.J. Dvorak. 1990, Spinger-Verlag: New York.
128. Yu, X., L. Zhang, and Y.W. Mai. *Modelling and finite element treatment of intra-ply shearing of woven fabric*. in *International Manufacturing Conference in China (IMCC2000)*. 16-17th August, 2000. Hong Kong.
129. Spencer, A.J.M., *Theory of fabric-reinforced viscous fluid.* Composites: Part A, 2000. **30**: p. 1311-1321.
130. McGuinness, G.B., et al., *A picture frame intra-ply sheet forming of composite materials.* Proceedings of the ASME Materials Division, ASME 1995: p. 1107-1118.
131. Behre, B., *Mechanical Properties of Textile Fabrics Part I: Shearing.* Journal of Textile Research, 1961. **31**(2): p. 87-93.
132. Long, A.C. and C.D. Rudd, *Chapter 5: Fabric drape modelling and preform design*. Resin Transfer Moulding for Aerospace Structures, ed. T.M. Kruckenberg and R. Paton. 1998: Springer Publishing Limited.
133. Kawabata, S., M. Niwab, and H. Kawai, *The finite-deformation theory of plain-weave fabrics Part III: The shear-deformation theory.* Journal of Textile Institute, 1973. **64**(2): p. 61-85.
134. Hu, J. and Y. Zhang, *The KES shear test for fabrics.* Journal of Textile Research, 1997. **67**(9): p. 654-664.
135. Rudd, C.D., et al. Liquid Moulding Technologies. 1997, Cambridge: Woodhead Publishing Limited.
136. http://nwbenchmark.gtwebsolutions.com/index.php, Last accessed: 27th January, 2008.
137. Peng, X.Q., et al., *Experimental and numerical analysis on normalization of picture frame tests for composite materials.* Composites Science and Technology, 2004. **64**: p. 11-21.
138. Potter, K., *The influence of accurate stretch data for reinforcements on the production of complex structural mouldings. Part I: Deformation of aligned sheets and fabrics.* Composites, 1979. **10**: p. 161-167.
139. Spivak, S.M. and L.R.G. Treloar, *The behaviour of fabrics in shear. Part III: The relation between bias extension and simple shear.* Journal of Textile Research, 1968. **37**: p. 963-971.
140. Potter, K., *Influence of the detailed structure of two variants of non-crimped carbon fabric on the drape properties.* Advanced Composites Letters, 2002. **11**: p. 285-292.
141. Buckenham, P., *Bias-extension measurements on woven fabrics.* Journal of Textile Institute, 1997. **88**: p. 33-40.
142. McBride, T.M. and J. Chen, *Unit-cell geometry in plain-weave fabrics during shear deformation.* Composites Science and Technology, 1997. **57**: p. 345-351.
143. Chen, J., et al., *Materials characterization methods and material models for stamping of plain woven composites.* International Journal of Forming Processes, 2001. **4**: p. 269-283.
144. Skelton, J., *Fundamentals of Fabric Shear.* Journal of Textile Research, 1976: p. 862-869.
145. Blagdon, M., *Characterisation of fabric deformation mechanisms during preform manufacture*. 1998, University of Nottingham, UK.

146. Leaf, G.A.V. and K.H. Kandil, *The initial load-extension behaviour of plain-woven fabrics.* Journal of Textile Institute, 1980. **71**(1): p. 1-7.
147. Leaf, G.A.V. and A.M.F. Sheta, *The initial shear modulus of plain-woven fabrics.* Journal of Textile Institute, 1984. **75**(3): p. 157-163.
148. Leaf, G.A.V., Y. Chen, and X. Chen, *The initial bending behaviour of plain-woven fabrics.* Journal of Textile Institute, 1993. **84**(3): p. 419-428.
149. Souter, B.J., *Effect of fibre architecture on formability of textile performs, Ph.D. Thesis*. 2001, University of Nottingham, UK.
150. Wiggers, J., *Analysis of Textile Deformation during Preforming for Liquid Composites Moulding, Ph.D. Thesis*. 2007, University of Nottingham, UK.
151. Lomov, S.V. and I. Verpoest, *Model of shear of woven fabric and parametric description of shear resistance of glass woven reinforcements.* Composites Science and Technology, 2006. **66**(7-8): p. 919-933.
152. Christensen, R.M., *Mechanics of Composite Materials*. 1979, New York: John Wiley & Sons.
153. Milani, A.S., et al. *The effect of fibre misalignment on parameter determination using picture frame test*. in *14th International Conference on Composite Materials (ICCM)*. 14-18th July, 2003. San Diego, California.
154. Peng, X.Q. and J. Cao, *A continuum mechanics-based non-orthogonal constitutive model for woven composite fabrics.* Composites: Part A, 2005. **36**: p. 859-874.
155. Chang, S.H., S.B. Sharma, and M.P.F. Sutcliffe, *Microscopic investigation of tow geometry of a dry satin weave fabric during deformation.* Composites Science and Technology, 2003. **63**: p. 99-111.
156. Boisse, P., J.C. Gelin, and H. Sabhi, *Forming of Glass Fibre Fabrics into Complex Shapes - Experimental and Computational Aspects.* Annals of the CIRP, 1992. **41**: p. 327-330.
157. Launay, J., et al. *Experimental analysis of in plane shear behaviour of woven composite reinforcements. Influence of tensions.* in *10th International ESAFORM Conference on Materials Forming*. 2007. Zaragoza, Spain.
158. Willems, A., et al. *Picture frame shear tests on woven textile composite reinforcements with controlled pretension*. in *10th International ESAFORM Conference on Materials Forming*. 2007. Zaragoza, Spain.
159. Lussier, D.S., *Shear characterization of textile composite formability, Master's thesis*. 2002, University of Massachusetts at Lowell, USA.
160. Breuer, U.P., et al., *Deep drawing of fabric-reinforced thermoplastic: wrinkle formation and their reduction.* Polymer Composites, 1996. **17**(4): p. 643-647.
161. Lebrun, G., M.N. Bureau, and J. Denault, *Evaluation of bias-extension and picture-frame test methods for the measurement of intraply shear properties of PP/glass commingled fabrics.* Composite Structures, 2003. **61**: p. 341-352.
162. Skordos, A.A. and M.P.F. Sutcliffe. *Stochastic geometric properties of woven textiles*. in *47th AIAA/ASME/ASCE/AHS/ASC Structures, Structural Dynamics, and Materials Conference*. 2006. Newport, USA.

163. Chen, J., et al. *The relationship between materials characterization methods and material models for stamping of woven fabric/thermoplastic composites*. in *4th International ESAFORM Conference on Materials Forming*. 2001. Liege, Belgium.
164. Page, J. and J. Wang, *Prediction of shear force and an analysis of yarn slippage for a plain-weave carbon fabric in a bias extension state.* Composites Science and Technology, 2000. **60**: p. 977-986.
165. Rogers, T.G. and A.C. Pipkin, *Asysmetric relaxation and compliance matrices in linear viscoelasticity.* 1963, ZAMP. **14**: p. 334-343.
166. Harrison, P., et al., *Constitutive modelling of impregnated continuous fibre reinforced composites: a micro-mechanical approach.* Plast Rubber Compos, 2002. **31**(2): p. 76-86.
167. Spencer, A.J.M., *A theory of viscoplasticity for fabric-reinforced composites.* Journal of The Mechanics and Physics of Solids, 2001. **49**: p. 2667-2687.
168. Lin, H., et al. *An experimental investigation into the factors affecting the forming performance of thermoset prepreg*. in *9th International ESAFORM Conference on Materials Forming*. 2006. Glasgow, UK.
169. Harrison, P., et al., *Design Optimisation of Textile Composite Structures (DOTComp)*. Progress Report 5, 12th January 2005, University of Nottingham.
170. Prodromou, A.G. and J. Chen, *On the relationship between shear angle and wrinkling of textile composite preforms.* Composites: Part A, 1997. **28**(A): p. 491-503.
171. Liu, L., et al., *Two-dimensional macro-mechanics shear models of woven fabrics.* Composites: Part A, 2005. **36**(A): p. 105-114.
172. Long, A.C., et al., *Effects of fibre architecture on reinforcement fabric deformation.* Plastics, Rubber and Composites, 2002. **31**(2): p. 87.
173. Long, A.C., P. Boisse, and F. Robitaille, *Chapter 2: Mechanical analysis of textiles*. Design and manufacture of textile composites, ed. A.C. Long. 2005, Cambridge: Woodhead Publishing Limited.
174. Evans, P., *Investigation into the effect of a Segmented Blank Holder on the forming of a textile composite*. 2005, BEng Individual Project, University of Nottingham, UK.
175. Spencer, A.J.M., *Theory of invariants*. Continuum physics, ed. A.C. Eringen. 1971, New York: Academic Press. 240-253.
176. Zheng, Q.S., *Theory of representations for tensor functions.* Applied Mech Rev, 1994. **47**: p. 554-587.
177. Johnson, A.F., *Rheological model for the forming of fabric reinforced thermoplastic sheets.* Compos Manufactur, 1995. **6**: p. 153-160.

Appendix 1.A Publications arising from thesis

- Wang, J., Long, A.C. Clifford, M.J. and Lin, H. *Energy Analysis of Reinforcement deformations during Viscous Textile Composite Forming*. in *10th International ESAFORM Conference on Materials Forming*. 2007. Zaragoza, Spain.

- Lin, H., Wang, J., Long, A. C., Clifford, M.J. and Harrison, P., *Predictive modelling for optimization of textile composite forming.* Composites Science and Technology, 2007. **67**(15-16): p. 3242-3252.

- Wang, J., Harrison, P. Long, A.C. and Clifford, M.J. *Prediction and Characterisation of the Shear Behaviour of Viscous Woven Textile Composites*. in *The 8th International Conference on Flow Processes in Composite Materials (FPCM8)*. 2006. Douai, France.

- Wang, J., Lin, H., Long, A.C. Clifford, M.J. and Harrison, P. *Predictive modelling and experimental measurement of the bending behaviour of viscous textile composites*. in *9th International ESAFORM Conference on Materials Forming*. 2006. Glasgow, UK.

- P Harrison, W R Yu, J Wang, A C Long, M J Clifford. *A predictive approach to simulating the forming of viscous textile composite sheet*, Revue Européenne des Éléments Finis,v**14**, n6-7, 2005, p. 613-631.

- Harrison, P., Yu, W. R., Wang, J., Baillie, T., Long, A. C., and Clifford, M.J. *Numerical Evaluation of a Rate Dependent Model for Viscous Textile Composites*. in *15th International Conference on Composite Materials*. 2005. Durban, South Africa.

Appendix 3.A Review of uniaxial continuum theory

The formulations described in this section have been derived in much greater detail elsewhere [33-35]. All vector and tensor components are referred to a Cartesian coordinate system with position coordinates x_i (where i=1,2,3). For example, components of velocity $\boldsymbol{v}$ are denoted by v_i. The deformation and stress are described in this system. The usual repeated suffix summation convention applies whenever necessary. δ_{ij} denotes the Kronecker delta (unity when $i = j$, zero otherwise). The local fibre directions are denoted by unit vectors $\boldsymbol{a}$ ($\boldsymbol{x}$,t) and $\boldsymbol{b}$ ($\boldsymbol{x}$,t) for biaxial CFRCs but only $\boldsymbol{a}$ ($\boldsymbol{x}$,t) for unidirectional CFRCs. $\boldsymbol{a}$ ($\boldsymbol{x}$,t) and $\boldsymbol{b}$ ($\boldsymbol{x}$,t) are variable unless the fibre reinforcement is straight. Both of them vary both spatially and in time.

The continuum approach ignores any further micromechanics, although the microstructure dictates the directions $\boldsymbol{a}$ and $\boldsymbol{b}$. This implies that neither detailed considerations of the interactions between individual fibres and the matrix nor the relations of the mechanical properties between the composite and its constituents are considered.

The deformation of the fluid considered depends on the position $\boldsymbol{x}$ and time t, i.e. a function of position and time, and can be represented by

$$\mathbf{x} = \mathbf{x}(\mathbf{X},t) \quad \text{or} \quad x_i = x_i(X_R, t) \tag{3.A.1}$$

where $\mathbf{X}$ is the position vector with components X_R, i, R=1, 2, 3.

The definition of the rate of deformation tensor **D** (with components D_{ij}) in the component form is given by:

$$D_{ij} = \frac{1}{2}\left(\frac{\partial v_i}{\partial x_j} + \frac{\partial v_j}{\partial x_i} \right) \quad \textbf{(3.A.2)}$$

where v_i are the components of **v**(**x**,t) at position x_i.

The rate of change of $\boldsymbol{a}$ can be found from the material derivative:

$$\frac{Da_i}{Dt} = \frac{\partial a_i}{\partial t} + \frac{\partial a_i}{\partial x_j} \times \frac{\partial x_j}{\partial t} = \frac{\partial a_i}{\partial t} + v_j \frac{\partial a_i}{\partial x_j} = (\delta_{ij} - a_i a_j) a_k \frac{\partial v_j}{\partial x_k} \quad \textbf{(3.A.3)}$$

The rate of change of $\boldsymbol{b}$ has an analogous relation.

In general, there are two important assumptions used in obtaining solutions in order to simplify stress analysis problems, namely material incompressibility (kinematic constraint) and fibre inextensibility (deformation constraint). Theories based on these two approximations have been effective in analysing forming processes for uniaxial fibre-reinforced composites. The incompressibility condition yields:

$$D_{ii} = \frac{\partial v_i}{\partial x_i} = 0 \quad \textbf{(3.A.4)}$$

And the fibre inextensibility conditions give:

$$a_i a_j D_{ij} = a_i a_j \frac{\partial v_i}{\partial x_j} = 0 \quad \text{and} \quad b_i b_j D_{ij} = b_i b_j \frac{\partial v_i}{\partial x_j} = 0 \quad \textbf{(3.A.5)}$$

If the latter condition applies, then Equation (3.A.3) is re-written as:

$$\frac{Da_i}{Dt} = a_k \frac{\partial v_i}{\partial x_k} \quad \textbf{(3.A.6)}$$

In quasi-static flows, the equilibrium equation

$$\frac{\partial \sigma_{ij}}{\partial x_j} = 0 \qquad \textbf{(3.A.7)}$$

holds, where σ_{ij} are the components of the stress tensor $\boldsymbol{\sigma}$.

For composite materials with two fibre directions , the stress tensor may be expressed as [35]:

$$\begin{aligned} \boldsymbol{\sigma} = \boldsymbol{\tau} &+ (\lambda\, \mathrm{tr}\mathbf{D} + \alpha_1\, \mathrm{tr}\mathbf{AD} + \alpha_2\, \mathrm{tr}\mathbf{BD} + \alpha_3\, \mathrm{tr}\mathbf{CD})\mathbf{I} \\ &+ (\alpha_1\, \mathrm{tr}\mathbf{D} + \beta_1\, \mathrm{tr}\mathbf{AD} + \beta_3\, \mathrm{tr}\mathbf{BD} + \beta_4\, \mathrm{tr}\mathbf{CD})\mathbf{A} \\ &+ (\alpha_2\, \mathrm{tr}\mathbf{D} + \beta_3\, \mathrm{tr}\mathbf{AD} + \beta_2\, \mathrm{tr}\mathbf{BD} + \beta_5\, \mathrm{tr}\mathbf{CD})\mathbf{B} \\ &+ (\alpha_3\, \mathrm{tr}\mathbf{D} + \beta_4\, \mathrm{tr}\mathbf{AD} + \beta_5\, \mathrm{tr}\mathbf{BD})\mathbf{C} \end{aligned} \qquad \textbf{(3.A.8)}$$

where λ, α_1, α_2, α_3, β_1, β_2, β_3, β_4, β_5 are model parameters; $\boldsymbol{\tau}$ is an extra stress tensor which requires another constitutive equation and will be discussed later; tr**D** and tr**AD**, for example, are the traces of **D** and **AD** respectively, with components:

$$\mathrm{tr}\mathbf{D} = D_{ii} \qquad \textbf{(3.A.9)}$$

$$\mathrm{tr}\mathbf{AD} = A_{ij}D_{ij} = a_i a_j D_{ij}$$

I denotes the unit tensor with components δ_{ij}; and **A**, **B** and **C** are the dyadic products defined as:

$$\mathbf{A} = \boldsymbol{a}\,\boldsymbol{a} \equiv \boldsymbol{a} \otimes \boldsymbol{a} \qquad \textbf{(3.A.10)}$$

$$\mathbf{B} = \boldsymbol{b}\,\boldsymbol{b} \equiv \boldsymbol{b} \otimes \boldsymbol{b}$$

$$\mathbf{C} = \boldsymbol{a} \otimes \boldsymbol{b} = \tfrac{1}{2}(\boldsymbol{a}\,\boldsymbol{b} + \boldsymbol{a}\,\boldsymbol{b})\,(\boldsymbol{a}.\boldsymbol{b})$$

with components:

$$A_{ij} = a_i a_j \qquad \textbf{(3.A.11)}$$

$$B_{ij} = b_i b_j$$

$$C_{ij} = 1/2\left(a_i b_j + a_j b_i\right) a_k b_k$$

The IFRM has more than nine model parameters, which would require a large number of experiments to determine. Hence, it is difficult to apply this model to practical examples, unless the two assumptions of incompressibility and fibre-inextensibility are made to simplify the model. Applying Equations (3.A.4) and (3.A.5), Equation (3.A.8) can then be simplified as:

$$\boldsymbol{\sigma} = \boldsymbol{\tau} - p\,\mathbf{I} + T_a \mathbf{A} + T_b \mathbf{B} \qquad \textbf{(3.A.12)}$$

where $-p$ is an arbitrary hydrostatic pressure by applying the incompressibility condition; T_a and T_b are arbitrary tensions in the fibre directions $\boldsymbol{a}$ and $\boldsymbol{b}$ respectively. These three terms are reaction stresses and do no work in any deformation conforming to the constraints. For uniaxial composites, the term $T_b \mathbf{B}$ is not needed.

To determine an appropriate form of $\boldsymbol{\tau}$ in the constitutive model, a physically-based assumption is generally made that $\boldsymbol{\tau}$ is a function of the rate of deformation tensor **D** and the fibre directions $\boldsymbol{a}$ and $\boldsymbol{b}$, i.e.:

$$\boldsymbol{\tau} = \boldsymbol{\tau}(\mathbf{D}, \boldsymbol{a}, \boldsymbol{b}) \qquad \textbf{(3.A.13)}$$

This relation must be form-invariant for rigid rotations, so $\boldsymbol{\tau}$ has to be an isotropic function of its arguments [129]. The solution of a tensor function of vectors and tensors can be directly obtained from tables [175, 176].

Composite materials can be treated as either a linear viscous fluid (analogous to Newtonian fluid) where $\boldsymbol{\tau}$ depends linearly on **D** or a non-linear viscous fluid. Although approximately linear viscous behaviour has been found in some unidirectional fibre-reinforced composites, others exhibit non-linearity. From tables of tensor functions and applying the constraints (3.A.4) and (3.A.5), for a viscous biaxial fibre-reinforced composite, the most general forms for $\boldsymbol{\tau}$ for the cases of linearity and non-linearity are shown in Equations (3.A.14) and (3.A.17) respectively [129].

$$\boldsymbol{\tau} = 2\eta\mathbf{D} + 2\eta_1(\mathbf{AD}+\mathbf{DA}) + 2\eta_2(\mathbf{BD}+\mathbf{DB}) + 2\eta_3(\mathbf{CD}+\mathbf{DC}^{\mathrm{T}}) + 2\eta_4(\mathbf{C}^{\mathrm{T}}\mathbf{D}+\mathbf{DC}) \tag{3.A.14}$$

where η , η_1 , η_2 , η_3 , η_4 are model parameters in which generally are functions of

$$a \cdot b = \cos 2\phi \tag{3.A.15}$$

2ϕ is the angle between the fibre directions, superscript T denotes the transpose.

The constraints (3.A.4) and (3.A.5) now can be re-written as:

$$\mathrm{tr}\mathbf{D} = 0, \quad \mathrm{tr}\mathbf{AD} = 0, \quad \mathrm{tr}\mathbf{BD} = 0 \tag{3.A.16}$$

$$\boldsymbol{\tau} = \psi_1\mathbf{D} + \psi_2\mathbf{D}^2 + \psi_3(\mathbf{AD}+\mathbf{DA}) + \psi_4(\mathbf{BD}+\mathbf{DB}) + \psi_5(\mathbf{CD}+\mathbf{DC}^{\mathrm{T}}) + \psi_6(\mathbf{C}^{\mathrm{T}}\mathbf{D}+\mathbf{DC}) + \psi_7(\mathbf{AD}^2+\mathbf{D}^2\mathbf{A}) + \psi_8(\mathbf{BD}^2+\mathbf{D}^2\mathbf{B}) \tag{3.A.17}$$

where the response functions $\psi_1,\ldots,\psi_8$ are functions of the invariants

$$\mathrm{tr}\mathbf{CD}, \quad \mathrm{tr}\mathbf{D}^2, \quad \mathrm{tr}\mathbf{AD}^2, \quad \mathrm{tr}\mathbf{BD}^2, \quad \mathrm{tr}\mathbf{CD}^2, \quad \cos 2\phi, \tag{3.A.18}$$

In the current study, we restrict to the linear form for $\boldsymbol{\tau}$. Even for the linear form, there are still 5 model parameters (functions of $\cos 2\phi$) needed to characterise the material. Any material symmetries will lead to simplify the form. Some special cases of Equation (3.A.14) have been discussed by Spencer [129]. One of them is:

$$\boldsymbol{\tau} = 2\eta \mathbf{D} + 2\eta_1 (\mathbf{AD} + \mathbf{DA} + \mathbf{BD} + \mathbf{DB}) + 2\eta_5 (\mathrm{tr}\mathbf{CD})(\mathbf{C} + \mathbf{C}^{\mathrm{T}}) \quad \textbf{(3.A.19)}$$

Rogers [35], Johnson [177] and McGuiness [22] derived analogous forms which require three material parameters. A convenient and intrinsic form was proposed by Rogers [35]:

$$\boldsymbol{\tau} = 2\eta_T \mathbf{D} + 2(\eta_L - \eta_T)(\mathbf{AD} + \mathbf{DA}) \quad \textbf{(3.A.20)}$$

This is a three-dimensional linear form for the extra stress tensor for viscous uniaxial CFRC. Now only two model parameters, η_L and η_T, appear in the model. These are the composite viscosities of the viscous composite, named longitudinal (LV) and transverse (TV) viscosity respectively, which were studied in Chapter 3.

Appendix 4.A: Determination of optimum bending specimen dimensions

The idea of this investigation is to assess the influence of the sample aspect ratio on bending behaviour. For the first part of this investigation, samples consisted of 3 plies ($0^o/0^o/0^o$, where 0^o is defined as the fibre direction of UD prepreg being along the loading direction) of UD HexPly® M21 prepreg described in Section 2.2.2 which were cut into 50mm lengths with widths, 30, 40, 50, 60 and 70mm. All of these tests were performed at room temperature and a displacement rate of 30mm/min. Repeats were performed for each case in order to assess experimental reproducibility. Results are shown in Figure 4.A.1. All samples with unexpected bending shapes during buckling, such as unsymmetrical shapes between two edges, wrinkles or vee-shape, were discarded. By observations during tests, it is more difficult to obtain the expected bending shapes for the samples of 50x30, 50x60 and 50x70mm than those of 50x50mm, which is reflected in Figure 4.A.1. It is speculated that unsymmetrical sample dimensions may increase the degree of influence of sample misalignment and hence cause some earlier buckling regions within the sample, leading to unsymmetrical bending shapes. This may suggest that symmetrical sample dimensions, such as 50x50mm, are suitable.

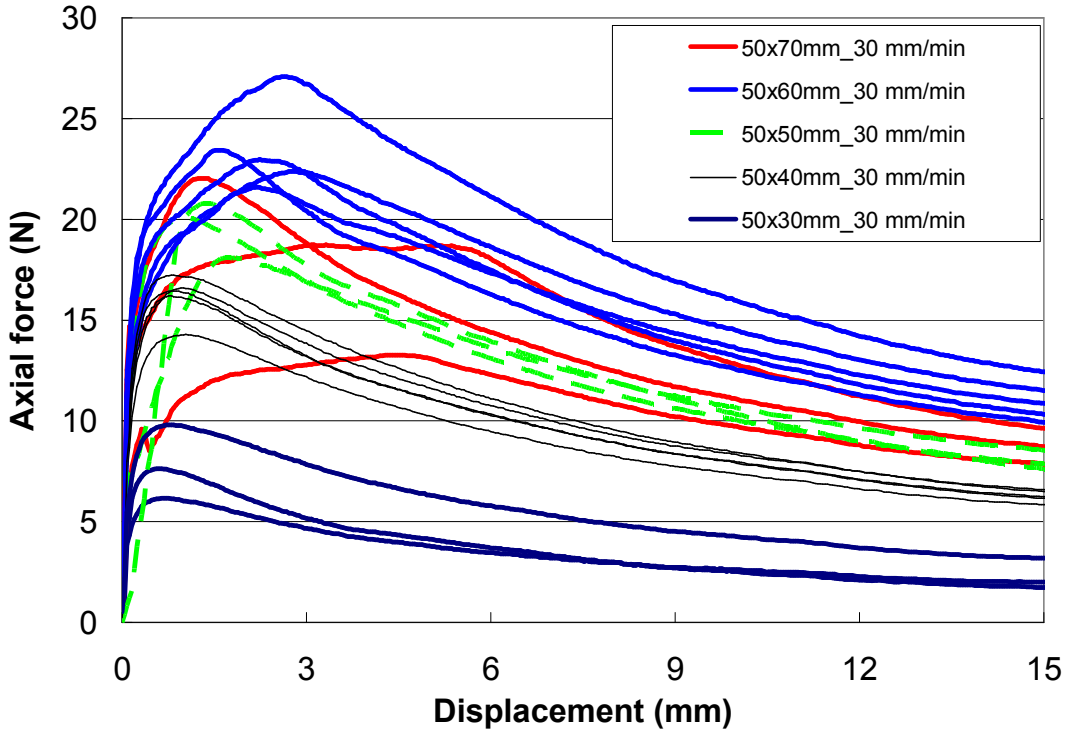

Figure 4.A.1. The crosshead force versus displacement from buckling tests at room temperature, 30mm/min displacement rate, for samples with various widths, 50x30, 50x40, 50x50, 50x60 and 50x70mm respectively.

The average force of all repeats for each case at 8 mm displacement from Figure 4.A.1 is normalised by the width of the sample and plotted against the sample width, as shown in Figure 4.A.2. It seems that the normalised force starts to stabilise from a width of 40mm, but becomes scattered unexpectedly at 60mm onwards. Due to difficulties in obtaining an expected bending shape for samples with 50x70 and 50x80mm mentioned above, the suitable sample width may be less 60 mm for a length of 50 mm. From Figure 4.A.2, the samples of 50x40 and 50x50 mm have a relatively equal normalised force, which might suggest that sample width between 40 and 60mm could be suitable for sample length 50mm, which supports the suggestion of 50x50mm.

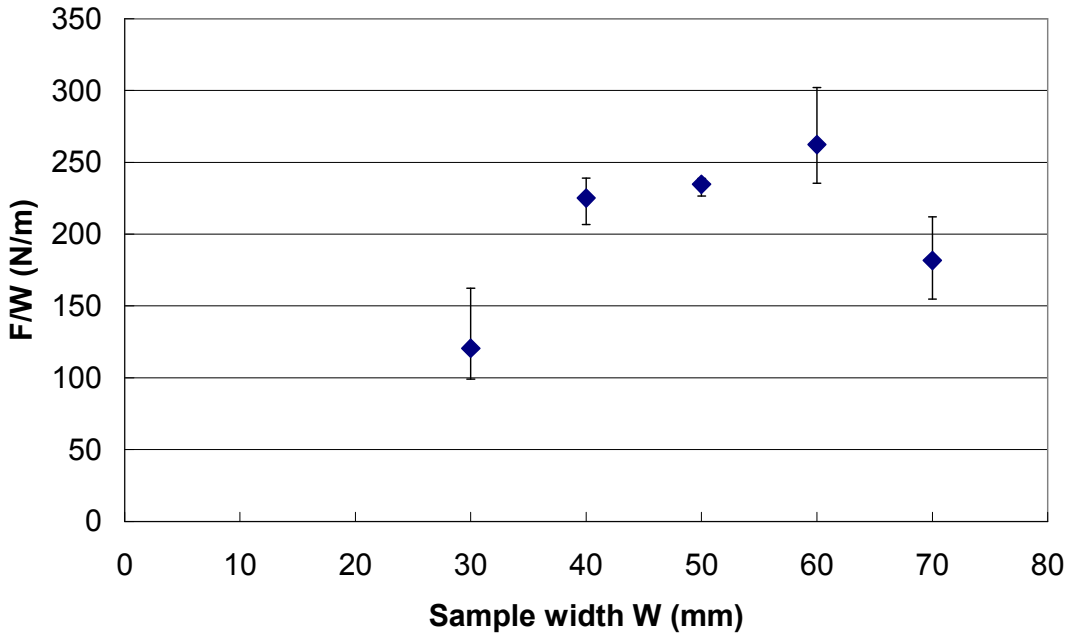

Figure 4.A.2. The average crosshead force at 8 mm displacement normalised by aspect ratio (R) versus the sample width from bending tests at room temperature, 30mm/min displacement rate, for samples with various widths, 50x30, 50x40, 50x50, 50x60 and 50x70mm respectively. Error bars indicate maximum and minimum values.

For the second part of this investigation, samples ($0^o/0^o/0^o$) were cut into 50mm widths with lengths, 30, 40, 50, 60, 70 and 80mm. Test conditions are the same. Experimental results are shown in Figure 4.A.3. There are also some difficulties in obtaining expected bending shapes for highly unsymmetrical sample dimensions, such as 70x50 and 80x50mm, although their force curves seem reasonable (Figure 4.A.3). For samples of 30x50mm, both bending shapes and force curves are unusual. It may be suggested that more symmetric sample dimensions are more suitable.

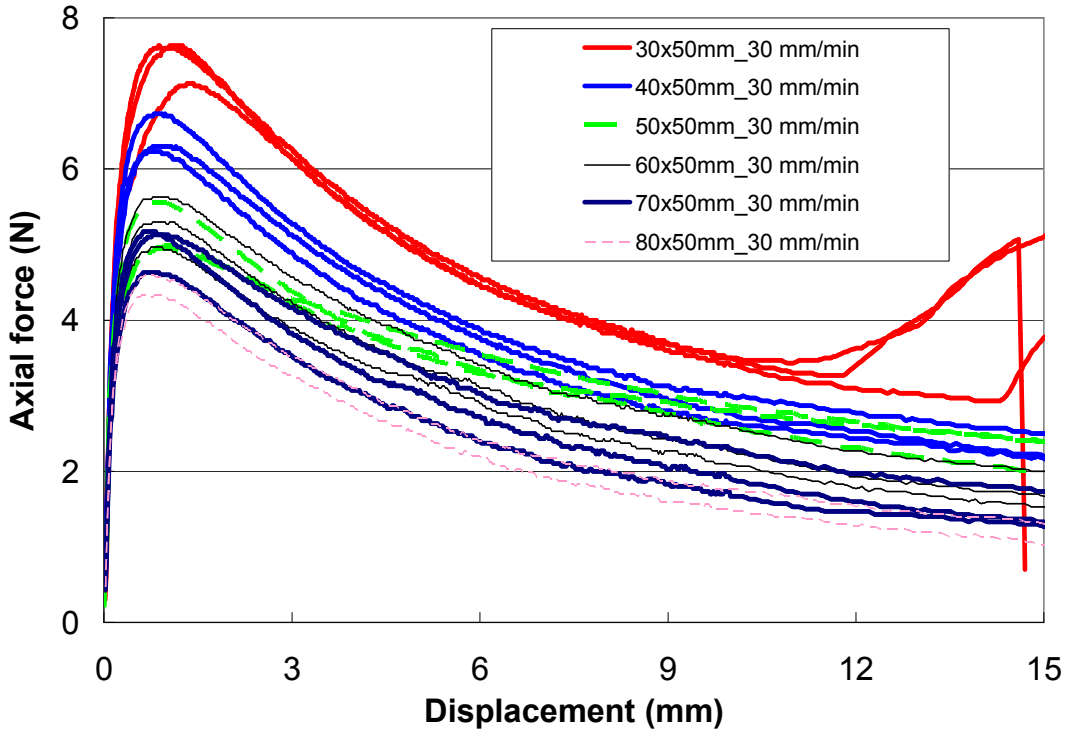

Figure 4.A.3. The crosshead force versus displacement from buckling tests at room temperature, 30mm/min of displacement rate, for samples with various lengths, 30x50, 40x50, 50x50, 60x50, 70x50 and 80x50mm respectively.

In conclusion, symmetric sample dimensions of 50x50 mm may be considered as the optimum dimensions for buckling tests.

Appendix 4.B: Experimental reproducibility of buckling tests

To assess reproducibility (defined as the difference between the maximum and minimum values divided by the average) for this test method, all tests were performed with three repeats. These three repeats were performed not only under the same testing conditions but also using the samples cut from the same batch (ensure the same curing history and same fibre orientation within lay-ups), using the same heat-up time (the difference between repeats is less than 1 minute), etc.

To investigate reproducibility of buckling tests, three aspects could be explored: rate dependence, temperature dependence and lay-up effects. Due to noise in force curves at high temperatures (wavy force curves) shown in Figure 4.6, temperature dependence of reproducibility might not be analysed accurately, and hence will not be presented here.

Reproducibility calculated from Figure 4.4 for both materials is shown in Figure 4.B.1. For material HexcelPly® 8552 UD prepreg, except at a displacement rate of 300mm/min reproducibility increases as the displacement rate increases by a logarithmic relation. For material HexcelPly® M21 UD prepreg, except for a displacement rate of 10mm/min reproducibility increases as the displacement rate increases by a linear relation. It can be seen that for material HexcelPly® 8552 UD prepreg the displacement rate has a significant effect on reproducibility which ranges from 10.4% to 59.5%, whereas for

material HexcelPly® M21 UD prepreg reproducibility is less significantly influenced by the rate.

From Figure 4.7, reproducibility for both materials can be calculated, as shown in Table 4.B.1. All calculated data for both materials seem scattered, which may suggest that the lay-up might not influence reproducibility for this test method.

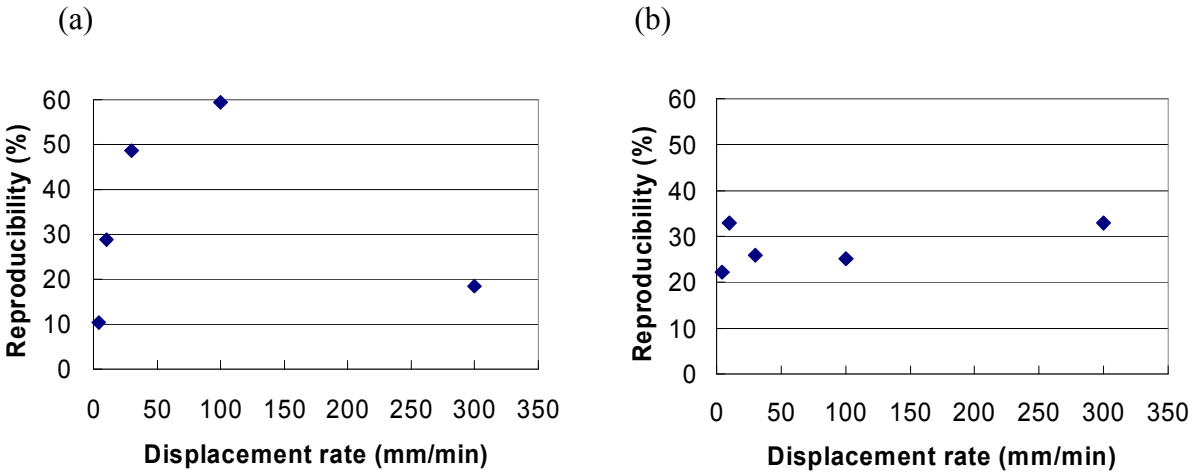

Figure 4.B.1. Reproducibility of bending tests for 50x50mm samples with 0/0/0° lay-up, performed at room temperature and various displacement rates, 4.4, 10, 30, 100 and 300 mm/min respectively. (a) HexPly® 8552 (b) HexPly® M21. Note that reproducibility is calculated at a displacement 8mm.

Table 4.B.1. Reproducibility of bending tests for the samples with different lay-ups for HexPly® 8552 and HexPly® M21. Note that reproducibility is calculated at a displacement of 8mm.

Lay-up	Reproducibility- HexPly® 8552 (%)	Reproducibility- HexPly® M21 (%)
0/0/0°	28.9	32.9
0/90/0°	25.4	19.5
45/0/-45°	51.8	30.9

Appendix 4.C: Derivation of the equation of offset curves for bending shape

Curve 1 (known): $y_1 = a\left[\cos\left(\frac{2\pi x_1}{L}\right) - 1\right]$ (In Figure 4.C.1, a = 2.63, L = 27 and thickness h =3) Curve 2 (unknown): $y_2 = f(x_2)$

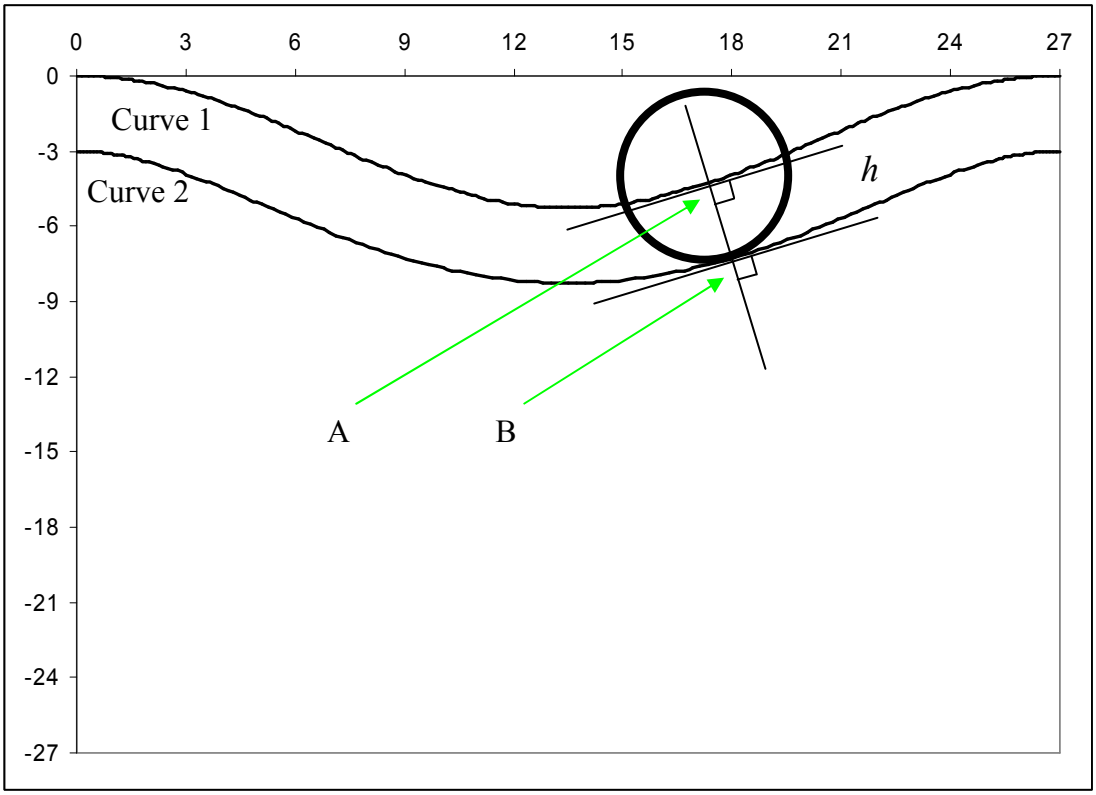

Figure 4.C.1. Schematic of two offset curves. The coordinates of points A and B are (x_1, y_1) and (x_2, y_2) respectively. Both are any points on the curve 1 and 2 respectively. thickness = h (offset distance)

The tangent of curve 1 at point A:

$$\tan\psi = \frac{dy_1}{dx_1} \qquad \textbf{(4.C.1)}$$

The slope of AB:

$$\frac{y_2 - y_1}{x_2 - x_1} = -\frac{1}{\tan\psi} \tag{4.C.2}$$

The distance AB:

$$h = \sqrt{(x_2 - x_1)^2 + (y_2 - y_1)^2} \tag{4.C.3}$$

Then Equations (4.C.2) and (4.C.3):

$$h^2 = (x_2 - x_1)^2\left(1 + \frac{1}{\tan^2\psi}\right) \tag{4.C.4}$$

Therefore:

$$x_2 = x_1 + h\sin\psi \tag{4.C.5}$$

Equations (4.C.2) and (4.C.5):

$$y_2 = y_1 - h\cos\psi \tag{4.C.6}$$

$$\tan\psi = -\frac{2\pi a}{L}\sin\frac{2\pi x_1}{L} \tag{4.C.7}$$

So,

$$\sin\psi = \frac{\tan\psi}{\sqrt{\tan^2\psi + 1}} \text{ and } \cos\psi = \frac{1}{\sqrt{\tan^2\psi + 1}} \tag{4.C.8}$$

From Equations (4.C.5), (4.C.6) and (4.C.8),

$$y_2 = a\left[\cos\frac{2\pi\left(x_2 - \frac{h\tan\psi}{\sqrt{\tan^2\psi + 1}}\right)}{L} - 1\right] - \frac{h}{\sqrt{\tan^2\psi + 1}} \tag{4.C.9}$$

In Figure 4.C.1, curve 2 is plotted using equation (4.C.9).